Muon Identification and B Physics Studies at the Tevatron Collider Experiment DØ

Chunhui Luo

Submitted to the faculty of the Graduate School
in partial fulfillment of the requirements
for the degree
Doctor of Philosophy
in the Department of Physics,
Indiana University

September, 2003

Accepted by the Graduate Faculty, Indiana University, in partial fulfillment of the requirements of the degree of Doctor of Philosophy.

Doctoral
Committee

Dr. Daria Zieminska
(Chairman)

Professor Rick Van Kooten

Professor Harold Ogren

July 8, 2003

Professor Andrzej Zieminski

To my parents and wife, and first baby Alex Junbin Luo.

Acknowledgements

First of all, my deepest gratitude goes to my advisors, Dr. Daria Zieminska and Professor Andrzej Zieminski. Throughout the years of my Ph.D. study, they were always willing to mentor, encourage, and support me. Their expertise and enthusiasm in the field of high energy physics, as well as their unique insightful way of approaching problems, are among the most valuable resources for me.

I would like to thank Prof. Harold Ogren and Dr. Fred Luehring for their constructive advice and expert suggestions concerning this thesis, I would like to thank Prof. Rick Van Kooten, who gave plenty of comments and corrections so that the dissertation became more and more mature.

I would also like to thank Dr. Serban Protopopescu for his kind help and instruction during my development of reconstruction software and analysis software. I have benefited from the frequent and valuable help of Professor Darien R. Wood and have always admired his capacity for hard work, his willingness to help. I appreciate the help provided by Herman Haggerty and Tom Marshall, when I have questions regarding the DØ hardware.

I would also like to thank Dave Hedin, Pushpalatha Bhat, Richard Jesik, Kin Yip, Ken Johns, Brad Abbott, Vivek Jain, Qizhong Li. They give me a great help in my research.

Finally, I would like to thank all of my friends through out the years. Especially, Jundong Huang, Abaz Kryemadhi, Yi Jiang, Xiaojian Zhang, Zhongmin Wang, etc. Discussions with them are very helpful.

Abstract

This dissertation describes muon particle identification and studies of final states, including the di-muon resonance J/ψ at the DØ experiment at the Fermilab Tevatron Collider.

Time-to-distance relation studies for the muon proportional drift tubes have led to a parametrization allowing the determination of the muon trajectory to an accuracy of 400 microns.

I present three early results based on the di-muon data collected in the running period 2001—2002: the first measurement of the inclusive J/ψ production cross section over an extended rapidity range (0.0-1.8) at $\sqrt{s}$=1.96 TeV, a preliminary measurement of the B_s^0 meson lifetime by using the decay mode $B_s^0 \rightarrow J/\psi\phi$, and a preliminary measurement of the B_d^0 meson lifetime via the decay mode $B_d^0 \rightarrow J/\psi K^*$.

Contents

List of Tables

List of Figures

Chapter 1

Introduction

This thesis concerns studies of elementary particles, the basic building blocks of matter, and their interactions. This is a very active field with experiments involving hundreds of physicists and taking many years to complete.

This chapter contains a brief summary of the current status of investigations and is based on several recent review papers [1] [2].

Experiments of the past decade have verified the $SU(3)_C \times SU(2)_L \times U(1)_Y$ gauge structure of elementary particle interactions, in a comprehensive and very precise way. By comparison, tests of the flavor interactions are not yet nearly as broad or detailed. The Standard Model, in which quark masses and mixing arise from Yukawa interactions with the Higgs field, still serves as the current foundation for discussing flavor physics. The standard flavor sector leads to the Cabibbo-Kobayashi-Maskawa (CKM) matrix, which contains a CP–violating parameter for three generations. By construction, the CKM matrix is unitary, which implies several relations among its entries and, hence, between CP–conserving and CP–violating observables.

Run II of the Tevatron collider started in March 2001. The DØ detector has undergone substantial upgrades, particularly in the tracking system, forward muon system and triggers. The improvement allows DØ to handle the higher rates as well as to better measure the products of the $p\overline{p}$ interactions.

With these enhancements, the DØ Run II has made significant progress in the past two years, and is expected to achieve spectacular physics results in the next six years. After

11 months of detector commissioning, timing, electronics improvement, data acquisition system and offline system development, the central tracking began to operate in February 2002. From May 2002 physics quality data have been collected, leading already to some exciting results.

After joining the DØ collaboration in 1998, the author contributed in several areas:

- Muon identification and analysis software;
- Time-to-distance studies for muon chambers;
- Level-3 muon software;
- Global monitoring software;
- Monte Carlo production;
- Computing management.

The original planned physics project was CP–violation studies in $B_d^0 \to J/\psi K_s$. However, due to the delay in the experiment's start and lower than expected luminosity delivered by December 2002, two other preliminary physics analysis were completed as theses topics. These are:

- J/ψ cross section measurement;
- B_s and B_d lifetime measurement.

The physics issues relevant for these analyses are discussed in chapter 2. The main features of the detector and software are discussed in chapter 3 and chapter 4, respectively. In chapter 5, the author concentrate on muon reconstruction. Determination of the time-to-distance relationship for the muon proportional drift tubes is presented in chapter 6. The physics results are discussed in chapters 7 through 9. First the author presents the J/ψ cross section measurement over an extended rapidity region (0.0–1.8) at $\sqrt{s}$=1.96 TeV, which is based on the first 5 pb^{-1} (taken between Feburary – May 2002) of Run II data. The author also discusses the J/ψ polarization. In chapter 8 a preliminary measurement of the B_s meson lifetime using the decay mode $B_s^0 \rightarrow J/\psi\phi$ is presented. Some further studies are also discussed in this chapter. B_d meson lifetime measurement, using the decay mode $B_d^0 \rightarrow J/\psi K^*$, is presented in chapter 9. The B_s and B_d lifetime measurements are based on the data taken in September – December 2002, with 47 pb^{-1} of integrated luminosity.

Finally, in the last chapter, the author summarizes the main results of our software and physics analysis and presents conclusions.

Chapter 2

Physics Topics

The physics goals of DØ Run II include: (1) the precise study of the known building blocks of the Standard Model, such as b quark mixing and CP violation, studies of the top quark, improvements in the understanding of QCD, precision measurements of properties of the W and Z bosons; and (2) the direct search for the light Higgs boson, search for new particles, forces beyond the Standard Model, such as that predicted by supersymmetry, extra dimensions, and other phenomena.

In this chapter, the Standard Model is first reviewed in section 2.1. CP violation in the Standard Model is then discussed in section 2.2. Section 2.3 gives a summary of expectations for measurements of the unitarity triangle based on global fits of kaon mixing and CP conserving observables in B physics.

The author's service work at DØ included muon calibration, muon reconstruction and analysis software development. B physics studies were therefore pursued. The physics topics involved are quarkonium production, which is discussed in section 2.4, and B_s physics, discussed in section 2.5 and 2.6.

2.1 Standard Model

The Standard Model (SM)[1] is a Lagrangian Quantum Field Theory based upon the idea of local gauge invariance [5] [6]. The SM Lagrangian is invariant under rotations and translations, Lorentz transformations, and the product of charge conjugation-parity-time reversal (CPT) transformations. Each of these symmetries corresponds to some conserved quantity: translational and rotational invariance imply conservation of momentum and angular momentum; Lorentz invariance implies the conservation of 4-momentum; and invariance under CPT transformations implies that the product of CPT eigenvalues is a conserved quantum number. These symmetries are respected by all the particles of the SM, independent of their internal quantum numbers, and their conservation is believed to be exact.

The gauge symmetry group of the Standard Model is $SU(3)_C \times SU(2)_L \times U(1)_Y$. $SU(3)_C$ is the symmetry group describing the strong (color) interactions, whereas $SU(2)_L \times U(1)_Y$ represents the symmetry group of the electroweak sector describing the weak and electromagnetic interactions.

The particle content of the model may be classified in terms of two groups, namely the fundamental fermions (spin $\frac{1}{2}$) and the gauge vector bosons (spin 1). The fundamental fermions are subdivided into two parallel classes of particles called quarks and leptons. Experiments have demonstrated that there are several species, or flavors, of quarks and leptons. The fermions are grouped into three parallel sets of lepton and quark doublets.

$$\mathbf{Q}uarks = \begin{pmatrix} u \\ d \end{pmatrix} \begin{pmatrix} c \\ s \end{pmatrix} \begin{pmatrix} t \\ b \end{pmatrix} \qquad \mathbf{L}eptons = \begin{pmatrix} \nu_e \\ e \end{pmatrix} \begin{pmatrix} \nu_\mu \\ \mu \end{pmatrix} \begin{pmatrix} \nu_\tau \\ \tau \end{pmatrix}. \tag{2.1}$$

There are three generations of quarks: the down-type quarks (d, s, b), and up-type quarks (u, c, t), with each type of quark exhibiting a further internal degree of freedom called color. Each quark flavor may exist in one of three possible color states. There are three generations of leptons, which are the charged leptons (e, μ, τ), and the neutral neutrinos (ν_e, ν_μ, ν_τ). Tables 2.1 and 2.2 list the six distinct types, or flavors of leptons

---

[1] This introduction to the Standard Model is based on Refs. [1] [2] [3].

and quarks. In Table 2.1, evidence of neutrino mixing leds to non-zero neutrino masses, only mass differences are measured.

Particle Name	Symbol	Generation	Charge	Mass (MeV)
electron	e^-	1	-1	0.511
electron neutrino	ν_e		0	≤ 0.007
muon	μ^-	2	-1	105.7
muon neutrino	ν_μ		0	≤ 0.27
tau	τ^-	3	-1	1777
tau neutrino	ν_τ		0	≤ 31

Table 2.1: Properties of fundamental leptons.

Particle Name	Symbol	Generation	Charge	Mass
up	u	1	2/3	$1.5 \sim 4.5$ MeV
down	d		$-1/3$	$5.0 \sim 8.5$ MeV
charm	c	2	2/3	$1.0 \sim 1.4$ GeV
strange	s		$-1/3$	$80 \sim 155$ MeV
top	t	3	2/3	173.5 ± 5.1 GeV
bottom	b		$-1/3$	$4.0 \sim 4.5$ GeV

Table 2.2: Properties of fundamental quarks

The forces between these elementary particles are mediated by the gauge vector bosons. Currently there are four known forces. In order of strength, they are the strong, electromagnetic, weak and gravitational force and their properties are shown in Table 2.3.

Electromagnetic interactions are described by Quantum Electrodynamics (QED), while strong interactions are described by Quantum Chromodynamics (QCD) [7]. Two properties which characterize QCD are called asymptotic freedom and infrared slavery. The first means that as $Q^2 \to \infty$ where Q is defined as the magnitude of the momentum transfer in a particle collision, the strong coupling constant $\alpha_s(Q^2) \to 0$ and the quarks appear "free".

The second is that in the limit as $Q^2 \to 0$ quarks are confined within hadrons. Quarks are assumed to carry one color charge of three colors (red, green and blue). While quarks carry color, the observed spectra of hadrons that they form appear as color neutral objects.

The strong or color force is responsible for holding the quarks together inside mesons and baryons. The strong force carriers are the gluons, which obey an SU(3) symmetry; therefore, there are $3^2 - 1$ =8 different color combinations, they are: $R\bar{G}$,$R\bar{B}$,$G\bar{R}$, $G\bar{B}$,$B\bar{R}$,$B\bar{G}$, $\sqrt{1/2}(R\bar{R} - G\bar{G})$, and $\sqrt{1/6}(R\bar{R} + G\bar{G} - 2B\bar{B})$. Because the $SU(3)_C$ symmetry of the color interaction is believed to be exact, the gluons are massless particles.

The electroweak sector of the Standard Model is also called the Glashow-Weinberg-Salam Model [8]. It is a gauge theory that unites the weak and electromagnetic interactions. The gauge symmetry group $SU(2)_L \times U(1)_Y$ requires $(2^2 - 1) + (1^2) = 4$ massless gauge vector bosons. However, in order to describe weak interaction phenomenology, it is required that the vector bosons mediating this force acquire a non-zero mass. This is accomplished through the process of spontaneous symmetry breaking [9], which is implemented via the so-called Higgs Mechanism [10]. The Higgs Mechanism requires the introduction of complex

Force	Carrier	Range (cm)	Strength	Mass (GeV)	Charge	Spin
Strong	gluons	10^{-13}	1	0	0	1
EM	photon	infinite	10^{-2}	0	0	1
Weak	W^+	10^{-16}	10^{-6}	80.4	1	1
	W^-			80.4	-1	1
	Z^0			91.2	0	1
Gravity	graviton	infinite	10^{-40}	0	0	2

Table 2.3: Properties of the four fundamental forces

scalar fields. By allowing the scalar field to acquire a non-zero vacuum expectation value, 3 of the 4 gauge vector bosons acquire a mass and these are identified with the $W^{\pm}$ (mediating charged-current weak interactions), and the Z^0 (mediating the neutral-current interactions). The remaining massless gauge vector boson is identified with the photon, γ (mediating the electromagnetic interactions). There remains one neutral scalar field which is called the Higgs field – associated with the Higgs boson. To date, this particle has not been experimentally observed, and it will be the main task of the Tevatron Run II at Fermilab and the Large Hadron Collider (LHC) at CERN.

2.2 *CP* Violation from a Unitary CKM Matrix

Within the framework of the Standard Model, CP violation[2] arises through a non-trivial phase in the Cabibbo-Kobayashi-Maskawa (CKM) mixing matrix. The CKM matrix is a unitary matrix that rotates the electroweak eigenstates into the mass eigenstates. To emphasize the physical transitions associated with the CKM matrix, it is usually written

$$V = \begin{pmatrix} V_{ud} & V_{us} & V_{ub} \\ V_{cd} & V_{cs} & V_{cb} \\ V_{td} & V_{ts} & V_{tb} \end{pmatrix}, \tag{2.2}$$

so that the entries are labeled by the quark flavors. The interaction amplitude represented by the vertex at which a b quark decays to a W^- boson and c quark is proportional to V_{cb}; similarly, the vertex at which a c quark decays to a W^+ boson and s quark is proportional

---

[2] This introduction to CP violation is based on Ref. [1]

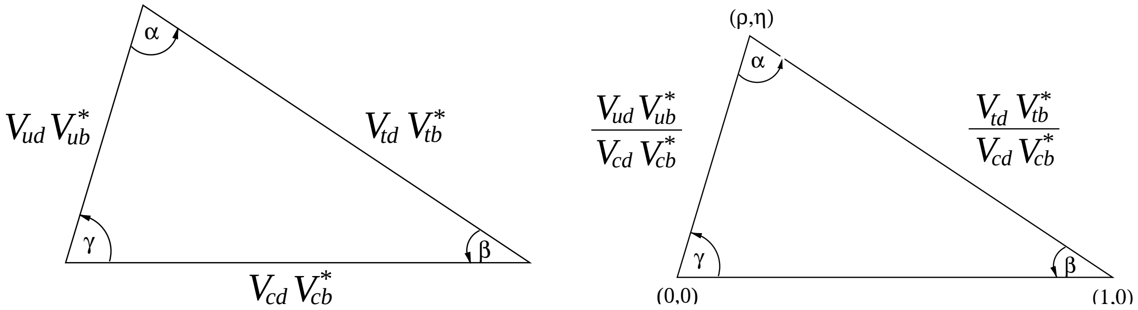

Figure 2.1: The unitarity triangle. The version on the left directly expresses Eq. (2.3). The rescaled version shows the definition of $(\bar{\rho}, \bar{\eta})$.

to V_{cs}^*. Because V is unitary, $|V_{ud}|^2 + |V_{us}|^2 + |V_{ub}|^2 = 1$, and similarly for all other rows and columns. These constraints give information on unmeasured (or poorly measured) elements of V. For example, because $|V_{cb}|$ and $|V_{ub}|$ are known to be small, $|V_{tb}|$ should be very close to 1—if, indeed, there are only three generations. Furthermore, $|V_{ts}|$ and $|V_{td}|$ must also be small.

Even more interesting constraints come from the orthogonality of columns (or rows) of a unitary matrix. Taking the first and third columns of V, one has

$$V_{ud}V_{ub}^* + V_{cd}V_{cb}^* + V_{td}V_{tb}^* = 0\,. \qquad (2.3)$$

Equation (2.3) illustrates that the three terms in the sum trace out a triangle on the complex plane. Because it is a consequence of the unitarity property of V, this triangle is called the "unitarity triangle", shown in Fig. 2.1. The lengths of the sides are simply $|V_{ud}V_{ub}^*|$, etc., and the angles are:

$$\alpha = \arg\left[-\frac{V_{td}V_{tb}^*}{V_{ud}V_{ub}^*}\right], \qquad \beta = \arg\left[-\frac{V_{cd}V_{cb}^*}{V_{td}V_{tb}^*}\right], \qquad \gamma = \arg\left[-\frac{V_{ud}V_{ub}^*}{V_{cd}V_{cb}^*}\right]. \qquad (2.4)$$

By construction $\alpha + \beta + \gamma = \pi$.

In the parameterization favored by the Particle Data Book [11],

$$V = \begin{pmatrix} c_{12}c_{13} & s_{12}c_{13} & s_{13}e^{-i\delta_{13}} \\ -s_{12}c_{23} - c_{12}s_{23}s_{13}e^{i\delta_{13}} & c_{12}c_{23} - s_{12}s_{23}s_{13}e^{i\delta_{13}} & s_{23}c_{13} \\ s_{12}s_{23} - c_{12}c_{23}s_{13}e^{i\delta_{13}} & -c_{12}s_{23} - s_{12}c_{23}s_{13}e^{i\delta_{13}} & c_{23}c_{13} \end{pmatrix}, \tag{2.5}$$

where $c_{ij} = \cos\theta_{ij}$ and $s_{ij} = \sin\theta_{ij}$. The real angles θ_{ij} may be chosen so that $0 \leq \theta_{ij} \leq \pi/2$, and the phase δ_{13} so that $0 \leq \delta_{13} < 2\pi$.

A convenient parameterization of the CKM matrix is due to Wolfenstein [12]. It stems from the observation that the measured matrix obeys a hierarchy, with diagonal elements close to 1, and progressively smaller elements away from the diagonal. This hierarchy can be formalized by defining λ, A, ρ, and η via

$$\lambda \equiv s_{12}\,, \qquad A \equiv s_{23}/\lambda^2\,, \qquad \rho + i\eta \equiv s_{13}e^{i\delta_{13}}/A\lambda^3\,. \tag{2.6}$$

From experiment, $\lambda \approx 0.22$, $A \approx 0.8$, and $\sqrt{\rho^2+\eta^2} \approx 0.4$, so it is phenomenologically useful to expand V in powers of λ:

$$V = \begin{pmatrix} 1 - \frac{1}{2}\lambda^2 & \lambda & A\lambda^3(\rho - i\eta) \\ -\lambda & 1 - \frac{1}{2}\lambda^2 & A\lambda^2 \\ A\lambda^3(1-\rho-i\eta) & -A\lambda^2 & 1 \end{pmatrix} + \mathcal{O}(\lambda^4)\,. \tag{2.7}$$

The most interesting correction at $\mathcal{O}(\lambda^4)$ for our purposes is $\operatorname{Im} V_{ts} = -A\lambda^4\eta$. One sees that CKM *CP* violation is small not because δ_{13} is small but because flavor violation must also occur, and flavor violation is suppressed, empirically, by powers of λ.

The unitarity triangle in Eq. (2.3) is special, because its three sides are all of order $A\lambda^3$. The triangle formed from the orthogonality of the first and third rows also has this property, but it is not accessible, because the top quark decays before the mesons needed to measure the angles are bound. The other triangles are all long and thin, with sides $(\lambda, \lambda, A\lambda^5)$ (e.g., for the kaon) or $(\lambda^2, \lambda^2, A\lambda^4)$ (e.g., for the B_s meson).

It is customary to rescale Eq. (2.3) by the common factor $A\lambda^3$, to focus on the less well-determined parameters (ρ, η). In the context of the Wolfenstein parameterization, there are many ways to do this. Since we anticipate precision in experimental measurements, and also in theoretical calculations of some important hadronic transition amplitudes, it is useful to choose an exact rescaling. We choose to divide all three terms in Eq. (2.3) by $V_{cd}V_{cb}^*$ and define

$$\bar{\rho} + i\bar{\eta} \equiv -\frac{V_{ud}V_{ub}^*}{V_{cd}V_{cb}^*}. \tag{2.8}$$

Then the rescaled triangle, also shown in Fig. 2.1, has its apex in the complex plane at $(\bar{\rho}, \bar{\eta})$. The angles of the triangle are easily expressed

$$\alpha = \tan^{-1}\left(\frac{\bar{\eta}}{\bar{\eta}^2 + \bar{\rho}(\bar{\rho} - 1)}\right), \quad \beta = \tan^{-1}\left(\frac{\bar{\eta}}{1 - \bar{\rho}}\right), \quad \gamma = \tan^{-1}\left(\frac{\bar{\eta}}{\bar{\rho}}\right). \tag{2.9}$$

Since $\bar{\eta}$, $\bar{\rho}$, and $1 - \bar{\rho}$ could easily be of comparable size, the angles and, thus, the corresponding CP asymmetries, could be large.

2.3 Standard Model Expectation at the Tevatron

This section outlines what is known about the CKM matrix at the present time, and what the pattern of expectations is for some of the most interesting processes in the Standard Model. The new CP violation tests were reported at the International Conference on High Energy Physics (ICHEP 2002) in Amsterdam. Both the Belle detector group at KEK and the BaBar detector group at SLAC observed subtleties in the decays of B mesons and measured the parameter $\sin 2\beta$. The value measured from both groups, with much better precision than ever before, is approaching the value predicted by the Standard Model, thus erasing past discrepancies [13]. The results and their interpretation were beautifully reviewed at the ICHEP by Yosi Nir [14].

In Nir's review [14] [15], the delicate relations of the unitarity triangle, which are overconstrained by the data, appear to be well obeyed. The dominant source of CP violation in the B and K systems thus appears, on the face of it, to derive from an irremovable complex phase appearing in the mixing matrix for 3 quarks, just as Kobayashi and Maskawa proposed. The intrinsic phase is not small; the relative smallness of CP violation in the K meson system, that for many years is all that has been available to examine, is because this system is fairly well insulated from what is going on in the heavy quark sectors.

The study of CP violation is, at last, experiment driven. Experiments have measured to date three independent CP violating parameters:

- Indirect CP violation in $K \to \pi\pi$ [16] and in $K \to \pi\ell\nu$ decays, given by the famous parameter ε, is referred to as "indirect" CP violation, as it is due to the fact that the K_{L} mass eigenstate is not an eigenstate of the CP operator with eigenvalue -1, but receives a tiny admixture of the CP eigenstate with eigenvalue $+1$.

$$|\varepsilon| = (2.28 \pm 0.02) \times 10^{-3}. \tag{2.10}$$

- Direct CP violation in $K \to \pi\pi$ decays, given by

$$\mathcal{R}e(\varepsilon'/\varepsilon) = (1.66 \pm 0.16) \times 10^{-3}. \tag{2.11}$$

(The world average given in Eq. (2.11) includes the new result from NA48 [17], $\mathcal{R}e(\varepsilon'/\varepsilon) = (1.47 \pm 0.22) \times 10^{-3}$, and previous results from NA31, E731 and KTeV.)

- The CP asymmetry in $B \to \psi K_S$ decay, measured to be:

$$\sin 2\beta = \mathcal{I}m\lambda_{\psi K} = 0.734 \pm 0.054. \tag{2.12}$$

(The world average given in Eq. (2.12) includes the new results from Belle [18], $\mathcal{I}m\lambda_{\psi K} = 0.719 \pm 0.074 \pm 0.035$, and BaBar [19], $\mathcal{I}m\lambda_{\psi K} = 0.741 \pm 0.067 \pm 0.033$, and previous results from OPAL, ALEPH and CDF.)

In addition, CP asymmetries in many other modes (neutral B decays into final CP eigenstates and non-CP eigenstates and charged B decays) have been searched for. We describe the implications of the new data for our theoretical understanding of CP violation.

Fig. 2.2 shows the $\bar{\rho}$-$\bar{\eta}$ plane. The radius of the large circles centered at $(1, 0)$ is proportional to $|V_{td}|$. The large annulus is from the measurement of Δm_d. The small annulus

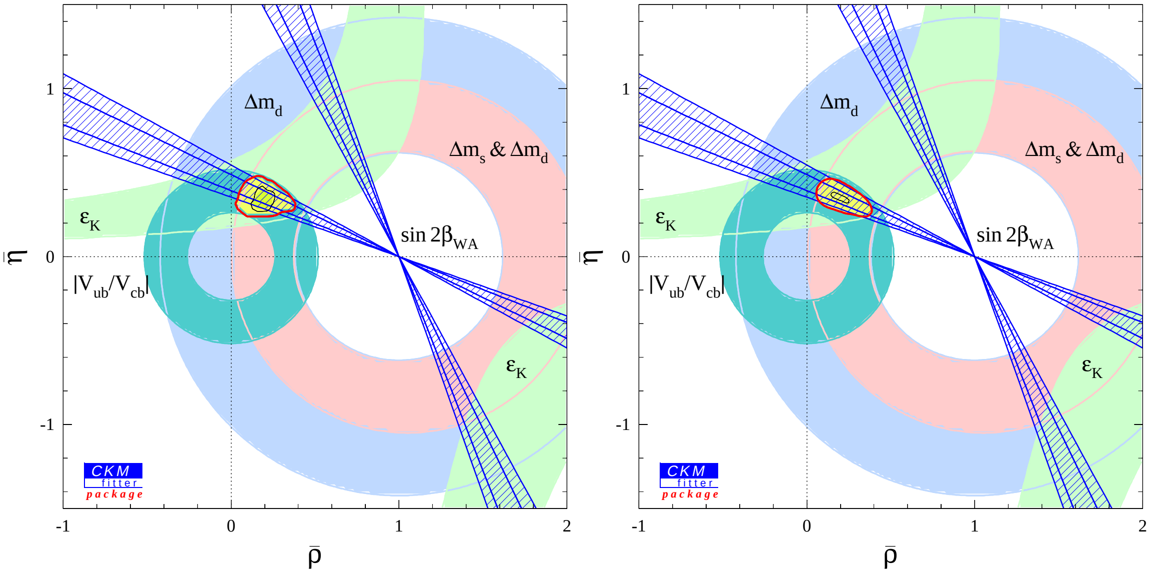

Figure 2.2: Constraints on the $(\bar{\rho},\bar{\eta})$ parameters from (left) CP conserving and the ε observables compared to the $\mathcal{I}m\lambda_{\psi K}$ constraint, and (right) from all observables.

that lies inside it is from the ratio $\Delta m_s/\Delta m_d$ and Δm_d combined, using the current lower bound on Δm_s. The measurement of Δm_s at the Tevatron will reduce the width of this annulus by about a half, making it one of the most precise measurements in the $\bar{\rho}$-$\bar{\eta}$ plane.

Within the Standard Model, there is a single CP violating parameter. Therefore, roughly speaking, a measurement of a single CP violating observable simply determines the value of this parameter. This situation is demonstrated in the left panel of Figure 2.2, where the constraints from all but the $\mathcal{I}m\lambda_{\psi K}$-measurement are used to produce an allowed range in the $(\bar{\rho},\bar{\eta})$ plane. A second measurement of a CP violating observable tests this mechanism, as demonstrated in the same Figure by overlaying the constraint from the measurement of $\mathcal{I}m\lambda_{\psi K}$. The allowed region in the $(\bar{\rho},\bar{\eta})$ plane from the combination of all observables is shown in the right panel of Figure 2.2. We can draw conclusions:

- The CKM matrix provides a consistent picture of all the measured flavor and CP violating processes.
- The recent measurement of $\mathcal{I}m\lambda_{\psi K}$ adds a significant constraint.

The time behavior [20] of $B^0-\bar{B}^0$ oscillations has been studied and precisely measured in the B_d^0 sector. The oscillation frequency Δm_d is known with a precision of about 1%. $B_s^0-\bar{B}_s^0$ oscillations have not been measured so far, but this search has pushed the experimental limit on the oscillation frequency Δm_s to well beyond any initial prediction. Today we know that B_s^0 mesons oscillate at least 30 times faster than B_d^0 mesons. The frequency of the $B_s^0-\bar{B}_s^0$ oscillations will be soon measured at the Tevatron. Nevertheless, the impact of the actual limit on Δm_s for the determination of the unitarity triangle parameters is crucial.

At the e^+e^- B factories operating at the $\Upsilon(4S)$ resonance, no B_s mesons are accessible, since $\Upsilon(4S)$ states decay only to $B_{u,d}$-mesons, but not to B_s. On the other hand, the physics potential of the B_s system is very promising for hadron machines, where plenty of B_s mesons are produced. Consequently, B_s physics is in some sense the "El Dorado" for B experiments at hadron colliders. There are important differences between the B_d and B_s systems [21]:

- Within the SM, the B_s^0–$\overline{B_s^0}$ mixing phase probes the tiny angle $\delta\gamma$ in the unitarity triangle.

$$\phi_s = -2\delta\gamma = -2\lambda^2\eta = \mathcal{O}(-2^\circ), \tag{2.13}$$

whereas $\phi_d = 2\beta = \mathcal{O}(50^\circ)$.

- A large $x_s \equiv \Delta M_s/\Gamma_s = \mathcal{O}(20)$ is expected in the SM, whereas $x_d = 0.775 \pm 0.012$. The present lower bound on ΔM_s is given as follows [22]:

  $$\Delta M_s > 14.4\,\mathrm{ps}^{-1}\ (95\%\ \mathrm{C.L.}). \tag{2.14}$$

- There may be a sizeable width difference $\Delta\Gamma_s/\Gamma_s = \mathcal{O}(-10\%)$ between the mass eigenstates of the B_s system, whereas $\Delta\Gamma_d$ is negligibly small [23]. The present CDF and LEP results imply [22]

  $$|\Delta\Gamma_s|/\Gamma_s < 0.31\ (95\%\ \mathrm{C.L.}). \tag{2.15}$$

  Interesting applications of $\Delta\Gamma_s$ are extractions of weak phases from "untagged" B_s data samples, where we do not distinguish between initially present B_s^0 or $\overline{B_s^0}$ mesons, as argued in [24].

Run II of the Tevatron is expected to yield interesting results on B_s physics, and should discover B_s^0–$\overline{B_s^0}$ mixing soon, which is an important ingredient for the "standard" analysis of the unitarity triangle. Prominent B_s hadronic decays are $B_s \to J/\psi\phi$, $B_s \to K^+K^-$ and $B_s \to D_s^{\pm}K^{\mp}$.

2.4 Quarkonium Production

Quarkonium production provides insight into the nature of strong interactions. It is a window on the boundary region between perturbative and non-perturbative QCD. Recent advances in the understanding of quarkonium production have been stimulated by the unexpectedly large cross sections for direct J/ψ and ψ' production at large p_T measured at the Fermilab Tevatron [95]. Three types of models have been used to describe charmonium formation [97]: the color-singlet model [29]; the color-evaporation model [30] (and a follow up soft color interaction model [31]); and the color-octet model [32]. In the color-singlet model, the charmonium meson retains the quantum numbers of the produced $c\bar{c}$ pair, and thus each J^{PC} state can only be directly produced via the corresponding hard scattering color-singlet sub-processes. In the color-evaporation model, the directly produced charmonium meson is not constrained to the same J^{PC} state as the $c\bar{c}$ pair produced in the hard scatter because of the emission of soft gluons during the meson's formation. The color-octet mechanism extends the color-singlet approach by taking into account the production of $c\bar{c}$ pairs in a color-octet configuration. The color-octet state evolves into a color-singlet state via emission of soft gluons. These models of charmonium formation lead to different expectations for the production rates and polarization of the charmonium states. A priori, the same sets of parameters should apply to a variety of processes involving quarkonium production, including

1. quarkonium production at Tevatron Collider;
2. quarkonium production in hadron-nucleon collisions at fixed target energies;
3. production polarization measurements;
4. inelastic charmonium production at HERA;

5. BR(Z→prompt $J/\psi + X$) at LEP;
6. associated production of a $J/\psi + \gamma$, double J/ψ production;
7. and related processes such as rapidity gaps in hadronic and ep collisions.

A given quarkonium state is produced by one of the following processes:

- Prompt production (charmonium particle produced at the primary vertex):
  - direct
  - indirect e.g. $\chi_c \to J/\psi\gamma$; $\psi(2S) \to J/\psi\pi^+\pi^-$
- b-quark decays (charmonium particle produced at the secondary vertex).

Charmonium production at the Tevatron has been studied by both the DØ [94] and CDF [95] in Run I. CDF measured the cross section for $p_T^{J/\psi} > 5$ GeV/c and the rapidity range $|y^{J/\psi}| < 0.6$ to be 17.4 ± 2.8 nb. In this kinematic region, 19% of produced J/ψ events are due to $B \to J/\psi$ inclusive decays, and 81% represents prompt J/ψ production. Corresponding numbers for $p_T^{J/\psi} > 8$ GeV/c at the same rapidity range are 2.08 ± 0.17 (stat) ± 0.46 (syst) nb (DØ) and 2.7 ± 0.45 nb (CDF). J/ψ inclusive cross sections were also measured in the forward region: by DØ in the $(2.5 <| \eta^{J/\psi} |< 3.7)$ range [94], and, very recently, by CDF in the $(2.1 <| \eta^{J/\psi} |< 2.6)$ range [96]. Results from the two experiments are consistent.

Most of the detailed studies on the J/ψ production at the Tevatron was done by the CDF Collaboration, which had a much better tracking system and was able to trigger on

J/ψ events with a much lower transverse momentum. The most important of their findings are:

- Direct J/ψ and $\psi(2S)$ production is in excess of the predictions of the Color Singlet Model by a factor ≈ 50.
- The fraction of J/ψ events due to B-hadron decays increases with transverse momentum from 15% at $p_T^{J/\psi} = 5$ GeV/c to close to 40% at 18 GeV.
- Fraction of prompt J/ψ due to χ_c meson decays is approximately 30%.
- J/ψ and $\psi(2S)$ polarization measurements donot appear to support the color octet model prediction that the ψ are transversely polarized at high p_T.

For a recent review of the experimental results on quarkonium production in Run I as well as from other relevant experiments, see Ref. [33].

In Run II, with luminosity increased by a factor of 20, the new tracking system, the expanded and improved muon coverage and the trigger system upgrade, DØ should record millions of J/ψ events. The expected numbers, based on model calculations and normalized to the CDF measurements, are compiled in Ref. [34]. With such impressive statistics we should be able to make definitive statements on various models of quarkonium production.

It was long thought[3], that J/ψ production at high transverse momentum proceeds via the process shown in Fig. 2.3(a), in which a color-singlet $c\bar{c}$ pair is produced. However,

---

[3] based on review by Scott Willenbrock, see Ref. [91].

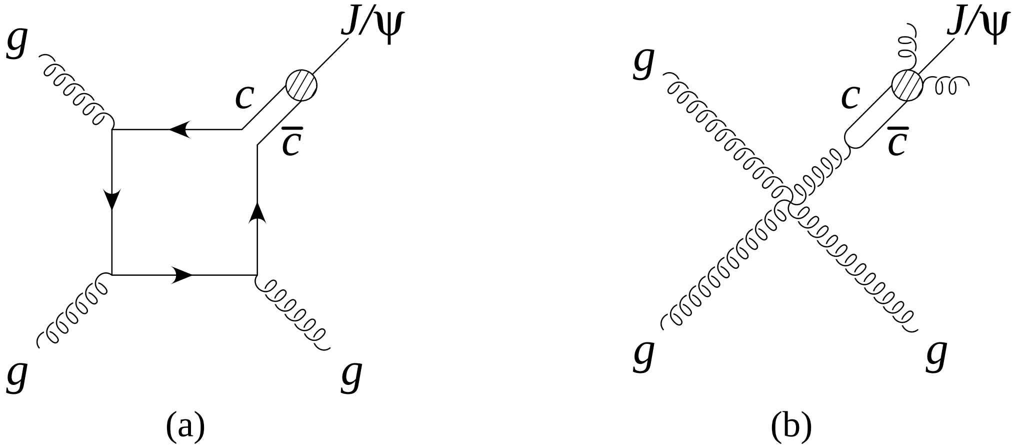

Figure 2.3: J/ψ production at high transverse momentum: (a) color-singlet mechanism, (b) color-octet mechanism.

this process yields a cross section that is more than an order of magnitude too small, and has the wrong transverse-momentum dependence, as shown by the curve labeled "LO color-singlet" in Fig. 2.4. The color-octet model predicts that the dominant production mechanism at high transverse momentum involves a gluon that produces a color-octet $c\bar{c}$ pair, which then fragments into a J/ψ by emitting two or more soft gluons, as shown in Fig. 2.3(b) [25]. For a suitable choice of the hadronic matrix element that parameterizes the fragmentation function, this gives a good description of the data, as shown in Fig. 2.4. This mechanism also makes an unambiguous prediction: the J/ψ should be transversely polarized at high transverse momentum, since it is emanating from a gluon, which has only transverse polarization states. The predicted polarization is shown in Fig. 2.5, along with the CDF data from Run I [27]; the agreement is far from perfect. We hope that the Run II data will put this to a decisive test.

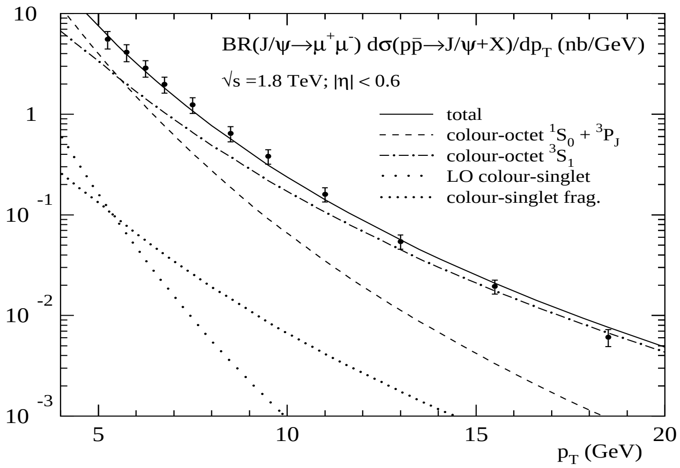

Figure 2.4: J/ψ transverse momentum distribution at the Tevatron (CDF results). The LO color-singlet contribution corresponds to Fig. 2.3(a); the color-octet $^3S_1$ contribution corresponds to Fig. 2.3(b). From Ref. [26].

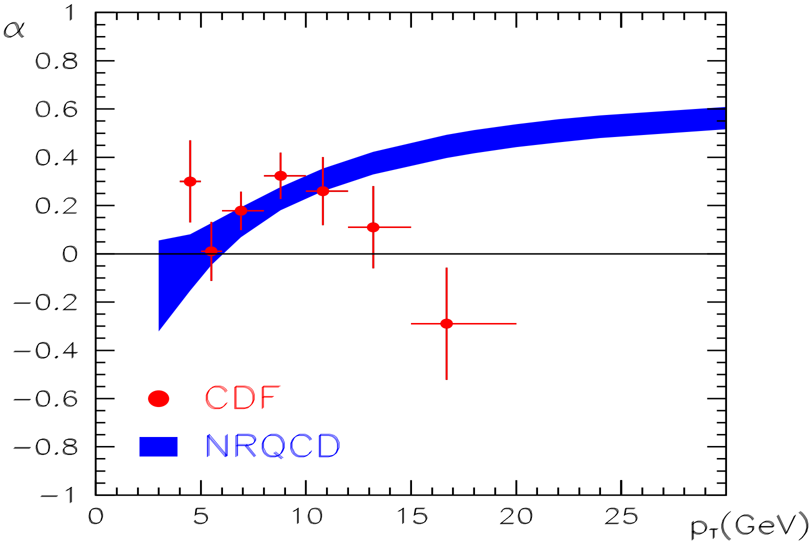

Figure 2.5: Polarization of J/ψ as a function of its transverse momentum (CDF results). The data are compared with the color-octet model. The parameter α describes the J/ψ polarization, see section 7.10.

2.5 B_s Physics

As discussed in section 2.3, CP violation is still one of the least tested aspects of the Standard Model. The greater the variety of CP violating observables measured, the more stringently will the Standard Model be tested. If deviations from the Standard Model predictions are observed, the information from different meson decays will provide crucial clues for the type of new physics that can account for such deviations.

This situation makes the search for CP violation in the B_s^0 decays highly interesting. As mentioned before, only the Tevatron experiments have access to the decays of the B_s mesons and b baryons, which are necessary to complete the program of over constraining the CKM matrix. B_s^0 mesons cannot be studied at the B-factories operating at the $\Upsilon(4S)$ resonance. Hadron colliders, on the other hand, with their high statistics, provide an opportunity to measure CP violation in the B_s^0 system with high accuracy in addition to allowing studies of certain B^0 modes.

The decay $B_s^0 \to J/\psi\phi$, proceeding through the quark subprocess $b \to c\bar{c}s$, is a B_s counterpart of the decay $B_d \to J/\psi K_s^0$. Because the final state is common to B_s^0 and its charge conjugate $\overline{B}_s^0$, the two meson states are expected to mix in such a way that the two CP eigenstates may have a relatively large lifetime difference of up to 20%. It is possible to separate the two CP components of $B_s^0 \to J/\psi\phi$ and thus to measure the lifetime difference by studying the time evolution of the polarization states of the vector mesons in the final state.

The goal is to establish the B_s signal, to measure its cross section and lifetime, and finally, to investigate the possibility of CP violation.

2.6 Decay channel $B_s^0 \to J/\psi\phi$

2.6.1 CP-odd and CP-even components in $B_s \to J/\psi\phi$

The most general amplitude for $B_s \to J/\psi\phi$ can be written in terms of the polarization states of the two vector mesons as [36, 37]:

$$\begin{aligned} A(B_s(t) \to J/\psi\, \phi) &= \frac{A_0(t)}{x}\, \epsilon^{*L}_{J/\psi}\, \epsilon^{*L}_{\phi} \\ &- A_{||}(t)\, \epsilon^{*T}_{J/\psi} \cdot \epsilon^{*T}_{\phi}/\sqrt{2} - iA_{\perp}(t)\, \epsilon^{*}_{J/\psi} \times \epsilon^{*}_{\phi} \cdot \hat{\mathbf{p}}_{\phi}/\sqrt{2}, \end{aligned} \tag{2.16}$$

where $x \equiv p_{J/\psi} \cdot p_\phi/(m_{J/\psi} m_\phi)$ and $\hat{\mathbf{p}}_\phi$ is the unit vector along the direction of motion of ϕ in the rest frame of J/ψ.

Since the "CP violation in decay" of $B_s \to J/\psi\phi$ is vanishing,

$$\overline{A}_0(0) = A_0(0)\,, \qquad \overline{A}_{||}(0) = A_{||}(0)\,, \qquad \overline{A}_{\perp}(0) = -A_{\perp}(0)\,. \tag{2.17}$$

The final state is thus an admixture of different CP eigenstates: A_0 and $A_{||}$ are CP-even amplitudes whereas $A_\perp$ is CP-odd. The decay rate is given by

$$\Gamma(t) \propto |A_0(t)|^2 + |A_{||}(t)|^2 + |A_{\perp}(t)|^2\,, \tag{2.18}$$

where the time evolutions of the individual terms are [38]

$$\begin{aligned} |A_{0,\|}(t)|^2 &= |A_{0,\|}(0)|^2 \left[e^{-\Gamma_L t} - e^{-\overline{\Gamma} t} \sin(\Delta m_s t)\delta\phi\right], \\ |A_\perp(t)|^2 &= |A_\perp(0)|^2 \left[e^{-\Gamma_H t} + e^{-\overline{\Gamma} t} \sin(\Delta m_s t)\delta\phi\right]. \end{aligned} \tag{2.19}$$

Here, $\bar{\Gamma} \equiv \Gamma_s = (\Gamma_L + \Gamma_H)/2$. Note that this is not the average lifetime of B_s as measured through its semileptonic decays [39].

The value of

$$\delta\phi \equiv 2\beta_s \approx 2\lambda^2\eta \approx 0.03 \tag{2.20}$$

is small in the Standard Model[4], so that the terms proportional to $\delta\phi$ in (2.19) can be neglected in the first approximation. The time evolution of (2.18) is then a sum of two exponential decays with lifetimes $1/\Gamma_H$ and $1/\Gamma_L$.

In principle, a fit to the time dependence of the total decay rate (2.18) can give the values of Γ_H and Γ_L separately, but $\Delta\Gamma_s/\bar{\Gamma}$ is expected to be less than 20%, and it is not easy to separate two closely spaced lifetimes. The inclusion of angular information will increase the accuracy in the measurement of $\Delta\Gamma_s$ multi-fold, as we'll see in the section 2.6.2 below.

2.6.2 The transversity angle distribution

Since there are four particles in the final state, the directions of their momenta can define three independent physical angles. Our convention for the definitions of angles [37, 38] is

---

[4] Generalizations of the formulae to the case of new physics can be found in [40].

as shown in Fig. 2.6. The x-axis is the direction of ϕ in the J/ψ rest frame, the z axis is perpendicular to the decay plane of $\phi \to K^+K^-$, and $p_y(K^+) \geq 0$. The coordinates (θ, φ) describe the direction of ℓ^+ in the J/ψ rest frame and ψ is the angle made by $\vec{p}(K^+)$ with the x axis in the ϕ rest frame. With this convention,

$$\mathbf{x} = \mathbf{p}_\phi, \qquad \mathbf{y} = \frac{\mathbf{p}_{K^+} - \mathbf{p}_\phi(\mathbf{p}_\phi \cdot \mathbf{p}_{K^+})}{|\mathbf{p}_{K^+} - \mathbf{p}_\phi(\mathbf{p}_\phi \cdot \mathbf{p}_{K^+})|}, \qquad \mathbf{z} = \mathbf{x} \times \mathbf{y},$$

$$\sin\theta\cos\varphi = \mathbf{p}_{\ell^+} \cdot \mathbf{x}, \qquad \sin\theta\sin\varphi = \mathbf{p}_{\ell^+} \cdot \mathbf{y}, \qquad \cos\theta = \mathbf{p}_{\ell^+} \cdot \mathbf{z}\,. \tag{2.21}$$

Here, the bold-face characters represent unit 3-vectors and everything is measured in the rest frame of J/ψ. Also

$$\cos\psi = -\mathbf{p}'_{K^+} \cdot \mathbf{p}'_{J/\psi}, \tag{2.22}$$

where the primed quantities are unit vectors measured in the rest frame of ϕ.

The θ_T defined here is the transversity angle [41], which separates out the CP-even and CP-odd components. The angular distribution in terms of θ_T is given by Ref [37]:

$$\frac{d\Gamma(t)}{d\cos\theta_T} \propto (|A_0(t)|^2 + |A_{||}(t)|^2)\,\frac{3}{8}\,(1+\cos^2\theta_T) + |A_\perp(t)|^2\,\frac{3}{4}\sin^2\theta_T\,, \tag{2.23}$$

where the time evolutions of the terms are as given in (2.19). The CP-even and CP-odd components are now separated by not only their different lifetimes (which are very close) but also by their decay angular distributions (which are distinctly different). The study of information content about the value of $\Delta\Gamma_s$ in the time and angular measurements [42]

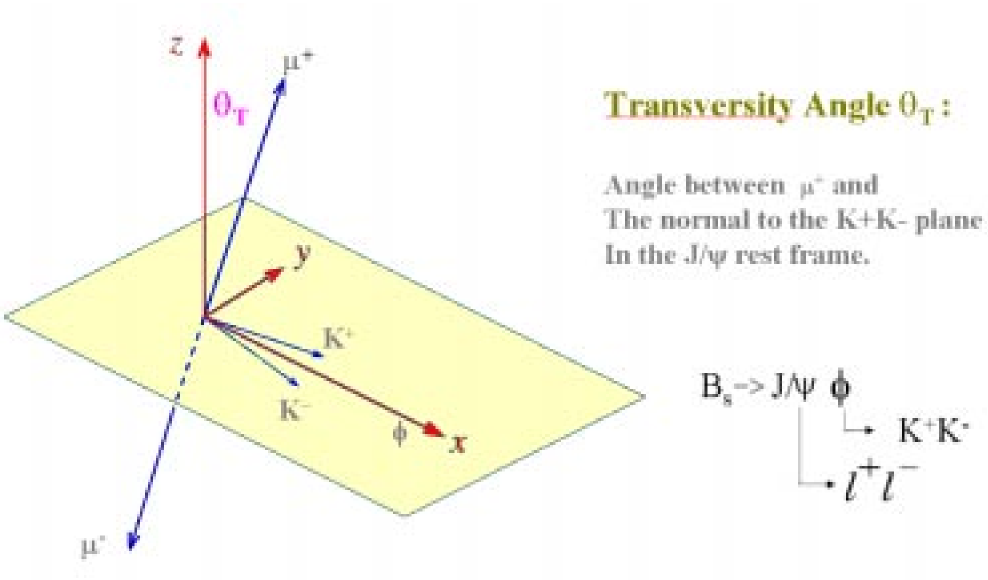

Figure 2.6: The definitions of the transversity angle θ_T.

suggests that, in order to get the same degree of accuracy in $\Delta\Gamma_s$ with only time measurements, one would need about two orders of magnitude more number of events than if both the time and angular measurements were used (see Fig. 3 in Ref. [42]). This indicates that the strategy of selecting one decay mode (e.g. $J/\psi\phi$) and studying its angular distribution will turn out to be more fruitful than trying to combine all CP eigenstate decay modes and determine Γ_H and Γ_L solely from their time evolutions. Note that, in the limiting case of $\Gamma_H = \Gamma_L$, the time evolution by itself cannot separate the CP even and odd components, whereas the angular measurements can.

A fit to the transversity angle distribution (2.23) with its complete time evolution (2.19) also gives the value of $\delta\phi$ and Δm_s, though a better measurement of the latter should be obtained through other decay channels.

The transversity angle distribution (2.23) is valid for any $B_s \to J/\psi(\to \ell^+\ell^-)C_1C_2$ decay, where C_1 and C_2 are (a) self-conjugate particles, or (b) scalars and CP conjugates of each other [41]. The particles C_1 and C_2 need not be the products of any resonance, and their total angular momentum is irrelevant. So the time and transversity angle measurements from all the resonant and non-resonant decays of this form may be combined to gain statistics. Here the values of $(|A_0(0)|^2 + |A_{||}(0)|^2)$ and $|A_\perp(0)|^2$ are just some effective average values, but the decay widths Γ_H and Γ_L are the same for all such decay modes, and hence for the whole data sample.

Chapter 3

The DØ Detector for Run II

This chapter describes the DØ detector and the Tevatron upgrade at Run II. It is based on Diehl's review [28]. Fig. 3.1 shows an elevation view of the DØ detector.

First in section 3.1 we define the coordinate system used in DØ detector. Section 3.2 describes the upgrades to the world's most highest energy accelerator, the Tevatron and its current status. Since the tracking system and muon spectrometer are crucial to B physics, and the author developed software for muon calibration, muon identification, trigger Level-3, global monitoring, and in addition, took many silicon shifts and provided PDT time-to-distance software, emphasis will be put on the muon detector and central tracking system in this chapter. Section 3.3 describes the new silicon vertex system. Section 3.4 describes the upgrades to the central fiber tracking system. Section 3.5 describes upgrades to the calorimeter systems. Section 3.6 describes the upgrades to the muon detectors. Section 3.7 describes the trigger systems. Section 3.8 describes the data acquisition system.

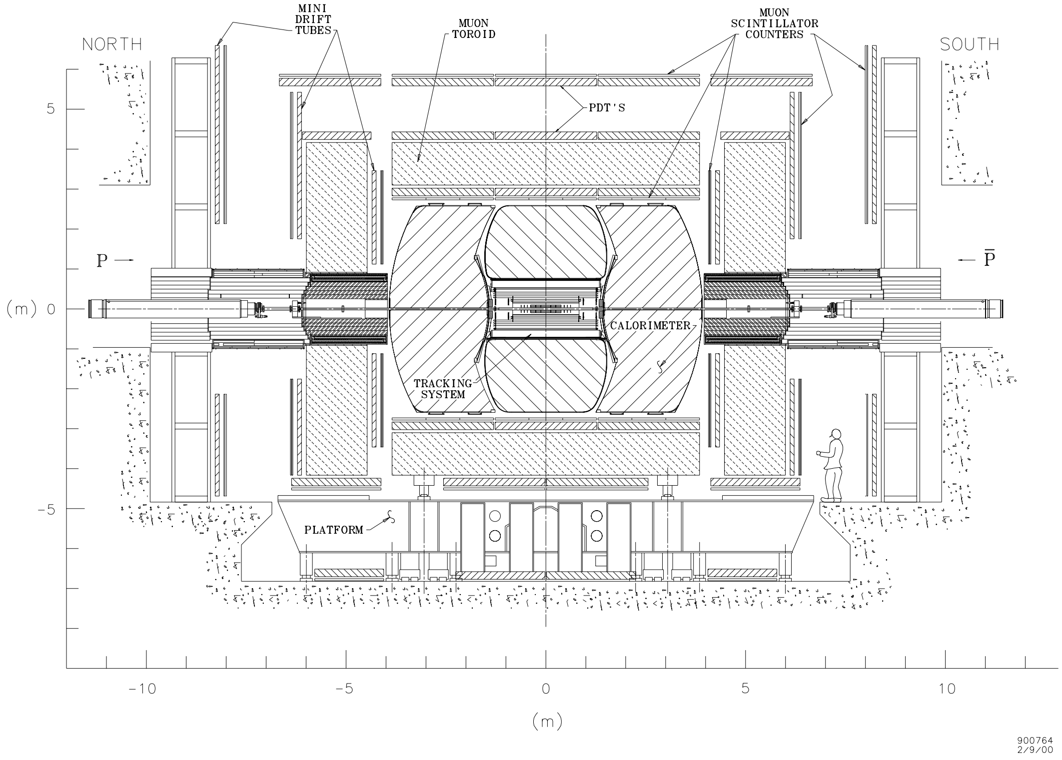

Figure 3.1: Elevation view of the upgraded DØ detector.

3.1 The DØ Coordinate System

At DØ, the primary coordinate system has the z-axis along the proton beam direction, and the positive y-axis pointing up, so that (x, y, z) make a right-handed Cartesian system.

Sometimes cylindrical (r, ϕ, z) coordinates are used, as are spherical (r, ϕ, θ) coordinates, r and θ, giving respectively the perpendicular distance and the angle from the z-axis. The azimuthal coordinate, ϕ, gives the angle from the x-axis in the $x - y$ projection.

The angular variables are defined so that $\theta = 0$ is along the positive z-axis direction, and $\phi = \pi/2$ is parallel to the positive y-axis.

The rapidity y is defined as

$$y = \frac{1}{2} \ln \frac{E + p_z}{E - p_z}, \tag{3.1}$$

where E is the energy, and p_z is the particle momentum on the z-direction.

The variable of pseudorapidity is often convenient, which is defined as

$$\eta = - \ln \tan \frac{\theta}{2}. \tag{3.2}$$

In the limit that $m \ll E$ (where m is the invariant mass), the pseudorapidity approximates the true rapidity.

"Transverse" momentum (p_T) is also commonly used. p_T is the momentum vector projected onto a plane perpendicular to the beam axis:

$$p_T = p \sin \theta. \tag{3.3}$$

This is particularly useful due to the fact that in a high energy collision, many of the products of the collision escape down the beam pipe, so the momenta along the beam of the colliding partons are unknown. However, their transverse momenta are very small compared to their momenta along the beam, so momentum can be considered to be conserved in the transverse plane.

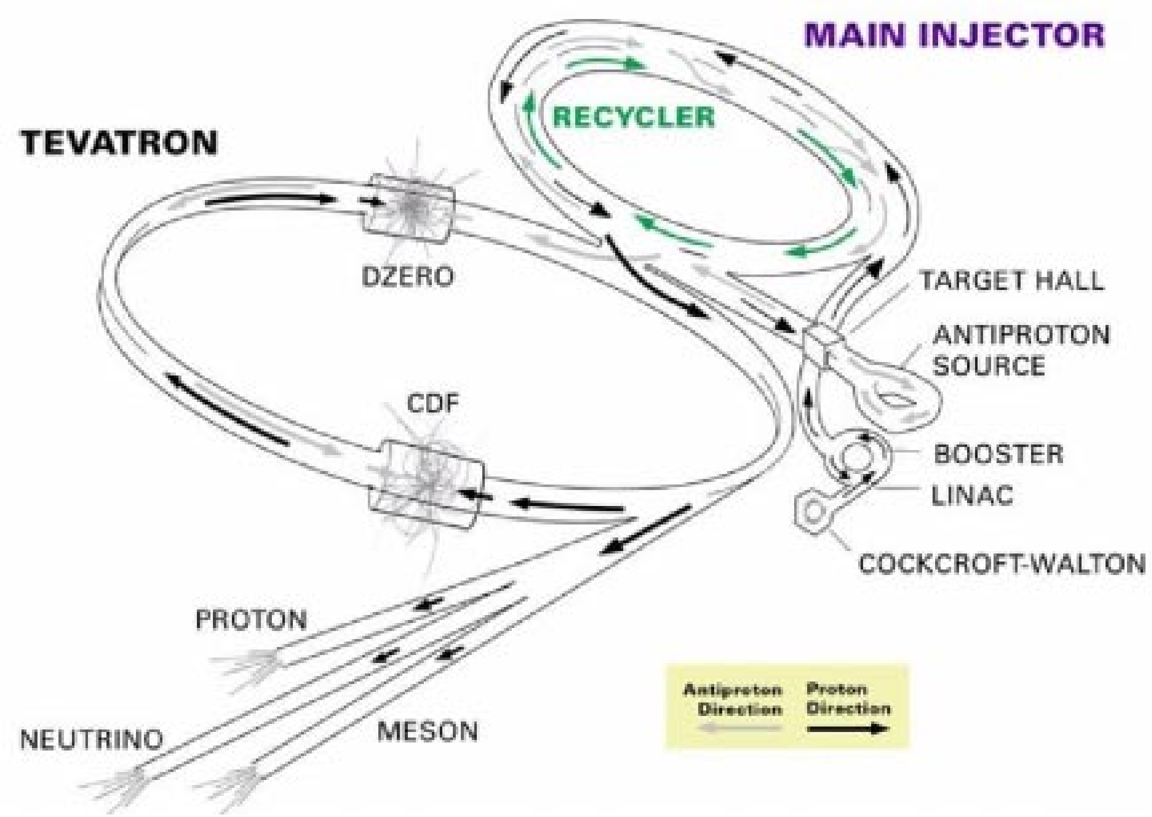

Figure 3.2: Fermilab Tavatron Collider

3.2 The Run II Accelerator Upgrade

In Run II, beginning in March 2001, the Tevatron collides protons with antiprotons at a center-of-mass energy of 1.96 TeV, which is a slightly higher energy than the 1.8 TeV available in Run I. In the first 2 years, half of the Run I integrated luminosity has been collected (by the end of December 2002). Fig. 3.2 is a schematic of the Fermilab Tevatron Collider.

In Run II, a large advance has been made with the construction of the Main Injector, a 150 GeV synchrotron, built in a separate tunnel from the Tevatron. The Main Injector has replaced the function of the Main Ring for antiproton production. It produces 2×10^{11} antiprotons per hour [43], four times the rate of the old Main Ring. A new permanent magnet "Recycler Ring" [44] allows recovery and reuse of uncollided antiprotons when the Main Injector has produced enough to merit injecting a new store into the Tevatron. Instantaneous luminosities in the range $5 - 20 \times 10^{31} \mathrm{cm}^{-2}\mathrm{s}^{-1}$ were available early in Run II. Because the number of protons per bunch is near the limit of the Tevatron, the number of bunches is increased from Run I's 6 bunches of protons and 6 of antiprotons to 36 (and ultimately up to 108) of each species. With an instantaneous luminosity of $20 \times 10^{31} \mathrm{cm}^{-2}\mathrm{s}^{-1}$, an average of 5.2 $p\bar{p}$ collisions occurs each bunch crossing. Increasing the number of bunches decreases the average number of collisions per bunch crossing. By decreasing the bunch width as the store is depleted by collisions, the luminosity can be maintained at an optimal level.

Such changes have profound implications for the detectors. Where in the past, there were 3.5 microseconds between each beam crossing, in Run II this is 396 ns for 36 bunches (and ultimately 132 ns for 108 bunches). This required all the front-end electronics from the detector to be replaced with electronics capable of faster response. Aside from the issues of shorter times between collisions, the detector improves its ability to identify leptons, energetic photons and charged particles, and particles emerging from a secondary vertex (daughters of long-lived parents). Increasing the collision rate by an order of magnitude also requires substantial upgrades of the trigger and data acquisition systems to handle the increased data flow.

3.3 Silicon Inner Trackers

The purposes of the silicon detectors are to identify tracks of charged particles that decay before they reach the outer tracker, to reconstruct the decay vertices of b-hadrons, and to extend or improve the track-finding and momentum resolution. Because the proton and antiproton beams are very thin ($\sigma_{\mathrm{transverse}} < 50\ \mu$m) and because their transverse positions can be maintained very close to the center of the beampipe, a typical b-hadron decay vertex can be identified by the impact parameters of the tracks $\sim 300\ \mu$m. This requires fine-pitched detectors oriented perpendicularly to the trajectories of the charged particles and mounted as close as practical to the decay vertices. The fine pitch and small radius necessary to achieve sufficient impact parameter resolution also improves the momentum resolution of the tracker systems.

The accelerator parameters contribute to the design decisions. The interactions are spread out over a length $\sigma_z = 25$ cm, setting the length scale and motivating the detectors to have extended geometries. The expected integrated luminosity implies a radiation dose of ≤ 1 Mrad during the life of the silicon detector. This, in turn, forces the sensors and readout chips to be radiation-hard and operated at cold temperatures, which mitigates some of the adverse effects of radiation.

The basic detector design is the "barrel geometry" comprised of layers of silicon detectors arranged in plates perpendicular to the beampipe. In addition to measuring separated vertices and improving the momentum resolution, DØ chose to use silicon detectors to extend the tracking coverage to high pseudorapidity with disk-shaped assemblies comprised of wedge-shaped silicon wafers arranged in plates oriented perpendicular to the beamline.

The DØ silicon detector [47] consists of six barrel modules, twelve small disks ("F-disks"), and four large disks ("H-disks"). The mixed barrel/disk geometry provides silicon detectors arrayed at normal incidence, as is optimal for good tracking resolution, to charged particles with $|\eta| < 3$. Figure 3.3 shows the DØ silicon barrel modules with barrel detectors parallel to the beamline and disks perpendicular to the beamline.

The six barrel modules are constructed with 4 layers of ladder assemblies with considerable overlap. Each barrel module is 12.4 cm in length and the total length of the barrel is 76.2 cm. The 4-layer coverage corresponds to the region $\eta = 1.5$ for interactions at $z = 0$. Barrel layers one and three are constructed from double-sided silicon sensors with axial $(r - z)$ and 90° stereo layers, except for the modules on each end of the barrel, modules one and six, which have single-sided axial strips. Those are single-sided because

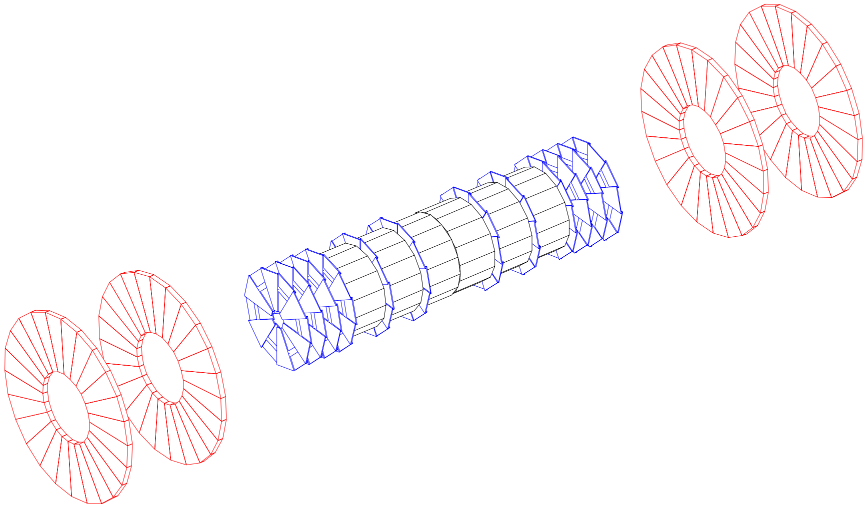

Figure 3.3: DØ silicon detector. The figure shows the configuration of the 6 barrel modules, the 12 "F-disks", and the 4 "H-disks".

stereo tracking is dominated by the information from the F-disks. Barrel layers two and four are constructed from double-sided detectors with axial and 2° stereo layers in all six barrel modules. All of the detectors are AC-coupled to the readout electronics.

The 12 "F-disks" are comprised of 12 trapezoidal wedges arranged into a plate with a hole for the beampipe. The active area inner radius is at 2.5 cm from the center of the beampipe and the outer is at 9.8 cm. The detectors are AC-coupled, double-sided, with strips angled at ±15° with respect to the vertical. The pitch of the p-side and n-side detectors is 50 μm and 62.5 μm, respectively, and the silicon wafers are 300 μm thick. Naturally, the strips are of different length depending on their locations on the wedge. The six innermost F-disks attached to the outer sides of the six barrel modules. The three additional F-disks are attached to each outer side of the barrel assembly, with the effect of extending the acceptance of the silicon system to higher pseudorapidity, especially for interactions which occur at larger z.

The four large "H-disks" are located at $z = \pm 94$ cm and $z = \pm 126$ cm. The inner radius of the active area is at 9.6 cm from the center of the beampipe and the outer is at 23.6 cm. The detectors are AC-coupled, single-sided, with 40 μm pitch strips (pairwise readout makes the effective pitch 80 μm) angled at $\pm 7.5^\circ$ from the vertical. Each plane has wedges glued together back-to-back to provide a 15° stereo angle. These forward disks are necessary to provide track stubs for forward particles which would otherwise exit the region of full solenoidal magnetic field without hitting the outer tracker. They cover a pseudorapidity range of approximately $2 \leq |\eta| \leq 3$.

All of the three detector types are able to withstand a radiation dose greater than 1 Mrad. The dose depends on the detector location and integrated luminosity. The innermost layer is expected to receive 0.5 Mrad/fb^{-1}. The effect of the radiation damage is to increase the leakage current, increase the bias voltage necessary for full depletion, and decrease the signal-to-noise ratio. The effects are temperature dependent and can be reduced by operated the detectors at low temperatures. The detectors are operated at temperatures between $5 - 10^\circ$ C using a cooling mixture of deionized ethylene glycol and water.

The DØ silicon detectors are read out using the SVX II chip [48]. SVX II is a 128 channel, radiation hard CMOS chip mounted directly on the "High Density Interconnects" (HDI's), kapton-based flexible circuit, wire-bonded to the sensors at the ends of the ladders and wedges. Each of the 128 channels in an SVX II chip features a preamplifier, a 32 stage analog pipeline with 4 μs delay, an 8-bit Wilkinson type ADC, and a latch-based sparsified readout. The chip is programmable for any interaction time from 132 to 396 ns. The pipeline depth, ADC ramp rate, preamplifier bandwidth, and thresholds are downloadable to each SVX II chip.

Connections to the outside world continue from the HDI's to 8-ft long "low-mass" cables that join the ends of the HDI's to unpowered "transition cards" mounted on the ends of the central calorimeter cryostat. Ultimately, these signals are gathered by a sequencer board connected by optical link to VME readout buffer electronics in the movable counting house. The DØ silicon detector has 792,576 channels.

3.4 Outer Tracker – Scintillating Fiber Tracker

The outer tracker [28] is the charged particle tracker at largest radius within the calorimeter. Outer trackers perform two functions. The first is measuring the momentum and charge of particles produced in the collision, and the second is to provide pattern recognition assistance for the silicon detectors.

A particle with non-zero charge q and momentum p in a solenoidal magnetic field along the z-direction of strength B will travel in a helix with radius r given by

$$r = \frac{p_T}{qB}, \tag{3.4}$$

where $p_T = \sqrt{p_x^2 + p_y^2}$. Therefore, by measuring the track's curvature in the $r - \phi$ plane, we effectively measure p_T. By measuring the track's direction in the $r-z$ plane, we measure p_T/p_z, which completes our measurement of the 3D momentum vector of the particle.

Tracks in these detectors typically have several dozen hits, which allows for highly efficient and pure identification of these tracks. Silicon trackers in these detectors have of order a half-dozen hits, and while they can be used standalone, a much better way to use them is to find the track in the outer tracker and project this track back into the silicon. Once the approximate trajectory in the silicon detector has been established, the tracking algorithm can search the silicon detector for hits and use these hits to improve the track measurement. This technique uses each component to its best advantage: the silicon tracker measures the track's point of origin and initial direction, and the outer tracker measures the track's momentum.

The DØ Solenoid and Scintillating Fiber Tracker

One substantial improvement to the DØ detector for Run II was the addition of a superconducting solenoidal magnet (2 Tesla). Having a magnetic field enhances the DØ detector. It has the ability to measure the momentum and charge of leptons and hadrons. The muon momentum can be measured in the central magnetic field, before the muon has scattered in the steel of the muon toroids, and this allows for the comparison of the muon's momentum as measured in the solenoid to the momentum as measured in the toroids. We can see that the muon momentum resolution is much improved after matching a muon local track with central track.

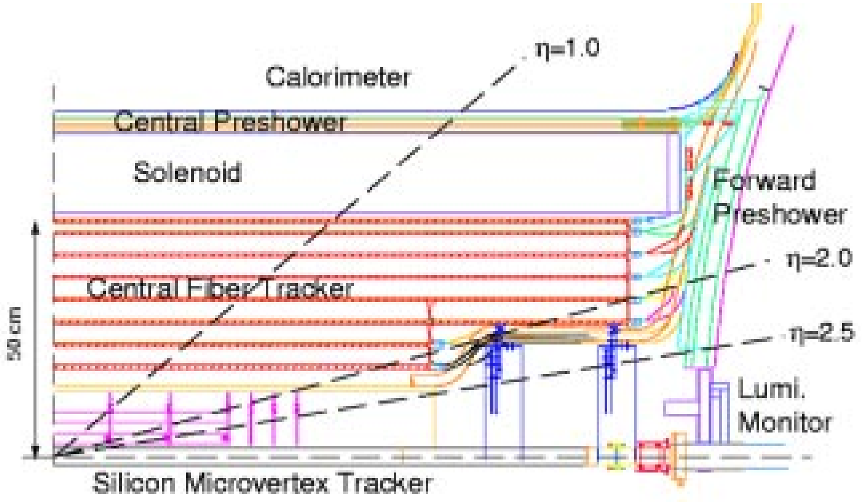

Figure 3.4: DØ's scintillating fiber tracker.

Mechanically, the DØ outer tracker is a simple device. Layers of scintillating fiber are placed on carbon-fiber composite cylinders. When a particle travels through one of these fibers, the scintillator emits light, which is totally internally reflected down the fiber, coupled to a clear fiber, and transported to a solid-state light detector. Fig. 3.4 shows a side view of the tracker.

In detail, the DØ central fiber tracker (CFT) [49] consists of scintillating fibers mounted on eight concentric cylinders made from a composite of layers of high modulus of elasticity carbon fiber sandwiching structural foam. The cylinders range in radius from 20 to 50 cm and are about 2.5 m in length, except for the inner two, which are about 1.7 m in length. The scintillating fibers are double clad, 835 microns in diameter, and are constructed in ribbons each 128 fibers wide composed of a "doublet" layer of fibers with the centers of one of the single layers in the space between the fibers of the other single layer. There are eight doublet axial (aligned along the beam axis) layers of scintillating fiber, as well as eight doublet stereo layers that make a ±3 degree angle with the beam axis. The outer (8th) layer is at the largest possible radius. The 7th layer is as close to the outer layer as is possible. The inner layer is at the least possible radius. The detector is divided into 80 sectors in phi. Each pie shaped slice has 960 fibers and the entire detector therefore has 76,800 channels.

The scintillation light from the fibers is totally internally reflected down the length of the fiber. A connection is made at the edge of the tracker to a clear fiber which transports the light to a solid-state light detector called a Visible Light Photon Counter (VLPC). The number of photons available at the VLPC's, for a charged particle which traverses through the center of a fiber, varies from 10 to 40, depending on the charged particle's pseudorapidity and on attenuation due to the distance from the clear fiber connector. The VLPC's are small silicon devices which have an array of eight photo sensitive areas, each 1 mm in diameter, on their surface. They operate at temperatures from 6 to 15 Kelvin, have a quantum efficiency of over 80% and have a gain of 20,000 to 50,000. The high quantum efficiency is important because of the low number of photons.

The momentum resolution is currently $\sigma(p_T)/p_T = 0.13\% \cdot p_T$ when scintillating fiber tracker measurements are combined with the silicon tracker. The p_T-dependent impact parameter resolution is currently 30 microns in the x and y direction, and 42 microns in z direction for high momentum tracks, if SMT and CFT information are combined.

3.5 Calorimeters and Preshower Detectors

Because of the dependence of the Tevatron's physics program on lepton identification and jet energy measurement, calorimetry is a critical aspect of Run II experiments. The calorimeters are used for identification and measurement of the electron, neutrino and jets from the decays of the top quarks in these events.

The calorimetry is divided into two parts, electromagnetic and hadronic. Nearest the vertex is the electromagnetic calorimeter that measures the energy of electrons and photons (including those from π^0 and η decay) and has improved position measurement at the point of maximum shower development. Farther in radius is the hadronic calorimeter which measures the energy of hadrons as they interact with the material of the calorimeter. Muons deposit a small amount of energy (due to ionization) in both sections, and the lack of a large energy deposit can be used to identify a particle as a muon. Neutrinos deposit no energy at all in these calorimeters, but the absence of energy deposition appears as a momentum imbalance in the transverse plane, also called "missing E_T".

DØ's hermetic, radiation-hard uranium and liquid-argon calorimeter [46] consists of three separate cryostats: the Central Calorimeter (CC), and the two Endcap Calorimeters (EC's). Each is segmented into an electromagnetic section, a hadronic section, and a coarse hadronic section (inside to outside), with many layers of sampling. Each is divided into pseudoprojective towers covering $\eta \times \phi = 0.1 \times 0.1$ rad. The readout of the electromagnetic section has four layers of longitudinal segmentation. The third electromagnetic layer, at EM shower maximum, has segmentation $\eta \times \phi = 0.05 \times 0.05$ rad. The readout of the hadronic sections have 4 (5) longitudinal layers in the CC (EC's). There are no projective cracks. The calorimeter provides hermetic coverage to $|\eta| < 4$. The energy resolution is $\sigma_E/E = 15\%/\sqrt{E(GeV)} \oplus 0.4\%$ for electrons and photons. For charged pions and jets the resolutions are approximately $50\%/\sqrt{E(GeV)}$ and $80\%/\sqrt{E(GeV)}$, respectively.

The Inter Cryostat Detectors (ICD's) augment the DØ liquid argon calorimeters by providing a measurement of the energy in between the central and endcap cryostats. This improves the energy measurement for jets that straddle the intercryostat region and improves the resolution of the missing transverse energy measurement. Sixteen new ICD detector segments form an annular ring of 1/2" thick scintillator covering $1.1 \leq |\eta| \leq 1.4$ on the hadronic section of the inner end of each EC cryostat. The sixteen segments are further segmented into sections of size $\Delta\eta \times \Delta\phi = 0.1 \times 0.1$. Each section has an embedded wavelength shifting fiber to collect light. These are in turn connected to long clear fibers which carry the light to photomultiplier tubes located underneath the cryostats, in a region with reduced magnetic field from the solenoid.

The primary purpose of the Central and Forward Preshower Detectors (CPS and FPS) is to exploit the difference between energy loss mechanisms of electrons and photons with that of the backgrounds, principally hadronic jets with leading π^0's, to improve the trigger and offline purity. Secondly, they provide a precision measurement of the starting point of the electromagnetic showers. The CPS is cylindrically shaped, mounted on the outside of the solenoid magnet, and covers the region $|\eta| \leq 1.3$. The FPS are shaped like annular rings, mounted on the inside of the EC's, and cover the region $1.5 \leq |\eta| \leq 2.5$. The FPS and CPS are shown in Fig. 3.5.

The DØ Run II luminosity monitor (Level-0) consists of two arrays of plastic scintillation counters located on the inside faces of the EC's and arranged symmetrically around the beampipe. The pseudorapidity coverage is $2.7 \leq |\eta| \leq 4.4$. Because the solenoid field is ~ 1 Tesla in that region, short magnetic field resistant photomultiplier tubes are used to read the light. A coincidence of hits in the counters on both sides of the interaction point provides the simplest indication that an inelastic collision occurred.

A new near beam detector called the "Forward Proton Detector (FPD)" is available for Run II. It is a series of small, retractable scintillating fiber detectors placed a few millimeters from the beamline in the region 20–60 meters from both sides of the interaction point. They are triggered by small scintillation counters and read out by multi-anode PMT's. Their purpose is to identify scattered protons and anti-protons in diffractive events.

3.6 Muon Systems

The muon detection strategy at DØ relies on the penetration power of muons. Several meters of absorber (including the calorimeters) absorbs the vast majority of hadrons, and any charged particle that penetrates this material is inferred to be a muon. Because they are at large radius, muon detectors are large, and to keep costs reasonable, they have very coarse granularity: typically they are single wire proportional chambers with drift times in excess of a microsecond. Fig. 3.6, 3.7 show an $r - z$ view of the DØ detector, and all components are illustrated in the graph.

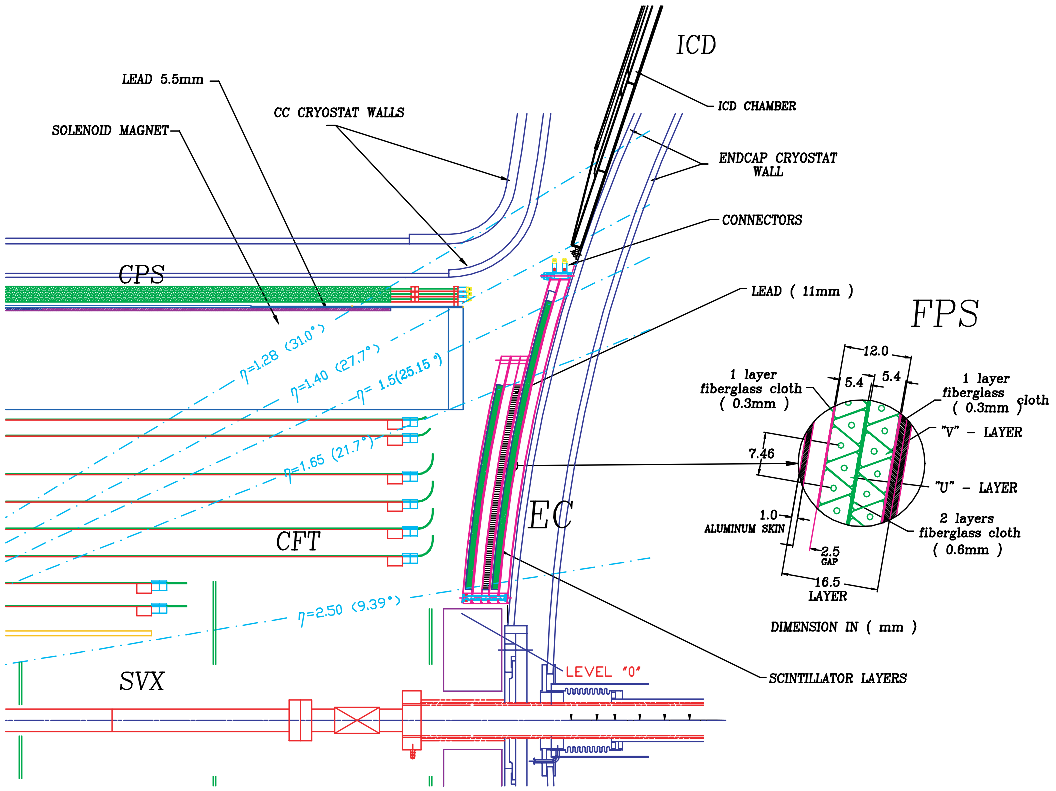

Figure 3.5: One quarter $r-z$ view of the end of the DØ trackers and the start of the EC, indicating the Central Preshower, the Level-0 detector, the solenoid magnet and calorimeter cryostats, and the Forward Preshower detector. The Forward Preshower detector is shown in detail in the inset.

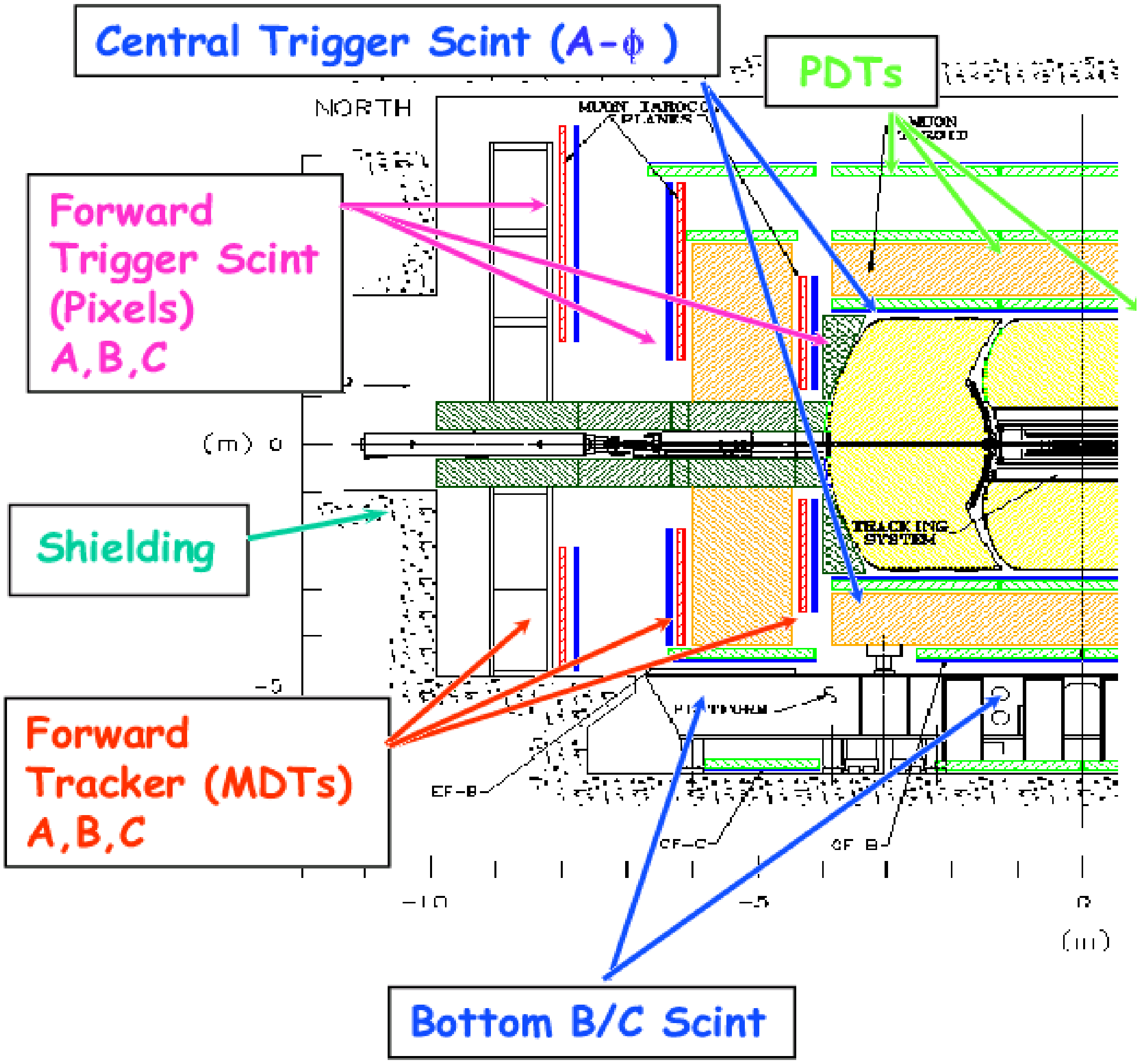

Figure 3.6: Half $r-z$ view of the DØ muon subdetector.

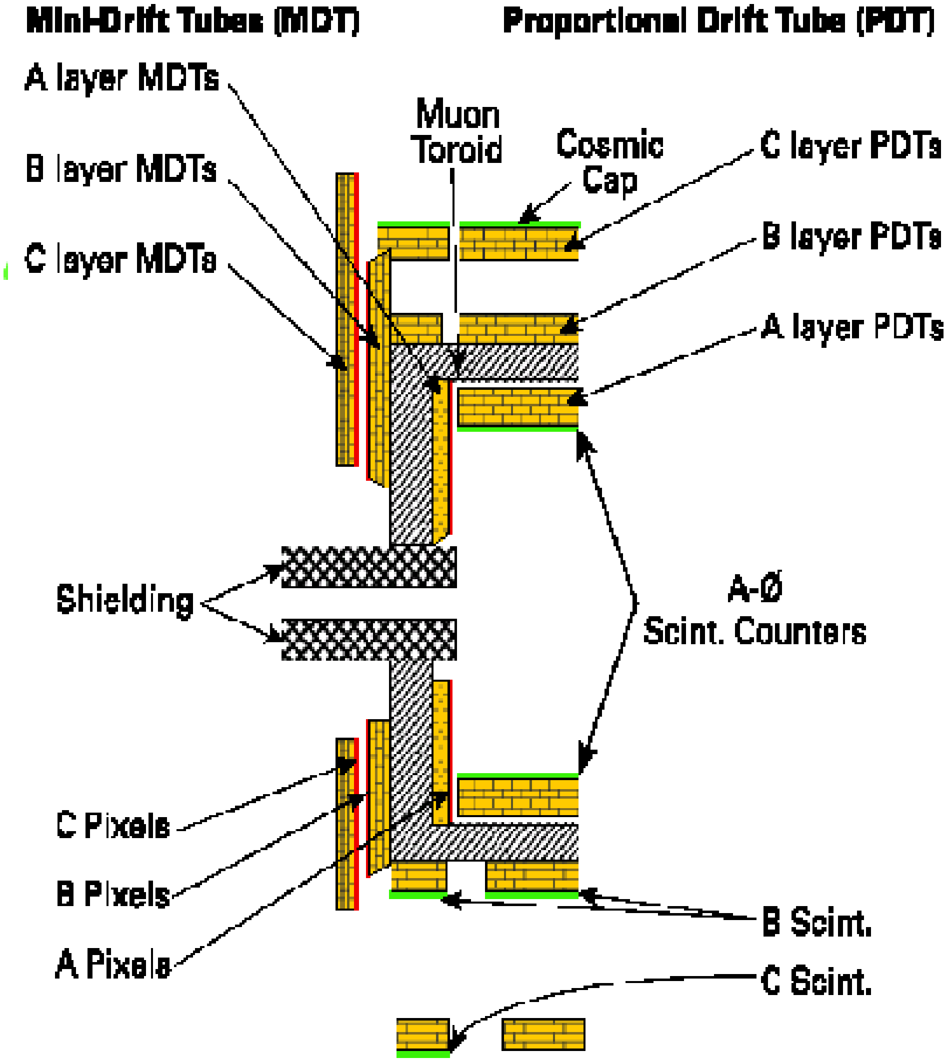

Figure 3.7: Illustration of the DØ muon subdetector components.

The muon detector consist of scintillator and drift tubes, with effectively complete coverage out to $|\eta| < 2$. As seen in the layout, the detector is split at $|\eta|$ of 1 into a central and forward system. Each has 3 layers (usually called A,B,C with A between the calorimeter and iron and the other two outside the iron) of drift tubes. In the central region are proportional drift chambers (called PDTs). In the forward region are minidrift tubes (called MDTs).

In Run II, scintillator counters are added adjacent to the chambers. Scintillator has a response time measured in nanoseconds, so that the coincidence between the counter and the chamber unambiguously determines the bunch crossing. Because the timing resolution is substantially better than the minimum required to resolve bunch crossings, we gain the ability to use timing to reject certain backgrounds: particularly out of time particles produced upstream of the interaction point and cosmic rays.

There is 2 or 3 layers of scintillator coverage with the forward scintillators sometimes called pixels, the central A-layer counters called A-phi, and the BC counters called the cosmic cap. Scintillator time is read out with both a 15-20 ns "trigger" gate and a 80-100 ns "readout" gate. The DØ detector relies on layers of scintillation counters and drift chambers to identify muons and measure their position and momentum.

The muon system has three large toroid magnets, one central and two forward, which act as absorber in addition to the calorimeter, provide a structure on which to mount the muon detectors, and provide a bend to the muons so the detectors can measure the momentum. The calorimeters contain between 7 and 10 interaction lengths of material, depending on the pseudorapidity. The thickness of the calorimeters plus the toroid magnets varies between 13 to 14 interaction lengths for $|\eta| \leq 0.9$, 10 to 15 interaction lengths for $0.9 \leq |\eta| \leq 1.2$, and 18 to 20 interaction lengths for $1.2 \leq |\eta| \leq 2.0$. Muons with momentum greater than ~ 1.4 GeV/c (~ 3.5 GeV/c) penetrate the calorimeter (toroid magnet) at $\eta = 0$. In addition, new massive shielding structures isolate the muon detectors from backgrounds generated near the beampipe and accelerator elements.

3.6.1 Central Muon System Drift Chambers

The central muon drift chambers were retained from Run I, but their electronics have been replaced. The drift chambers are made from extruded aluminum cells of 4-inch width and lengths up to 228 inches. The wires in the cells are parallel to the field in the toroid magnets so that the bending of the track in the toroids takes place in the drift ordinate. Refer to Fig. 3.6, 3.7.

Individual drift chambers (PDT's) in the C- and B-layers consist of three staggered decks of up to 24 cells each. Drift chambers in the A-layer consist of four staggered decks of 24 cells each, except for the ones on the bottom, which are three deck PDT's. The top and bottom of each cell has a copper-clad cathode pad. The copper has a milled cut separating it into an inner and outer pad such that the width of the inner pad alternately increases and decreases along its length. The wavelength of the vernier is 24 inches. Pairs of wires are connected through a delay chip at the end away from the front-end electronics. Fig. 3.8 shows the geometry of a PDT cell.

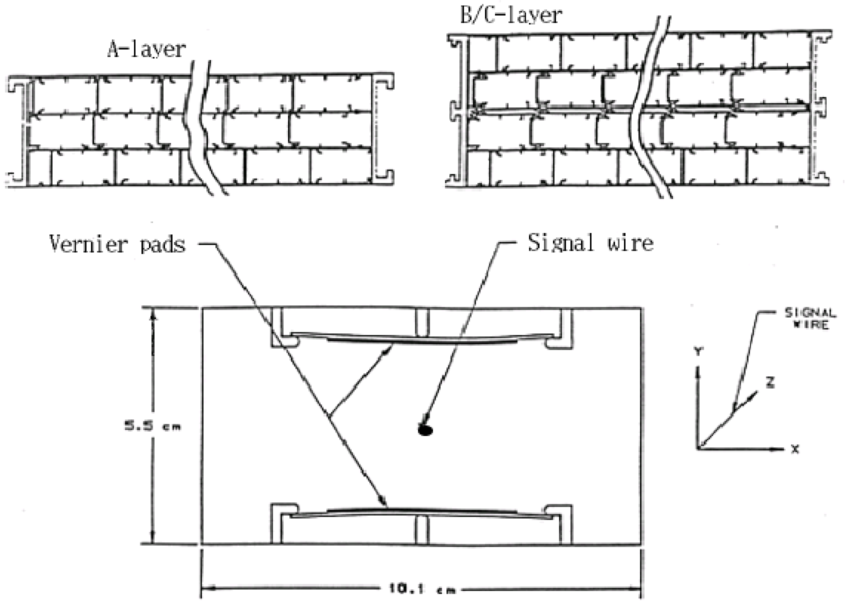

Figure 3.8: Geometry of a PDT cell.

On passing through a cell, a muon will cause a hit in the cell and a hit in the neighbor cell which is some time later depending on the muon's proximity to the far end. Charge is accumulated on the inner and outer pads of the cell through which the muon passed. The drift time is derived from the sum of the two cells times. The distance along the wire is derived from the difference. The normalized difference of the integrated pad charge provides the distance along a pad wavelength.

The Run I A-layer PDT's were rebuilt so as to increase their effective lifetimes. The ends of the PDT's were removed. The cathode pads, which outgassed a dielectric that coated the anode wires in Run I, were replaced with new G-10 pads that do not outgas. The lifetime of the B- and C-layer PDT's is long enough so that aging won't pose a problem for these detectors.

The PDT's use a drift gas composed of 80% argon, 10% CF_4, and 10% CH_4. The maximum drift time is approximately 500 ns, longer than the bunch spacing. This poses no problem for the electronics, which records each hit in as many crossings in that it could have occurred. The time measurements are made in 1.8 ns bins. The drift ordinate resolution is $\sim$ 500 μm per hit, limited by the fluctuations in the drift time due to the gas. Normally the drift velocity is about 0.1 mm/ns.

The muon momentum is calculated from the bend in the toroid magnet as determined from the difference in slopes between the line formed from the interaction point and the A-layer hits and the line through the B- and C-layer hits. The momentum resolution is expected to be $\sigma(1/p) = 0.18/p \otimes 0.005$ with p in GeV/c. This momentum resolution is worse than that expected from the fiber tracker measurement, especially at low p_T.

3.6.2 Central Muon System Scintillation Counters

An important part of the upgrade is two new layers of scintillation counters. These detectors not only tag the bunch crossing from which the muons originate for the slow drift chambers, but also reject background particles which leave hits at times other than expected from a muon originating at the interaction point. Refer to Fig. 3.6, 3.7.

The A-layer contains 630 "A-phi" counters, each approximately 32" long and spanning 4.5° in azimuthal angle. There are 9 counters in a row spanning $-1.0 \leq \eta \leq 1.0$. Each row has a slight overlap with a neighboring row so as to minimize the cracks between counters.

The counters are made from 1/2 inch thick Bicron scintillator plates with many Bicron BCF'92 wavelength shifting fibers embedded in deep grooves. The fibers collect and transmit the light to a single photomultiplier tube (PMT). The counters have a time resolution of $\sigma = 4$ ns and are expected to discriminate between muons produced in the collisions and the background, that is composed of particles backscattered from the calorimeter exit, and arrives 14 ns later than a muon. The "A-phi" counters span 93% of the azimuthal angle. There is a gap in the A-layer coverage where the calorimeter is supported by the detector platform.

A layer of scintillation counters has been added on the outside of the muon toroid magnet. The 240 "Cosmic Cap" C-layer scintillation counters were deployed late in the second half of Run I and previously have been described in detail [51]. These counters are between 81.5 and 113 inches long and 25 inches wide. Eight of them are mounted on the outside of each C-layer PDT on the top and sides of the central muon detector. Underneath the toroid magnet, the three layer coverage is broken up because of the support structure for the central platform and toroid magnets. 120 new "Cosmic Bottom" counters are arrayed on bottom C-layer and B-layer PDT's. The Cosmic Cap and Cosmic Bottom counters are made from 1/2 inch thick Bicron scintillator with Bicron BCF'91A wavelength shifter fibers embedded in grooves. Each counter is read out with two photomultiplier tubes. One advantage of using two PMT's is that coincidental tube noise is improbable. Another is the immediate redundancy available in case one of the PMT's fails.

The scintillation counters have an LED pulser calibration system capable of providing a clocked, timed, amplitude-controlled photon pulse. Each PMT is connected by a light-shielded optical fiber to a light-tight box which houses bundles of LED's glued into a clear acrylic block. A single box may provide the photon pulse for up to 100 PMT's. The stability of the photon pulse is monitored with a light-sensitive diode housed in the clear block. This system allows the timing and amplitude to be monitored and controlled.

The muon system has a wide range of options available for triggering. Triggers may be composed of coincidences of in-time hits in scintillation counters, hits in layers of the PDT's, and tracks found in the central tracker. Low-p_T muons would rely on hits only in the A-layer detectors and fiber tracker. High-p_T muons would also use scintillation counters and PDT's in the B- and C-layers.

3.6.3 Forward Muon System Drift Tubes

The Mini-Drift Tube (MDT) system [52] is comprised of three planes of drift-tubes, with one plane in front of, and two planes behind the forward toroid magnet. The layers are divided into octants with tubes of different length depending on position in the octant. As in the central region, the MDT A-layer has four decks of drift tubes and the B and C-layers have three decks each. The drift tubes, made from long aluminum extrusions of eight 1 cm square cells, are contained in plastic sleeves. Wires in the cells are oriented parallel to the magnetic field of the forward toroid magnet. The sleeves of tubes are mounted on an aluminum support structure which also provides mechanical support for the infrastructure. A plane of MDT counters is shown in Fig. 3.9.

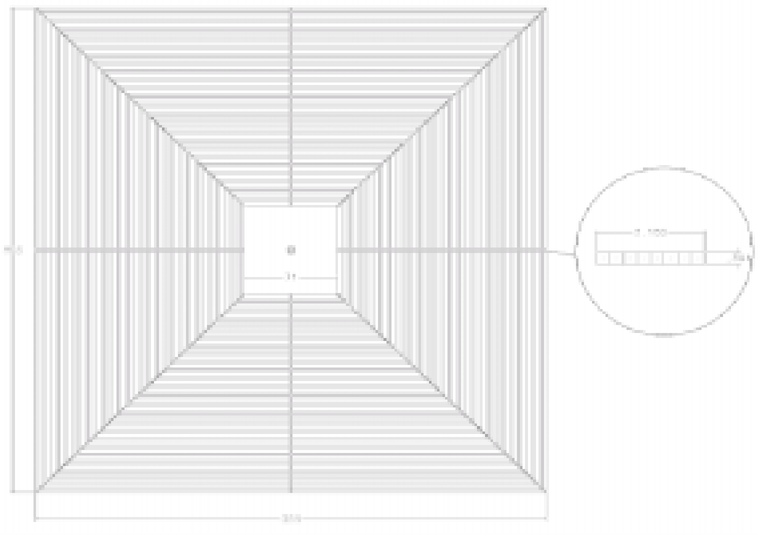

Figure 3.9: DØ forward muon mini-drift tube (MDT) plane. The octant boundaries are shown.

The MDT's use a non-flammable gas mixture composed of 90% CF_4 and 10% CH_4, with a maximum drift time of about 60 ns. The momentum resolution is limited by multiple Coulomb scattering in the iron toroid and the hit resolution of the detector. The MDT electronics uses a coarse digitization of the drift time (18.8 ns time bin). The momentum resolution is roughly $\sigma(p_T)/p_T = 0.2$. Importantly, it is on par with the resolution of DØ's central tracker in the forward region where the full coverage of the fiber tracker's layers has ended.

3.6.4 Forward Muon System Scintillation Counters

Three layers of "Pixel" scintillation counters [52] are added to the forward region (approximately $1.0 \leq |\eta| \leq 2.0$). Their primary role is muon triggering. The ~ 4800 Pixel counters

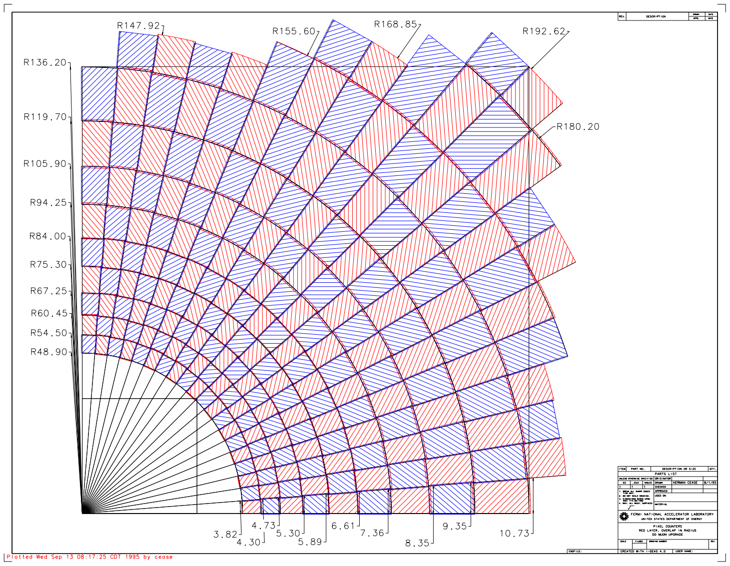

Figure 3.10: Two DØ forward muon pixel octants.

have segmentation 0.1 × 4.5° in $\Delta\eta \times \Delta\phi$. Most of the trapezoidal shaped pixel counters are made from 0.5" thick Bicron scintillator with wavelength shifting bars. They are each read out by a single PMT. The counters are held in protective aluminum containers with a steel fastener, on one corner, which mates to the magnetic shield of the PMT. A few of the counters have special space constraints and are made with wavelength shifting fiber so as to allow more flexibility in the orientation of the PMT and magnetic shield. The same kind of LED pulser calibration system used in the central muon scintillators is used for the Pixel counters.

The counters are assembled into octants of ~ 100 counters each. The octants provide mechanical support for the counters and their infrastructure. These are mounted directly onto the A- and B-layer sides of the forward toroid magnets and onto the inside face of the C-layer support frame. Two octants are shown in Fig. 3.10.

Forward muon triggers are formed from coincidences in the three layers of scintillation counters consistent with a muon of a given momentum. The MDT's provide a p_T measurement at trigger level, especially important in the fiducial region where the fiber tracker has reduced coverage.

3.6.5 Shielding

The purpose of shielding is to shield the muon detectors from backgrounds generated at high $|\eta|$ from the interaction of the beam jets with forward elements of the detector and accelerator hardware, such as the beampipe and low-beta quadrupole magnet. The shielding is built in several large, movable sections extending from the endcap calorimeters, through the forward toroid magnets, to the Tevatron tunnels. The shields themselves totally contain the accelerator elements within the collision hall, including the low-beta quadrupole magnet, inside a case of 20 inches of iron, six inches of polyethylene, and two inches of lead. The shielding is shown in Fig. 3.6, 3.7.

3.7 Trigger

One of the defining features of hadron collider physics is the necessity to select the small fraction of all bunch crossings containing interesting collisions. A fast selection process, called the "trigger", sorts events into categories of various levels of interest. An event that passes the trigger is written to magnetic tape for later analysis. An event that fails the trigger is lost forever. An event can fail to pass the trigger because the collision was a well understood process, because the event was mistaken for a well understood process (trigger inefficiency), or because the trigger or data acquisition were busy processing previous collisions (dead time).

There are three trigger levels. After Level-1 trigger, the event rate is reduced from 7 MHz to 10 KHz. Level-2 trigger reduces the event rate 10 times more. We can further reduce the event rate 20 times by the Level-3 software trigger. After Level-3, 50 events are written to tape per second.

3.7.1 Trigger Level-1

The first element of the trigger is the formation of trigger primitives. These are collections of a few bits of data that represent the status of various detector elements. For example, one set of trigger primitives are the calorimeter cells with energy above a particular threshold. Another would be which muon chambers have detected a particle, and whether this particle is consistent with a high p_T muon, a low p_T muon, or neither. Another would be the number and position of tracks found in the outer tracker (silicon is not in the trigger at this stage).

A limited amount of processing is then applied to these trigger primitives. Typically, this is performed in Field Programmable Gate Arrays (FPGA's) with inputs from the front-end detector electronics. In DØ, for instance, Level-1 muon primitives are formed from combinations of in-time hits in scintillation counters, coincidences of hit cells in the drift chambers, and tracks formed from hit patterns in the axial scintillating fibers of the central tracker.

The primitives are sent to the global Level-1 trigger. Combinations of trigger primitives are compared against a runtime programmable list containing the definitions of triggers to be used in the run. The DØ Level-1 trigger system can support up to 128 different unique triggers. If the trigger primitives satisfy at least one of the triggers, the event is passed to the next trigger level. A block diagram of DØ's trigger is shown in Fig. 3.11.

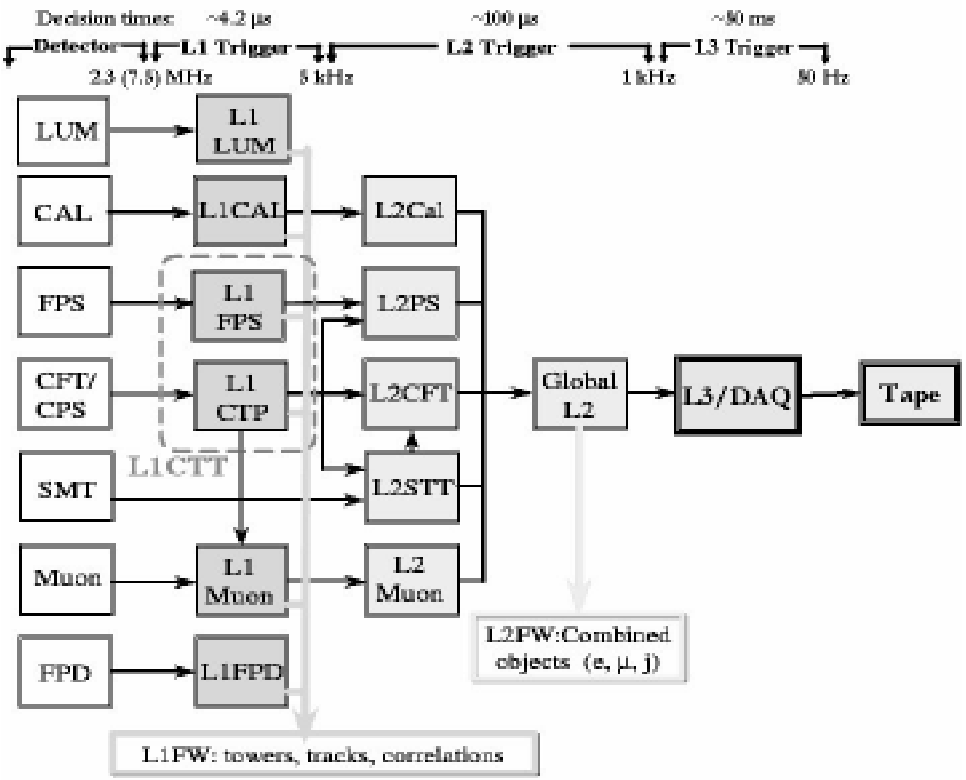

Figure 3.11: Design of the DØ triggers.

It takes time to form the primitives and to make a Level-1 trigger decision. Meanwhile collisions continue to occur. Since the trigger needs to be ready for the next crossing while it is processing an event, the data from the detectors is placed in a pipeline (a microprocessor's "assembly line" for executing program instructions; a pipelined function unit in a processor separates the execution of an instruction into multiple stages) which increments every crossing.

The DØ Level-1 trigger has a deadtimeless output rate of 10 kHz. If any single one of the 128 combinations is positive, and the DAQ system is ready for acquisition, then the Level-1 framework issues an accept, and the event data is digitized and moved into a series of 16 event buffers to await a Level-2 trigger decision.

The central Level-1 trigger logic is performed locally in the detector octants. A muon low p_T trigger is defined using only centroids found in the A-layer, while a high p_T trigger is defined by using correlations between centroids found in the A-layer and B- or C-layer. Four thresholds (2, 4, 7 and 11 GeV/c) are defined using the CFT information. The information for each octant in each region is combined in the muon trigger manager, which produces global muon trigger information. The muon trigger manager makes a trigger decision based on the p_T threshold (2, 4, 7 and 11 GeV/c), pseudorapidity region ($|\eta| < 1.0, |\eta| < 1.5$ and $|\eta| < 2.0$), quality (Loose, Medium and Tight) and multiplicity information. This trigger decision is sent to the Level-1 Trigger Framework where it is included in the global physics trigger decision.

3.7.2 Trigger Level-2

At Level-2, the Level-1 decision is confirmed, or not, using the additional time to provide more and better information. This is done in two stages. The first stage, called the preprocessor stage, uses FPGA's to refine the trigger primitives found by Level-1 and to prepare the data for the second stage. The second stage, called the global processor stage, combines and correlates information from the trigger primitives.

The preprocessor FPGA's have about 50 μs to perform refinements to the trigger primitives. For example, the first stage photon primitive, formed from a single tower at Level-1, is required to have a shape that looks like an isolated electromagnetic shower at Level-2. The additional time is used to compare the energy of the tower of interest with nearby towers. Additional related information can also be used, such as energy in the shower maximum. Because of the increased accuracy of the measurement, thresholds can be set tighter in Level-2, producing a great deal of the rejection in the global processor stage.

The global processor stage for DØ is a VME-based CPU card using a Digital Alpha processor. Using a general purpose CPU at this level of the trigger provides a great deal of flexibility – essentially all of the Level-1 primitives are available at Level-2, where they can be combined in ways not possible at Level-1. For instance, Level-1 can produce photon triggers and it can produce jet triggers. However, Level-2 provides the ability to correlate the two in ways not possible by the dedicated hardware of Level-1. For example, requiring that the jet be opposite the photon in ϕ and having similar E_T. This can be used to select events of a given topology with particularly interesting kinematics, for example. Perhaps more importantly, though, is that this design provides added flexibility for implementing new triggers during the Run II even if they have not been anticipated before the run begins. This might be in response to better than promised luminosity from the accelerator, or it might be in response to early physics results.

Level-2 is where the information from the silicon vertex trigger (SVT) becomes available. Layers of silicon are read out into this trigger, which uses an associative memory and roads provided from the outer tracker to identify silicon tracks. This provides improved momentum resolution, but more importantly, it also provides impact parameter resolution for each track sufficient to identify particles from displaced vertices. Since the vast majority of two track triggers are not from heavy flavor decay, the SVT provides three orders of magnitude rejection. Silicon information doesn't just improve the impact parameter resolution, it also improves the momentum resolution, because the two tend to be highly correlated. The maximum deadtimeless output rate of Level-2 is about 1000 Hz at DØ.

By shifting a 3-tube wide window over all the cells in an octant, and looking for wire triplets with a matching scintillator hit, the muon preprocessor first finds track stubs separately in the A-layer and the BC-layer. The track stubs found are reported to an ALPHA preprocessor board that matches track stubs in the A layer with that in the BC-layer, and creates Level-2 objects from matched or unmatched stubs. These Level-2 objects hold the ϕ, η and p_T of the muon, and are reported to the Level-2 global processor. Upon a Level-2 Accept, the Level-2 objects are sent to Level-3 for more precise muon track reconstruction.

3.7.3 Trigger Level-3

The third level trigger is often described as an event filter. It is a software based system characterized by parallel data paths which transfer data from the detector front-end crates to a farm of processors. It reduces the input rate of 1 kHz to an output rate of 50 Hz.

DØ's farm of 500 parallel commodity CPU's builds the event into the offline format, runs a modified (for faster execution time) version of the offline reconstruction on the event, and makes a decision to accept or reject the event. If the event is accepted, it is already in or close to the proper format for offline analysis. Additionally, this trigger level can be used to characterize the event and decide whether an event should receive priority in reconstruction. Reconstructing a small fraction (say 1%) of events in an "express stream" can be used to provide rapid feedback on the detector's performance and health. The overall output rate of Level-3 is about 50 Hz, with some variation depending on luminosity and dataset selection requirements.

Running what is effectively the offline reconstruction online also provides an excellent monitor of the health of the experiment. The full offline reconstruction lags a day or two behind the data taking in order to use the final calibration constants, but the Level-3 reconstruction lags only a fraction of a second. Serious problems can therefore be detected before a large amount of data is collected. As an additional benefit, because Level-3 looks at the output of Level-2 and offline looks at the output of Level-3, monitoring at Level-3 examines many times more events than offline monitoring, also improving the probability to spot trouble sooner.

Using commodity processors has a number of advantages. First, the nature of an event filter naturally lends itself to parallel processing: each CPU processes an entire event, with a supervisor process assigning incoming events to CPUs that finish their events and become ready for new ones. Second, these computers are inexpensive, and getting more so with time, and finally, the system is highly expandable: additional CPU's can be added at a later date, until the bandwidth into Level-3 becomes the limiting factor.

The muon Level-3 trigger utilize some aspects of the offline muon reconstruction. Level-3 muons have more complete information on the vertex and inner tracking components that will improve momentum resolution, and has the ability to require that multiple muons come from the same vertex. Similar fits are done in Level-1 as in the final offline reconstruction. Requirements on matching the muon track to the inner tracking can reduce remnant combinatorics plus punchthroughs. Level-3 also uses the calorimeter information to reduce combinatorics, and separate muons into isolated and non-isolated. Level-3 improves on Level-2's ability to separate muon sources into prompt, slow, or out-of-time by fitting the available scintillator hits along a track to the particle's velocity. Level-3 can remove a cosmic ray muons both by their being out-of-time and by looking for evidence of a penetrating track on the opposite side of the detector. Level-3 can also clean up single muon events that Level-1 and Level-2 identified as dimuons, such as those which pass through the FAMUS–WAMUS overlap region.

A combinatorial algorithm is used in the Level-3 segment finding, because it is faster than the linklist algorithm (chapter 5). The steps are:

- Segments are first grouped in pairs.
- Some quantities related to pair of segments are calculated: residual in the drift direction and residual in axial direction.
- The list of segment pairs is sorted in increasing order of residuals in the drift direction.
- Tracks are created using pairs of segments with residuals in the drift and axial direction lower than some maximum values. The track momentum is evaluated using a parameterization depending on the difference in angles of A and B-C segments [53].
    - for WAMUS

      $$p = \frac{0.98}{\theta_{drift}},$$

      where θ_{drift} is the difference in angles of A and B-C segments in the drift direction.
    - for FAMUS

      $$p = \frac{0.9}{\theta_{\sin}} + \left| \frac{1.0}{\cos(\theta_A)} + \frac{1.1}{\cos(\theta_B)} \right| * \mathrm{sign}(\theta_{\sin}),$$

      where θ_A and θ_B are the polar angles of A and B-C segments in spherical coordinates and where $\theta_{\sin}$ is defined by: $\theta_{\sin} = \sin(\theta_B) - \sin(\theta_A)$.

3.7.4 *B* Triggers with DØ

B hadron observability depends strongly on the detector capabilities to trigger on soft lepton(s) present in semi-leptonic channel or in J/ψ's produced in *B* decays. Hadronic *B* triggers are not considered in the following.

The Level-1 muon hardware trigger is based on the combination of low p_T track candidates measured in the CFT, spatially matched with hits in the scintillator planes and/or drift chambers. Single muon events with $p_T^\mu > 4$ GeV/c run prescaled currently, and dimuons with $p_T^\mu > 2$ GeV/c are expected to run unprescaled.

The electron trigger is aimed at soft electron pair detection. Level-1 candidates are selected separately in EM calorimeter trigger towers ($\Delta\eta = \Delta\varphi = 0.2$) with a transverse energy deposit $E_T > 2.0$ GeV, and in the tracking system with a low p_T track coincident with pre-shower cluster. Electron candidates of both systems are then required to match within a quadrant in φ and to have opposite signs.

Level-2 triggers include setting of the invariant mass window and angular cuts in dilepton channels to select J/ψ decays and improve background rejection.

3.8 Data Acquisition

The data flow in trigger Level-3/data acquisition is illustrated in Fig. 3.12. Events will be reconstructed on the FNAL processor farm system, with that portion dedicated to DØ capable of matching the 50 Hz data acquisition rate. Following reconstruction, data are stored on a tightly coupled disk and robotic tape system, and made available for analysis on a centralized analysis processor.

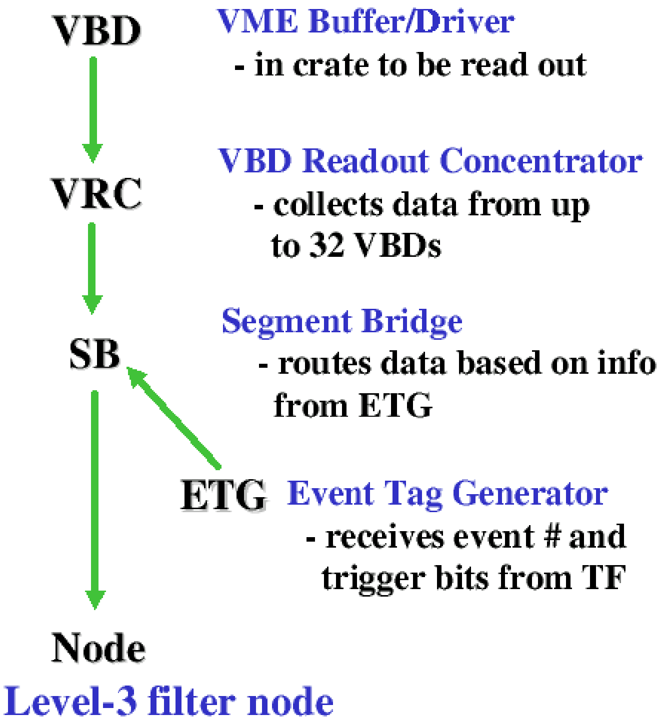

Figure 3.12: Simplified data flow in Level-3/DAQ for DØ Run II.

Chapter 4

The DØ Run II Software

The software [70] used by DØ can be thought of in three classes: Monte Carlo simulation, event reconstruction and the global monitoring system. In this chapter a brief description is given of how Monte Carlo events are generated (Monte Carlo simulation), then we briefly describe the reconstruction of physics objects (such as muon, electrons, etc) from the raw data and corrections that need to be applied to the reconstructed parameters of these objects prior to analysis. Finally, we review DØ global monitoring and the data handling system.

4.1 Monte Carlo Simulation

Monte Carlo event generators [65] constitute an extremely important and commonly used class of tools utilized by high energy particle physicists. The term "Monte Carlo" refers to numerical simulations of processes that may be characterized by sets of random numbers. These variables assume values in accordance with prescribed probability distributions. The distributions themselves are based on the process of random number generation. These techniques may be used to simulate the collision of interesting hadrons and to model the observation of the scattered collision products within an appropriately designed detector. In general, this proceeds in four steps:

- event generation, where simulation of the physics collisions is done.
- detector response simulation, where the simulation of the interaction of the particles passing through the detector is done.
- event reconstruction.
- trigger simulation.

4.1.1 Event Generation

Event generators are programs [65] that generate the physics of a $p\bar{p}$ interaction; their output is usually just a list of vertices and particles that come out of those vertices. These programs are typically the intellectual property of the theoretical physicists who developed the model which is implemented in the program. The generators most used by DØ are `Pythia` [55], `Isajet` [60]. Generally these programs are used only to predict the shapes of the differential cross-sections, not for absolute cross-sections. DØ has tuned the parameters of its event generators to match its Run I data.

The event generators have been carefully developed to simulate the properties of $p\bar{p}$ collisions but much less care was taken in their model of how b hadrons decay. To circumvent this, the b and c hadrons produced by the event generators sometimes are handed to separate code to simulate their decay. Until recently, this code was usually the `QQ` [61] code, which was developed and maintained by CLEO, and which contains their integrated knowledge about the decays of B's and D's. The BaBar and CLEO collaborations have developed a program, `EvtGen` [62], which is especially useful in complex sequential decays such as semileptonic decays and CP violating decays. The basic steps in all these event generators are similar but they differ in the details of their implementation:

- A primary hard scattering is generated according to the appropriate physics process studied.
- QCD radiative corrections are added for both the initial and the final state.
- Partons are fragmented into hadrons independently, and particles with lifetimes less than about 10^{-12} seconds are decayed. This process is known as fragmentation or hadronization. As this cannot be done in perturbative QCD, different event generators utilize different empirical schemes for hadronization, for example, `Pythia` uses LUND string fragmentation scheme [63].
- The final step is to evolve and hadronize the leftover partons known as "spectators". There is no unique way of dealing with the leftover partons. `Pythia` uses an extension of the LUND Color Scheme [63].

For the "minimum bias"(minbias) process, there is no hard scattering at all, so that the event consists only of beam jets. At high energy the jet cross sections become large. To represent the total cross section it is better to use a sample of minbias events to give a cross section equal to the inelastic cross section.

4.1.2 Detector Simulation

The next step in a typical simulation [70] is to compute the detector response to the simulated events. DØ has both a fast simulation program and a detailed simulation program. A typical fast simulation program uses a simplified and/or parameterized description of the detector response and directly produces smeared 4-vectors for the tracks which were input to it. It may also declare that a track is outside of the fiducial volume and is not reconstructible. The output of the fast simulation can usually be used to perform the simulated analysis.

A typical full simulation is based on the `GEANT` [56] program from CERN. This is a program that can be used to describe true geometry of a detector by building it up from a library of known shapes. It also has extensive knowledge of the interactions of particles with materials. It takes tracks from the event generator and propagates them through the detailed description of the detector, at each step checking to see how the track interacted with the material. If a particle interacts in the detector material to produce new particles, those new particles are also propagated through the detector. If a shower starts in material, `GEANT` will follow the daughters through each stage of the shower, and deposit the energy of the shower in the appropriate detector cells. The output of this simulation is typically a list of pulse heights and/or arrival times for hits in individual detector cells. The actual `GEANT` program at DØ is named `D0gstar` [57].

The program `D0Sim` [58] uses `D0gstar` output as input and does the digitization for each detector, pileup (overlapping minbias events) and raw data simulation. This information is then passed to the reconstruction and trigger simulation programs. `D0Sim` performs the following functions:

- Merges hard scatter and minbias events.
- Add calorimeter pileup from previous events.
- Make L1CalTTowerChunk for L1 simulation.
- Add SMT, CFT, calorimeter and muon noise and inefficiencies.

This information is then passed to the reconstruction program and the trigger simulation.

4.1.3 Trigger Simulation

It is also necessary to simulate the trigger electronics and the effects of the trigger on data selection. This is taken care of by a separate program: `D0TrigSim` [59]. The simulator uses the same trigger configuration files that are used at the time of data taking.

The trigger simulation code starts with the same raw hits as the reconstruction code. The code emulates the trigger hardware and produce trigger decisions which should very closely represent the real trigger behavior.

The output of `D0Sim` and `D0TrigSim` is in the same format as the data recorded by the D0 data acquisition system, but contains additional Monte Carlo information to make it possible to correlate detector information with the original generator information.

4.2 Event Reconstruction

The events recorded by the data acquisition system (raw data format) contain information like timing information in the muon system, hits in the central tracking system, and digitized counts in the calorimeter cells, etc. We need to convert the raw data into interesting physics objects, such as muons, jets, electrons, photons, etc. This process is called event reconstruction [66]. At DØ, the executable of the whole process is called "`D0Reco`".

The reconstruction code starts with raw hits, either from the detector or from a simulation of the detector, calibrates them, finds tracks, fits them, applies the particle identification (such as muon identification, electron identification, etc) algorithms and finally identifies particle candidates. The output is the measured properties of tracks and energy deposits, which can be used directly for physics analysis.

The reconstruction program performs four major tasks:

- `Hit finding.` The digitized signals from the wires of the tracking detectors are converted into spatial locations of hits, while signals from calorimeter cells are converted to energy deposits.
- `Tracking and Clustering.` The tracking hits are combined together to form tracks. The calorimeter energy depositions in the cells are grouped to form clusters.
- `Primary and secondary vertexing.` The location of the $p\bar{p}$ interaction is calculated and used in the calculation of various kinematic quantities. The vertices are essential for particle identification.

- `Particle identification.` The tracking and calorimeter information is combined to form candidates for muons, electrons, photons, etc.

4.2.1 Vertex Reconstruction

The ability to reconstruct primary and secondary vertices [64] is of crucial importance for a modern high-energy physics experiment. The position of primary vertex is a fundamental quantity of every event and must be reconstructed with high precision to allow the precise determination of many physical quantities, like the transverse momentum of each track or the transverse energy of jets. Displaced vertices arise from the decay of long lived particles, e.g., B and D mesons. Their reconstruction is fundamental to perform efficient b tagging. This identification of b-quark jets will play an important role in both the high and low p_T physics program of the DØ experiment during Tevatron Run II. Fig. 4.1 show simulated SMT hits for some typical $p\bar{p} \to t\bar{t}$ events at DØ.

Primary Vertex

The primary vertex can refer to either the hard-scatter primary vertex that triggered the event (the interaction point, IP) or the vertex where additional interactions occurred. Primary vertex finding starts from a vertex seeds and “tear down” on that seed. The finding starts with a set of N_{trk} good quality tracks, and uses iterative procedure to find the primary vertex:

1. Fit a vertex from the set of N_{trk} tracks and compute $\chi^2(N_{trk})$.

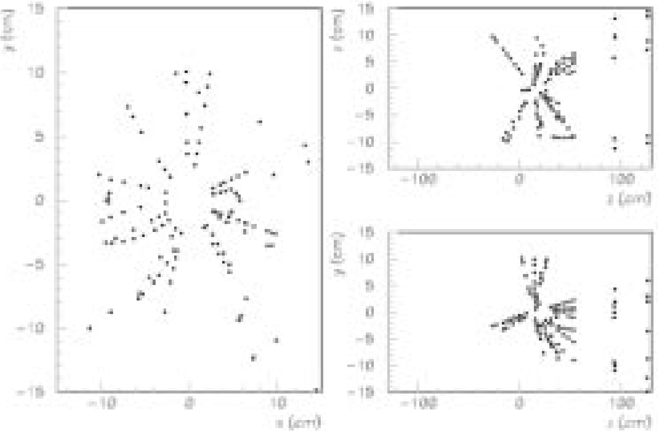

Figure 4.1: Simulated SMT hits for some typical *pbarp* → *tbart* events at DØ.

2. Compute the contribution to χ^2 from each track: $\Delta_a = \chi^2(N_{trk}) - \chi^2(N_{trk} - 1)$.
3. Search for the track with maximum contribution (Δ_{max}) among the Δ_a.
4. Exclude a track from valid set if "$\Delta_{max} > \Delta_{threshold}$" and go back to step 1.
5. Save the fitted vertex if ($N_{trk} \geq 2$) and ($\chi^2(N_{trk}) < \chi^2_{max}$).

Secondary Vertex

Secondary vertex finding starts from a vertex seed and "tears down" on that seed. The finding starts with a set of quality tracks, and uses an iterative procedure similiar to primary vertex finding:

1. Form a secondary vertex hypothesis with two tracks, not belonging to a previously found hypothesis.

2. Fit a secondary vertex from the set of N_{trk} valid tracks and compute $\chi^2(N_{trk})$.
3. Loop over the other tracks and compute contribution to χ^2 when a track added to this hypothesis: $\Delta_a = \chi^2(N_{trk}+1) - \chi^2(N_{trk})$.
4. Search minimal contribution (Δ_{min}) among the Δ_a.
5. Add track to valid set if "$\Delta_{min} < \Delta_{threshold}$" and go back to step 2.
6. Save vertex hypothesis if ($N_{trk} \geq 2$) and ($\chi^2(N_{trk}) < \chi^2_{max}$).

It should be noted that these secondary vertices are found generically in all events in the general reconstruction code. Secondary vertices used by the analysis described later are found using a different procedure.

4.2.2 Electron Reconstruction

In the calorimeter [67], hit finding converts the raw information of digitized counts from each cell to energy, deposited with appropriate calibrations. Corrections are applied to account for cell-by-cell variations in gain and pedestals. The cell energies are converted to transverse energy values by using the position of the interaction primary vertex. Cells with the same η and ϕ are grouped together to form towers. These towers are used in the next stage for electron, photon and jet identification.

4.2.3 Muon Reconstruction

Reconstruction of the muon tracks starts from conversion of the raw hits and time information into three dimensional position information. After the individual hits are found, track segments in each layer are formed by fitting groups of hits in a straight line. The tracking is done separately for segments before and after the toroid magnet. The segments are then matched and the momentum is determined from the measurement of the bend of the track while passing through the magnetized iron. By matching tracks in the central tracking system to local muon tracks, the momentum is corrected for the loss of energy in the calorimeter. The last step in the offline muon reconstruction is combining the results of the object reconstruction in the muon system with the information provided by the central tracking system and the calorimeter, and constructing a muon object suitable for physics analysis. The muon reconstruction will be described in more detail in chapter 5.

4.2.4 Jet Reconstruction and Missing E_T

Jet reconstruction uses a cone jet algorithm [69], which proceeds as follows:

- Preclustering: First the calorimeter towers are ordered in E_T. Starting from the highest E_T tower, for every tower with $E_T > 1$ GeV, a precluster is constructed from all adjacent towers with $\Delta\eta < 0.3$, $\Delta\phi < 0.3$. It continues until all the towers with $E_T > 1$ GeV are assigned to a precluster.

- Cone Clustering: The axis of the corresponding candidate jet is defined by the E_T-weighted centroid of each precluster. From it, all towers within a radius of 0.7 in $\eta - \phi$ space (isolation, i.e. $\Delta_R = \sqrt{(\Delta\eta)^2 + (\Delta\phi)^2}$, where η, ϕ are in radians) are assigned to the cluster. The centroid of this new jet and its new axis are recalculated. This process is repeated until it stabilizes.
- Merging and splitting: No towers should be shared among jets. However during cone clustering if two jets share some towers, the fraction of total energy that is shared between them is examined. If it is more than 50% of the E_T of the softer jet, the two jets are merged and the jet axis is recalculated. Otherwise, they are split into two jets with each tower being assigned to the closest jet.
- Suppress noise fluctuations: an E_T threshold of 8 GeV is set.

The missing transverse energy (E_T^{miss}) is a simple inclusive variable that can be the signature of particles escaping from the detector without interacting in it. These can be either neutrinos or particles emitted at very low angle along the beampipe, or new particles as predicted for instance in supersymmetric theories. However, experimentally, the E_T^{miss} measurement is distorted by several effects, some of which are inherent to the experimental method (energy resolution), and others can be corrected for, like the occurrence of so-called "hot cells", which can be generically characterized as energy deposition not related to the real event. The transverse/scalar missing energy distributions display a correct behavior in most of the runs, after hot cell removal and application of energy threshold (100 MeV on cells or 200 MeV on towers).

4.3 Global Monitoring and Data Handling System

Online monitoring of the collider data is crucial to ensure that the detectors are working properly and that the data are of high quality. The goal is to monitor detector performance, triggers, and data quality for physics.

Detector monitoring programs have been developed to various levels of maturity for the Silicon Micro-strip Tracker (SMT), Central Fiber Tracker (CFT), Calorimeter (CAL) and for the Muon System (MUO). Most have online and offline versions. The online Examines sample triggered events and produce histograms of raw data (ADC counts, energies, times, pulse heights, etc) as well as reconstructed objects (hits, segments, tracks). These histograms are stored in either HBook [71] or ROOT [72] files. There are a large number of histograms in these detector examines that detector experts can look at for monitoring the detector performance in detail. The programs are run by detector shifters in the control room. A subset of the histograms are usually examined at by shifters to monitor the health and performance of the detector for which they are responsible. Figure 4.2 is an example of muon performance during a typical run.

The Sequential Access via Meta-data (SAM) data handling system [73], is a software system that oversees the functions of cataloging data, transferring data in and out of mass storage systems, transferring data among different computer systems, allocating and monitoring computing resources, and keeping track at the user process level of file delivery status. SAM can be interfaced to different mass storage systems and to different batch schedulers. Files are stored in SAM using interfaces that require appropriate metadata for each file. The files are organized, according to the metadata provided, by data tier, and by production information.

The SAM system gives users access to all the files created by the DØ experiment (both detector data and simulation data), in a very flexible and transparent manner – the user does not need to know where the files are physically stored, nor worry about exactly how they are delivered to his/her process. SAM also provides the experiment with considerable flexibility in apportioning its computing resources.

There are currently over two dozen operational production SAM stations deployed at Fermilab and remote institutions including the online data logger, the FNAL reconstruction farm, the Central Analysis system (d0mino), a large cluster of Linux desktop machines called ClueD0, an analysis and calibration station, and test stations. Six major processing centers have been using these stations for two years to send Monte Carlo data to the central tape storage system at FNAL. The author was involved in the setup of the remote analysis center of a Linux cluster for the Indiana group. As one of the administrators for ClueD0 system, the author provided support for users and tested SAM system performance.

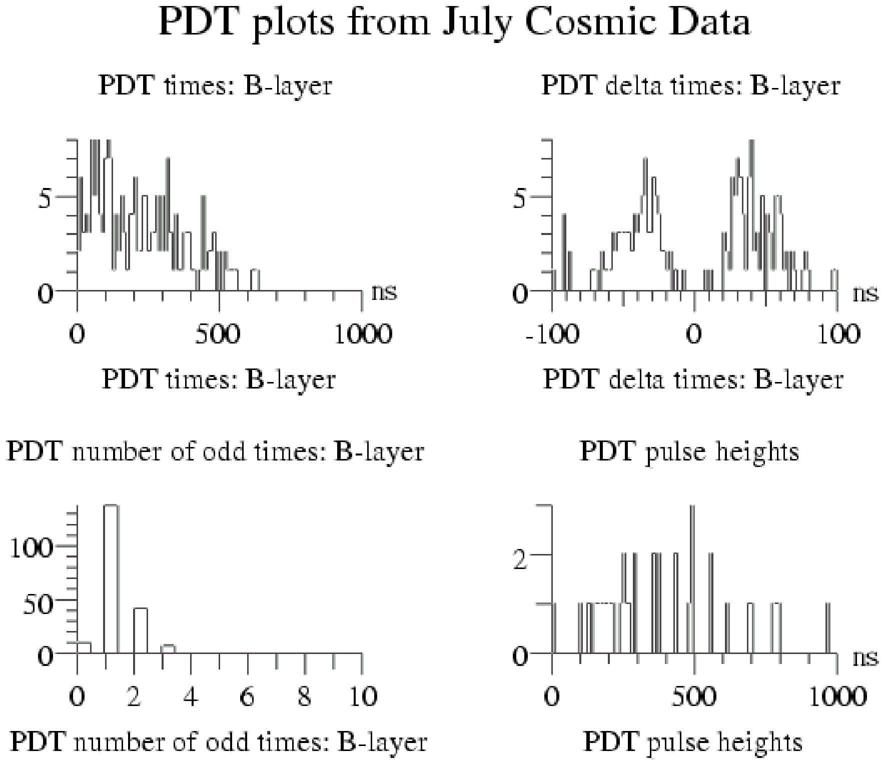

Figure 4.2: Global monitoring: distribution of time, delta time, number of odd times, and pulse height for muon proportional drift chamber (PDT–131).

Chapter 5

Muon Identification

There are several successive stages to identify a muon. After unpacking the electronic signal information from the muon spectrometer into physical quantities (such as wire hits, drift time, etc.), muon hits, segments and local muon tracks are reconstructed. Then a matching between a local muon and a charged particle detected from the central tracking system is done, and a global track fit is performed. Information from all these stages is used for muon identification and for quality classification of the muon candidate. In this chapter, we discuss different aspects of muon reconstruction, identification, as well as storing of the relative muon information.

5.1 Muon Hit Reconstruction

As shown in chapter 3, the muon spectrometer has a central region ($|\eta| \leq 1$) and forward region ($1 \leq |\eta| \leq 2$). Each region has 3 layers (usually called A,B and C layer, from inside toward outside).

There are three types of muon hit reconstruction, one for each type of muon system hardware [74]:

- PDT (proportional drift tubes in the central region).
- MDT (mini drift tubes in the forward region).
- MSC (scintillators in the central and forward regions).

5.1.1 PDT Hit Reconstruction

In the central region, there are 94 proportional drift tube (PDT) chambers, each chamber is composed of many cells filled with a gas mixture, each cell has a wire in the middle. Most of the wires in the central region are paired, so we can read out both drift time (the time it takes the signal to reach the wire), and axial time (the time it takes the signal to reach the clock from the place where it first hit the wire).

Because the the relation of drift time and distance depends on the incident angle of the track which created the hit, and there is a left-right ambiguity for each wire hit, the drift distance is not stored. The studies of time-to-distance relationship for the PDTs are discussed in chapter 6.

The first hit reconstruction assumes the incident angle to be 0 (perpendicular to the wire). Only later, when the first pass of the segment reconstruction is completed, a more precise determination of the hit position is possible.

5.1.2 MDT Hit Reconstruction

In the forward region, there are 6080 mini drift tubes (MDTs). Each tube (cell) has one wire. Unlike PDT's, there is only readout from one side of the wire. The wires are not linked to their neighbors; therefore, based on the information from the MDT itself, it is impossible to know where the hit occurred along the wire. The stored readout time is the the sum of the drift time and axial time. It is assumed that the hit in the MDT has occurred at the middle of the wire. The position uncertainty along the wire direction corresponds to half of the MDT wire length (the maximum wire length for A–layer is 3571 mm, for B–layer 5066 mm, for C–layer 5830 mm). This coordinate is more precisely measured from the scintillator information.

Because of the square profile of the MDT cells and their relatively small size, the relation between the drift time and the drift distance is practically linear, and does not depend significantly on the incident angle of the track.

5.1.3 MSC Hit Reconstruction

In both the central and forward region, scintillators provide timing information. The position of a hit is assumed to have occurred in the middle of the scintillator, and the position resolution is equal to half the relevant dimension of the scintillator. The time resolution is about 1 ns for the smaller counters, and 2–3 ns for the large outer counters.

5.2 Muon Segment Reconstruction

Muon segment reconstruction is the part of the muon reconstruction where the pattern recognition is performed. Hits in the muon chambers are combined, and a straight line segment is fitted through the hits. Originally the segment reconstruction was based on a combinatorial segment reconstruction algorithm; however, multiple algorithms were desired, and a linked list algorithm was consequently developed and used as the default algorithm [75]. Figure 5.1 illustrates a muon segment reconstructed from muon hits.

The algorithm is divided in 8 steps:

1. Transformation of "global" hits to "local" hits.
2. Creation of links between hits.
3. Matching of links into local segments.
4. Fitting of local segments.
5. Using vertex constraint for A-layer segment (if applicable).
6. Matching of local segments.
7. Applying a chisquare cut.
8. Filtering of local segments; transformation back to global segments

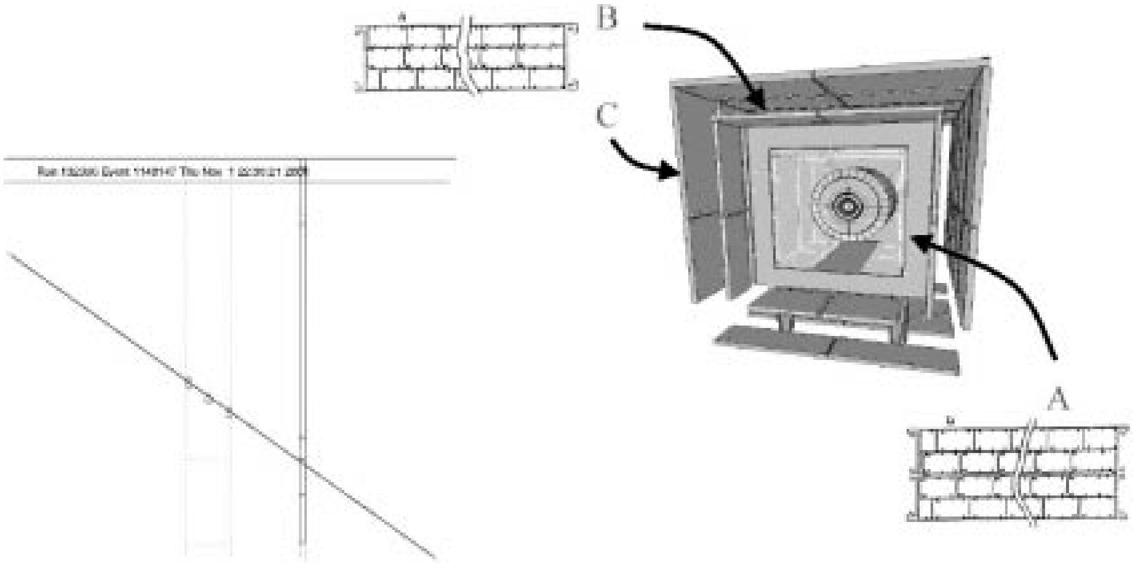

Figure 5.1: Muon reconstruction: from muon hits to segment. There are 4 planes of tubes in the A-layer, and 3 planes of tubes in the B-C layer.

5.3 Muon Local Track Reconstruction

The goal of the muon local track reconstruction [76] is to identify and determine the momentum of muon tracks from pairs of segments (two segments respectively in A and B-C layers) in the muon system. There are two different approaches for muon track finding: a combinatorial algorithm and a fit algorithm. The combinatorial algorithm is used in the Level-3 software trigger (chapter 3), and the fit algorithm is used in the offline muon reconstruction. Figure 5.2 illustrates a muon local track reconstruction from A and B-C segments.

The fitting algorithm reconstructs a muon track from a pair of segments by taking into account the propagation of the track in the toroidal magnetic field, multiple Coulomb

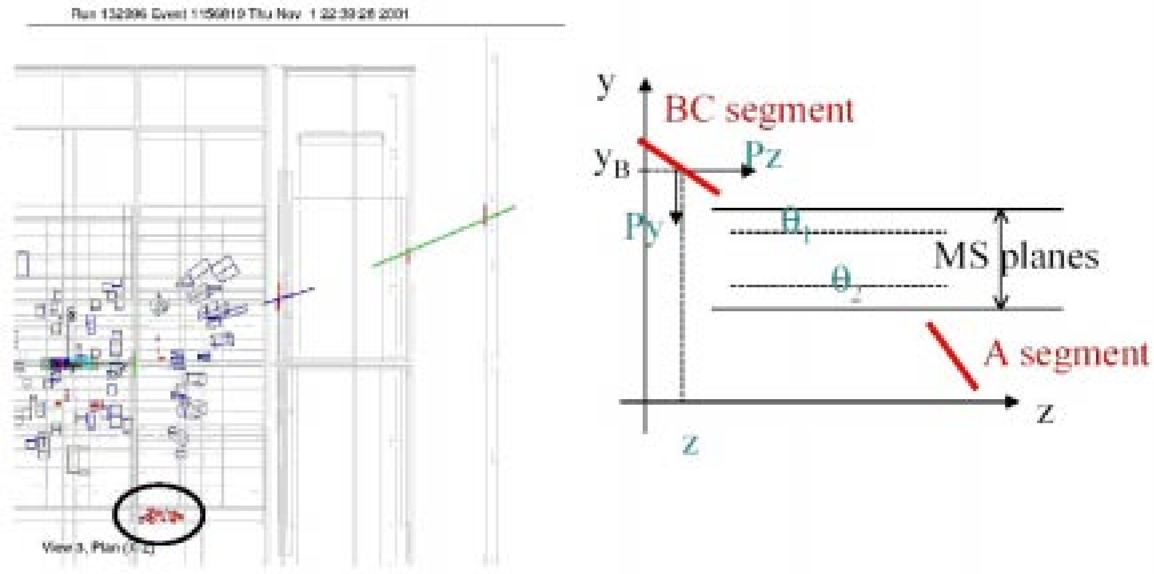

Figure 5.2: Muon reconstruction: from muon segments to local track. X-Z view (left) and Y-Z view (right).

scattering and the energy loss in the toroid. The steps are:

1. Grouping segments into pairs.

2. Computing an estimate of the track momentum from a geometrical calculation.

   The magnetic field in the toroid is set to be constant (1.8 Tesla). If L represents a straight line approximation of the particle path in the toroid and θ the angle between A and BC segments in the deviation plane, an estimation of the track transverse momentum is given by:

   $$p_T = \frac{300 \text{ MeV} \times B \times L}{\theta}.$$

   The p_T value is corrected by a constant energy loss of $0.016 \times L$ (MeV). This first quick estimation is used as an input for the fit.

3. A simple toroid geometry corresponding as much as possible to the `GEANT` geometry is used. The track is propagated step by step from the center of gravity of BC segment to the one of A segment using circular helices in space. At each step, an energy loss correction is performed using a function giving dE/dx as a function of momentum.

4. This propagation allows a 2D fit in the bend plane of the pair of segments using MINUIT with 5 parameters. As a result of the fit, we obtain the position of the track at y_A (the position of the center of gravity of segment-A along y-axis) and the track momentum components along y and z axis (ie, p_y, p_z) at y_A.

5.4 Muon Central Match

The goal of the Muon Central Match is to combine muon tracks with central tracker tracks by using error matrix propagation [77]. The matching procedure takes into account:

- the magnetic field in both solenoid and toroid; and
- multiple Coulomb scattering and energy loss in the toroid and calorimeter.

The matching is performed at the distance of closest approach to the beam axis (DCA). The error matrix of the local muon track is propagated in (x, y, z, px, py, pz) coordinates through the toroid and the calorimeter. Then we transform the propagated muon error matrix from the coordinates (x, y, z, px, py, pz) to the central tracker variables: (r, z, ϕ, $\tan\lambda$, $\frac{q}{p_T}$) for a combination at the DCA point. Finally the two tracks and the two error

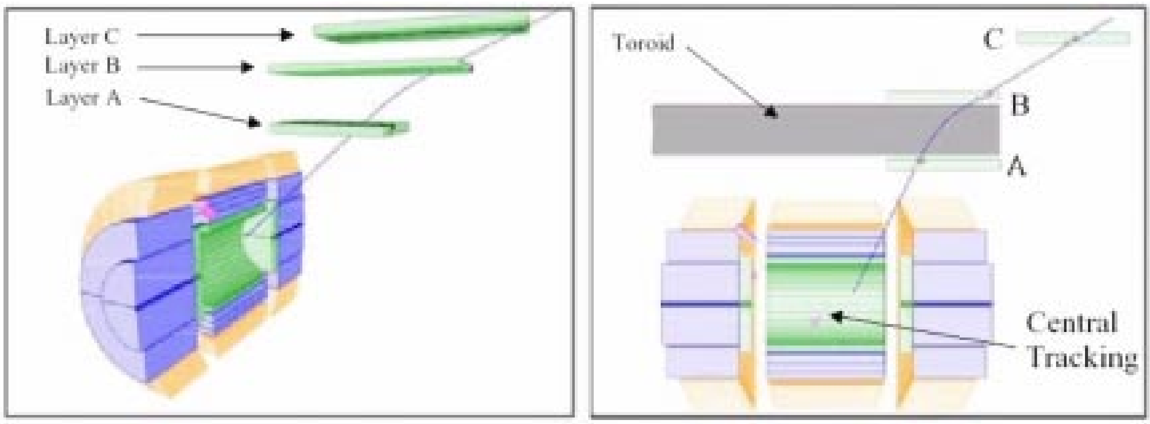

Figure 5.3: Muon reconstruction: match between local muon track and central track

matrices are combined to obtain the final track parameters. Figure 5.3 illustrates a match of a muon local track with a central track.

5.5 Muon Identification

The offline muon identification [78] is based on a match between a charged particle detected in the central tracker and a signal in the muon system. ChargedParticles are objects made by associating tracks detected in the SMT and CFT detectors, jointly called GTracks, and reconstructed vertices. To be used as a seed for a muon object, a charged particle is required to have transverse momentum greater than 1.5 GeV. The signal detected in the muon system can be a track penetrating the toroid, a track segment reconstructed inside the toroid (and A-layer segment), or just a set of hits detected in the muon system.

The status of the match is reflected by the value of a variable called **Idnseg**:

- Track Match (**Idnseg=3**)

  If there is a reconstructed local muon track, we loop over central tracks, and find the one which best matches the muon track as described in section 5.4, the χ^2 from the match error matrix is the smallest.

- Segment Match (**Idnseg=2,1**)

  If there is no matched track, but there is a reconstructed local muon segment, Segment-A (Idnseg=1) or Segment-BC (Idnseg=2), we loop over central tracks, and find the one that matches the muon segment.

- Hit Match (**Idnseg=0**)

  If there is a central track, but no local muon segment or track, then we do hit matching and calorimeter confirmation. We can measure the muon isolation by using the energy in a 3 by 3 tower around the muon direction in the calorimeter, and use this information to determine if the test is successful.

- UnMatch Track(**Idnseg=-3**)

  If there is a local muon track, but no central track match.

We define standard quality criteria for “tight”, “medium”, and “loose” muons that reflect the number and quality of the track elements.

A “tight” muon is defined as a local muon track that has:

- at least two wire hits in the A layer (inside the toroid).

- at least three wire hits in the B/C layers (outside the toroid).
- at least one matching scintillator hit.
- a successful fit ($\chi^2 > 0$).

For a “medium” quality muon we require:

- at least two wire hits in the A layer (inside the toroid).
- at least two wire hits in the B/C layers (outside the toroid).
- at least one matching scintillator hit.

For a “loose” muon, we allow one of the above tests to fail, with the scintillator hits and wire hits requirements treated as one test.

The contents of the Muonid root branch (the output of `muo_analyze`) for the `D0Reco` production version p11 is shown in Appendix A.

5.6 Muon Thumbnail

The muon object, MuonParticle, is one of the reconstructed physics objects available in the Thumbnail (TMB) files that reside on disks, for all data collected in Run II so far.

Thumbnail data format [79] is created in order to face the huge amount of data expected for the Run II. It is aimed at providing a basic data structure with a size as small as possible, with a maximum size per event not exceeding 10 Kbytes. The muon thumbnail part is limited to 1.5 Kb per event. Two operations are included in the construction of the thumbnail:

- packing: creating a thumbnail file with muon related information coming from MuonParticle. This compression is more powerful than the usual gzip algorithm, and care is taken that it preserves the necessary precision of the data to be stored.
- unpacking: reconstructing the original MuonParticle Chunk from the thumbnail file.

The contents of the Muon Thumbnail, for the production version p13 is shown in Appendix B.

5.7 Muon Analysis Package

An analysis package, `muo_analyze`, makes use of all the available methods for retrieving muon reconstruction results. The package makes a root tuple that includes all GTracks with $p_T > 1.5$ GeV, muon hits, segments, local muon tracks, the final muon objects (MuonParticle's), and Monte Carlo information on muons if available. The package `muo_analyze` can be run independently or as a part of the overall event analysis, `reco_analyze`, if the user is interested in other reconstructed objects (e.g. jets, electrons, etc.). The documentation, including the contents of the branches, is available through the standard DØ software at [81].

5.8 Performance of the Muon Reconstruction

In this section, the achieved performance of the muon reconstruction is briefly summarized [78]. First the momentum resolution for local muon tracks is studied. For this purpose, we define a dimensionless quantity:

$\texttt{mures} = \sigma(q/p)/(q/p) = (q(chp) \times q(loc) \times p(chp))/p(loc) - 1,$

where $q(loc)$ and $p(loc)$ denote the charge and momentum of the track reconstructed in the muon system, and $q(chp)$ and $p(chp)$ are the charge and momentum of the matching ChargedParticle (explained in section 5.5). Neglecting the finite resolution of the central tracking system, we study the behavior of the variable `mures` as a function of $p(chp)$ for a track reconstructed in WAMUS and in FAMUS. We select "tight" muons (as defined earlier, with an additional requirement of at least 4 wire hits behind the toroid.

We fit the variable `mures` to the functional form:

$$\frac{\sigma_p}{p} = \frac{\alpha(p-\beta)}{p} \oplus \gamma\, p,$$

where p is in GeV/c. The α term results from multiple Coulomb scattering and the γ term is a measure of the position resolution. The variable β has an average value of 2 GeV/c, and represents the energy loss [82].

All of the available DØ production version p11.07 muon data was combined for this analysis. The results are shown in Fig. 5.4, together with the parametrization of $\frac{\sigma_p}{p}$ quantity. The observed σ_p for FAMUS muons is close to the expectation from the Monte Carlo studies [78]. On the other hand, at this stage of the analysis, the momentum resolution for WAMUS muons requires further improvements for a good match to Monte Carlo expectations.

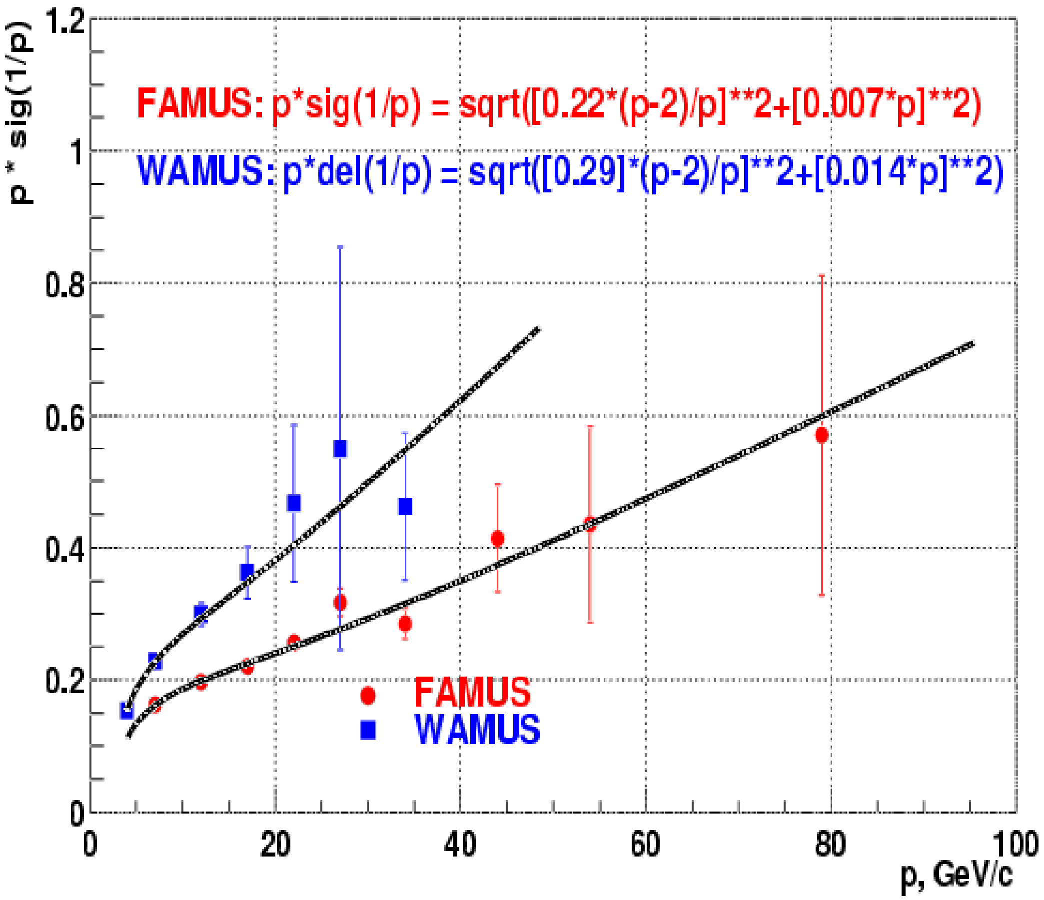

Figure 5.4: $\frac{\sigma_p}{p}$ vs central track momentum for WAMUS and FAMUS.

The muon momentum resolution is much improved when there is a match between the local muon track and the tracks from the central system.

Figure 5.5 shows the $J/\psi \to \mu^+\mu^-$ invariant mass calculated by using local muon

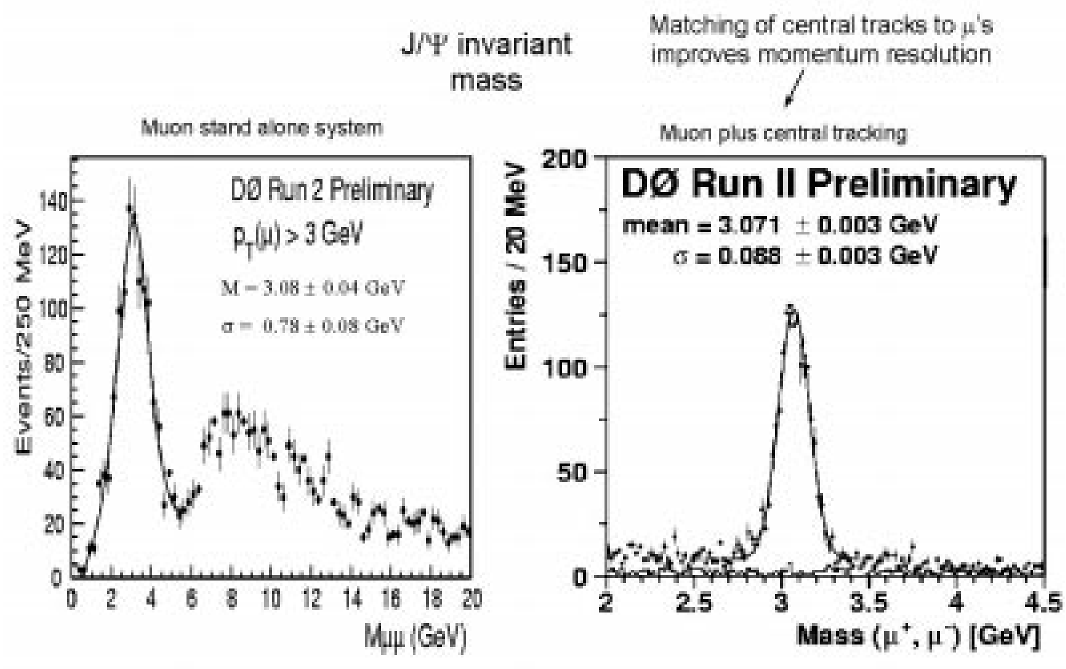

Figure 5.5: Comparison of $J/\psi \rightarrow \mu^+\mu^-$ mass resolution. Left: muon system alone (local muon only); Right: muon candidate with central track match.

information only, and then by using the momentum of muons matched with central tracks. The mass resolution in the latter case is improved by an order of magnitude.

Figure 5.6 is an example of an event display available in the DØ control room. The event shown is a $Z \rightarrow \mu^+\mu^-$ candidate.

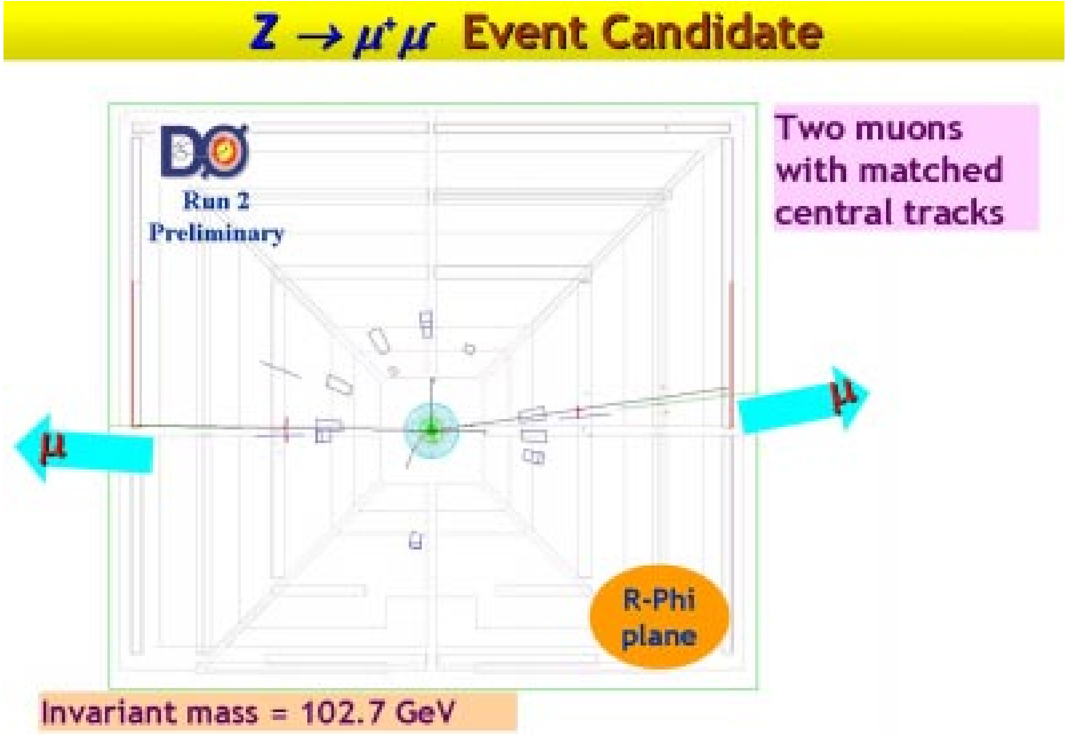

Figure 5.6: Event display ($R - \phi$ plane) of a $Z \to \mu^+\mu^-$ event candidate. Two muons are detected by the muon spectrometer.

Chapter 6

PDT Time-to-Distance Studies

6.1 Introduction

As discussed in chapter 3, Proportional Drift Tube (PDT) chambers are located in the central region of the muon spectrometer. They consist of cells approximately 10 cm wide, 5 cm high and several meters long with a high voltage wire strung in the center. A muon track passing through a cell ionizes the gas filling the chamber. Electrons from ionization drift toward the positively charged wire and the time of the generated electric signal is recorded. To get an exact position of the muon trajectory with respect to the wire, one has to determine the relationship between the drift time and the drift distance. For convenience, and also for some historical reasons, this distance is measured in the middle plane of a cell. The time-to-distance relationship is not linear, and, in addition, depends on the incident angle of the muon. It is parametrized with a third-order polynomial in time and a third-order polynomial in the incident angle, resulting in 16 parameters needed to be experimentally determined (the full form of the relationship is shown in a later section). In general, this parametrization depends on the gas composition and it is observed that a

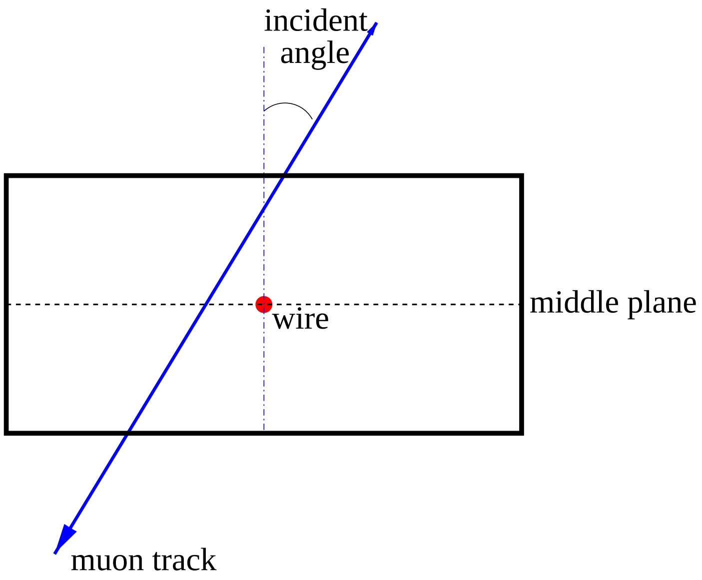

Figure 6.1: A schematic view of a muon track penetrating a proportional drift tube. The cell is 10 cm wide, filled with mixed gas. The incident angle θ is defined as the angle between muon track and the normal to the middle line.

small change of gas mixture can cause a large difference in the drift velocity. The typical gas mixture used in Run II is Argon with an 8.2% addition of CF_4 and an 8% of Methane (CH_4). Every six months, DØ flushes the gas flowing in the PDTs. An arrival of a new gas trailer requires the time-to-distance relation (simply called “t2d”) to be re-evaluated and corrections, if necessary, to be made. Figure 6.1 shows a muon track penetrating a muon proportional drift tube and the definition of the middle plane of the cell as well as the incident angle.

The original procedure adopted for these studies used a stand-alone setup of 8 PDT cells (“canary”). Two scintillating counters were used to trigger on cosmic ray muons. Changing the relative positions of the counters allowed the selection of muons with different incident

Trailer	CF_4 (%)	Methane (%)	Arrival Date	Connection date to the detector
478-1	8.26	8.63	March 2001	March 2001
467-1	7.88	7.63	November 2001	January 2002
478-2	8.07	7.99	May 2002	November 2002
467-2	8.05	8.30	May 2003	May 2003

Table 6.1: Gas compositions circulating in the DØ Run II muon system

angles. This setup is similar to the one used in the Run I studies described in Ref. [83]. However, the operating gas used for the PDTs in Run I was different (a mixture of 90% Ar, 5% CO_2 and 5% CF_4). In addition, the Run II setup does not include proportional wire chambers (PWC), which were used to measure the trajectory of a cosmic ray in Run I. We have to extract all necessary information, including solving left-right ambiguities and calculating the incident angle of a muon track etc, from the fitted trajectory. This requires several additional steps in the procedure. The advantage of this approach is its applicability to both the stand alone cosmic ray setup and the collider data.

The author established the "t2d" relation for two different gas mixtures prior to the beginning of the run and twice for the gas circulating in the detector. The data from the "canary" setup was initially used, and later a procedure was developed using the selected muon data from the detector.

The gas composition circulating in the detector is summarized in Table 6.1. The original 16-parameter "t2d" relationship was established for gas from trailer 478-1, using canary data. It was later noticed by Zieminski (using "canary" data for selected conofiguration) that the gas from the trailer 467-1 was 6% faster and the original parametrization was scaled by a factor of 1.06. Analysis of the chamber resolutions for the B and C layer PDTs did not contradict this adjustment.

However, the observed track resolution for the A-layer PDTs continued to be considerably worse than expected, at the level of 2 mm. This effect was traced down to a slightly different gas circulating through the A-layer PDTs and four other B-layer PDTs. This gas ("clean") undergoes further purification and is slower than the nominal ("dirty") gas circulating in the B/C layer PDTs and also used in the canary setup. The observed difference has been qualitatively attributed to some additional water vapor and oxygen (O_2) admixture in the purified gas. According to theoretical calculations, the presence of 0.12% of H_2O can reduce the drift velocity by 6% [87]. We therefore developed a special procedure of extracting the "t2d" parametrization directly from data. Since October 2002, two different sets of "t2d" parameters have been used in the reconstruction program, one for the PDTs on the A-layer gas circuit and the other for the remaining PDTs. The achieved averaged resolution for PDTs illuminated with small incident angle muons is approximately 700 μm.

6.2 "Canary" Experimental Setup

The stand alone apparatus is shown schematically in Figure 6.2. The minichamber has eight drift cells arranged in four planes. The cells have a similar construction to the muon PDT chambers used in the DØ collision hall.

The readout electronics had free running gates interrupted by a coincidence in the scintillators. For a given event, drift times, delta times, and pad signals were digitized and stored on memory for a later transfer to the analysis PC. The Signal-data flow chart is shown in Fig. 6.3.

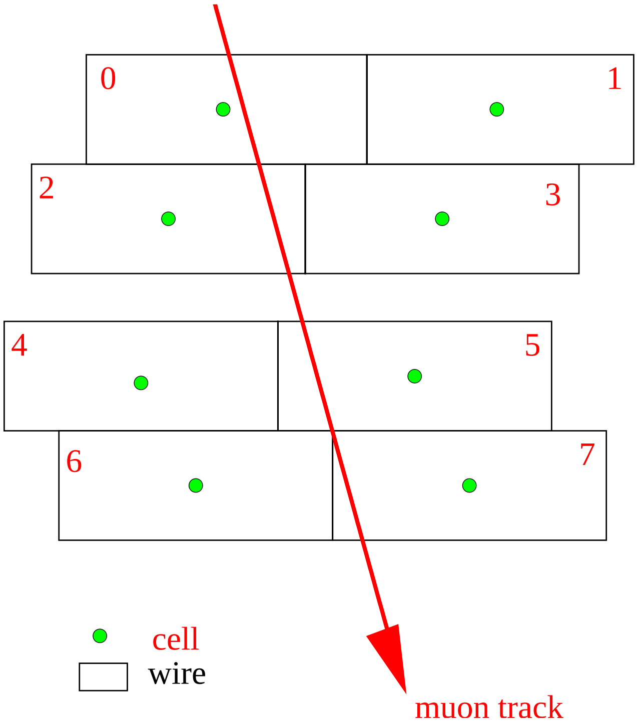

Figure 6.2: Schematic of the experimental apparatus for “canary” data.

6.3 Analysis

From Run I experience, we know that for a given muon trajectory, its distance from the wire, measured at the middle plane, $d(t, \theta)$, is well described by a function of the form:

$$\begin{aligned} d(t,\theta) &= (\alpha_{10} + \alpha_{11}\theta + \alpha_{12}\theta^2 + \alpha_{13}\theta^3)t + (\alpha_{20} + \alpha_{21}\theta + \alpha_{22}\theta^2 + \alpha_{23}\theta^3)t^2; \\ &+ (\alpha_{30} + \alpha_{31}\theta + \alpha_{32}\theta^2 + \alpha_{33}\theta^3)t^3 + (\alpha_{40} + \alpha_{41}\theta + \alpha_{42}\theta^2 + \alpha_{43}\theta^3)t^4, \end{aligned} \quad (6.1)$$

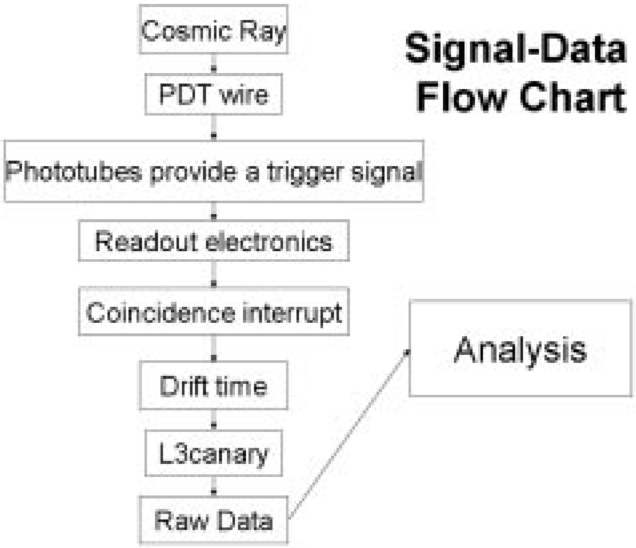

Figure 6.3: Signal data flow chart for “canary” experimental setup.

where t is the drift time, and θ is the track incident angle. The parameters α_i can be determined from a least squares fit to the data using a multi-stage procedure. For a fixed θ angle, Eq. 6.1 translates into a polynomial dependence of the form:

$$d(t) = \beta_1 t + \beta_2 t^2 + \beta_3 t^3 + \beta_4 t^4. \tag{6.2}$$

Muon track candidates were required to have four hits, one in each plane. Data collected with the “canary” setup were divided into groups depending on the configuration of wires providing the signal (Table 6.2). These groups spanned different ranges of incident angles.

The fit minimized χ^2 contributions summed over all events with a successful straight line fit to a muon trajectory. Only tracks with a $\chi^2 < \chi^2_{max}$ were accepted. The value of χ^2_{max} varied depending on the shape of the fitting. A typical value used was χ^2_{max}=30, however, the final results were insensitive to the χ^2_{max} selection between 10 – 200.

In addition, for each muon candidate we considered up to 16 left-right combinations (the actual number of valid combinations for a given group was smaller). The configuration with the smallest χ^2 was selected and the χ^2 for this fit was added to the overall χ^2 obtained from summing individual event contributions. The fit parameters included the startup time, T_0, with respect to which the drift time was measured. After a preliminary fit with a very loose χ^2_{max} cut, events within a given wire configuration group were subdivided into subsamples corresponding to different incident angles and the parameters β_i were fitted for each subsample. Once the values of parameters β were known, their dependence on the incident angle was parametrized as a third order polynomial, as described by Eq. 6.1.

The fit χ^2 for a given track is defined as a sum over planes of $(\Delta d_i)^2$, where $\Delta d_i = d(t)_i - d0(t)_i$, with $d(t)_i$ being the expected drift distance for a given drift time and "t2d" parametrization, and $d0(t)_i$ the fitted distance from the wire. Distributions of $(\Delta d_i)^2$ for individual planes can be translated into a per plane resolution of the chamber, σ. The relevant relations for a four (or three) plane chamber with equal spacing between planes are:

(i) for 4-plane chambers:

$$\begin{aligned} \sigma &= \sqrt{3} \times \sigma \text{ (plane 1 or plane 4)}, \\ \sigma &= \sqrt{3/2} \times \sigma \text{ (plane 2 or plane 3)}. \end{aligned} \tag{6.3}$$

(ii) for 3-plane chambers:

$$\begin{aligned} \sigma &= \sqrt{6} \times \sigma \text{ (plane 1 or plane 3)}, \\ \sigma &= \sqrt{3/2} \times \sigma \text{ (plane 2)}. \end{aligned} \tag{6.4}$$

where σ (plane i) represents the width of a Gaussian fit to the Δd_i distribution for that plane.

When analyzing the data from the "canary" setup we defined seven different data sets (COL1, DIAG1, DIAG2, EDGE, DIAGAZ, DIAGXAZ, COL2), corresponding to different wire configurations, as listed in Table 6.2. Data from each set were analyzed separately and only β parameters obtained from different sets were subject to a global fit for their dependence on the incident angle.

Setup	COL1	DIAG1	DIAG2	EDGE	DIAGAZ	DIAGXAZ	COL2
plane 1	0	1	0	0	1	0	1
plane 2	2	3	3	3	3	2	3
plane 3	4	5	5	5	4	5	5
plane 4	6	6	7	6	6	7	7

Table 6.2: "Canary" setup for 7 different wire configurations. The numbers correspond to cell numbers on Fig. 6.2.

6.4 Monte Carlo Analysis

The fitting procedure was tested using a Monte Carlo technique. We generated four data sets, corresponding to the experimental setups of COL1, DIAG1, DIAG2, and EDGE (see Table 6.2). We assumed a drift velocity of 0.1 mm/ns, $T_0 = 50$ ns and a Gaussian smearing of the coordinate in the wire plane of 2 mm. Using this information we calculated appropriate drift times and prepared input data in the same format as real data. The results of the fit for 1000 Monte Carlo events in each group are summarized in Table 6.3. As an example, the fitted drift distance as a function of drift time is shown in Fig. 6.4 for the DIAG1 configuration.

Setup	T_0(ns)	velocity(mm/ns)
COL1	50.1560	0.100125
DIAG1	50.0585	0.100136
DIAG2	50.0747	0.100113
EDGE	51.1109	0.099776

Table 6.3: Monte Carlo fitting results for T_0 and drift velocity for 4 different configurations.

We find that our procedure reproduces the input parameters with sufficient accuracy. The fitted values of T_0 are within 0.3% (for COL1, DIAG1, DIAG2), and 2.2% (for EDGE), and the fitted velocity within 0.14% (for COL1, DIAG1, DIAG2), and 0.22% (for EDGE) of the input values.

6.5 “Canary” Data Analysis – step by step Procedure

Here is the step-by-step description of the fitting procedure. The geometry of the setup was hardwired in the program. We used MINUIT minimization routines within a ROOT package macro.

1. Extraction of raw times from the “canary” output.

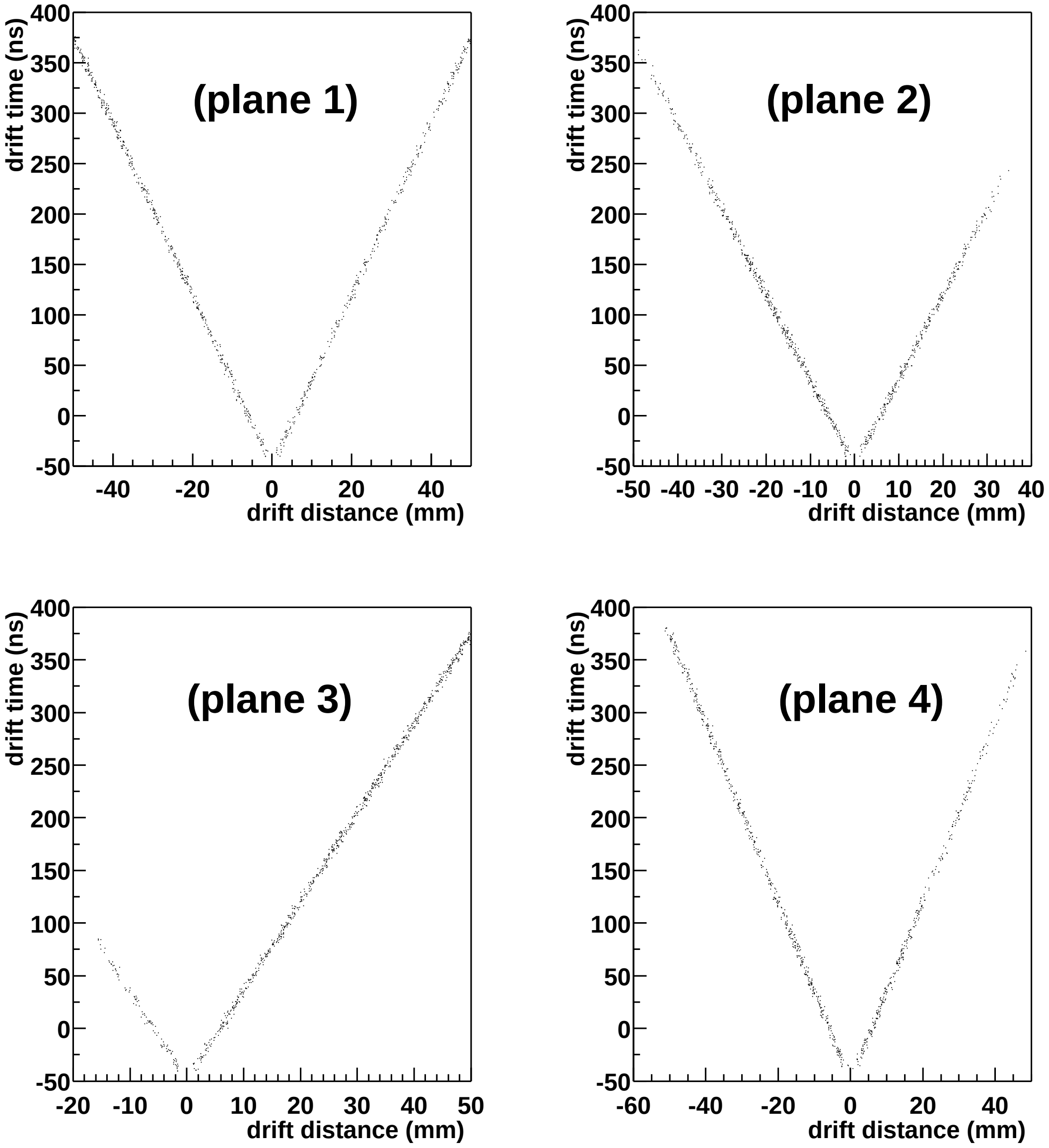

Figure 6.4: Monte Carlo analysis: drift distance versus time for individual planes using the DIAG1 wire configuration.

Events collected with the "canary" setup were unpacked, a given wire configuration selected and raw times calculated. An ASCII file with this information was produced.

2. T_0 determination.

   We used events with small incident angles to fit T_0 (together with up to three drift velocity parameters) .

3. Separation of data into incident angle range subgroups.

   The "t2d" relation for events in a given data set is fitted as a polynomial (up to third order in drift time). The incident angle is calculated, and data are separated into subgroups of events with similar incident angles (within a 5 degree range).

4. The "t2d" four parameter fits.

   The "t2d" relation for events from a given angular subgroup was established using Eq. 6.2. We used up to four parameters. Because of the possible correlations between the fit parameters we applied an iterative procedure. After the initial fit with all parameters free we plotted the dependence of the fitted parameters β_1 versus angle, separately for different original data sets defined in Table 6.2. We checked the consistency of results and parametrized β_1 as a function of the incident angle. We then repeated the fit to the data with the parameter β_1 calculated for a given event and fixed, and with the rest of parameters allowed to vary. Next, we found the dependence of β_2 on the angle, parametrized it and proceeded until the β_3 and β_4 dependences on θ were established.

Fig. 6.5 describe the dependence of parameters β_i on the incident angle. A good consistency between results from different data sets is observed.

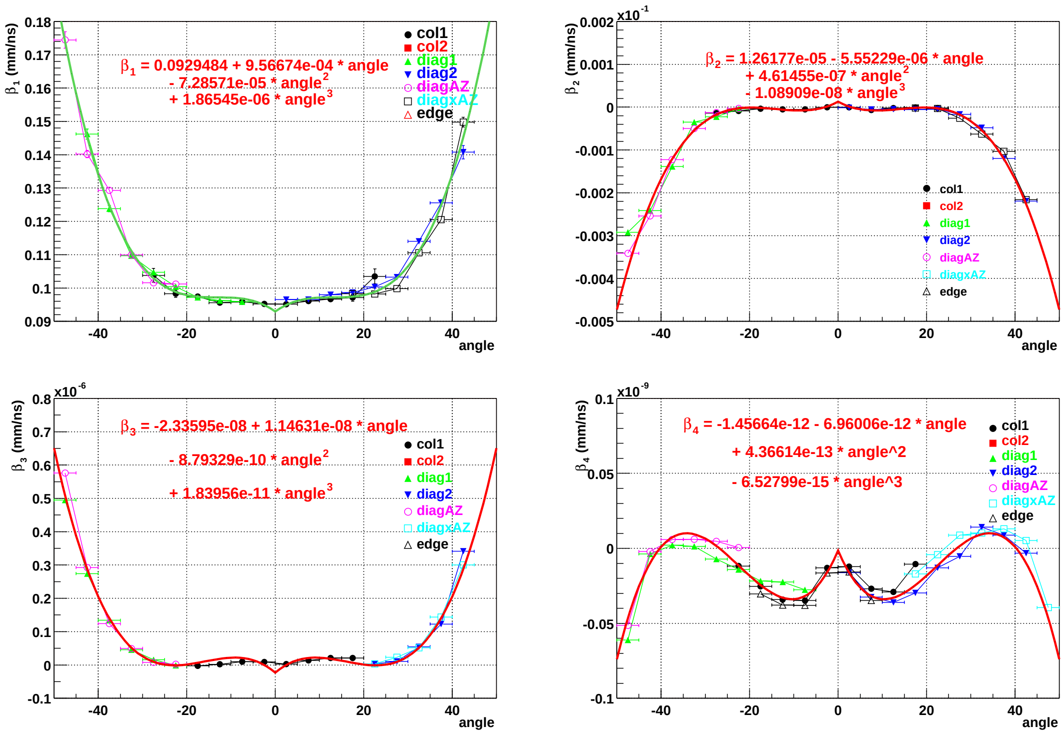

Figure 6.5: Canary: β_1, β_2, β_3, β_4 vs incident angle.

The time-to-distance relation for three incident angles $(0°, 35°, 50°)$ is plotted in Figure 6.6(a). The corresponding “t2d” dependence obtained for the gas used in Run I is shown in Figure 6.6(b).

The “t2d” relation for a given cell geometry and gas mixture can be estimated using a computer simulation program Garfield [84]. The programme starts with computing the electric field in the tube for the given tube geometry, wire position, wire thickness and high voltage on the wire. Garfield accepts two and three dimensional field maps computed by finite element programs such as Maxwell [86], as basis for its calculations. The program can calculate the drift time and drift distance distributions. These "t2d" simulations do not include electronic responses and can only serve as an approximate benchmark.

The relevant Garfield calculations were performed for the nominal Run II gas mixture by Gomez from the Universitates of Andes [85]. His results are shown in Figure 6.6(c), and compared to our findings for the unpurified gas in Fig. 6.10. A good agreement is observed at large drift distances, where the effects of the electronic readout are expected to be less pronounced. However, when we applied the Garfield parametrization to the data the resulting χ^2 was much worse than for the parametrization derived experimentally.

6.6 Run II Collider Data

The "t2d" parametrization illustrated in Fig. 6.5 was initially used for the reconstruction of the Collider data. However, it was noticed that the gas from a new trailer, 467-1 (see Table 6.1) had slightly different properties. We used the "canary" data to compare fitted drift velocities for the new gas compared to that for the gas from trailer 478-1. A 6% increase in the gas velocity was observed, both for small and large incident angles. In addition, we have noticed that the B and C-layer segment resolutions for the Collider data could be improved if we introduced a similar correction in the reconstruction program. The achieved hit resolution was close to the expected value of 700 microns. However, similar resolution could not be achieved for the A-layer PDTs, which were hooked up to a different

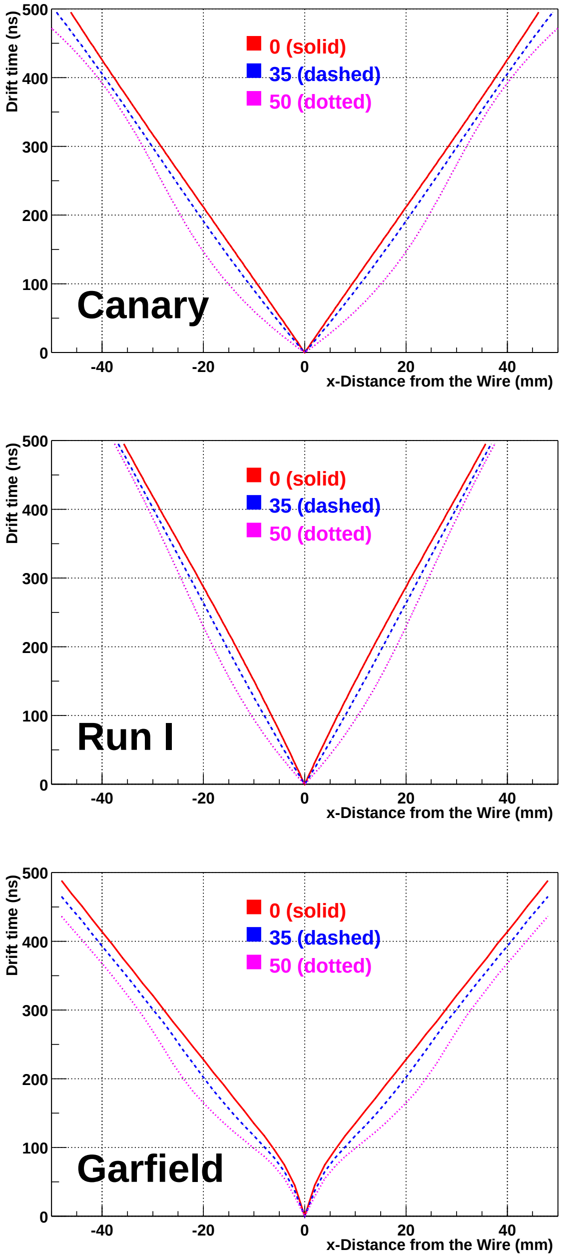

Figure 6.6: Drift distance versus time for three angles ($\theta = 0°, 35°, 50°$): (a) measured for the Run II "dirty" gas, (b) Run I results (c) Garfield program predictions for the Run II nominal gas (no water admixture).

gas circulation circuit. Therefore, we decided to use real data to determine the “t2d” relation for these PDTs.

Wood of Northeastern University provided us with ASCII files of wire positions and drift times for individual PDTs. The data came from the skimmed “muon plus jet” events and the applied cuts included a requirement of a “tight” muon with hits in all planes and momentum measured in the muon system greater than 10 GeV, plus the presence of a jet with transverse energy greater than 12 GeV. We used the data from twelve four-plane PDTs for the “t2d” relation extraction. The remaining data were used for cross checking.

6.6.1 A-layer Real Data Fitting Strategy

The fitting strategy is described below.

1. For a given PDT, fit the data using three parameters: correction to T_0, β_1, β_2. Allow the empirical $\chi^2_{max} = 50$ in the fit. Use the fitted parameters to calculate incident angle for each event and create new data files with improved drift times corresponding to different angular regions.
2. Combine data for a given angular region from all twelve PDTs.
3. Refit combined data in a given angular region using four parameters: ΔT_0 (to check consistency – expected to be 0), β_1, β_2 and β_3.
4. Plot β_1 versus angle and parameterize this dependence.
5. Fix β_1, and refit data with remaining parameters free.

6. Plot β_2 versus angle and parameterize this dependence.
7. Fix β_1 and β_2, and refit the data with remaining parameters free.
8. Plot β_3 versus angle and parameterize this dependence.
9. Fix β_1, β_2 and β_3, and refit the data with the β_4 parameter free.
10. Plot β_4 versus angle and parameterize this dependence.
11. For each angle range, get distributions of Δd residuals.

6.6.2 Results

Figure 6.7 illustrates the dependence of parameters β_i on the incident angle. The fitted time-to-distance relation for three incident angles $(0^\circ, 35^\circ, 50^\circ)$ is plotted in Figure 6.8 and compared to the "canary" results, used originally for the B/C layer PDTs, in Figure 6.9. The "A-layer" parametrization has a 3% slower drift velocity for tracks with a zero incident angle, $\theta = 0^\circ$. The difference increases to 6% at $\theta = 35^\circ$. The observed difference in shape at $\theta = 50^\circ$ requires further investigation.

The average drift velocity for $\theta = 0^\circ$ tracks is 0.091 mm/ns and 0.094 mm/ns for the "A-layer (clean)" and "canary (dirty)" gas, respectively. These results have been verified by flowing the two types of the gas in the "canary" setup. The corresponding two data sets were collected, within a week from each other, in September 2002. The "EDGE" wire configuration was used. The analysis of these data, performed by Zieminski, indicated a $2.2 \pm 0.2\%$ difference in the drift velocities, with the absolute values of 0.093 ± 0.02 mm/ns

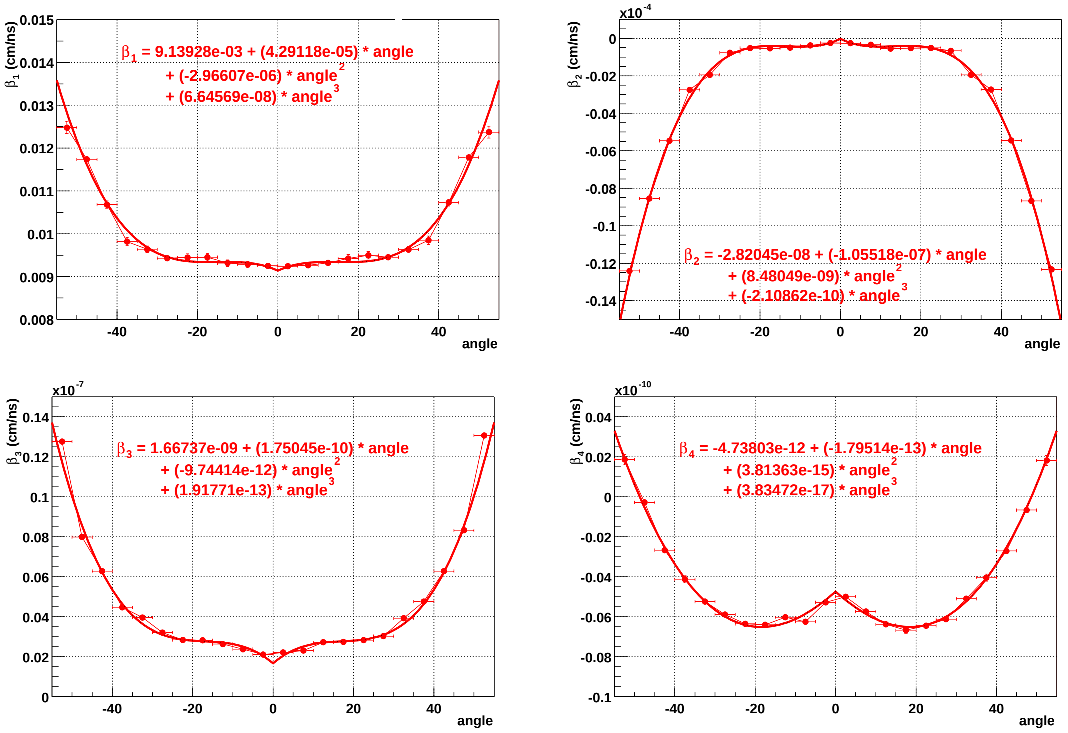

Figure 6.7: Dependence of parameters β_1, β_2, β_3, β_4 on the incident angle for the A-layer ("clean") gas.

and 0.095 ± 0.02 mm/ns for the "clean" and "dirty" gas respectively. The uncertainties reflect a 5 ns uncertainty in the T_0 parameter for the setup.

The difference between the "clean" and "dirty" gas can be attributed to the different content of water in each gas. The analysis of gas content by Rucinski from Fermilab (done in September 2002) indicated that there is 0.12% of water in the "clean" gas compared to at most 0.06% of water in the "dirty" gas. The presence of water is known to reduce the drift velocity for a given gas. The strength of this effect is illustrated in Table 6.4, based on the Garfield calculations by Yatsunenko [87]. The Table shows the drift time T* needed to cover a distance of 4.8 cm for the various concentration of the water admixture.

Water(%)	CF_4(%)	CH_4(%)	Ar(%)	T*[ns]
0.00	8.00	8.00	84.00	500
0.06	7.98	7.98	83.98	515
0.12	7.96	7.96	83.96	530
0.30	7.90	7.90	83.90	610

Table 6.4: Drift time dependence on the concentration of water admixture. T* is the drift time needed to cover a distance of 4.8 cm for the various concentration of the water admixture.

The predicted drift velocity for 0.12% water admixture is 4.8 cm / 530 ns = 0.091 mm/ns, exactly the value found in our analysis.

6.6.3 Relationship between Residuals and Incident Angles

As discussed earlier, a residual Δd is defined as the difference between the fitted coordinate and the hit coordinate obtained from the measured drift time and the "t2d" relationship, and calculated in the middle plane of a cell. Results of Gaussian fits to the Δd_i distributions, performed for data corresponding to different ranges of incident angle are summarized in Table 6.5. The last column translates measured quantities into the hit resolution per plane using Eq. 6.3 and Eq. 6.4. The hit resolution increases with incident angle from 700 μm for $\theta = 0°$ to 1400 μm for $\theta = 50°$. The increase is somewhat faster than a simple $1/\cos\theta$ dependence. (Since the residual is along the midplane, the drift distance should be equal to the product of residual times $\cos\theta$).

The observed dependence of the hit resolution on the incident angle is reflected in hit

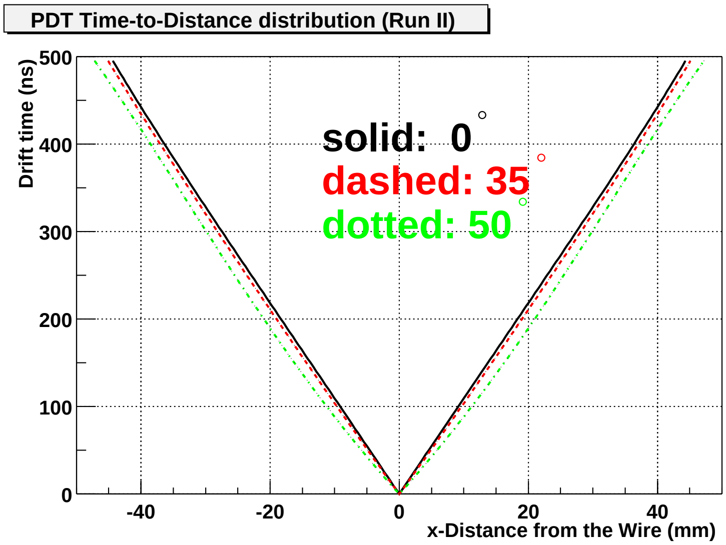

Figure 6.8: Drift distance versus time for the A-layer ("clean") gas for three values of the incident angle. (The unit of angle is degree).

resolutions measured for individual PDTs and collected in Table 6.6. The resolution for PDTs in barrel number "2" is approximately 800 μm, as expected for small incident angles. The hit resolution for PDTs located further from the collision center (barrel numbers "1" and "3") is worse, but consistent with results from Table 6.5. Similar hit resolutions were obtained for the BC-layer PDTs, using the "canary × 1.06" parametrization, as illustrated in Table 6.7.

As examples, residuals for PDT 020 (A-layer) and PDT 120 (B-layer) are shown in Figure 6.11 and Figure 6.12, respectively.

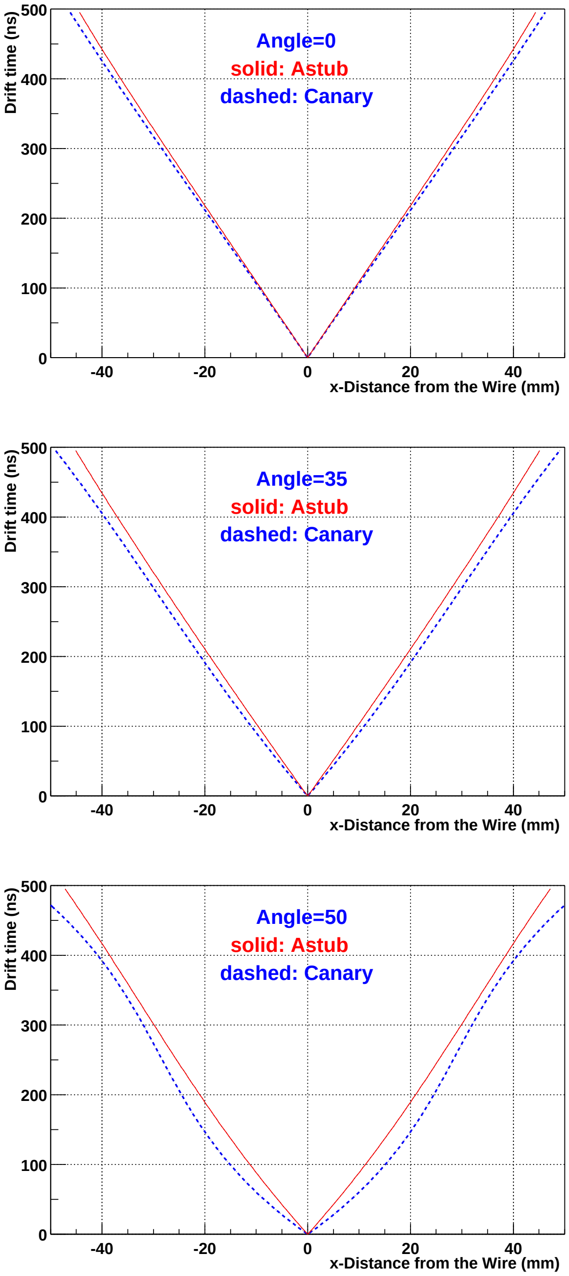

Figure 6.9: Comparison of the “t2d” parametrization for the “clean” (Astub) and “dirty” (Canary) gas: (a) incident angle $\theta = 0°$; (b) incident angle $\theta = 35°$; (c) incident angle $\theta = 50°$.

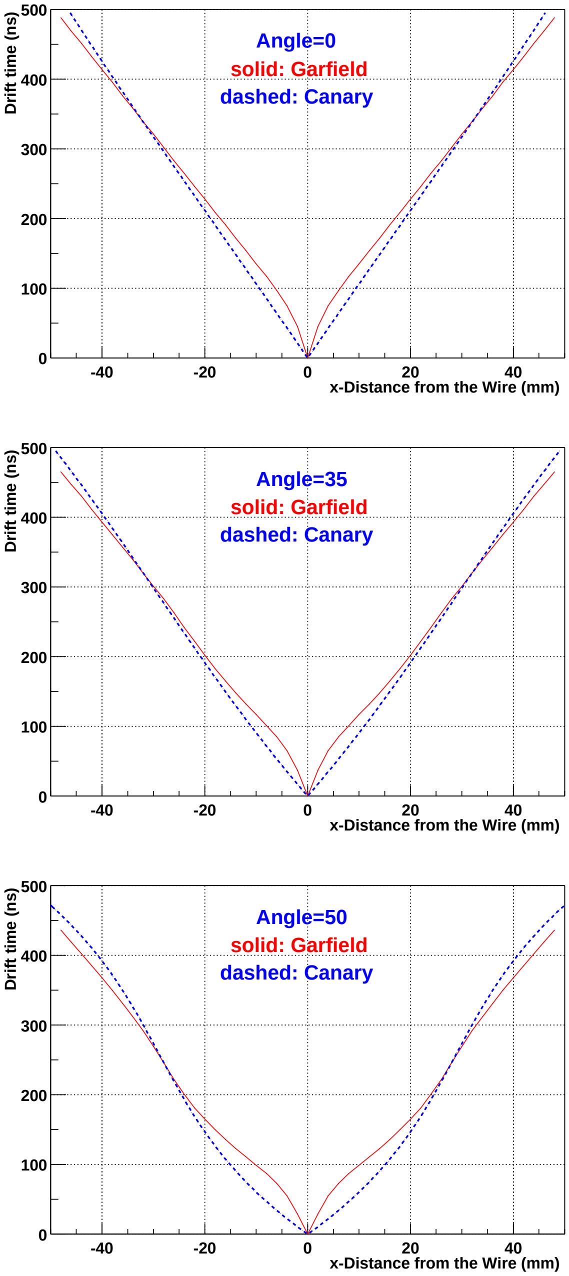

Figure 6.10: Comparison of the “t2d” parametrization for Canary and Garfield: (a) incident angle $\theta = 0°$; (b) incident angle $\theta = 35°$; (c) incident angle $\theta = 50°$.

Angle Regions	σ(plane 1)	σ(plane 2)	σ(plane 3)	σ(plane 4)	σ(hit)
-05 — 00	393 μm	545 μm	567 μm	418 μm	691 μm
00 — 05	431 μm	613 μm	538 μm	376 μm	702 μm
-10 — -05	500 μm	604 μm	610 μm	499 μm	804 μm
05 — 10	417 μm	575 μm	622 μm	429 μm	733 μm
-15 — -10	521 μm	699 μm	628 μm	487 μm	843 μm
10 — 15	478 μm	700 μm	669 μm	469 μm	829 μm
-20 — -15	584 μm	799 μm	675 μm	506 μm	923 μm
15 — 20	573 μm	781 μm	743 μm	551 μm	953 μm
-25 — -20	593 μm	878 μm	910 μm	624 μm	1074 μm
20 — 25	621 μm	887 μm	840 μm	594 μm	1055 μm
-30 — -25	570 μm	815 μm	832 μm	577 μm	1001 μm
25 — 30	553 μm	761 μm	813 μm	576 μm	971 μm
-35 — -30	582 μm	925 μm	865 μm	571 μm	1047 μm
30 — 35	518 μm	765 μm	807 μm	539 μm	939 μm
-40 — -35	722 μm	1060 μm	1047 μm	736 μm	1276 μm
35 — 40	681 μm	960 μm	966 μm	678 μm	1178 μm
-45 — -40	821 μm	1197 μm	1194 μm	848 μm	1455 μm
40 — 45	755 μm	1104 μm	1106 μm	772 μm	1338 μm
-50 — -45	817 μm	1123 μm	1198 μm	864 μm	1438 μm
45 — 50	790 μm	1121 μm	1064 μm	769 μm	1344 μm
-55 — -50	1073 μm	1449 μm	1442 μm	1045 μm	1802 μm
50 — 55	1018 μm	1196 μm	1306 μm	915 μm	1603 μm

Table 6.5: Residuals and sigma for the “A-layer (clean)” gas

Chambers	σ(plane 1)	σ(plane 2)	σ(plane 3)	σ(plane 4)	σ(hit)
PDT 010	735 μm	961 μm	927 μm	691 μm	1196 μm
PDT 011	613 μm	885 μm	804 μm	569 μm	1029 μm
PDT 012	665 μm	908 μm	886 μm	673 μm	1129 μm
PDT 013	771 μm	1084 μm	1000 μm	778 μm	1309 μm
PDT 015	534 μm	1021 μm	534 μm		1289 μm
PDT 016	565 μm	946 μm	565 μm		1309 μm
PDT 020	496 μm	669 μm	610 μm	465 μm	808 μm
PDT 021	463 μm	634 μm	634 μm	461 μm	788 μm
PDT 022	443 μm	619 μm	628 μm	454 μm	770 μm
PDT 023	551 μm	728 μm	647 μm	481 μm	868 μm
PDT 025	844 μm	1541 μm	844 μm		2007 μm
PDT 026	375 μm	693 μm	375 μm		896 μm
PDT 030	734 μm	1000 μm	964 μm	723 μm	1232 μm
PDT 031	695 μm	968 μm	950 μm	707 μm	1195 μm
PDT 032	598 μm	803 μm	787 μm	552 μm	985 μm
PDT 033	742 μm	996 μm	987 μm	692 μm	1228 μm
PDT 035	632 μm	1036 μm	632 μm		1455 μm
PDT 036	514 μm	968 μm	514 μm		1235 μm

Table 6.6: Residuals for the A-layer PDTs. The typical uncertainty for the derived hit resolution, σ(hit), is 10 μm (see Eq. 6.4).

Chambers	σ(plane 1)	σ(plane 2)	σ(plane 3)	σ(plane 4)	σ(average)
PDT 100	572 μm	985 μm	572 μm		1336 μm
PDT 110	459 μm	837 μm	459 μm		1091 μm
PDT 120	267 μm	529 μm	267 μm		652 μm
PDT 130	446 μm	815 μm	446 μm		1061 μm
PDT 140	604 μm	1044 μm	604 μm		1413 μm
PDT 200	627 μm	1097 μm	627 μm		1471 μm
PDT 220	286 μm	564 μm	286 μm		697 μm
PDT 240	634 μm	1040 μm	634 μm		1460 μm

Table 6.7: Residuals for selected B/C layer PDTs

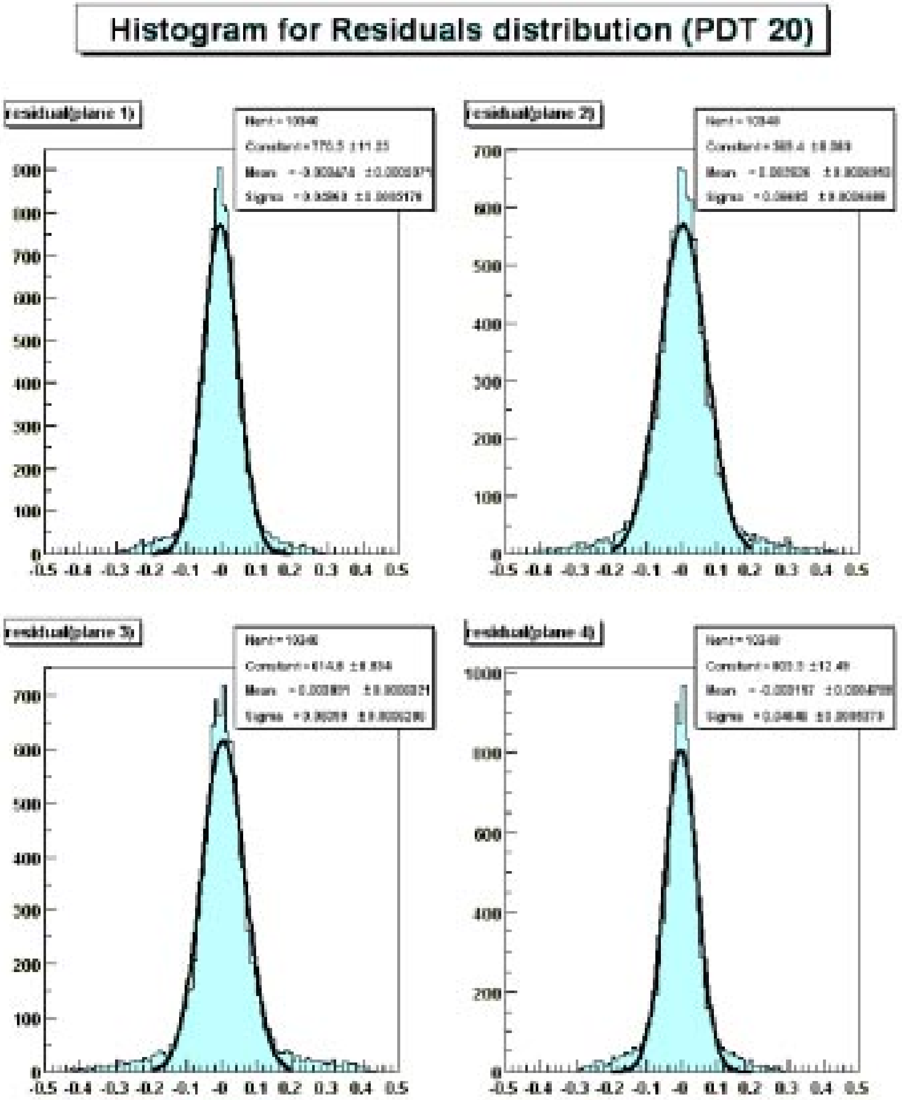

Figure 6.11: Examples of residual plots for individual planes. Results are shown for PDT-020 ("clean" gas circuit). The x-axis is residual (unit: cm), and the y-axis is number of events.

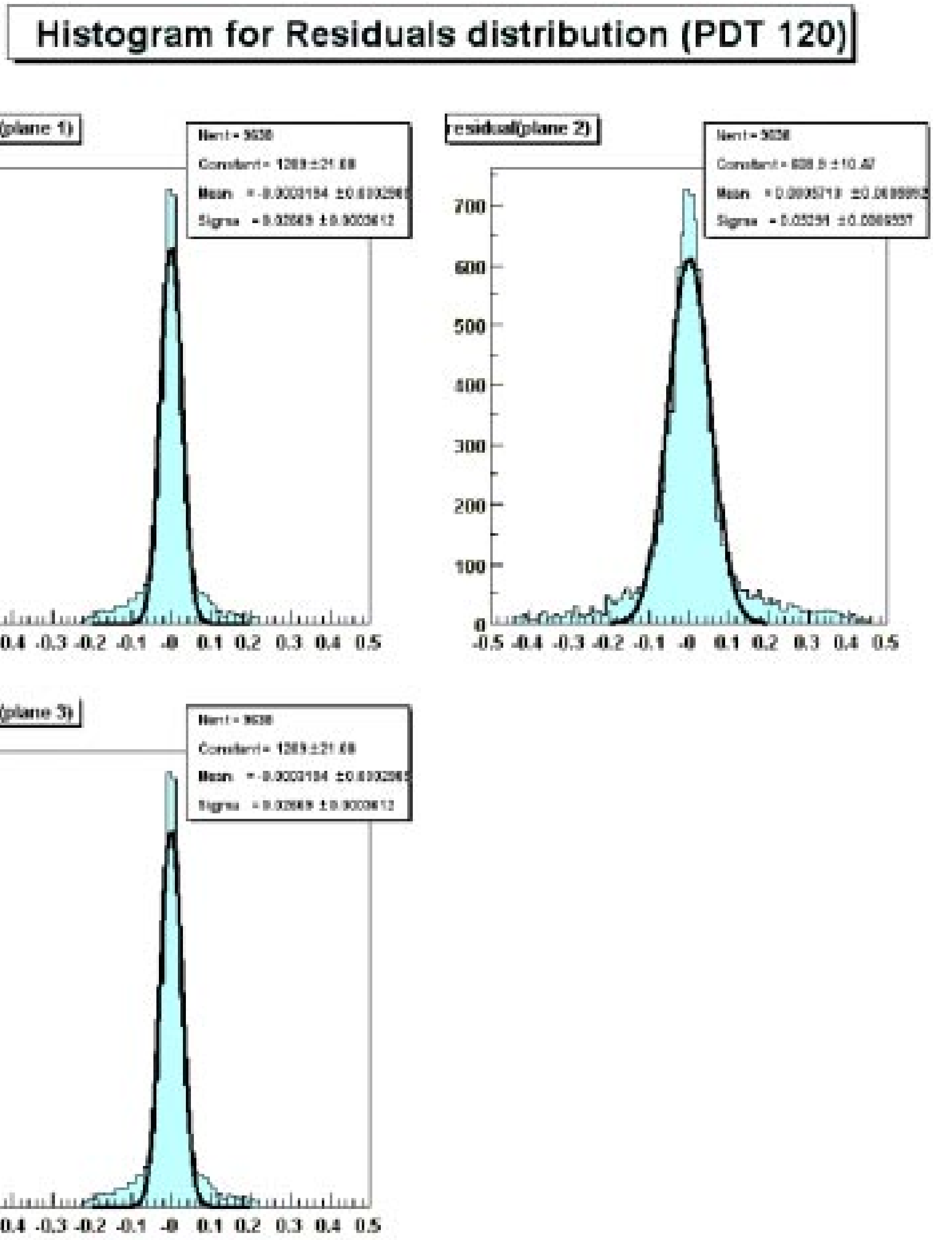

Figure 6.12: Examples of residual plots for individual planes. Results are shown for PDT-120 (“dirty” gas circuit). The x-axis is residual (unit: cm), and the y-axis is number of events.

6.7 Summary

The time-to-distance parametrizations for the “A-layer (clean)” and “B/C-layer (dirty)” gases, obtained in this study, are summarized in Tables 6.8 and 6.9, respectively. This analysis is also documented at the web site [88].

β (θ)	θ^0	θ^1	θ^2	θ^3
β_1	9.13928e-03	4.29118e-05	−2.96607e-06	6.64569e-08
β_2	−2.82045e-08	−1.05518e-07	8.48049e-09	−2.10862e-10
β_3	1.66737e-09	1.75045e-10	−9.74414e-12	1.91771e-13
β_4	−4.73803e-12	−1.79514e-13	3.81363e-15	3.83472e-17

Table 6.8: “t2d” parameterization for the “clean” gas flowing in A-layer and four BC-layer PDTs.

β (θ)	θ^0	θ^1	θ^2	θ^3
β_1	9.85253e-03	1.01407e-04	−7.72285e-06	1.97738e-07
β_2	1.33748e-06	−5.88543e-07	4.89143e-08	−1.15444e-09
β_3	−2.47611e-09	1.21509e-09	−9.32089e-11	1.94994e-12
β_4	−1.54404e-13	−7.37766e-13	4.62811e-14	−6.91967e-16

Table 6.9: “t2d” parameterization (1.06 factor included) for the “dirty” gas flowing in the majority of the BC-layer PDTs.

Chapter 7

J/ψ Production Cross Section Measurement

7.1 Introduction

This analysis was motivated as much by the physics interest as by a need for a comprehensive study of the muon detector performance. The detector (the scintillating fiber tracker, in particular) was not fully commissioned at the time of this study and an extra effort had to be made to estimate various efficiencies. The results presented here remain preliminary, but were shown at many international conferences between Summer of 2002 and Spring of 2003 [89, 90, 92, 93]. The analysis of the data collected after May 2002 is in progress, but without the author's participation. The physics interest in the inclusive J/ψ production cross section is summarized in chapter 2.

In this study, we determine the J/ψ production cross section for two transverse momentum ranges: $p_T^{J/\psi} > 5$ GeV/c and $p_T^{J/\psi} > 8$ GeV/c, each in five different rapidity regions, within the $|y^{J/\psi}| < 1.8$ range. The $0.6 < |y^{J/\psi}| < 1.8$ range has not been covered in the previous analysis [94]. We have not attempted to separate contributions from prompt J/ψ production and production via $B-$hadron decays.

The analysis required two tracks in the muon detector reconstructed as "medium" quality muons, each matched to a central track using Hasketh's macro for `D0Reco` version 10.15, described in section 7.6 [98].

The cross sections for a given kinematic range is given by:

$$\sigma(J/\psi) = \frac{N(J/\psi)}{\mathcal{L} \cdot \varepsilon_{pre-geant} \cdot \varepsilon_{acceptance} \cdot \varepsilon_{trigger} \cdot \varepsilon_{dimureco} \cdot \varepsilon_{trkmatch}}. \tag{7.1}$$

where $\mathcal{L}$ is the integrated luminosity for the data sample used, $N(J/\psi)$ is the number of observed (fitted) J/ψ events, and ε_i represent various efficiency and acceptance factors. The muon acceptance and reconstruction efficiency is based on the Monte Carlo analysis and has been factorized into two parts: losses due to kinematic cuts on muon momenta before the Monte Carlo events were processed through the simulation/reconstruction packages ($\varepsilon_{pre-geant}$), and an acceptance/reconstruction efficiency for muons that had a chance to be reconstructed ($\varepsilon_{acceptance}$). In addition, we have introduced a factor ($\varepsilon_{dimureco}$) to account for the differences in the muon reconstruction efficiency between the Monte Carlo and the data. The latter was provided by the muon ID group and obtained by scanning a large number of events by experienced physicists in the collaboration. The dimuon trigger efficiency ($\varepsilon_{trigger}$) for reconstructed dimuons was estimated by running a trigger simulator, and, independently, directly from the data using single muon triggers with known prescale factors. The central track matching efficiency ($\varepsilon_{trkmatch}$) was derived from the data.

A detailed discussion of each contribution to the cross section calculations is covered in the rest of this chapter.

7.2 Data Used

Data used span runs 145150 – 153888 (February 1 – May 13, 2002). Dimuon events were selected by Castilla and his colleagues, requesting two "medium" quality muon objects. There are two data samples processed with `D0Reco` version p10.15.01:

(a) the "56000" sample, subject to an unfortunate 10 GeV dimuon mass cut (irrelevant except for normalization for this analysis), and

(b) the "63000" sample without the mass cut. This sample included events beyond run 153888 that suffered from a loss of WAMUS muons due to a software bug. Starting mid May 2002, the data processing farm used `D0Reco` version p10.15.02 with a new Linux compiler 7.1 operating with the "maxopt" option. It turned out that the muon index did not work correctly with the new compiler when the maxopt option was imposed. Therefore, data from runs beyond 153888 were removed from the sample (13k events lost).

There are 110,215 events in the two samples, however 19% of them were marked by Diehl as bad [99]. A further cleanup, selecting of dimuon triggers only, removing runs marked as bad for central tracking, reduced the samples to 58,434 events in total. We have verified that the two samples have very similar event properties and they have been merged for the rest of the analysis.

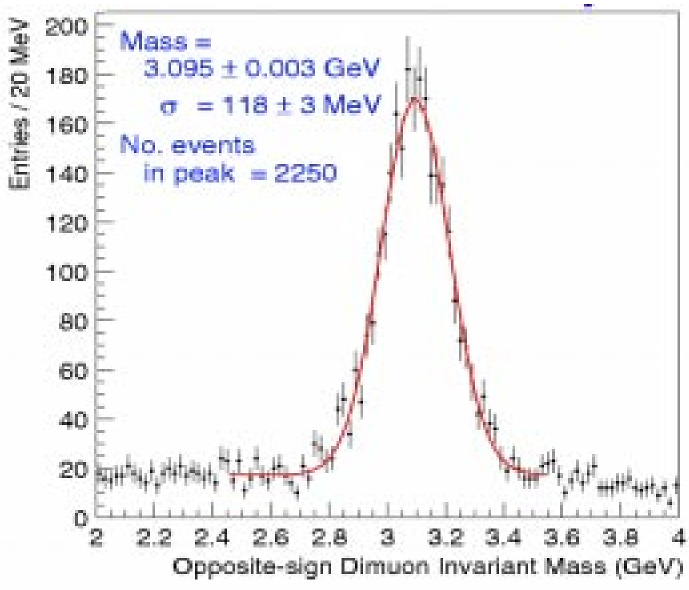

Figure 7.1: Dimuon Mass distribution

The measured luminosity for the “63000” sample (for good runs before run 153888) was 1.92 pb^{-1}. The luminosity information for the “56000” was not kept during the event selection process. From the number of dimuons with mass less than 10 GeV, compared to what was observed in the “63000” sample, we estimated the luminosity for the combined data samples as 4.74 pb^{-1}. Peters determined the luminosity for the same run range (but for the “jet+muon” sample) directly from the luminosity information for each run and obtained 4.8 pb^{-1} [115], a number consistent with result. There is a nominal 10% uncertainty for the luminosity determination that we increased to 15% due to the estimates and assumptions made.

The dimuon mass plot is shown in Fig. 7.1. The muon momenta used are those of the matching charged tracks. There are 2250 J/ψ candidates in the sample and the width of the signal is 118 ± 3 MeV.

Kinematic distributions for dimuons and for muons from the J/ψ decay (defined here to be dimuons in the mass window: 2.8–3.4 GeV) are shown in Figs. 7.2 through 7.5. We show dimuon p_T spectra in five rapidity bins as well as muon p_T^μ, η^μ, ϕ^μ distributions for J/ψ with $p_T > 5$ GeV, again in five different ranges of J/ψ rapidity (absolute value). Similiar plots for the Monte Carlo events are discussed in section 7.4.

Opposite charge dimuon mass distributions for different kinematic regions, shown in Fig. 7.8 and Fig. 7.9 were used to extract the number of J/ψ candidates. Two methods were used: (i) a fit of a Gaussian (signal) plus linear function for the background, and (ii) a background subtraction in the 2.8–3.4 GeV mass window. Numbers of found J/ψ candidates are listed in Table 7.6. The quoted uncertainties reflect both statistical errors and differences in the numbers of candidates obtained with the two methods. Signal to background ratio improves from 3:1 at small rapidities to 5:1 at forward rapidities.

7.3 Pre-GEANT Efficiency

Our acceptance and reconstruction efficiencies are calculated with respect to the following kinematic cuts for muons:

(a) $p_T^\mu > 2.0$ GeV/c; $|y^\mu| < 1.9$;

(b) $p_T^\mu > 3.5$ GeV/c; $|y^\mu| < 0.8$.

The actual preselection of events for passing through `GEANT` was less restrictive to allow

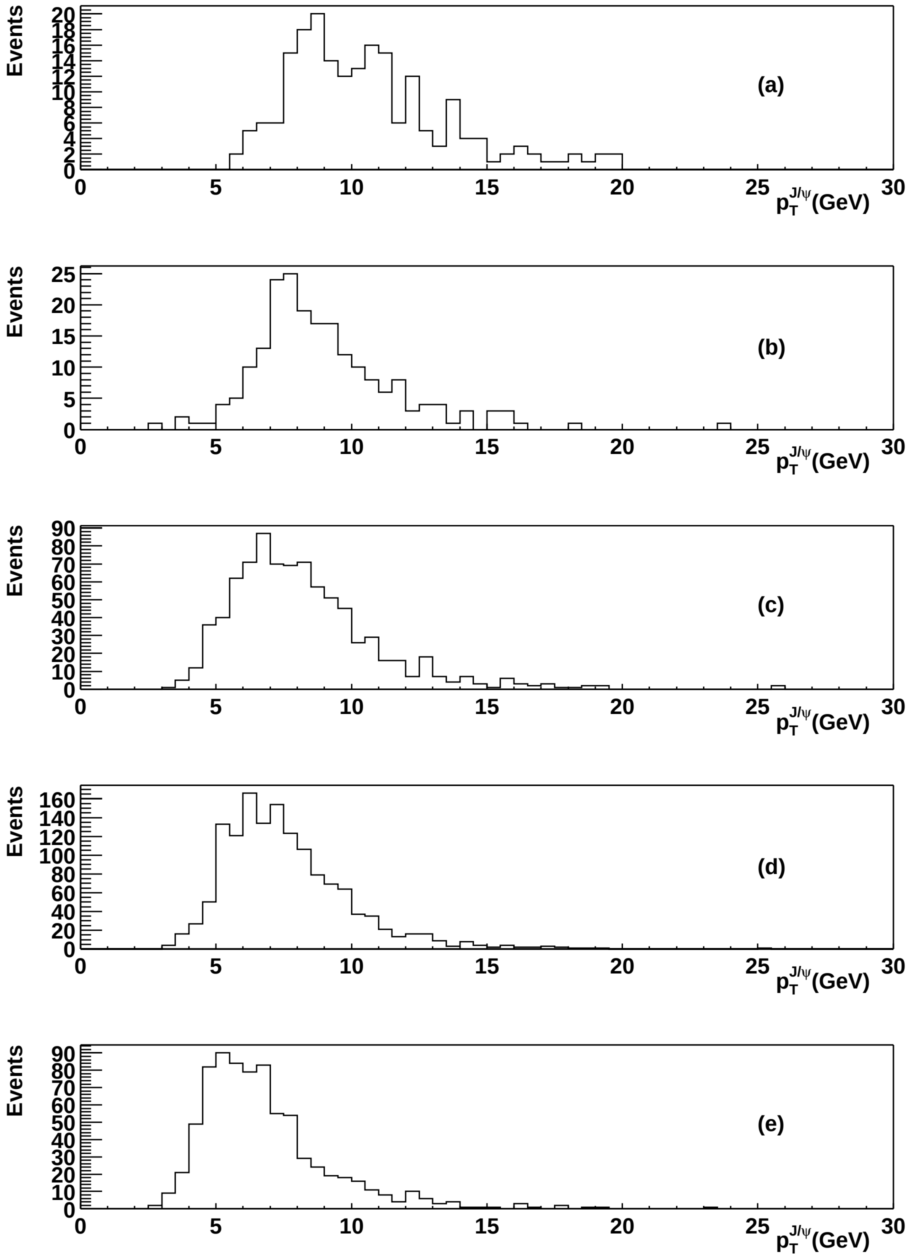

Figure 7.2: J/ψ p_T distribution for five J/ψ rapidity regions (absolute value): (a) 0.0–0.6 (b) 0.6–0.9 (c) 0.9–1.2 (d) 1.2–1.5 (e) 1.5–1.8 .

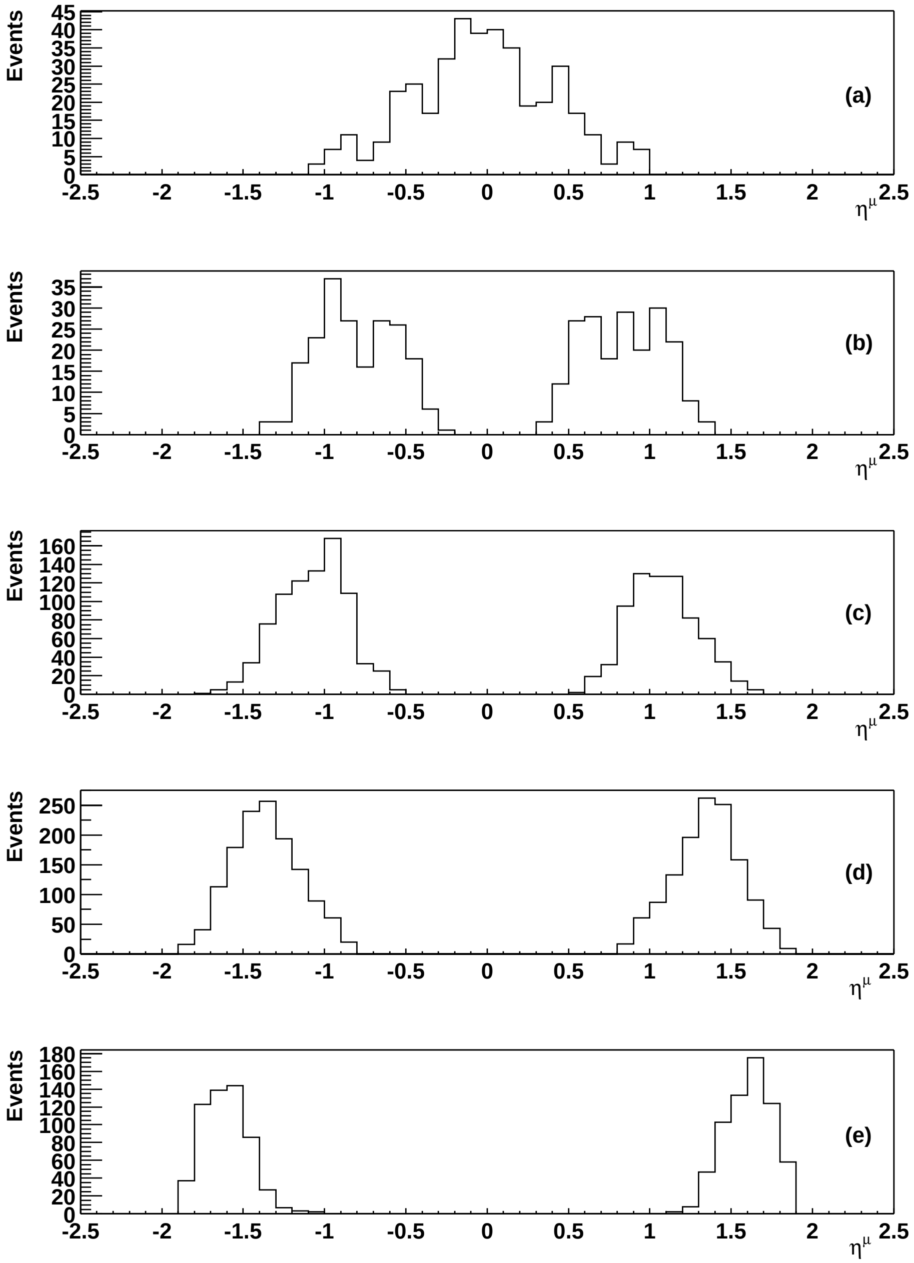

Figure 7.3: Muon pseudorapidity (η) distribution ($p_T^{J/\psi} > 5$ GeV) for five J/ψ rapidity regions (absolute value): (a) 0.0–0.6 (b) 0.6–0.9 (c) 0.9–1.2 (d) 1.2–1.5 (e) 1.5–1.8 .

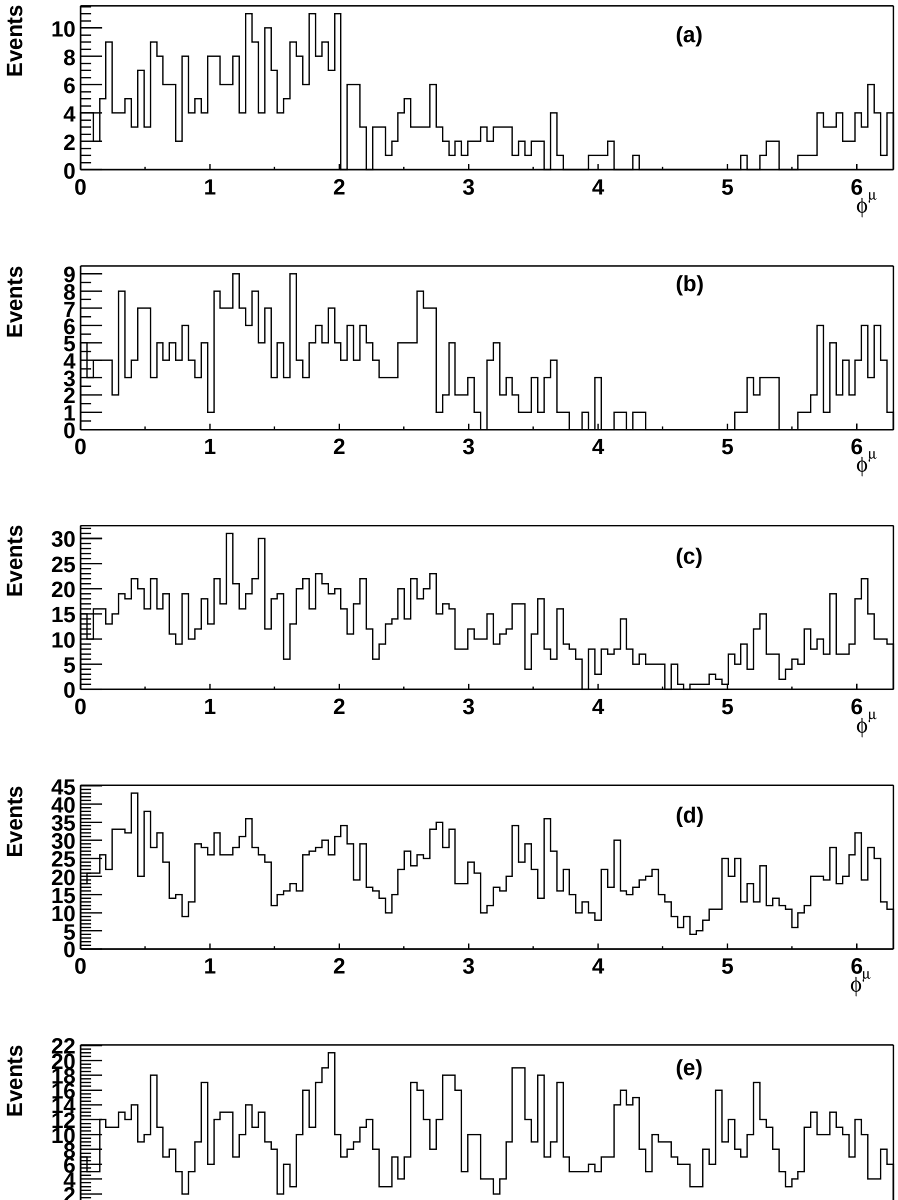

Figure 7.4: Muon azimuthal angle (ϕ) distribution ($p_T^{J/\psi}$ >5 GeV) for five J/ψ rapidity regions (absolute value): (a) 0.0–0.6 (b) 0.6–0.9 (c) 0.9–1.2 (d) 1.2–1.5 (e) 1.5–1.8 .

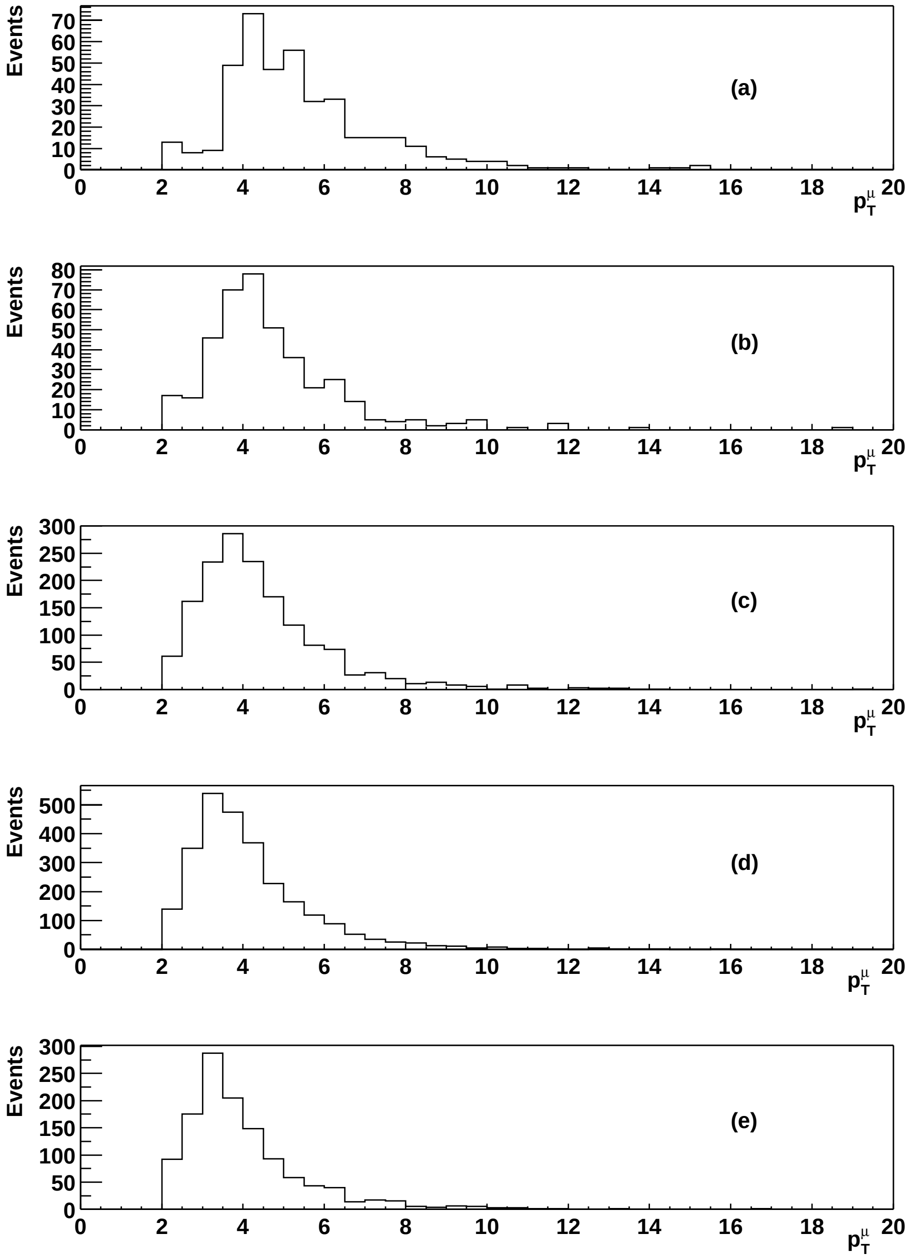

Figure 7.5: Muon p_T distribution ($p_T^{J/\psi} > 5$ GeV) for five J/ψ rapidity regions (absolute value): (a) 0.0–0.6 (b) 0.6–0.9 (c) 0.9–1.2 (d) 1.2–1.5 (e) 1.5–1.8 .

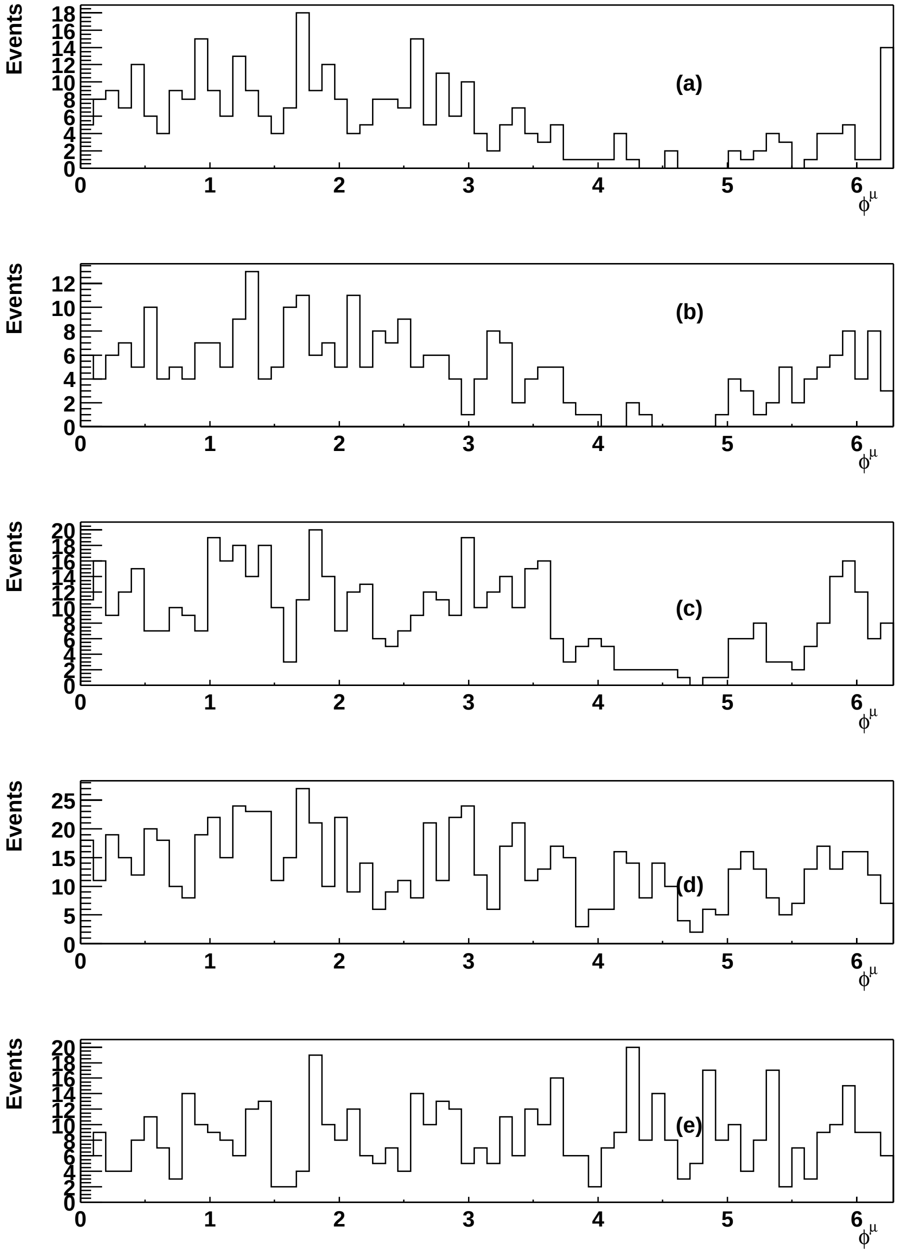

Figure 7.6: Monte Carlo: Muon azimuthal angle (ϕ) distribution ($p_T^{J/\psi}$ >5 GeV) for 5 J/ψ rapidity regions (absolute value): (a) 0.0–0.6 (b) 0.6–0.9 (c) 0.9–1.2 (d) 1.2–1.5 (e) 1.5–1.8
.

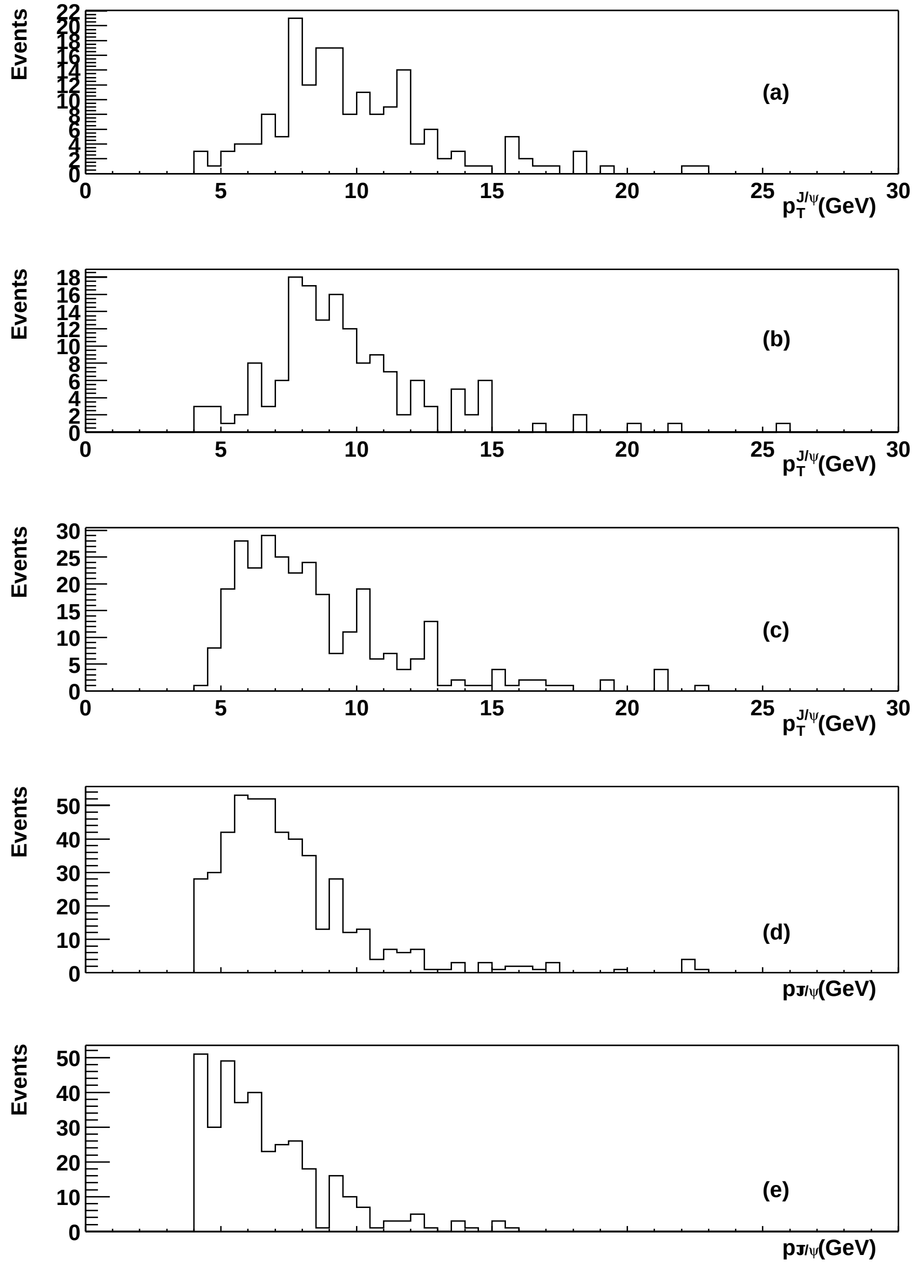

Figure 7.7: Monte Carlo: J/ψ p_T distribution for five J/ψ rapidity regions (absolute value): (a) 0.0–0.6 (b) 0.6–0.9 (c) 0.9–1.2 (d) 1.2–1.5 (e) 1.5–1.8 .

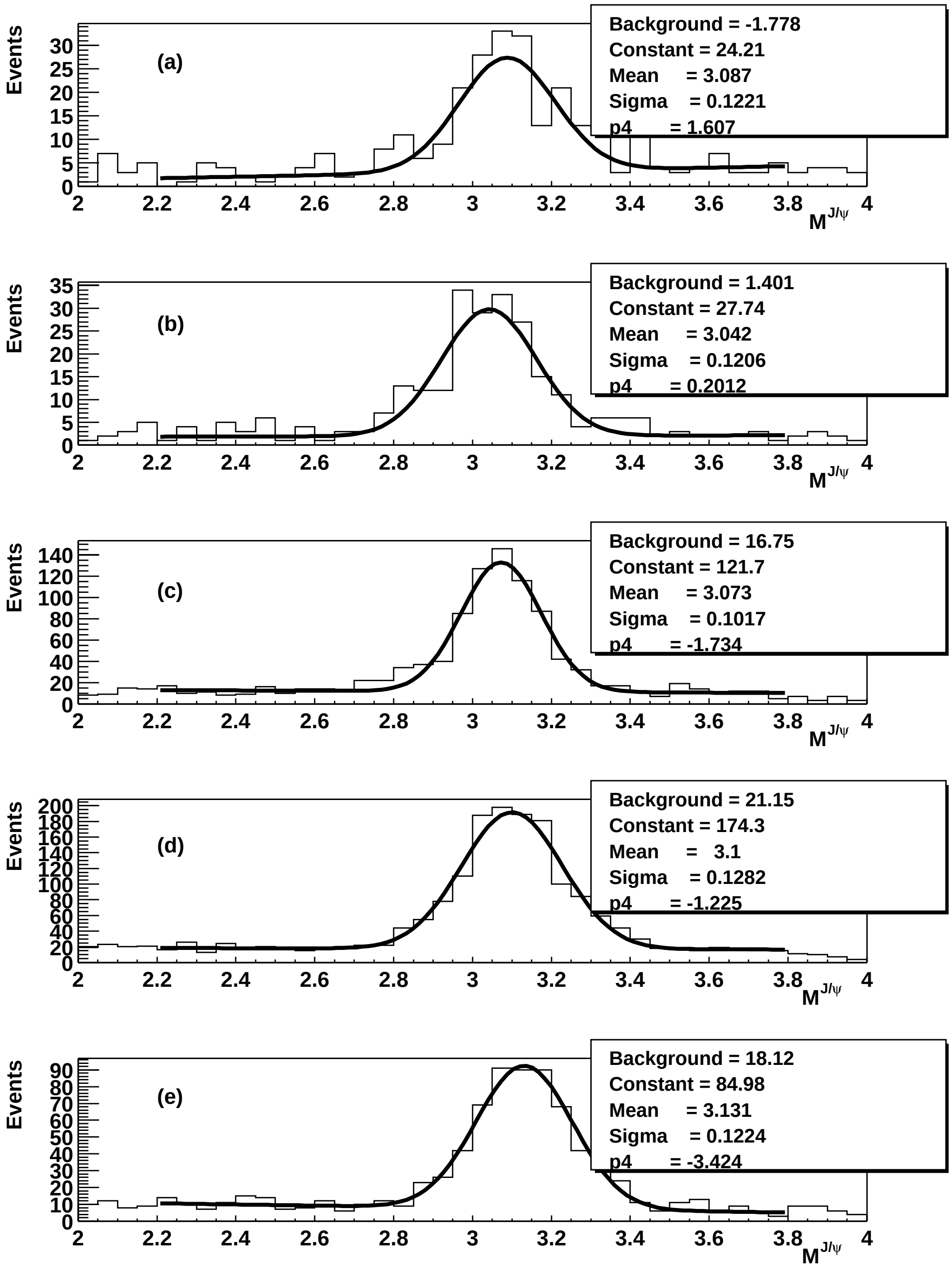

Figure 7.8: J/ψ mass distribution ($p_T^{J/\psi} > 5$ GeV) for 5 J/ψ rapidity (absolute value) regions: (a) 0.0–0.6 (b) 0.6–0.9 (c) 0.9–1.2 (d) 1.2–1.5 (e) 1.5–1.8 .

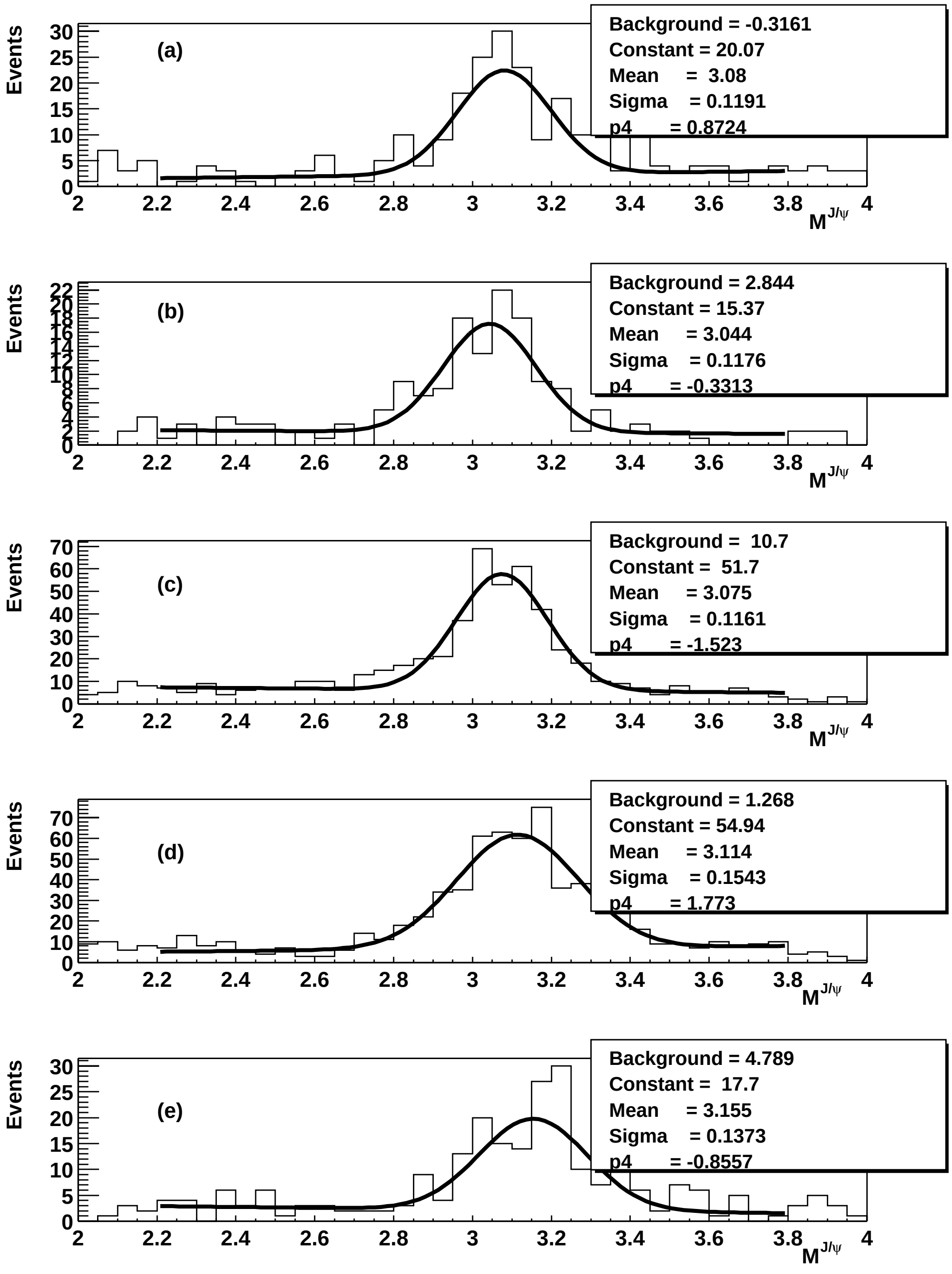

Figure 7.9: J/ψ mass distribution ($p_T^{J/\psi} > 8$ GeV) for five J/ψ rapidity regions (absolute value): (a) 0.0–0.6 (b) 0.6–0.9 (c) 0.9–1.2 (d) 1.2–1.5 (e) 1.5–1.8 .

for a spill over of events after reconstruction.

Efficiencies for this preselection were calculated using several models and are summarized in Table 7.1. We used five approaches:

1. Original calculations, done by A. Zieminski, were based on the `Isajet` Monte Carlo events, with the generated b-quark p_T-spectra weighted to reproduce predictions of the α^3 NLO QCD calculations as coded by the MNR program [97] (COM-1).
2. Same technique applied to the `Isajet` generated J/ψ p_T spectra reweighted to reproduce predictions of the Color Octet Model (COM) for direct J/ψ production [32] (B-decay).
3. Color octet calculations, with the event weighting technique, were repeated PYTHIA events (COM-2).
4. Two additional models describing prompt J/ψ production: `Pythia` 6.155 modelling of the direct J/ψ production (Pythia-direct), and
5. `Pythia` 6.155 approximation of the J/ψ production via the Drell-Yan process (Pythia-DY).

Results from these calculations are summarized in Table 7.1. Additional information is available from the web page in Ref. [100], which also includes the `Pythia` model's predictions for J/ψ kinematic distributions. In addition, Huang has checked that the $B \to J/\psi K^*$ Monte Carlo predictions, discussed in the next section, are consistent with the MNR results presented in Table 7.1.

The pre-GEANT efficiency was calculated as a weighted average between predictions for the direct J/ψ production (80%) and the B–hadron decay predictions (20%) to be consistent with the CDF Run I measurement [95]. Uncertainties reflect the observed maximum-minimum variations between model predictions.

$p_T^{J/\psi} > 5$ GeV/c						
Kinematic Region	B-decay	COM-1	COM-2	Pythia direct	Pythia DY	Average
$\|y\| < 0.6$	0.141	0.101	0.089	0.070	0.114	0.10 ± 0.02
$0.6 < \|y\| < 0.9$	0.192	0.137	0.159	0.152	0.177	0.17 ± 0.02
$0.9 < \|y\| < 1.2$	0.295	0.224	0.236	0.233	0.257	0.25 ± 0.02
$1.2 < \|y\| < 1.5$	0.395	0.344	0.323	0.322	0.338	0.33 ± 0.03
$1.5 < \|y\| < 1.8$	0.268	0.209	0.181	0.178	0.196	0.20 ± 0.03
$p_T^{J/\psi} > 8$ GeV/c						
Kinematic Region	B-decay	COM-1	COM-2	Pythia direct	Pythia DY	Average
$\|y\| < 0.6$	0.401	0.364	0.353	0.310	0.385	0.36 ± 0.03
$0.6 < \|y\| < 0.9$	0.444	0.413	0.378	0.370	0.392	0.39 ± 0.03
$0.9 < \|y\| < 1.2$	0.544	0.514	0.506	0.471	0.548	0.51 ± 0.04
$1.2 < \|y\| < 1.5$	0.538	0.500	0.527	0.499	0.591	0.53 ± 0.04
$1.5 < \|y\| < 1.8$	0.454	0.421	0.359	0.330	0.387	0.38 ± 0.04

Table 7.1: Pre-GEANT efficiencies for J/ψ Monte Carlo production.

7.4 Monte Carlo Production

Three Monte Carlo files were used for this analysis: (a) $B \to J/\psi K_s$ – `D0Reco` version p10.11 – 6,189 events; (b) $B \to J/\psi K^*$ – `D0Reco` version p10.14 – 10,229 events; and (c) `Pythia` Drell-Yan with dimuon mass imposed at 3.1 GeV – `D0Reco` version p10.15

Kinematic Region	Data p_T(GeV)	Monte Carlo p_T (GeV)
$\|y\| < 0.6$	10.6 ± 0.2	10.0 ± 0.3
$0.6 < \|y\| < 0.9$	9.0 ± 0.2	10.0 ± 0.4
$0.9 < \|y\| < 1.2$	8.2 ± 0.1	8.9 ± 0.2
$1.2 < \|y\| < 1.5$	7.6 ± 0.1	7.7 ± 0.2
$1.5 < \|y\| < 1.8$	6.8 ± 0.1	6.7 ± 0.1

Table 7.2: Average transverse momentum for data and Monte Carlo

– 11,500 events. Monte Carlo events of type (a) and (b) are described in the DØ B-physics web page [105]. Events passing through `GEANT` were preselected with $p_T^\mu > 1.2$ GeV/c and $\eta^\mu < 2.2$ (asymmetric cut - a mistake). Only 291 events were reconstructed as "medium-medium" dimuons, with the standard requirement of at least one hit in the A and BC scintillators, and at least two wire hits in both A and (BC) layers. Details of event generation for sample (c) are available from the web page in Ref. [101]. For this sample 722 events were reconstructed as "medium-medium" dimuons.

The analysis of Monte Carlo events was performed by Huang and Zieminski. Various control plots are available from Ref. [102]. In particular, the average transverse momentum (in a given rapidity bin) of the reconstructed Monte Carlo J/ψ events was compared with the data (see Table 7.2). We consider this a measure of the Monte Carlo sample compatibility with the data. The plots of J/ψ p_T distribution for data and Monte Carlo are shown in Figs. 7.2 and 7.7.

In Figs. 7.4 and 7.6, we compare distribution of the muon azimuthal angle ϕ^μ for the data and Monte Carlo events. The geometry acceptance effects (holes in the ϕ^μ distribution) are observed in both cases. The pre-GEANT selection efficiencies are also checked for samples

(a) and (b) to be consistent within (5-10)% with the MNR calculations discussed in the pre-GEANT section of this chapter.

7.5 Monte Carlo Acceptance

Monte Carlo acceptances are normalized to the preselection cuts described in the pre-GEANT selection section. They are based on limited statistics. For a given Monte Carlo input event, it was checked if there were two reconstructed medium quality muons in the detector with an invariant mass (based on local muon momenta) between 1.0 and 10.0 GeV (see relevant plots in the Monte Carlo section). We accepted events even if the two reconstructed muons had the same charge. It was noticed that about 50% of the reconstructed medium-medium type pairs has the same sign. This "charge flip" for medium muons is also observed at a similar level in the data. This charge flip is very much reduced for tight muons.

Monte Carlo acceptance is expected to take into account geometrical holes in the detector (e.g. the WAMUS azimuthal angle hole in the $3.6 < \phi^{\mu} < 5.6$ region, and similar, but smaller holes in the FAMUS), losses due to muons ranging out in the detector, and some track reconstruction losses.

To estimate reconstruction losses for Monte Carlo events, we selected muons from the fully instrumented parts of the detector, with transverse momentum greater than 5 (4) GeV/c (in FAMUS). We find that at least 85% of these muons are reconstructed. There still could be some geometrical edge effects, not visible with our limited Monte Carlo statistics.

$p_T^{J/\psi} > 5$ GeV			
Kinematic Region	Eff. (direct)	Eff. (B-decay)	Eff. (average)
$\|y\| < 0.6$	0.14 ± 0.02	0.11 ± 0.02	0.131 ± 0.012
$0.6 < \|y\| < 0.9$	0.10 ± 0.02	0.12 ± 0.02	0.109 ± 0.012
$0.9 < \|y\| < 1.2$	0.15 ± 0.015	0.22 ± 0.03	0.169 ± 0.013
$1.2 < \|y\| < 1.5$	0.21 ± 0.01	0.22 ± 0.011	0.217 ± 0.005
$1.5 < \|y\| < 1.8$	0.31 ± 0.03	0.39 ± 0.05	0.327 ± 0.024
$p_T^{J/\psi} > 8$ GeV			
Kinematic Region	Eff. (direct)	Eff. (B-decay)	Eff. (average)
$\|y\| < 0.6$	0.17 ± 0.02	0.11 ± 0.03	0.155 ± 0.016
$0.6 < \|y\| < 0.9$	0.16 ± 0.03	0.26 ± 0.05	0.175 ± 0.023
$0.9 < \|y\| < 1.2$	0.24 ± 0.03	0.26 ± 0.05	0.243 ± 0.027
$1.2 < \|y\| < 1.5$	0.25 ± 0.02	0.25 ± 0.02	0.247 ± 0.019
$1.5 < \|y\| < 1.8$	0.22 ± 0.04	0.37 ± 0.09	0.250 ± 0.033

Table 7.3: Monte Carlo acceptance

Therefore, we claim that the reconstruction efficiency for the WAMUS Monte Carlo medium type muons is $92 \pm 8\%$. This value with its uncertainty covers the discussed range of Monte Carlo efficiencies between 85 % and 100 %. It is much higher than the reported $63 \pm 3\%$ (statistics error) reconstruction efficiency for the WAMUS muons, found from scanning [104]. Therefore, we corrected Monte Carlo reconstruction efficiency by including an additional factor of $68 \pm 6\% (0.92 * 0.68 = 0.63)$. The corresponding, additional efficiency factor for the FAMUS muons is assumed to be $96 \pm 4\%$ (the reported reconstruction efficiency from scanning is $92 \pm 3\%$). These extra efficiencies are not included in the Table 7.3, but are used to calculate dimuon reconstruction efficiency $\varepsilon_{dimureco}$ listed in the summary Table 7.6. This extra dimuon reconstruction efficiency $\varepsilon_{dimureco}$ is a product of efficiencies for individual muons.

7.6 Central Track Matching

J/ψ candidates were identified by matching medium muon tracks with central tracks of different kind, using Hesketh's macro [98]. In addition to fully reconstructed central tracks, the macro included matching to "silicon only" and "CFT axial" tracks. Only central tracks with transverse momentum $p_T > 2$ GeV/c were used for matching, but the matching itself was based solely on the spatial matching between the extrapolated central track and local muon track at the A-layer muon chamber position. Matching efficiency could not be determined from Monte Carlo, which does not include partially reconstructed tracks (e.g., CFT-only, etc). There were also some hardware improvements between February and May 2002.

We tried several methods to estimate track matching efficiency for dimuons. None of the methods is fully satisfactory, but we considered method (ii), described below, more reliable and easier to test. Therefore this method was adopted for the analysis.

Method (i): "tight" muons were grouped in two p_T ranges and in many rapidity bins to establish this efficiency for individual muons. Relevant plots for the "56000" and "63000" samples are available from Ref. [102]. The results for the two samples were consistent, with the latter sample showing slightly increased efficiency at medium rapidities and some reduction in efficiency for WAMUS. The dimuon matching efficiency was then calculated as a product of efficiencies for individual tracks. This method underestimates the matching efficiencies. The normalization is with respect to the number of muon tracks which includes some fake muons. However, attempts to increase constraints on tight muons have not given substantially different results. The method also does not take into account correlations in muon reconstruction.

Method (ii): we used dimuon mass spectra in the 1–6 GeV mass region, with mass calculated from the "local" muon momenta (tight muons only, dimuon mass resolution for medium-medium pairs is too poor), plotted: (i) without and (ii) with a condition that there be two matching charged tracks found. The ratio of the number of events in the two plots was taken as the dimuon matching efficiency. Figs. 7.10 and 7.11 show the dimuon mass distributions before and after track match for $p_T^{J/\psi} > 5$ GeV and J/ψ different rapidity regions. The plots are available from the web site [102].

This method would be perfect, if we could reliably estimate the number of the J/ψ candidates, with and without central matches. Unfortunately, the local momentum resolution for p10.15 was too poor to enable a reliable estimate of the number of J/ψ events using local tracks only. Comparison of dimuon mass plots is based on: (i) the central track information and (ii) local track momenta, indicated that events in the 1-6 GeV mass range, with both tracks matched, are a 50/50 mixture of J/ψ candidates and a flat background. We assumed that the background has the same matching/reco probability as J/ψ candidates. This assumption was supported by matching/reco efficiencies for the like-sign dimuons, also tabulated in Table 7.4. The track match/reco efficiencies for the "56000" and "63000" samples were comparable within statistical errors. Uncertainties listed in Table 7.4 are statistical only. In addition, based on the difference between ε_{dimu} efficiencies for unlike-sign and like-sign pairs, we assume a 15% overall systematic uncertainty for this efficiency.

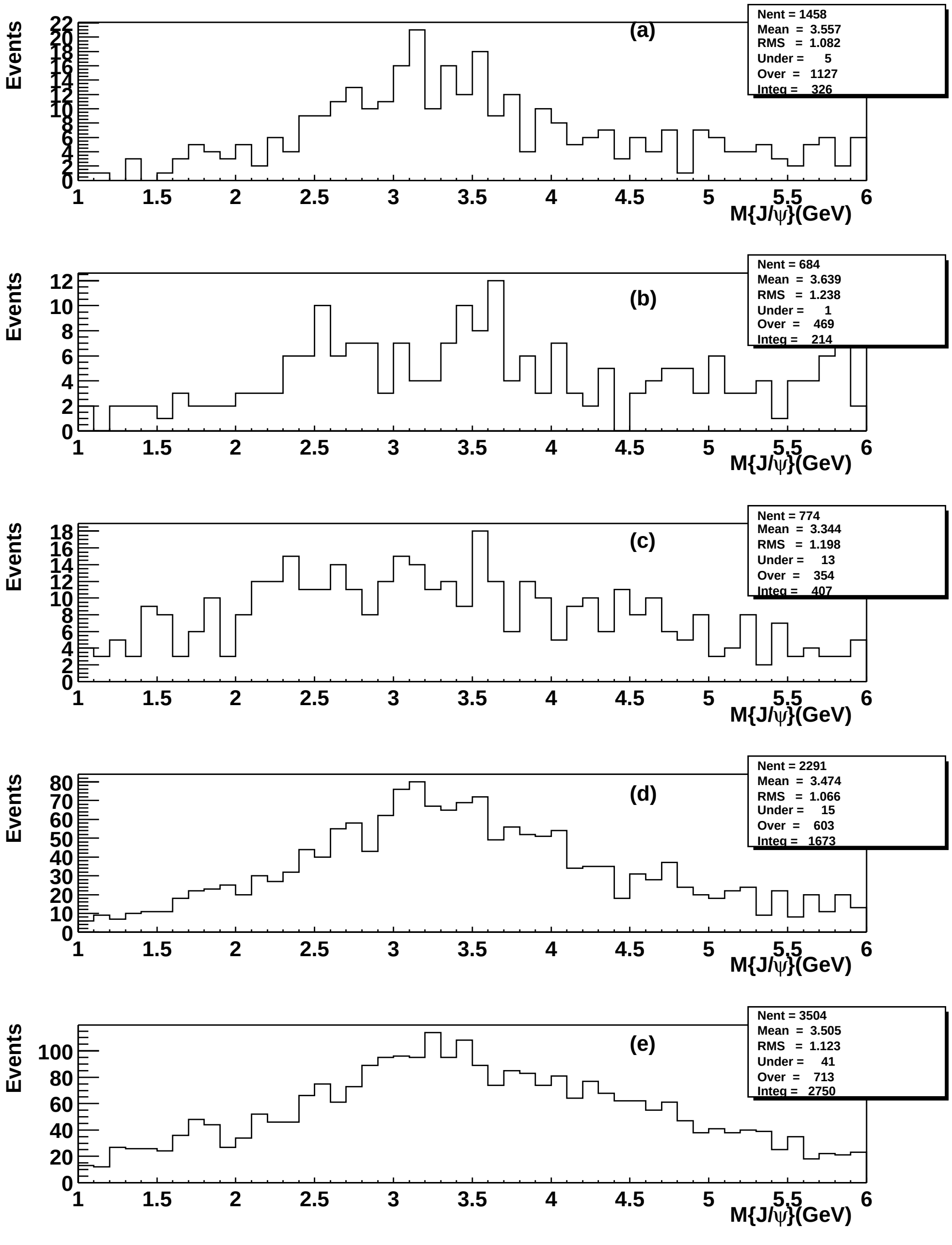

Figure 7.10: Unlike dimuon local mass distribution before track match ($p_T^{J/\psi} > 5$ GeV) for 5 J/ψ rapidity (absolute value) regions: (a) 0.0–0.6 (b) 0.6–0.9 (c) 0.9–1.2 (d) 1.2–1.5 (e) 1.5–1.8 .

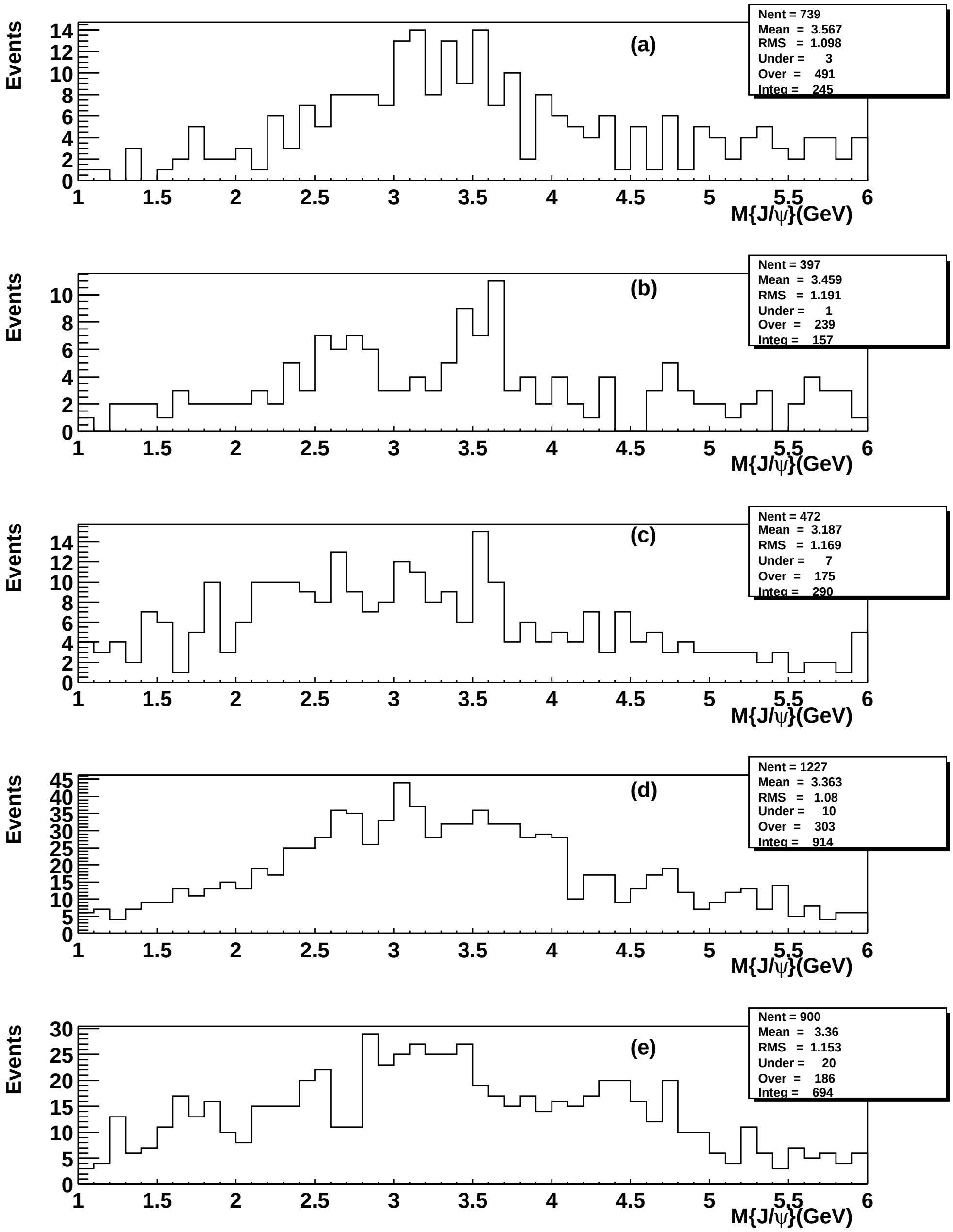

Figure 7.11: Unlike dimuon local mass distribution after track match ($p_T^{J/\psi} > 5$ GeV) for 5 J/ψ rapidity (absolute value) regions: (a) 0.0–0.6 (b) 0.6–0.9 (c) 0.9–1.2 (d) 1.2–1.5 (e) 1.5–1.8 .

Kinematic Region	ε_{track}	ε_{dimu} unlike-sign	ε_{dimu} like-sign
$p_T^{J/\psi} > 5$ GeV			
$\|y\| < 0.6$	0.52	0.75 ± 0.03	0.70 ± 0.03
$0.6 < \|y\| < 0.9$	0.60	0.73 ± 0.03	0.64 ± 0.05
$0.9 < \|y\| < 1.2$	0.53	0.71 ± 0.03	0.64 ± 0.03
$1.2 < \|y\| < 1.5$	0.31	0.55 ± 0.02	0.50 ± 0.02
$1.5 < \|y\| < 1.8$	0.135	0.25 ± 0.01	0.26 ± 0.01
$p_T^{J/\psi} > 8$ GeV			
$\|y\| < 0.6$	0.51	0.77 ± 0.03	
$0.6 < \|y\| < 0.9$	0.60	0.75 ± 0.03	
$0.9 < \|y\| < 1.2$	0.555	0.75 ± 0.03	
$1.2 < \|y\| < 1.5$	0.36	0.56 ± 0.02	
$1.5 < \|y\| < 1.8$	0.155	0.26 ± 0.01	

Table 7.4: Central track matching efficiencies. The errors for ε_{track} are smaller than 0.01.

7.7 Dimuon Trigger Efficiency

Two methods were used to estimate dimuon trigger efficiency. The first was based on the number of J/ψ events due to single muon triggers and relevant prescale factors. The second method was based on the dimuon trigger simulator results for our J/ψ Monte Carlo sample. Both methods gave consistent results (see Table 7.5). The simulator method was adopted.

(1) Prescale method.

We found that 95.7% of our events were due to a dimuon trigger, a fraction that was stable over the entire data taking period. The remaining 4.3% were due to a prescaled single muon trigger. The single muon trigger was known to be better than 70% and 75% efficient for WAMUS and FAMUS muons, respectively [106]. Therefore, we assumed that the WAMUS single muon trigger was 90% efficient for triggering on an event with two muons (95% for the FAMUS trigger). A 10% uncertainty on this number, denoted ε_{s2mu}, has only 2-3% effect on the estimation of the dimuon trigger efficiency. The dimuon trigger efficiency was determined from the formula:

$$\varepsilon_{trigger} = \frac{Nevt_{dimuon-trigger}}{Nevt_{dimuon-trigger} + PRESCALE \times \frac{Nevt_{single-mu-only}}{\varepsilon_{s2mu}}}. \tag{7.2}$$

Input numbers for the $\varepsilon_{trigger}$ calculations are available from Ref. [102].

(2) Trigger imulator results for the "mu2ptxatxx" term, which requires two muons with $p_T > 2$ GeV and full geometry coverage).

The efficiency is normalized to numbers of dimuons with both muons satisfying medium type criteria, described in Chapter 5. Muons were also subject to pre-GEANT kinematic cuts.

7.8 Cross Section Calculations

Information needed for cross section calculations is collected in Table 7.6. Quoted cross sections are normalized per unit of rapidity, therefore a factor of 1/1.2 was used for the first rapidity bin and a factor 2/1.2 for the remaining rapidity bins (e.g. for $0.6 < |y| < 0.9$ and higher). Our results are summarized in Figure 7.12. The overall systematic uncertainty, discussed in the next section, is approx 30%, and is not shown in the plot. As seen from Figure 7.12, our results are consistent with the Run I CDF measurement in the limited

Kinematic Region	Nevts with MM dimu	Nevts with trigger	Eff trigsim	Eff prescale
$p_T^{J/\psi} > 5$ GeV				
$\|y\| < 0.6$	94	46	0.49 ± 0.07	0.48 ± 0.11
$0.6 < \|y\| < 0.9$	61	35	0.57 ± 0.06	0.60 ± 0.10
$0.9 < \|y\| < 1.2$	126	90	0.71 ± 0.04	0.66 ± 0.08
$1.2 < \|y\| < 1.5$	262	199	0.76 ± 0.03	0.74 ± 0.05
$1.5 < \|y\| < 1.8$	175	147	0.84 ± 0.03	0.76 ± 0.05
$p_T^{J/\psi} > 8$ GeV				
$\|y\| < 0.6$	75	40	0.53 ± 0.06	0.48 ± 0.11
$0.6 < \|y\| < 0.9$	44	26	0.59 ± 0.07	0.58 ± 0.10
$0.9 < \|y\| < 1.2$	70	64	0.77 ± 0.05	0.67 ± 0.08
$1.2 < \|y\| < 1.5$	94	80	0.85 ± 0.04	0.75 ± 0.05
$1.5 < \|y\| < 1.8$	46	42	0.91 ± 0.04	0.76 ± 0.05

Table 7.5: Dimuon trigger efficiencies

rapidity range of $|y^{J/\psi}| < 0.6$ [103]. The measured cross sections do not exhibit significant rapidity dependence, in agreement with theoretical predictions, e.g., presented in Ref. [94].

7.9 Systematics

Several common systematic uncertainties have been identified that are not included in the cross section error bars shown for a given rapidity bin.

(i) The pre-GEANT efficiencies could be separated as theoretical uncertainties. However, these uncertainties were already included in the uncertainties for individual data points.

(ii) 15% was assigned for an overall Monte Carlo acceptance uncertainty due to the approximate muon detector geometry used (in particular relative positions of wire chambers

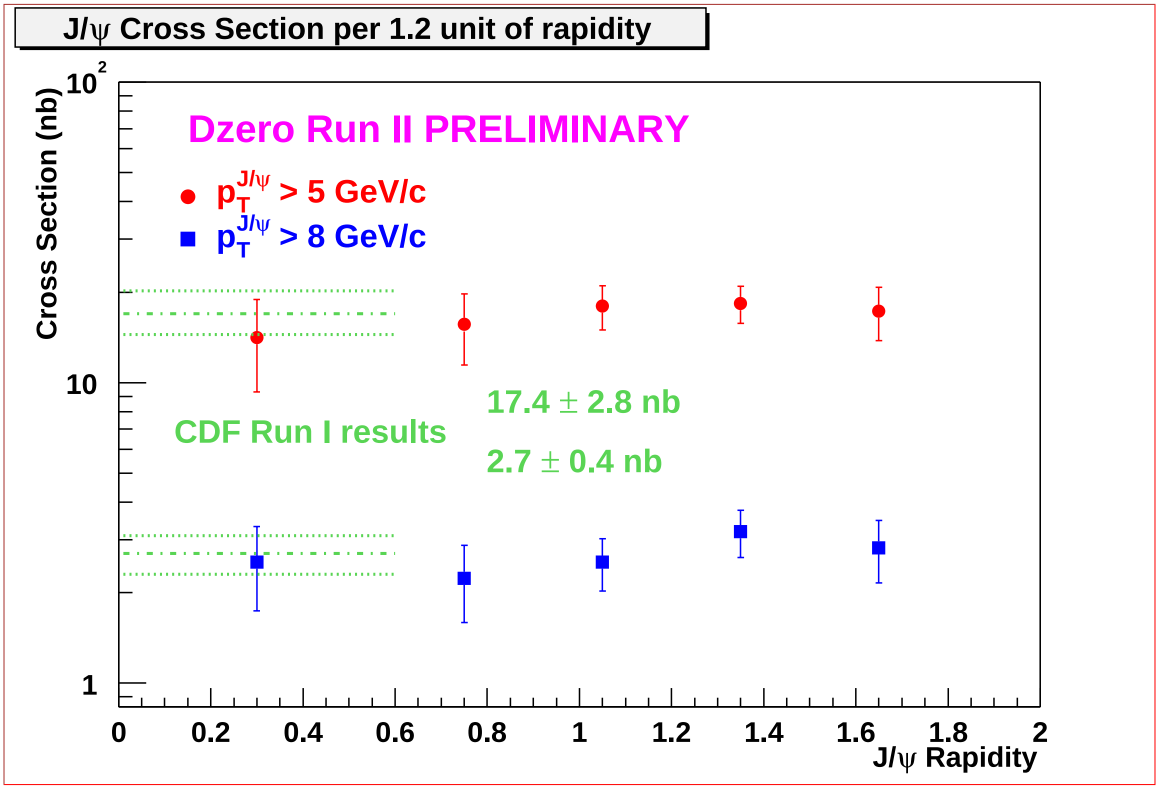

Figure 7.12: J/ψ production cross section per 1.2 unit of rapidity.

Kinem. Region	Nevents	$\varepsilon_{pre-geant}$	$\varepsilon_{acceptance}$	$\varepsilon_{trkmatch}$	$\varepsilon_{dimureco}$	$\varepsilon_{trigger}$	σ(nb)
$p_T^{J/\psi} > 5$ GeV							
$\|y\| < 0.6$	163 ± 21	0.10 ± 0.02	0.13 ± 0.01	0.75 ± 0.03	0.51 ± 0.10	0.49 ± 0.07	11.7 ± 4.0
$0.6 < \|y\| < 0.9$	177 ± 21	0.17 ± 0.02	0.11 ± 0.01	0.73 ± 0.03	0.62 ± 0.08	0.57 ± 0.06	13.0 ± 3.5
$0.9 < \|y\| < 1.2$	643 ± 40	0.25 ± 0.02	0.17 ± 0.01	0.71 ± 0.03	0.70 ± 0.06	0.71 ± 0.04	15.0 ± 2.1
$1.2 < \|y\| < 1.5$	1121 ± 48	0.33 ± 0.03	0.22 ± 0.01	0.55 ± 0.02	0.86 ± 0.07	0.76 ± 0.03	15.3 ± 2.1
$1.5 < \|y\| < 1.8$	518 ± 31	0.20 ± 0.03	0.33 ± 0.02	0.25 ± 0.01	0.92 ± 0.07	0.84 ± 0.03	14.4 ± 2.9
$p_T^{J/\psi} > 8$ GeV							
$\|y\| < 0.6$	139 ± 23	0.36 ± 0.03	0.16 ± 0.02	0.77 ± 0.03	0.51 ± 0.10	0.53 ± 0.06	2.11 ± 0.66
$0.6 < \|y\| < 0.9$	99 ± 16	0.39 ± 0.03	0.18 ± 0.02	0.75 ± 0.03	0.62 ± 0.08	0.59 ± 0.07	1.86 ± 0.54
$0.9 < \|y\| < 1.2$	309 ± 28	0.51 ± 0.04	0.24 ± 0.03	0.75 ± 0.03	0.72 ± 0.06	0.77 ± 0.05	2.11 ± 0.42
$1.2 < \|y\| < 1.5$	417 ± 28	0.53 ± 0.06	0.25 ± 0.03	0.56 ± 0.02	0.88 ± 0.07	0.85 ± 0.04	2.66 ± 0.48
$1.5 < \|y\| < 1.8$	138 ± 17	0.38 ± 0.04	0.25 ± 0.04	0.26 ± 0.01	0.92 ± 0.07	0.91 ± 0.04	2.35 ± 0.55

Table 7.6: Summary of J/ψ cross-section calculations

and scintillators in FAMUS, approximate z distances, drift velocity etc).

(iii) Track matching efficiency was a problem specific to `D0Reco` version p10.15 and has been much easier to handle after global muon tracks were used (p11.07 etc). Also, an improved local muon geometry has allowed separation of the J/ψ signal using local muons only. For our study, a 15% uncertainty was assumed for this efficiency, as discussed in section 7.6.

(iv) Uncertainty for luminosity was 15%. This reflected the nominal luminosity uncertainty of 10%, and a 10% uncertainty related to the method used to estimate the luminosity for the "56000" sample.

(v) An additional 15% uncertainty was included for the dimuon trigger efficiency, since only one production model Monte Carlo was used in its evaluation. It also reflects the differences between results of two methods used to estimate the dimuon trigger efficiencies.

The overall systematic uncertainty was estimated to be 30%.

7.10 J/ψ Polarization Studies

In this section, we briefly discuss possible future directions of the J/ψ production studies with the DØ Run II data with more statistics. Cross sections will be soon re-evaluated using much better quality data, as illustrated in Fig. 7.13. By December 2002, DØ accumulated approximately 130,000 J/ψ candidates with an integrated luminosity of 50 pb^{-1}. With such statistics, it will be possible to tackle the very interesting and challenging topic of J/ψ polarization. The Run I CDF results on this subject have not been conclusive [27].

As discussed in chapter 2, the color-octet mechanism leads to a prediction that ψ charmonia produced directly will be increasingly transversely polarized at high p_T due to the dominance of gluon fragmentation, and the preservation of the gluon's transverse polarization as the $c\bar{c}$ evolves into a bound ψ state. On the other hand, the color evaporation model (CEM) predicts an absence of polarization.

The angular distribution for $J/\psi \to \mu^+\mu^-$ is defined as:

$$\omega(\theta) = \frac{3}{2(\alpha+3)}(1 + \alpha \cos^2\theta),$$

where θ is the angle between the μ^+ from J/ψ decay in the J/ψ rest frame with respect to the direction of J/ψ in the lab frame. The parameter α describes the J/ψ polarization: $\alpha = 1$ corresponds to transverse polarization, and $\alpha = -1$ to longitudinal polarization.

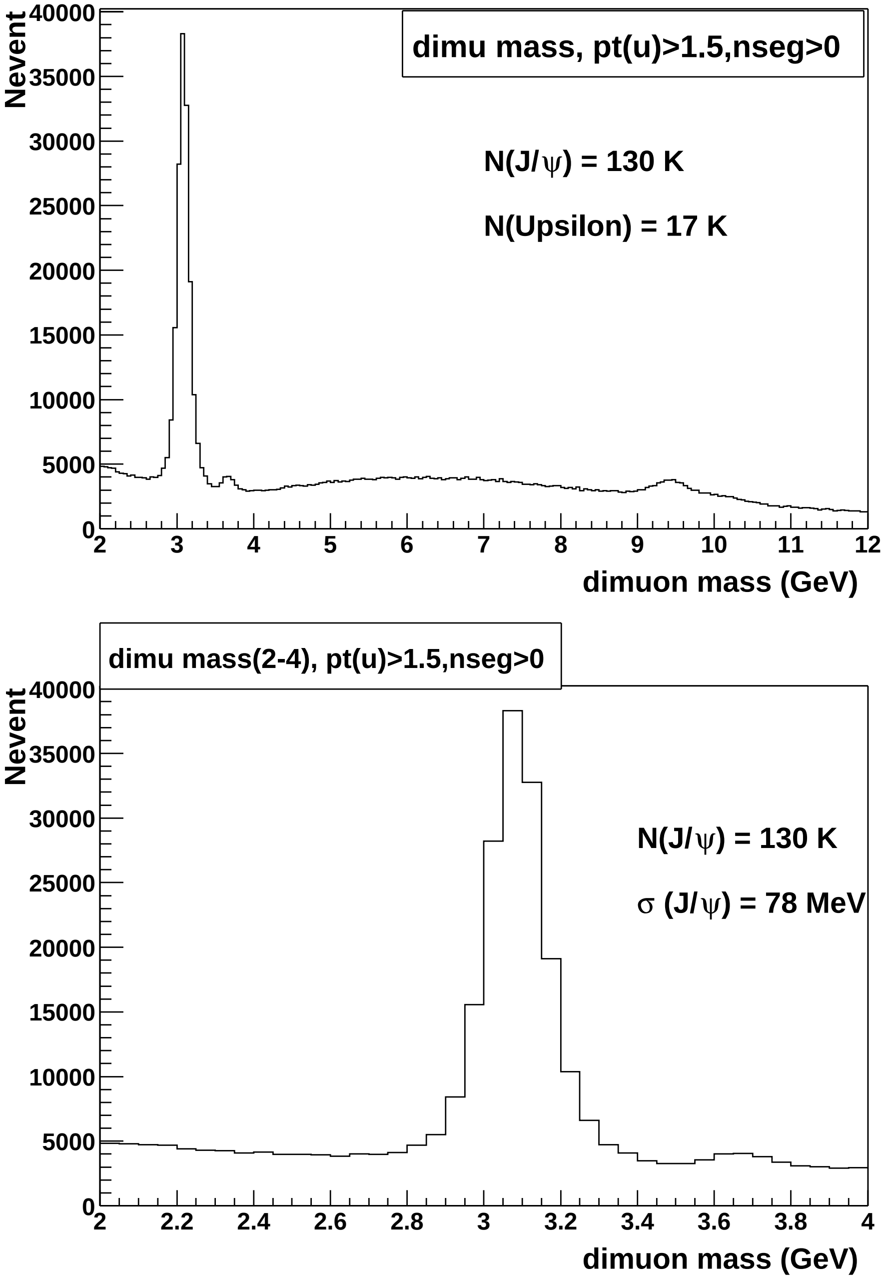

Figure 7.13: Di-muon mass distribution by December 2002. The lower plot is a subset of the upper plot.

Figure 7.14 shows the generated $\cos\theta$ distribution for the two extreme cases ($\alpha = \pm 1$), with $p_T^{J/\psi} > 10$ GeV/c and muon momenta within the DØ acceptance range ($p_T^{\mu} > 1.5$ GeV/c, $|\eta^{\mu}| < 1.9$. This template will be used to derive the J/ψ polarization from the DØ Run II data.

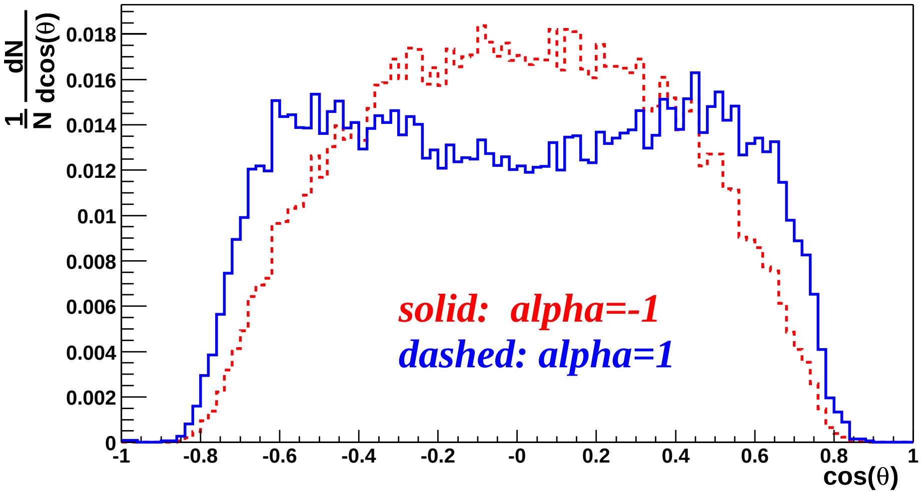

Figure 7.14: $J/\psi \cos\theta$ for two extreme cases (MC) with p_T^{μ} >1.5 GeV.

Chapter 8

Study of $B_s^0 \rightarrow J/\psi\phi$ Decays

In this chapter, a preliminary measurement of the B_s meson lifetime using the decay mode $B_s^0 \rightarrow J/\psi\phi$ is presented. The data sample corresponds to an integrated luminosity of 47 pb^{-1}. 33±7 B_s^0 candidates were found, and the lifetime of the B_s^0 meson was determined to be $\tau(B_s)$=$1.25^{+0.30}_{-0.22}$(stat)±0.14(syst) ps. The result is consistent with previous B_s meson lifetime measurements.

8.1 Introduction

In chapter 2, the physics of B_s has been thoroughly presented and discussed. The decay channel $B_s^0 \rightarrow J/\psi\phi$, proceeding through the quark subprocess $b \rightarrow c\bar{c}s$, is a B_s counterpart of the decay $B_d \rightarrow J/\psi K_s^0$. Because the final state is common to B_s^0 and its charge conjugate $\overline{B}_s^0$, the two meson states are expected to mix in such a way that the two CP eigenstates may have a relatively large lifetime difference of up to 20%. It is possible to separate the two CP components of $B_s^0 \rightarrow J/\psi\phi$ and thus to measure the lifetime difference by studying the time evolution of the polarization states of the vector mesons in the final state.

The author presents here a preliminary study of the dimuon data collected in the DØ running period (September – December 2002). In this statistics-limited analysis, the B_s^0 lifetime (CP-even and CP-odd average) is extracted. The time-integrated ratio of the CP-odd and CP-even rates is also estimated.

An unbinned maximum likelihood fit to the data is performed, including mass and lifetime information. The MINUIT program is utilized within the root framework (the class TMinuit). A reference to the source code and user-friendly instructions for alternative applications is provided.

8.2 Data and Monte Carlo Event Samples

8.2.1 Dimuon Data Sample

This analysis is based on sets 1 – 10 of the the B physics groups's dimuon sample [107]. The preselected events pass a dimuon trigger and include two reconstructed muons with a transverse momentum greater than 1.5 GeV. Each muon is required to be detected as a track segment in at least one layer of the muon system and matched to a central track ("Saclay algorithm"). In this application, the input consists of a central track (GTrack found using CFT and SMT data), and track segments found in the muon system inside and outside the toroid (MuoSegment objects). Events containing an opposite charge pair of muons with the invariant mass in the range 2 – 4 GeV were reprocessed with a modified `D0Reco` program, version p13.05, using the tracking algorithm combination `htfAA` [108]. This algorithm has been recommended to be used as default in the DØ event reconstruction by the TARC (Tracking Algorithm Recommendation Committee) [108].

To reconstruct the decay sequence $B_s^0 \to J/\psi\phi$, $J/\psi \to \mu^+\mu^-$, $\phi \to K^+K^-$, the vertex-finding and fitting package d0root_analysis [108] is used. In this package, Global Vertex Fitting [109] is implemented via a constrained vertex fit of a set tracks. The input is a list of GTracks and the output is an object of the class Vertex constaining the position of the vertex and the re-fitted vertex-constrained tracks. The fit consist of the minimization of a χ^2 of 2 terms:

- the spatial distance between the tracks and the reconstructed vertex.
- the distance between the reconstructed track momentum and the propagated track momentum at the vertex.

The Root algorithm is mathematically equivalent to the "Kalman Filter algorithm" [110] implemented in the framework, but consists of a global fit of position and momenta at the same time, instead of the recursive Kalman Filter (Smoother formalism).

To select the final B_s candidate sample, further kinematic and quality cuts are applied. Transverse momentum thresholds for the B_s and ϕ mesons are necessary to control the signal to background ratio and to minimize the statistical uncertainty of the lifetime measurement. In this analysis, the p_T thresholds are set at 6.0 GeV/c for B_s, 2.0 GeV/c for ϕ, and 1.0 GeV/c for each ϕ decay product.

To ensure well measured momenta and space coordinates of particles coming from the

B_s decay, tracks from the ϕ decay are required to have at least four hits in the central tracking system, including at least one hit in the SMT detector. The decay length is also required to be well measured for both J/ψ and ϕ, namely the decay length error for J/ψ to be less than 0.02 cm and for ϕ to be less than 0.2 cm.

J/ψ candidates are accepted if the two muons are found to be consistent with originating from a common vertex (vertex global fitting of two muons returns χ^2 less than 100) and if the invariant mass resulting from the vertex fit is in the range 2.8 – 3.4 GeV. Tighter cuts are imposed on muons for events where the J/ψ mass is less that 2.9 GeV or greater than 3.3 GeV: both muons must penetrate the toroid and have at least 2 SMT matching hits and at least 8 CFT hits.

ϕ candidates are formed by pairing oppositely charged tracks with a transverse momenta greater than 1 GeV, and assigning them the K^+ mass. They are accepted if they satisfy a fit to a common vertex (vertex global fitting of K^+K^- returns χ^2 less than 100), and the invariant mass is in the range 1.008 – 1.032 GeV.

The dimuon mass distribution and the K^+K^- candidate distribution are shown in Fig. 8.1. The mass resolution of the J/ψ signal is 76 ± 13 MeV, and the ϕ mass resolution is 6.2 ± 1.1 MeV. They are about 20% larger than the values expected from the MC simulation, 61 ± 4 MeV and 4.6 ± 0.3 MeV, respectively, shown in Fig. 8.4 in the next section.

The B_s candidate sample is selected by requiring a $(J/\psi, \phi)$ pair to be consistent with coming from a common vertex, and to have a mass in the range 5.1 – 5.7 GeV. Finally, an event is rejected if the number of tracks other than muons in a cone $\Delta R < 1.0$ (isolation, i.e. $\Delta_R = \sqrt{(\Delta\eta)^2 + (\Delta\phi)^2}$, where η, ϕ are in radians) around J/ψ is less than 2 or greater than 15. The first cut is to insure that at least one of the Kaons is within the cone; the second cut is to reject events with too high combinatorics. This sample of 143 events is used in the B_s lifetime measurement. The resulting invariant mass distribution of the $(J/\psi, \phi)$ system is shown in Fig. 8.2 (top plot). The curve is a projection of the maximum likelihood fit, described later. The fit assigns 33±7 events to the B_s^0 decay. The B_s signal is more pronounced if background due to prompt J/ψ production is suppressed by requiring the B_s candidate's measured decay proper time to be greater than 3 times its uncertainty, see the bottom plot in Fig. 8.2.

8.2.2 Monte Carlo Event Samples

MC Signal $B_s^0 \rightarrow J/\psi\phi$

To simulate the decay chain $B_s^0 \rightarrow J/\psi\phi$, $J/\psi \rightarrow \mu^+\mu^-$, $\phi \rightarrow K^+K^-$ we use the `SVV_HELAMP` model in the `EvtGen` generator [62] interfaced to the `Pythia` program [55]. The decay amplitude is specified by the helicity amplitudes which are given as arguments for the decay. The arguments are H_+, H_0, and H_-, specified as magnitude and phase. Here we use the parameters (1.0 0.0 0.0 0.0 1.0 0.0), which corresponds to an CP-even state. This choice corresponds to $A_{||} = 1$, $A_\perp$=0, and A_0=0 in the linear polarization basis.

The decay $J/\psi \rightarrow \mu^+\mu^-$ is simulated using the `VLL` model of the `PHOTOS` package. The `VSS` model is used in the decay $\phi \rightarrow K^+K^-$. The amplitude for this decay is given by $A = \varepsilon^\mu v_\mu$ where ε is the polarization vector of the parent particle and the v is the (four) velocity of the first daughter.

```
Decay anti-B_s0

1.000    J/psi   phi             SVV_HELAMP 1.0 0.0 0.0 0.0 1.0 0.0;

Enddecay

Decay J/psi

1.000    mu+  mu-                PHOTOS  VLL;

Enddecay

Decay phi

1.000   K+   K-                          VSS;

Enddecay

End
```

The input B_s^0 average proper decay length is 439 μm, and the B_d^0 average proper decay length is 464 μm.

Before passing the generated events through the suite of programs for the detector simulation, hit simulation, trigger simulation, track and particle reconstruction, the following "pre-GEANT" selection cuts are applied:

- presence of the decay chain $\overline{B_s^0} \to J/\psi\phi$.
- $p_T^\mu > 1.5$ GeV and 0.8< $|\eta^\mu| < 2.0$, or $p_T^\mu > 3$ GeV and $|\eta^\mu| < 0.8$.

The suite of kinematic and quality cuts are applied as described in the next section on the data sample. The expected number of reconstructed B_s^0 events in the present sample is estimated, considering the following factors.

- acceptance of the "pre-GEANT' cuts for B_s^0 mesons at $p_T > 6$ GeV and $|y| < 1$ is 0.1989.
- The number of generated B_s events at $p_T > 6$ GeV and $|y| < 1$ (corrected for the acceptance for the "pre-GEANT" muon kinematic cuts) is 56078.
- The inclusive B^+ production cross section at $|y| < 1$ is 3.6±0.6 μb at 1.8 TeV (CDF Run I, see Ref. [112]).
- The increase of the B cross section by a factor of 1.15 at 1.96 TeV, compared to Run I.
- The ratio of production cross sections of B_s^0 to B^+ mesons is $f_{B_s} = 0.273 \pm 0.035$. (=10.6/38.8, PDG02 [4]).
- The branching fraction for the decay chain $B_s^0 \to J/\psi\phi$, $J/\psi \to \mu^+\mu^-$, $\phi \to K^+K^-$ is 2.7×10^{-5}. (PDG02 [4]).

Note that we normalize to the CDF Run I measurement of the B^+ cross section that was limited to the central rapidity region, $|y| < 1$. We do **not** restrict the rapidity range in this analysis. The projected rapidity distribution for the B_s^0 signal and background in this data is shown in Fig. 8.18.

The number of events passing all event selection criteria is equal to 456. Dropping the cuts on the J/ψ and ϕ proper decay time uncertainty, which are up to about 72% efficient in MC and more than 95% efficient in data (see Figs. 8.7, 8.8), we estimate the number of expected events per 1 pb^{-1} to be $2\times456/0.72/1838 = 0.68\pm0.3$. Hence, in this analysis, we would expect 32 reconstructed B_s^0 events with a 40% uncertainty.

MC Background $B_d^0 \to J/\psi K^*$

We use a sample of simulated events of the B_d^0 decay to estimate the background contribution from this channel. The event generation is described in chapter 9 on the B_d^0 lifetime measurement. The invariant mass distribution obtained under the $B_s^0 \to J/\psi\phi$ hypothesis is shown in Fig. 8.5.

This sample corresponds to an integrated luminosity of 251 ± 47 pb^{-1}. We expect 0.028 ± 0.01 $B_d^0 \to J/\psi K^*$ events to pass the B_s^0 selection criteria per 1 pb^{-1}. In the present sample, we expect 1.3 events, with 0.4 events in the signal mass region. We conclude that the $B_d^0 \to J/\psi K^*$ process is not source of a serious bias, and is adequately treated as part of the inclusive background.

8.3 B_s^0 Lifetime Measurement

8.3.1 The Proper Decay Length

The signed decay length of a B_s^0 meson is defined as the vector pointing from the primary vertex to the decay vertex projected on the B_s^0 momentum in the transverse plane:

$$L_{xy}^B = (\vec{x}_B - \vec{x}_{prim}) \cdot \vec{p}_T/p_T, \tag{8.1}$$

where $\vec{p}_T$ is the measured transverse momentum vector and p_T is its magnitude. The primary vertex is reconstructed individually for each event [111]. The proper lifetime, τ, and the proper decay length, $c\tau$, are then defined by the relation:

$$c\tau = L_{xy}^B \cdot M_{B_s^0}/p_T, \tag{8.2}$$

where $M_{B_s^0} = 5.3696$ GeV is the world average mass of the B_s^0 meson [4]. The distribution of the measured $c\tau$ uncertainty peaks at about 30 μm, as shown in Fig. 8.6. It is well simulated by MC, although the MC distribution has a larger tail.

We also compare the uncertainty distributions of the proper decay length of J/ψ and ϕ candidates in data and MC (see the appropriate distributions in Fig. 8.7 and Fig. 8.8).

The tail in the decay length resolution in Monte Carlo is related to the presence of events with a low number of SMT hits on tracks. For comparison, in Fig. 8.9 we show the pseudorapidity distribution of all J/ψ mesons, and then with the total number of SMT hits on the two muons less than 2, for data and MC events.

8.3.2 The Proper Decay Time Distributions

We divide the B_s^0 mass range into three bands: "low side": $(5.1 < M(B) < 5.22)$ GeV, "middle": $(5.22 < M(B) < 5.46)$ GeV, and "high side", $(5.46 < M(B) < 5.7)$ GeV. The middle mass band includes the signal; all three contain comparable numbers of background events. The proper lifetime distributions in the three mass bands are compared in Fig. 8.10. The low and high sides are dominated by short lifetime background, the mean values are

20±25 μm and 1±9 μm. We assume the same parametrization of the background shape in the entire mass region.

To test the dependence of the data on the detector regions, the proper lifetime distributions is compared for events in the central and forward rapidity ranges, $|y(B)| < 1$ and $|y(B)| > 1$, respectively. The B_s^0 signal in this sample is found to be evenly distributed in rapidity, and the lifetime distributions in the two plots are similar, see Fig. 8.11.

Focusing on the events at $ct > 0.005$ cm, we find 24 entries in each plot, with means of 0.0333±0.0050 cm and 0.0342±0.0070 cm, respectively.

8.3.3 The Fitting Procedure

The MINUIT minimization program in root (TMinuit class) is used in this analysis. Refer to Appendix D for more detail about how we implement the unbinned maximum likelihood fitting for B_s mass and lifetime.

The proper decay length and invariant mass distribution of the B_s candidates are fit simultaneously using an unbinned maximum log-likelihood method. The likelihood function $\mathcal{L}$ is given by:

$$\mathcal{L} = \prod_{i=1}^{N}[f_{sig}\mathcal{F}_{sig}^{i} + (1 - f_{sig})\mathcal{F}_{bck}^{i}], \tag{8.3}$$

where N=143 is the total number of events, $\mathcal{F}_{sig}^{i}$ is the product of the signal mass and proper decay-length probability density functions, $\mathcal{F}_{bck}^{i}$ is the product of the background mass and proper decay-length probability density functions, and f_{sig} is the fraction of signal.

The mass distribution of the signal is parametrized by a Gaussian function, with the mass fixed at 5.37 GeV, and the width fixed at the value of 0.044 GeV, obtained in the MC simulation, see Fig. 8.3. The mass distribution of the background is parametrized by a straight line with a free slope, normalized to unity in the range (5.1,5.7) GeV. The lifetime distribution of the signal is parametrized by an exponential convoluted with a Gaussian function. The lifetime resolution of background is approximated by a superposition of a Gaussian function centered at zero, one exponential for the negative $c\tau$ region and one exponential for the positive $c\tau$ region, with free slopes. The width of the Gaussian functions is taken from the event-by-event measurement. To allow for the possibility of the lifetime uncertainty to be systematically underestimated, we introduce a free scale factor ε.

Fit to the data

parameter	central value ± error
f_{sig}	0.232 ± 0.05
slope-massbkg	-0.75 ± 0.62
$c\tau$	$0.0375^{+0.0090}_{-0.0065}$ cm
ε	1.01 ± 0.17
slope-bkg-neg	0.005 ± 0.003 cm^{-1}
slope-bkg-pos	0.018 ± 0.011 cm^{-1}
norm-bkg-neg	0.119 ± 0.079
norm-bkg-pos	0.185 ± 0.119

Table 8.1: Unbinned maximum likelihood fitting results

The fit results are summarized in Table 8.1. The lifetime distribution with the fit results overlaid is shown in Fig. 8.12. Figure 8.13 shows the behaviour of the likelihood function versus $c\tau$ around its minimum. For the B_s^0 mean proper decay length we obtain

$$c\tau(B_s^0) = 375^{+90}_{-65}\ \text{(stat)}\ \mu\text{m}. \tag{8.4}$$

The fitted fraction of signal in the sample is $f_{sig} = 0.23 \pm 0.05$. The fitted value of the lifetime resolution scale factor, ε=1.01±0.17, is consistent with unity.

8.4 Systematic Uncertainties

8.4.1 Monte Carlo verification

We have tested the entire procedure on Monte Carlo samples (i.e, passing through D0geant simulation, D0reco reconstruction, *d0root_analysis* analysis, and the maximum likelihood fitting). For the B_s^0 mean proper decay length we obtain (see Fig. 8.14):

$$c\tau(B_s^0(MC) = 419 \pm 35\text{(stat)}\ \mu\text{m}, \tag{8.5}$$

which is consistent with the input of 439 μm. We found no significant bias in the fit results, to the accuracy, limited by MC statistics, of 35 μm.

8.4.2 Sensitivity to the Choice of the $p_T(B)$ Threshold

We have tested the sensitivity of the result to the choice of the B_d^0 transverse momentum threshold by repeating the fit to the MC signal sample, varying the minimum $p_T(B)$ in 1 GeV steps between 5 and 14 GeV. The results are shown in Fig. 8.15.

We see no significant bias due to the choice of the $p_T(B)$ threshold. From the spread of the results in the range 5 – 10 GeV we assign the systematic uncertainty of 20 μm.

In the case of data, lowering the $p_T(B)$ threshold below 6 GeV leads to an increase in the rate of the "long-lived" background and hence to an increased uncertainty in the measured lifetime due to the unknown background shape. On the other hand, there is no enough data to raise the cut much above 6 GeV.

8.4.3 The Signal Mass Parameterization

We have repeated the fit with B_s^0 mass resolution altered by one standard deviation with respect to the default value. The resulting systematic uncertainty is 3 μm for the B_s^0 lifetime.

8.4.4 Background Level

The sensitivity of the result to the level of background in the selected data sample has been tested, by performing alternative fits to the data, with a larger and smaller ϕ mass window, corresponding to the change in the background level by approximately $\pm 15\%$. We find the result for the B_s^0 lifetime measurement to be stable to within 7 μb.

8.4.5 Background parametrization

To test the sensitivity of the results to the parametrization of the shape of the background lifetime distribution, we have compared the fits allowing one and two "positive" exponential.

The difference between the results obtained with one and with two positive exponentials is 6 μm for B_s^0 decay. We assign the systematic error of 6 μm in this case. This test was performed on a larger data sample which became available after this analysis was completed.

8.4.6 Uncertainty of the decay length resolution

This test was performed on the larger data sample. It was found that the scale factor ε is 1.23 ± 0.06. Varying the decay length resolution scale in the range (1.17, 1.29) corresponds to a negligible change of the lifetime result.

8.4.7 Alternative calculation of the secondary vertex

In this analysis we use the common $(J/\psi, \phi)$ vertex position to calculate the decay length. Alternatively, we could use the dimuon vertex as an approximation of the B vertex. The difference between the lifetime values obtained with the B vertex and J/ψ vertex has a distribution centered at 0 and the width of 42 μm. The B_s^0 lifetime fit using the J/ψ vertex is shown in Fig. 8.16. The fitted mean value for the B_s^0 lifetime is 374 μm, to be compared with 375 μm obtained with the B_s^0 vertex. We find these results consistent; we do not assign a systematic error due to this difference.

8.4.8 Summary of the systematic uncertainties

The systematic uncertainties are summarized in Table 8.2. At present, the largest source of the systematic uncertainty is the quality of the MC test of the fitting procedure and the sensitivity of the results to the kinematic cuts, due to the limited MC statistics.

Source	B_s^0 decay
Fitting procedure	35 μm
Choice of the $p_T(B)$ threshold	20 μm
Mass width	3 μm
Background level	7 μm
Background lifetime parametrization	6 μm
Decay length error scale	negligible
Total	41 μm

Table 8.2: Summary of systematic uncertainties for the B_s^0 lifetime measurement.

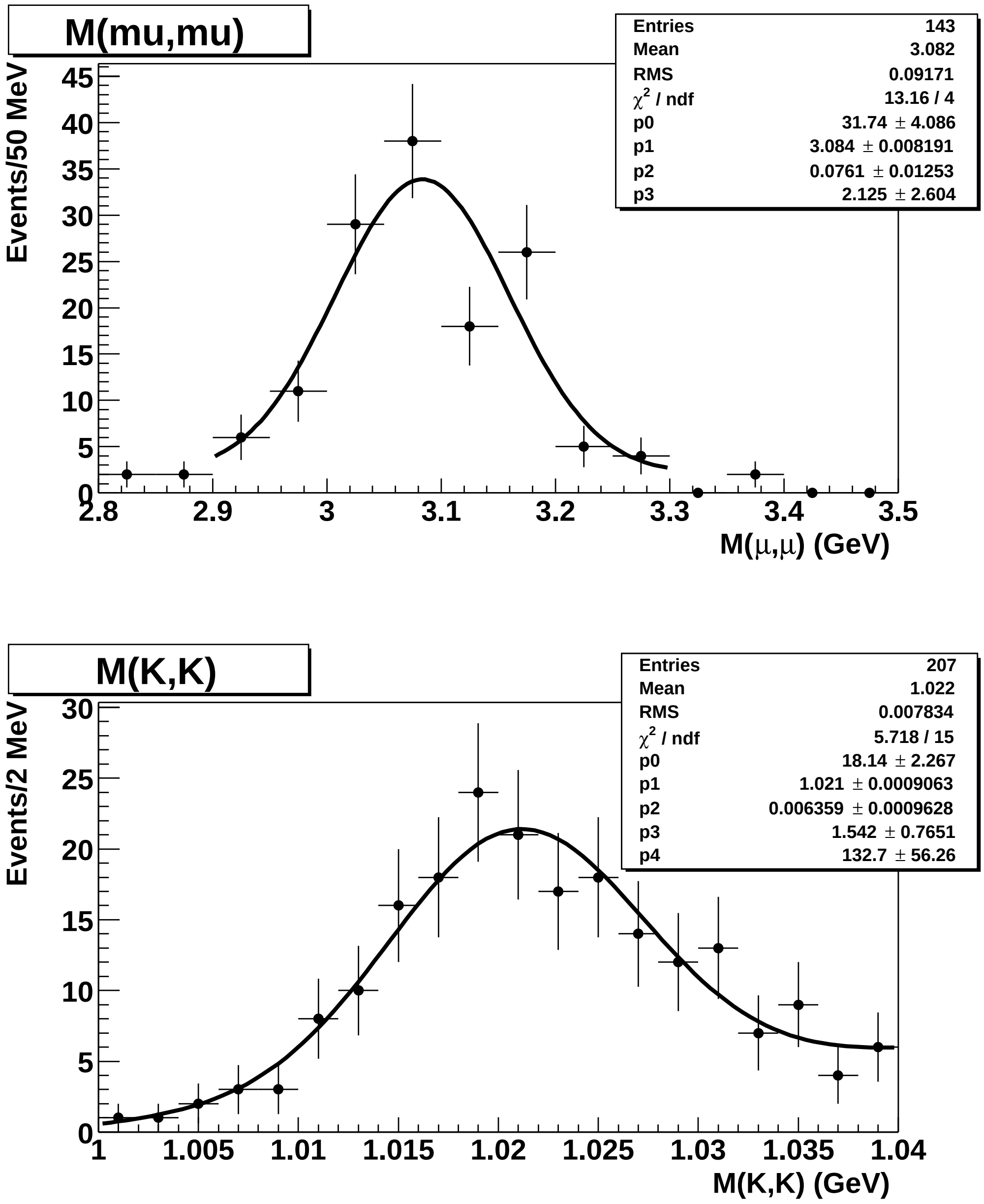

Figure 8.1: Invariant mass distribution of (μ^+, μ^-) pairs (top), and of (K^+, K^-) pairs (bottom). The curves are fit to a Gaussian distribution and a linear background.

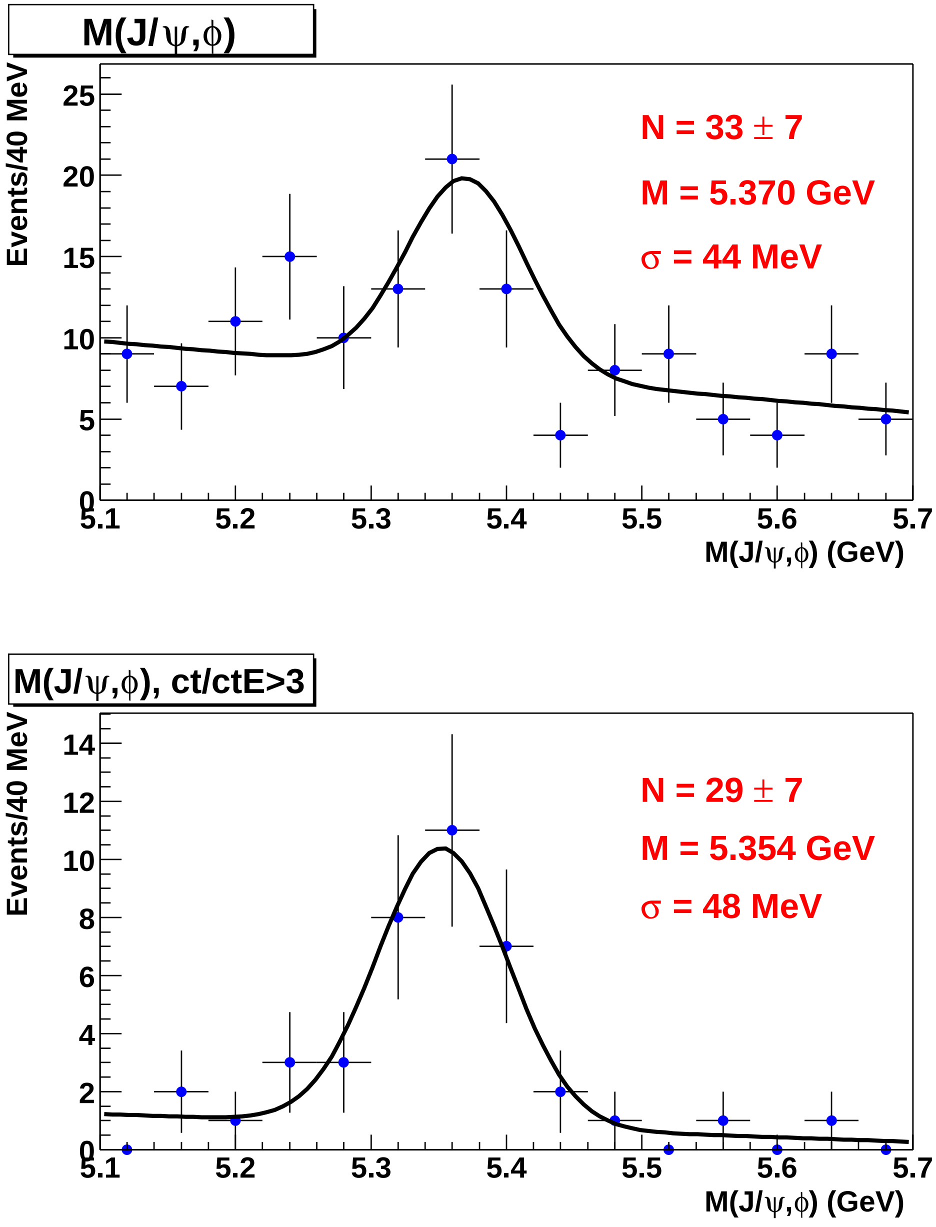

Figure 8.2: The invariant mass distribution of the $(J/\psi, \phi)$ system for all B_s^0 candidates (top), and for events with the prompt background suppressed (bottom) (see text). The curves are fits to a Gaussian distribution, with a fixed width of 44 MeV and a linear background.

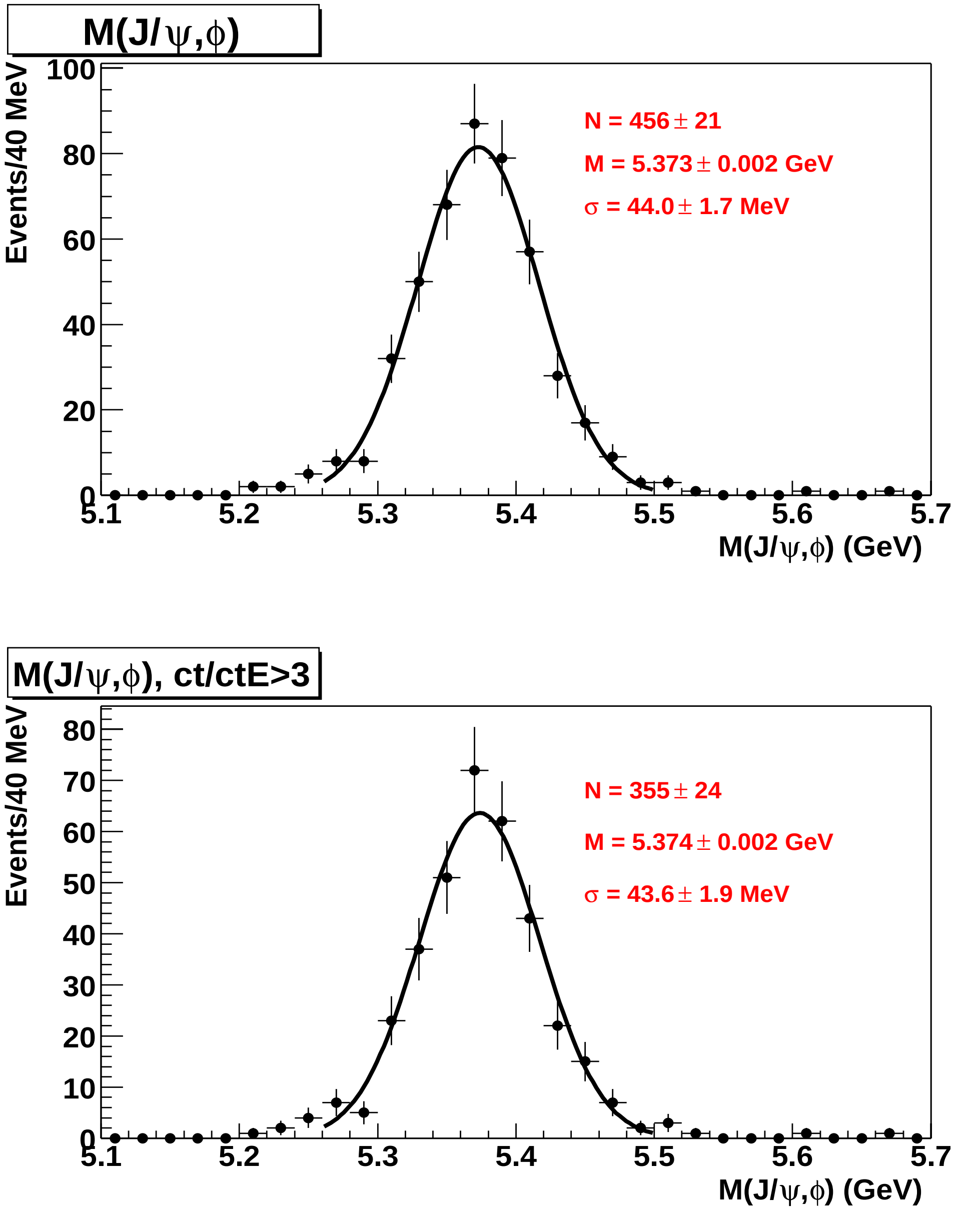

Figure 8.3: MC simulation of the invariant mass distribution of B_s^0 candidates (top), and for events with a cut to suppress the prompt background (bottom) (see text). The curves are fits to a Gaussian distribution and a linear background.

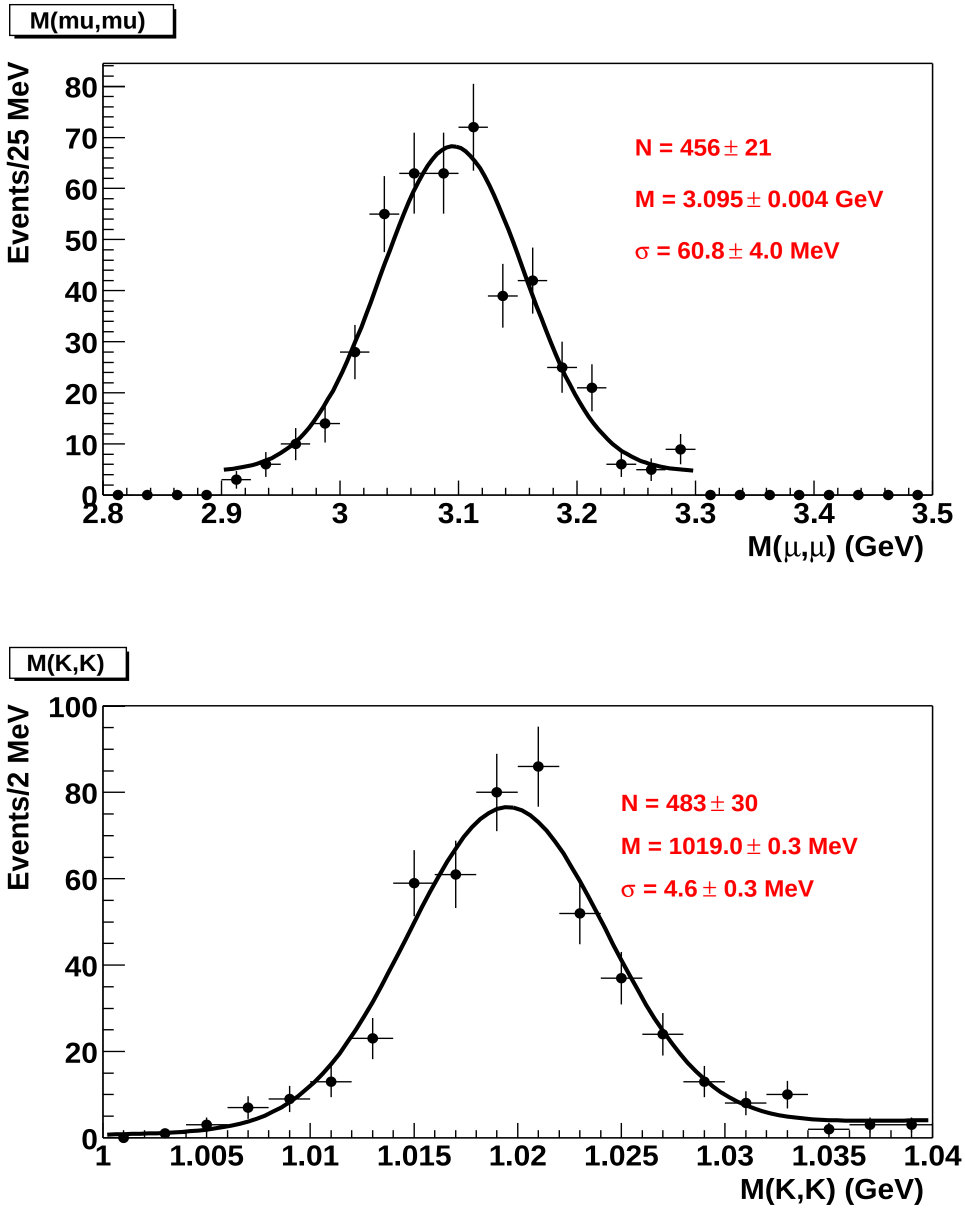

Figure 8.4: MC simulation of the invariant mass distribution of (μ^+, μ^-) pairs (top), and of (K^+, K^-) pairs (bottom) from B_s^0 decays. The curves are fits to a Gaussian distribution and a linear background.

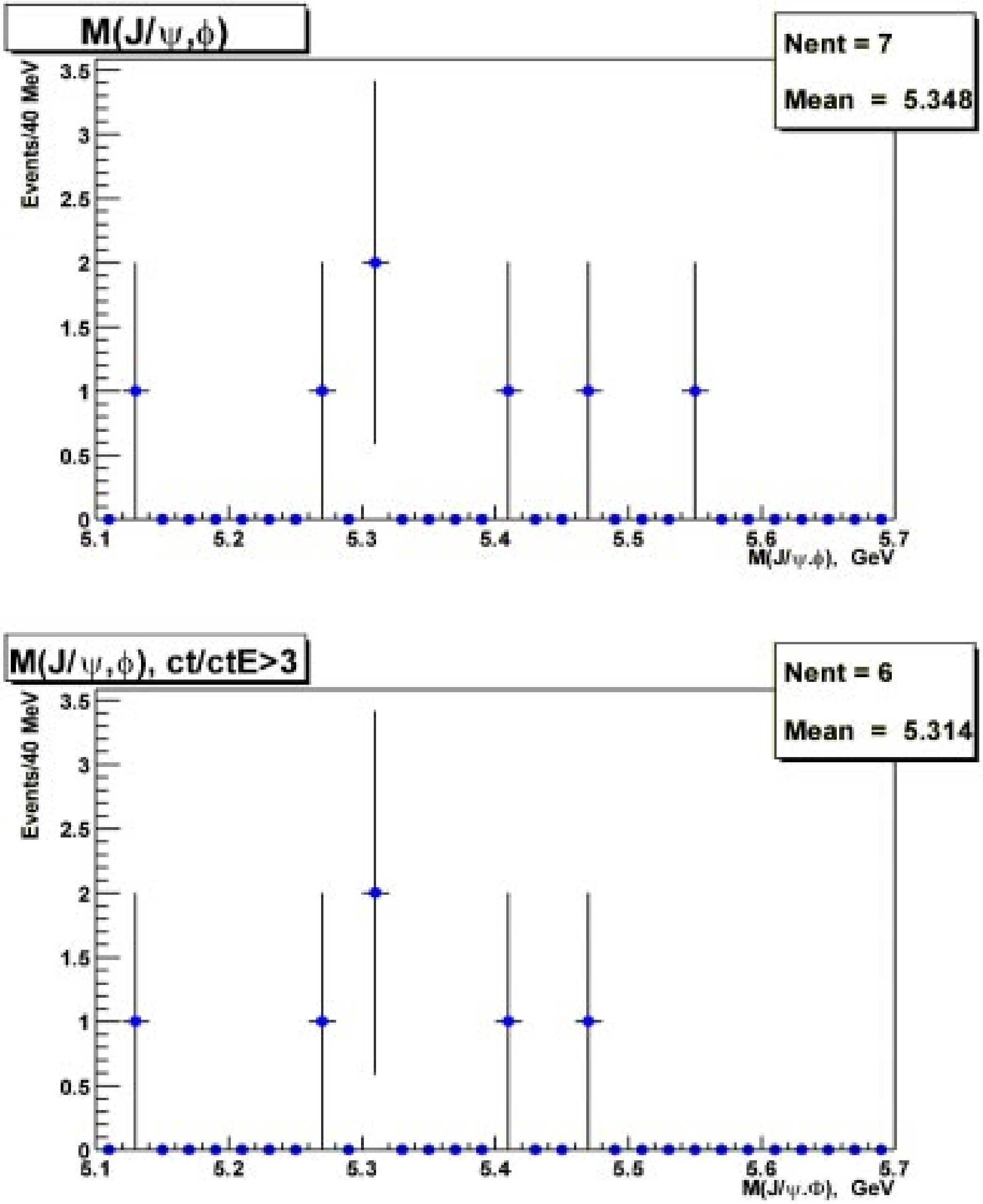

Figure 8.5: MC simulation of the $B_d^0 \to J/\psi K^*$ background contribution to the B_s^0 signal, for all events (top), and for events with the prompt background suppressed (bottom) (see text).

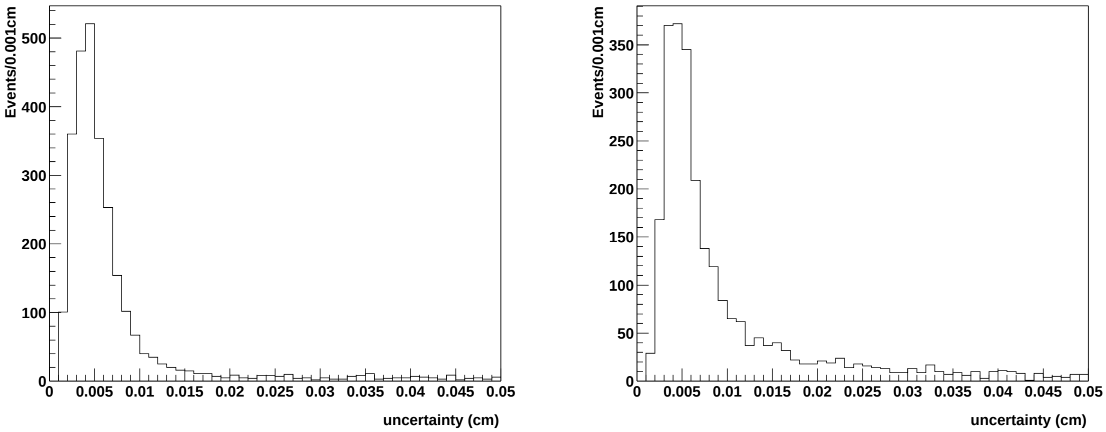

Figure 8.6: Distribution of the uncertainty of the decay length of B_s^0 candidates. (left: Data; right: MC)

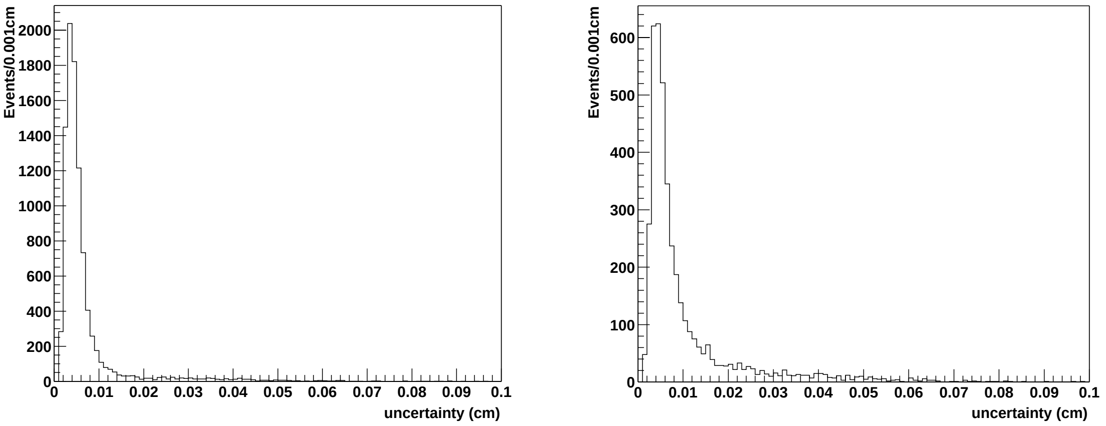

Figure 8.7: Distribution of the uncertainty of the decay length of J/ψ candidates. (left: Data; right: MC)

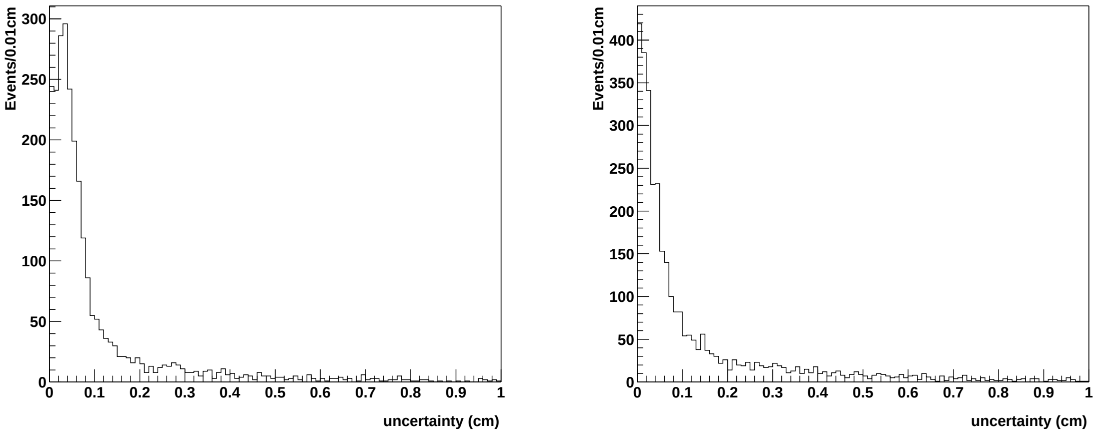

Figure 8.8: Distribution of the uncertainty of the decay length of ϕ candidates. (left: Data; right: MC)

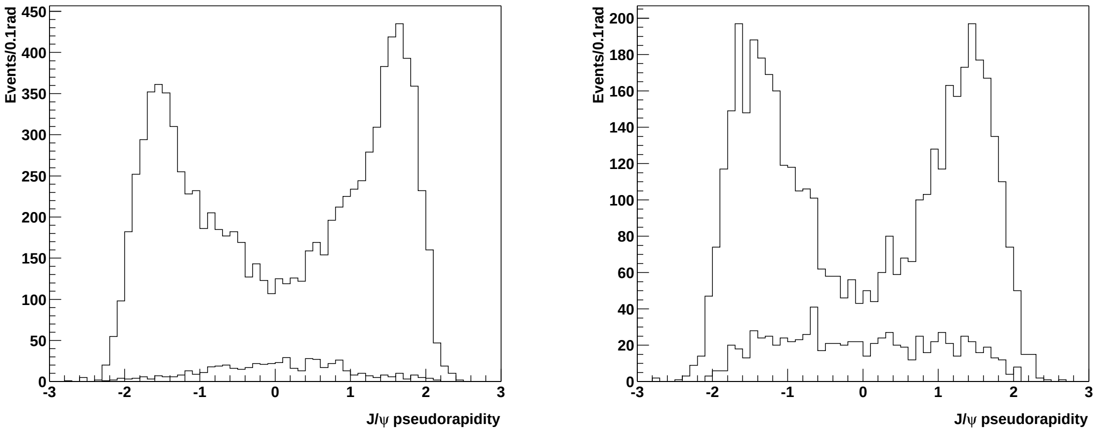

Figure 8.9: J/ψ pseudorapidity distribution for the case SMT1+SMT2<2 and all events (left: Data; right: MC).

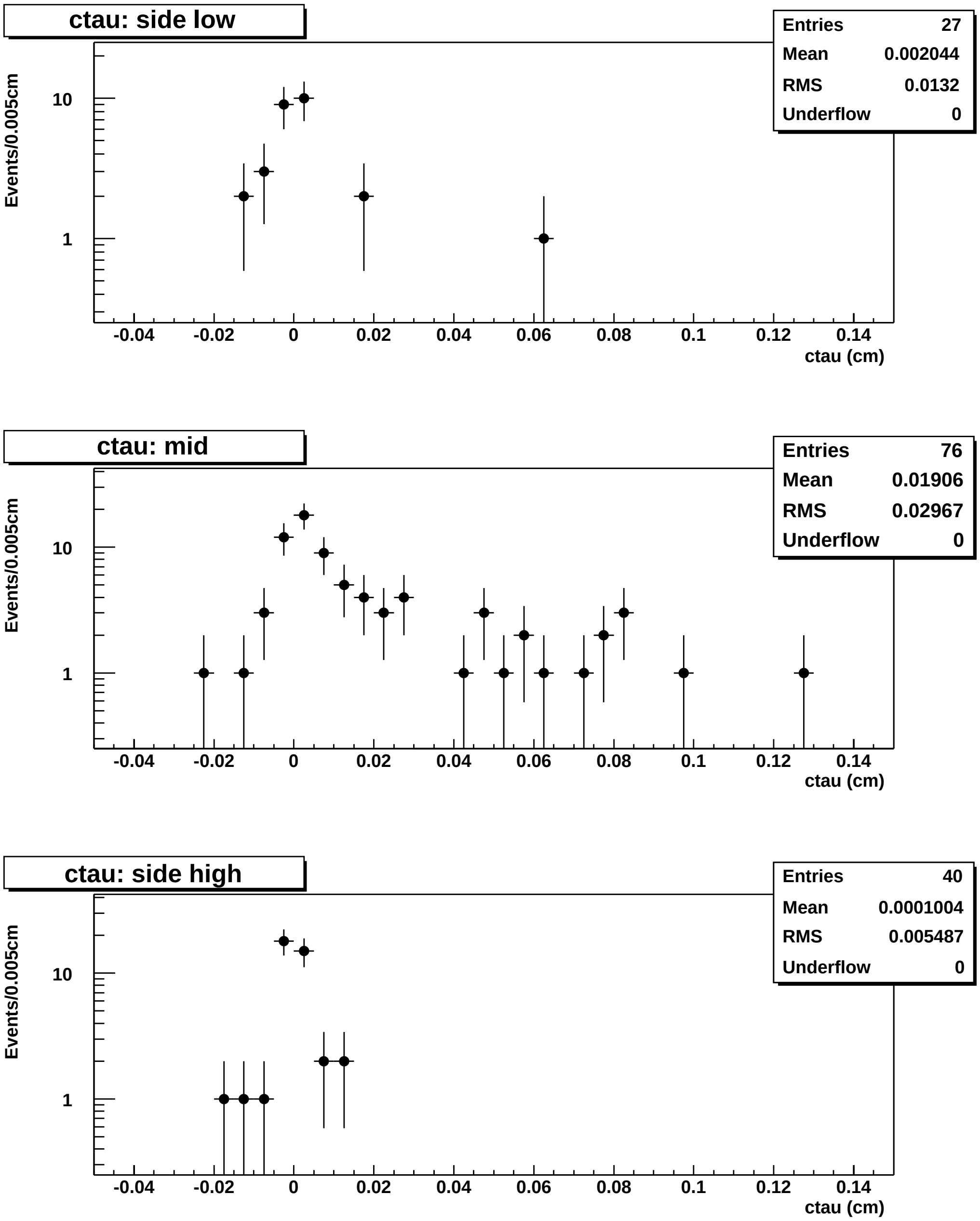

Figure 8.10: The proper lifetime distribution in three mass bands (see text).

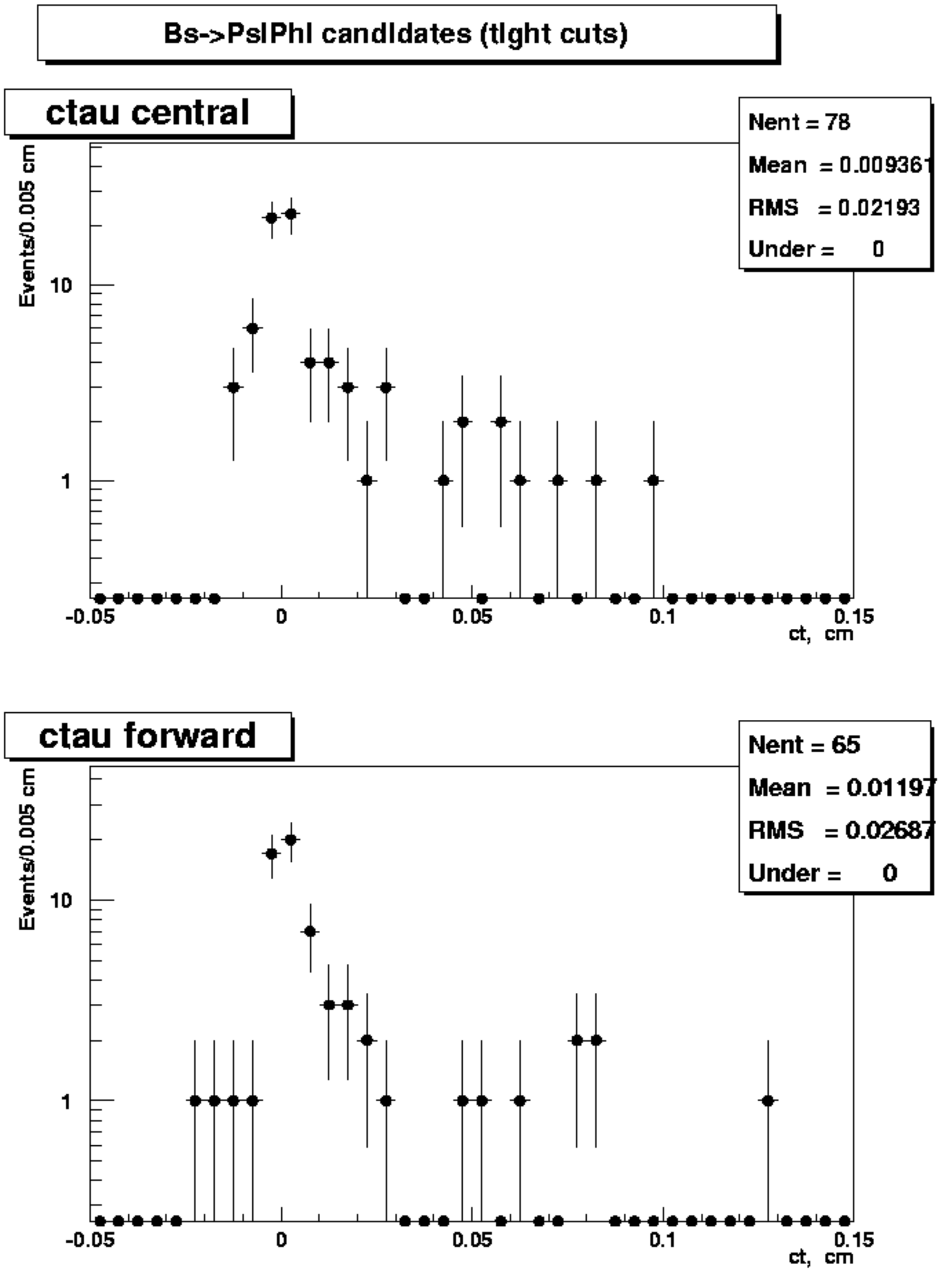

Figure 8.11: The proper lifetime distribution for central and forward B_s^0 candidates.

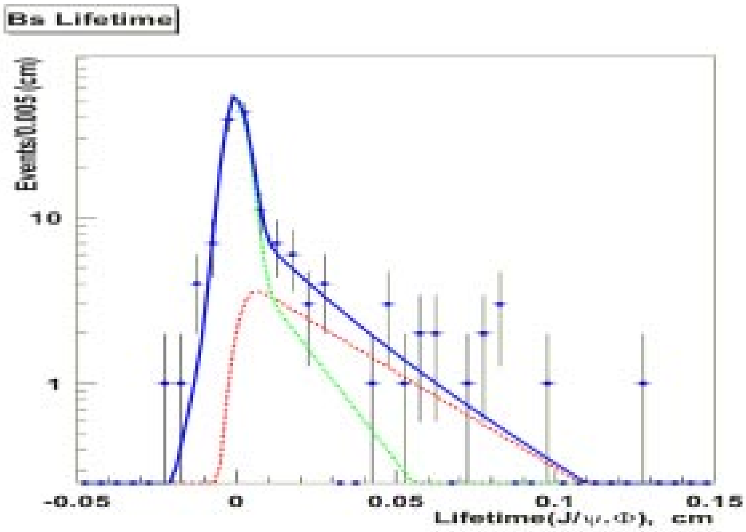

Figure 8.12: The proper decay length, $c\tau$, of the B_s^0 candidates. The curves show: the signal contribution (dotted); the background (dashed); and total (solid).

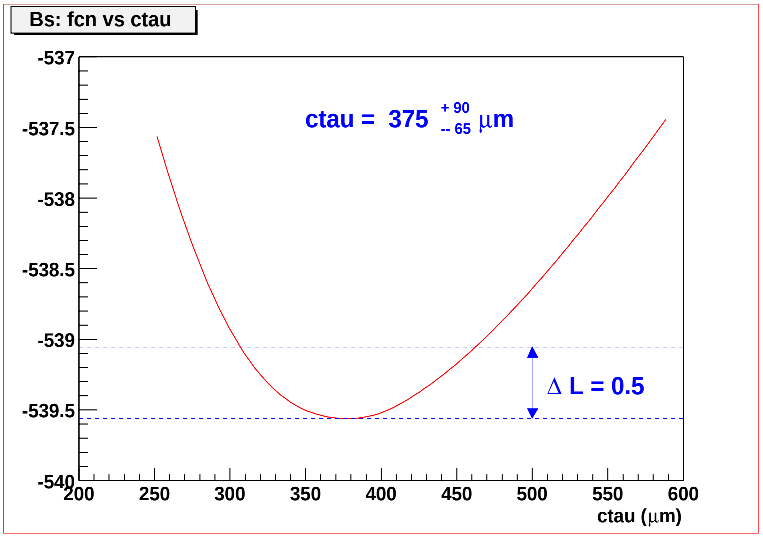

Figure 8.13: The dependence of the likelihood function vs $c\tau$ around its minimum.

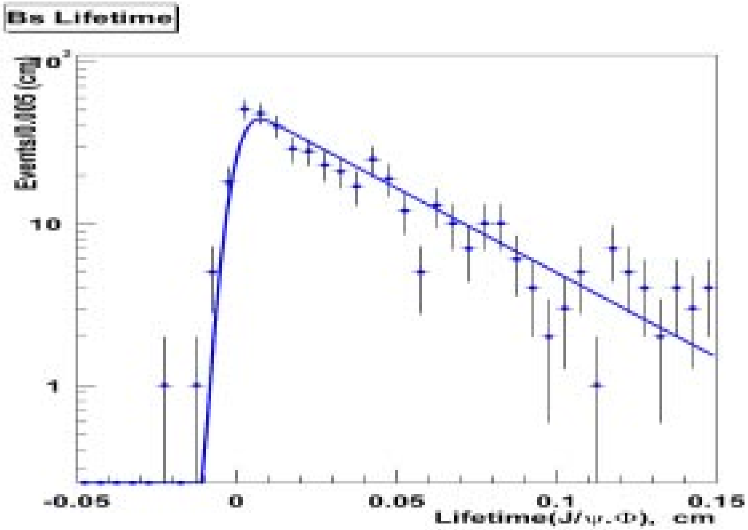

Figure 8.14: The proper decay length, $c\tau$, of the B_s^0 candidates in Monte Carlo events. The curve shows the fitted signal distribution.

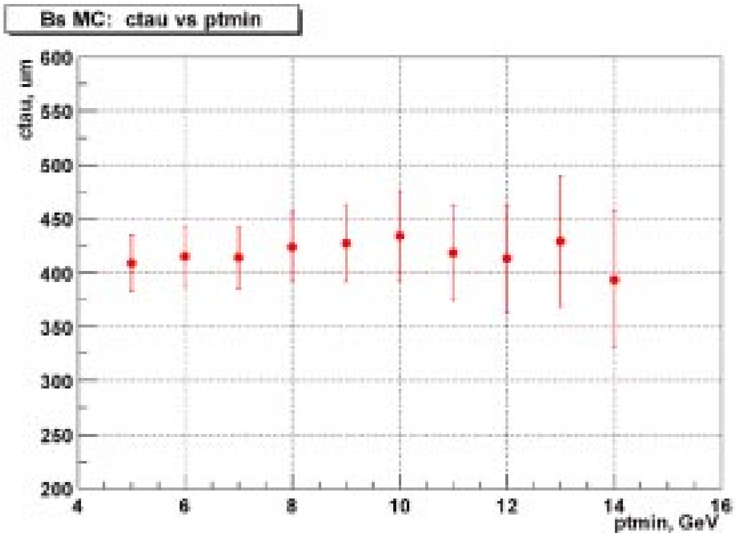

Figure 8.15: The fitted proper decay length, $c\tau$, for the B_s^0 MC sample as a function of the $p_T(B)$ threshold.

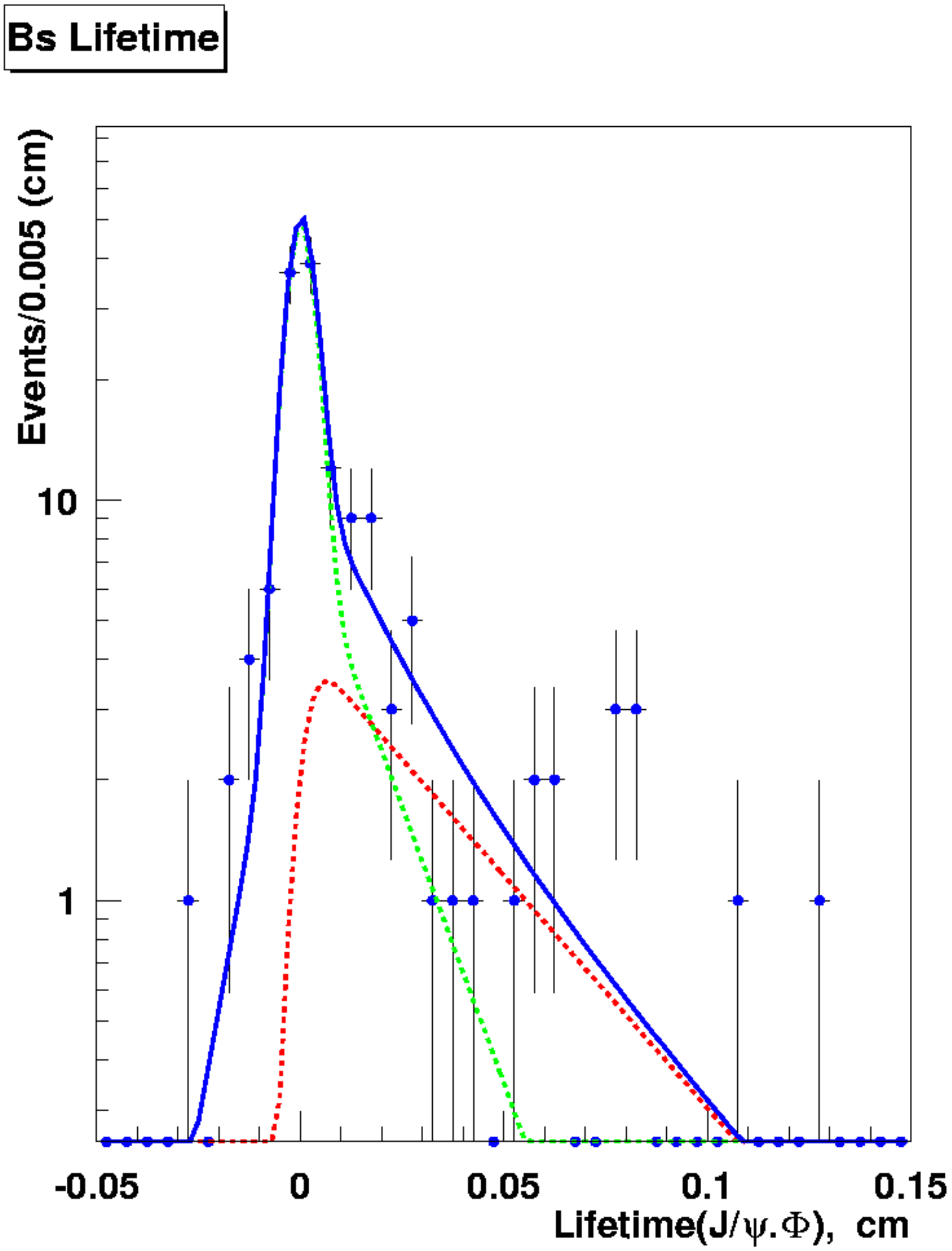

Figure 8.16: The alternative proper decay length distribution, $c\tau$, of the B_s^0 candidates, using the J/ψ vertex rather than the reconstructed B_s^0 vertex. The curves show: the signal contribution (dotted); the background (dashed); and total (solid).

8.5 Further Studies

Using the fit results for the signal and background parameters, we can define the probability that a given event is due to the signal or background, w_{sig} and w_{bkg}, respectively:

$$w_{sig} = \frac{f_{sig} \cdot \mathcal{F}_{sig}^{mass} \cdot \mathcal{F}_{sig}^{life}}{f_{sig} \cdot \mathcal{F}_{sig}^{mass} \cdot \mathcal{F}_{sig}^{life} + (1 - f_{sig}) \cdot \mathcal{F}_{bkg}^{mass} \cdot \mathcal{F}_{bkg}^{life}}, \tag{8.6}$$

where f_{sig} $\mathcal{F}_{sig}^{mass}$ is the normalized mass signal function, $\mathcal{F}_{sig}^{life}$ is the normalized lifetime signal function, with analogous symbols for background.

$$w_{bkg} = 1 - w_{sig}. \tag{8.7}$$

Using these probabilities as weights in a histogram, we can obtain projected distributions of various observables. Figure 8.17 shows the invariant mass distribution of (K^+, K^-) pairs due to signal (top) and background (bottom). The distribution assigned to the signal is consistent with being entirely due to the ϕ decay, while background is found to be composed of ϕ decay and a non-resonant part. Note that the (K^+, K^-) distribution is not used as input to the maximum likelihood fit, and the above projections constitute a prediction of the distributions for signal and background. In Fig. 8.18 we show the rapidity distribution of the $(J/\psi, \phi)$ system for signal and background.

The transversity angle (θ_T) has been presented in section 2.6.2. It is defined as the angle between μ^+ and the normal to the K^+K^- plane in the J/ψ reset frame, and it separates out the CP-even and CP-odd components. Studies of angular correlations and decay time in the process of $B_s^0 \to J/\psi\phi$ continue at DØ.

8.6 B_s^0 Summary

The lifetime of the B_s^0 meson has been measured to be

$$\tau(B_s^0) = 1.25^{+0.30}_{-0.22}(\mathrm{stat}) \pm 0.14(\mathrm{syst})\ \mathrm{ps}. \tag{8.8}$$

This result is consistent with the world average [4] of $\tau(B_s^0) = 1.461\pm\ 0.057$ ps.

Using results of the simultaneous maximum likelihood fit to the invariant mass and proper decay length distributions of B_s^0 candidates, we have defined event weights to separate signal from background that allow us to make predictions for distributions of observables that have not been used in the fit.

Although the data used in this study are limited to events collected in the 2nd half of 2002, re-processed by a private version of the offline reconstruction program, with known deficiencies, the results look promising. We are looking forward to adding the 2003 data, processed with an upgraded version of `D0Reco`. DØ should be able to carry out a competitive measurement of the B_s^0 lifetime and its decay amplitudes, and, in the further future, of the possible lifetime difference of the two B_s^0 states.

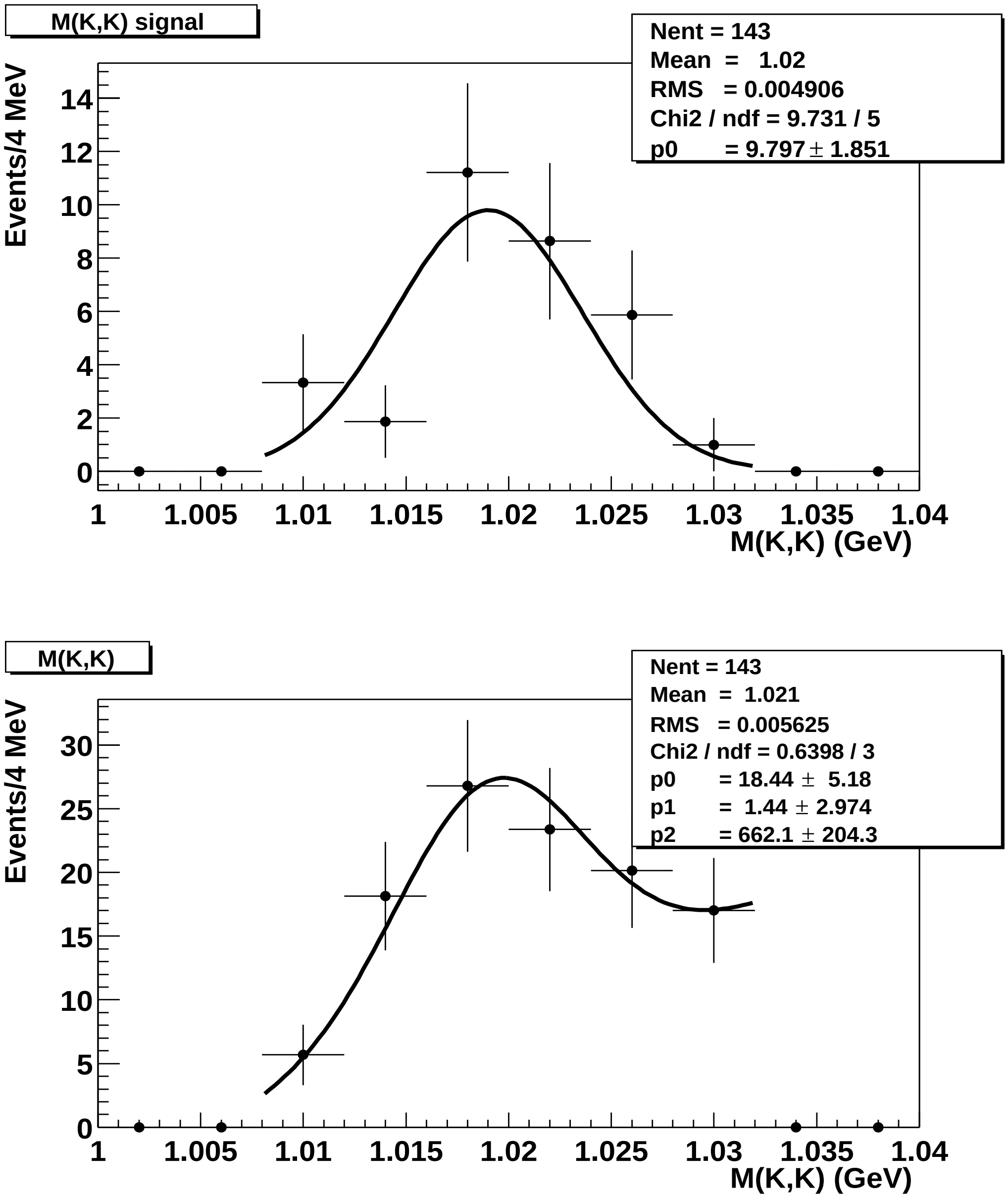

Figure 8.17: Projected invariant mass distribution of (K^+, K^-) pairs for the signal B_s signal (top) and for background (bottom) based on the maximum likelihood fit to the data.

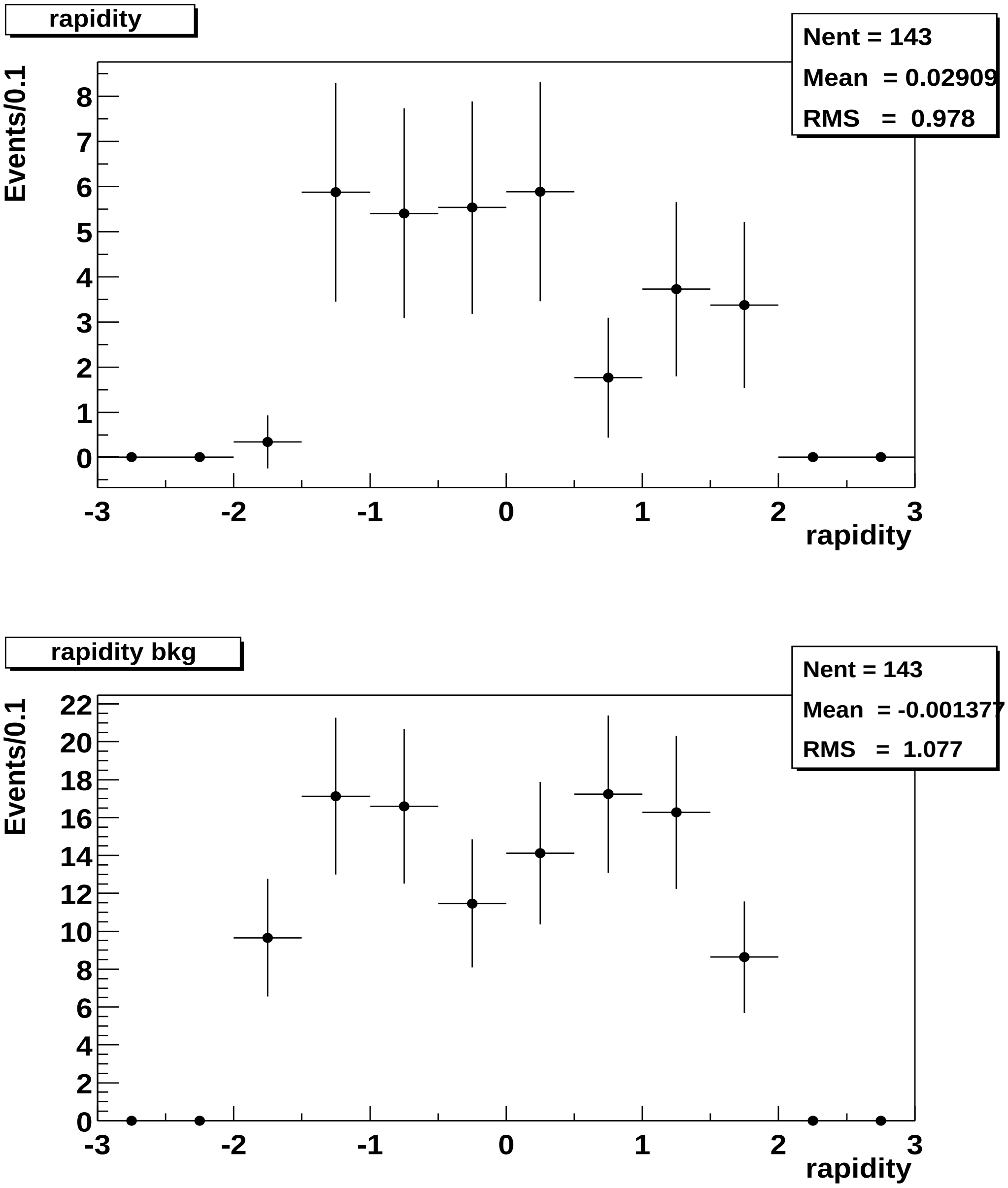

Figure 8.18: Projected rapidity distribution of the reconstructed B_s^0 candidates for the signal signal (top) and for background (bottom) based on the maximum likelihood fit to the data.

Chapter 9

Study of $B_d^0 \to J/\psi K^*$ Decays

In this chapter, a preliminary measurement of the B_d meson lifetime is presented by using the decay mode $B_d^0 \to J/\psi K^*$. The data sample corresponds to an integrated luminosity of 47 pb^{-1}. 57±19 B_d^0 candidates are found, and the lifetime of the B_d^0 meson is determined to be $\tau(B_d)$=$1.43^{+0.30}_{-0.23}$(stat)± 0.20 (syst) ps. Using the result $\tau(B_s)$=$1.25^{+0.30}_{-0.22}$(stat)±0.14(syst) ps obtained for the same sample, the ratio of the lifetimes is determined to be $\tau(B_s)/\tau(B_d) = 0.87 \pm 0.24$. These results are consistent with previous B meson lifetime measurements.

9.1 Data and Monte Carlo Event Samples

9.1.1 Dimuon Data Sample

The same dimuon sample described in the previous chapter is also used for B_d^0 analysis. Also muon selection criteria and most kinematic cuts on the B_d^0 decay products are the same as B_s^0 studies. We set the thresholds at 6.0 GeV for B_d and 2 GeV for K^*, and 1 GeV for each K^* decay product. To ensure well measured momenta and space coordinates of particles coming from the B_d decay, tracks from the K^* decay are required to have at least 4 hits in the central tracking system, including at least 1 hit in the SMT detector. We also require the decay length to be well measured for both J/ψ and K^*, namely the decay length error for J/ψ to be less than 0.02 cm and for K^* to be less than 0.2 cm.

J/ψ candidates are accepted by using the same criteria as in last chapter. K^* candidates are formed by pairing oppositely charged tracks with a transverse momenta greater than 1 GeV, and assigning the higher p_T track the K^+ mass, and the lower p_T track the π^+ mass. Candidates are accepted if they satisfy a fit to a common vertex, and the invariant mass is in the range 0.8 – 1.0 GeV.

The B_d candidate sample is selected by requiring a $(J/\psi, K^*)$ pair to be consistent with coming from a common vertex, and to have a mass in the range 5.0 – 5.6 GeV. Finally, an event is rejected if the number of tracks other than muons in a cone $\Delta R < 1.0$ (isolation, i.e. $\Delta_R = \sqrt{(\Delta\eta)^2 + (\Delta\phi)^2}$, where η, ϕ are in radians) around J/ψ is less than 2 or greater than 15. This sample of 521 events is used in the B_d lifetime measurement. The dimuon mass distribution and the $K^\pm, \pi^\mp$ candidate distribution are shown in Fig. 9.1. The mass width of the J/ψ signal is 78 ± 11 MeV, and the K^* mass width is 25 ± 1.6 MeV.

The invariant mass distribution of the $(J/\psi, K^*)$ system is shown in the top plot of Fig. 9.2. The curve is a projection of the maximum likelihood fit, described later. The fit assigns 57±19 events to the B_d^0 decay. The B_d signal is more pronounced if background due to prompt J/ψ production is suppressed by requiring the B_d candidate's measured decay proper length to be greater than 3 times its uncertainty, see the bottom plot in Fig. 9.2.

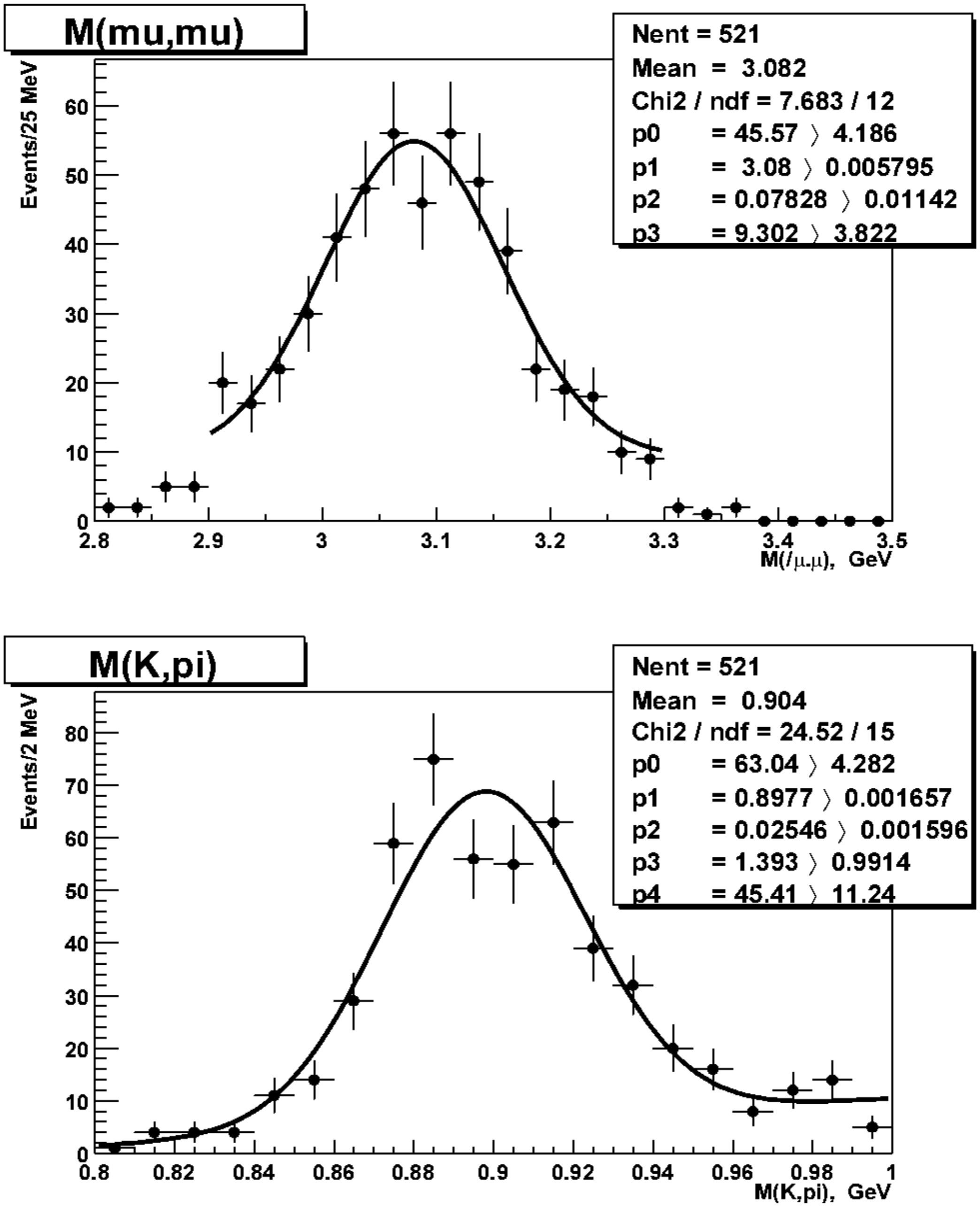

Figure 9.1: The invariant mass distribution of (μ^+, μ^-) pairs (top), and for $(K^\pm, \pi^\mp)$ pairs (bottom). The curves are fits to a Gaussian distribution and a linear background.

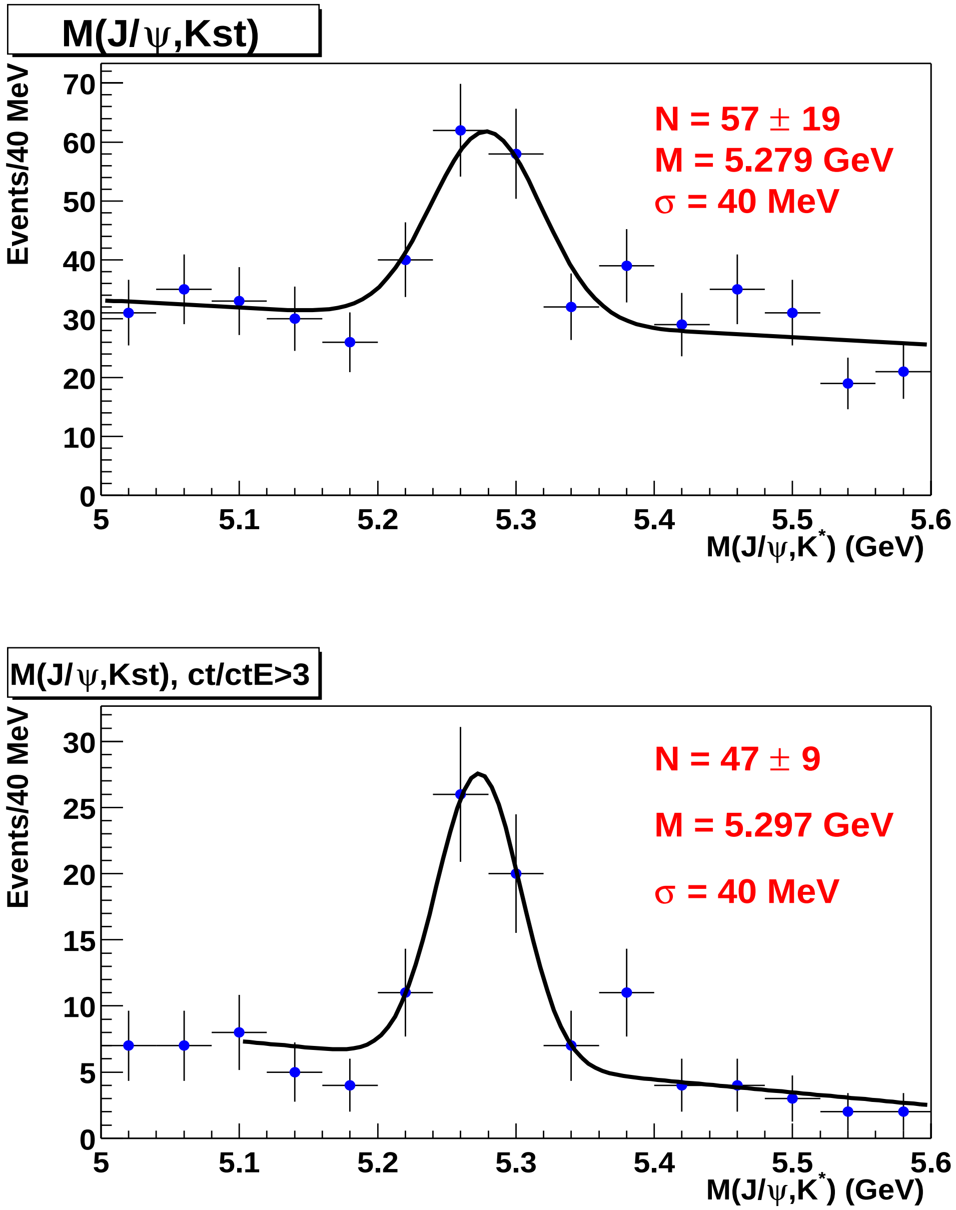

Figure 9.2: Invariant mass distribution for all B_d^0 candidates (top), and for events with the prompt background suppressed (bottom) (see text). The curves are fits to a Gaussian distribution and a linear background.

9.1.2 Monte Carlo Event Samples

MC Signal $B_d^0 \to J/\psi K^*$

To simulate the decay chain $B_d^0 \to J/\psi K^*$, $J/\psi \to \mu^+\mu^-$, $K^* \to K^\pm\pi^\mp$ we use the `QQ` generator [61] interfaced to the `Pythia` program [55]. In this simulation, the generated B_d^0 mesons are unpolarized, and the mixing parameter is turned off.

```
DECAY  B0B
CHANNEL  0 1.000 PSI   K*B
ENDDECAY

DECAY  PSI
ANGULAR_HELICITY  -1   1.  0.  1.
ANGULAR_HELICITY   0   1.  0. -1.
ANGULAR_HELICITY   1   1.  0.  1.
CHANNEL  40 1.000 MU+   MU-
ENDDECAY

DECAY  K*B
ANGULAR_HELICITY  -1   1.  0. -1.
ANGULAR_HELICITY   0   0.  0.  1.
ANGULAR_HELICITY   1   1.  0. -1.
```

```
CHANNEL  0 1.000  K-    PI+

ENDDECAY


MIXING B0 B0B 0.0
```

The B_d^0 proper lifetime is 464 μm in the `QQ` ptable file.

Before passing the generated events through the suite of programs for the detector simulation, hit simulation, trigger simulation, track and particle reconstruction the following selection cuts are applied:

- presence of the decay chain $\overline{B_d^0} \to J/\psi K^*$.
- ${p_T}^\mu > 1.5$ GeV and 0.8$< |\eta| < 2.0$ or ${p_T}^\mu > 3$ GeV and $|\eta^\mu| < 0.8$.

30,000 events are generated for this channel, passing the above cuts.

Below we estimate the expected number of the reconstructed B_d^0 events in the present sample, considering the following factors:

- Acceptance of the "pre-Geant' cuts for B_d^0 mesons at $p_T(B) > 6$ GeV and $|y| < 1$ 0.253.
- The number of generated B_d events at $p_T > 6$ GeV and $|y| < 1$ is 53265.
- The inclusive B^+ production cross section at $|y| < 1$ is 3.6±0.6 μb at 1.8 TeV (CDF Run I).

- The increase of the B cross section by a factor of 1.15 at 1.96 TeV, compared to Run I.
- The branching fraction for the decay chain $B_d^0 \to J/\psi K^*$, $J/\psi \to \mu^+\mu^-$, $K^* \to K^\pm\pi^\mp$ is 5.14×10^{-5} (PDG [4]).

The number of events passing all event selection criteria is 173. Dropping the cuts on the J/ψ and K^* proper decay time uncertainty, which are $\approx$ 72% efficient in MC and more than 95% efficient in data, we estimate the number of expected events per pb^{-1} to be $2{\times}173/0.72/251 = 1.9{\pm}0.6$. Hence, in this analysis, we expect 90 reconstructed B_d^0 events with a 30% uncertainty.

9.2 B_d^0 Lifetime Measurement

The mass and lifetime distributions are fitted simultaneously using the unbinned maximum likelihood method, as in the last chapter. The mass distribution of the signal is parametrized by a Gaussian function, with the mass fixed at 5.279 GeV, and a width fixed at the value of 40 MeV, obtained in the MC simulation, see Fig. 9.3. Like B_s^0, the B_d^0 lifetime and mass are fit simultaneously using maximum likelihood fitting. The fitting procedure and the likelihood function are described in chapter 8 on the B_s^0 decay analysis.

The results are presented in Fig. 9.5. Figure 9.6 shows the behavior of the likelihood function versus $c\tau$ around its minimum.

For the B_d^0 mean proper decay length we obtain

$$c\tau(B_d^0) = 428^{+90}_{-70}\ (\mathrm{stat})\mu\mathrm{m}. \tag{9.1}$$

The fitted fraction of signal in the sample is f_{sig} 0.109±0.03. The fitted value of the lifetime resolution scale factor is $\varepsilon = 1.190 \pm 0.095$, close to unity.

9.3 Systematic Uncertainties

9.3.1 The Signal and Background Parametrization

We have tested the fitting procedure and the signal parametrization by performing a fit to the $B_d^0 \to J/\psi K^*$ MC sample described earlier. Although the input consists of pure signal, we allow for the fit to vary the amount of background, which in this case corresponds to events where one of the tracks has been mismeasured or the K^* decay products have been misidenitified. For the B_d^0 mean proper decay length we obtain (see Fig.9.7):

$$c\tau(B_d^0(MC)) = 424 \pm 56 \text{ (stat)}\mu\text{m}, \tag{9.2}$$

which is consistent with the input of 464 μm.

We have tested the sensitivity of the result to the choice of the B_s^0 transverse momentum threshold by repeating the fit to the MC signal sample, varying the minimum $p_T(B)$ in 1 GeV steps between 5 and 14 GeV. The results are shown in Fig. 9.8. We see no significant bias due to the choice of the $p_T(B)$ threshold. From the spread of the results in the range 5 – 10 GeV we assign the systematic uncertainty of 20 μm.

Like in last chapter, the B_d^0 systematic uncertainties are summarized in Table 9.1. At present, the largest source of the systematic uncertainty is the quality of the MC test of the

Source	B_d^0 decay
Fitting procedure	56 μm
Choice of the $p_T(B)$ threshold	20 μm
Mass width	5 μm
Background level	7 μm
Background lifetime parametrization	6 μm
Decay length error scale	negligible
Total	60 μm

Table 9.1: Summary of systematic uncertainties for the B_d^0 lifetime measurement

fitting procedure and the sensitivity of the results to the kinematic cuts, due to the limited MC statistics.

9.4 Further Studies

Like in chapter 8, by using the probabilities as weights in a histogram, we can obtain projected distributions of various observables. Figure 9.9 shows the invariant mass distribution of $(K^{\pm}, \pi K^{\mp})$ pairs due to signal (top) and background (bottom). The distribution assigned to signal is consistent with being entirely due to the K^* decay, while background is found to be composed of K^* decay and a non-resonant part.

9.5 Summary

The lifetime of the B_d^0 meson has been measured to be

$$\tau(B_d^0) = 1.43^{+0.30}_{-0.23}(\text{stat}) \pm 0.20(\text{syst})\text{ps}. \tag{9.3}$$

This result is consistent with the world average of $\tau(B_d^0) = 1.542\pm$ 0.016 ps [4].

In chapter 8 the lifetime measurement of the B_s^0 meson is presented using the same data sample and similar kinematic cuts. Major contributions to the systematic uncertainties cancel out in the ratio of the lifetimes.

The lifetime ratio is determined to be:

$$\tau(B_s)/\tau(B_d) = 0.87 \pm 0.24. \tag{9.4}$$

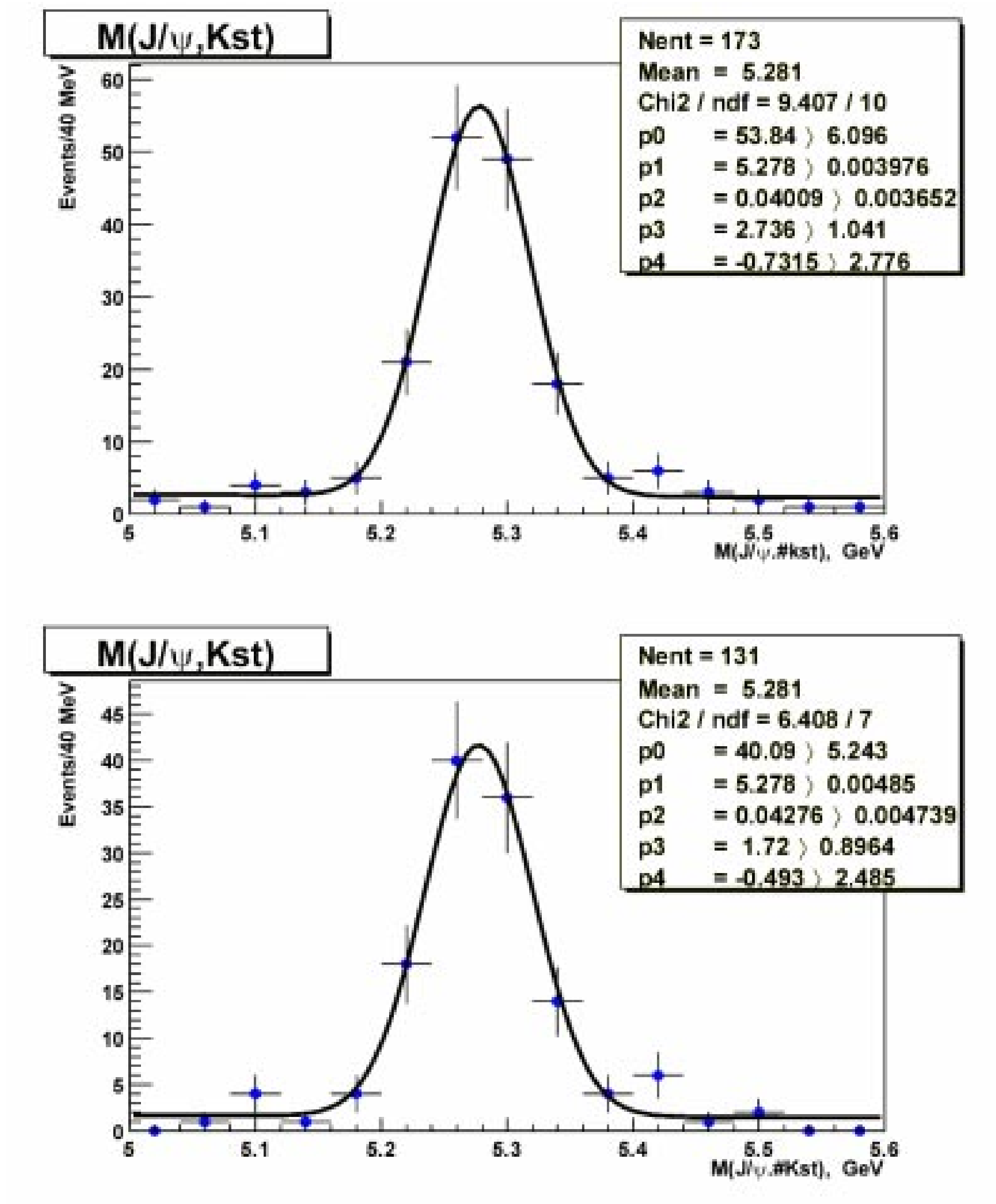

Figure 9.3: MC simulation of the invariant mass distribution of B_d^0 candidates (top), and for events with the prompt background suppressed (bottom) (see text). The curves are fits to a Gaussian distribution and a linear background.

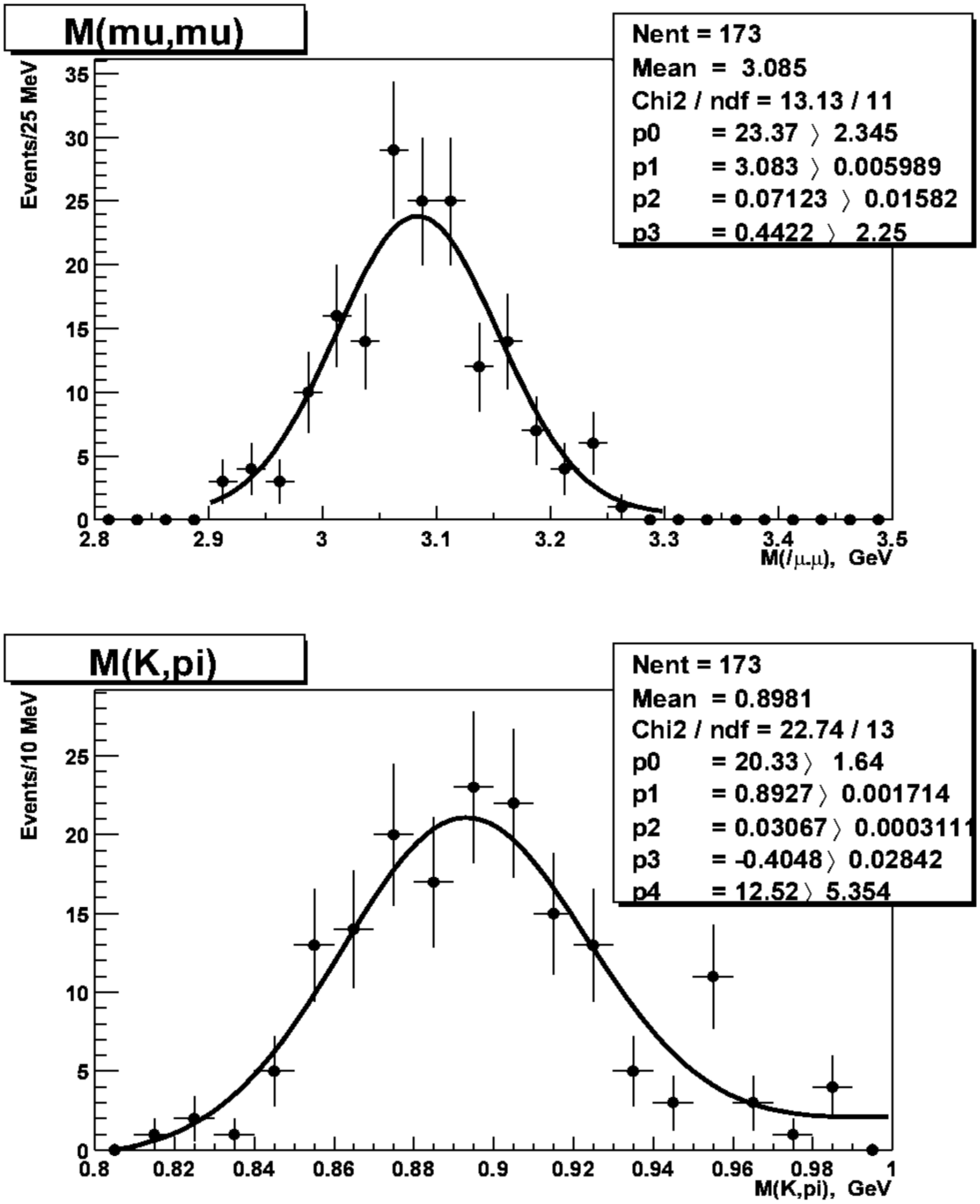

Figure 9.4: MC simulation of the invariant mass distribution of (μ^+,μ^-) pairs (top), and for ($K^\pm,\pi^\mp$) pairs (bottom). The curves are fits to a Gaussian distribution and a linear background.

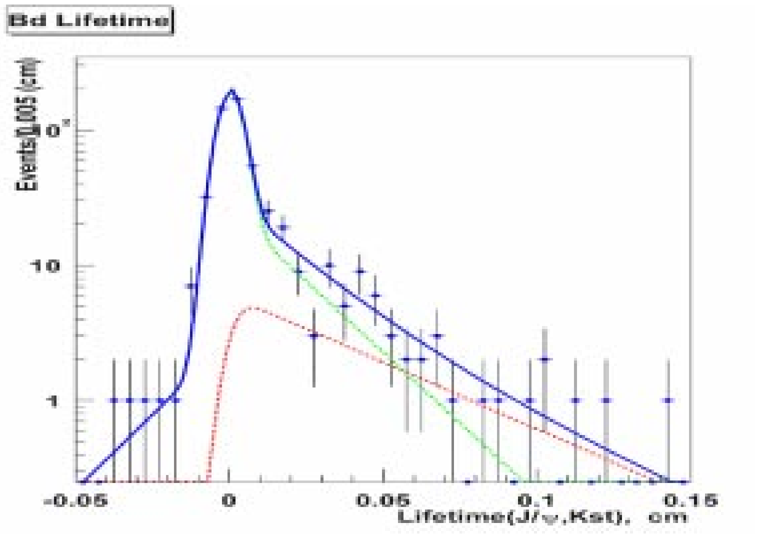

Figure 9.5: The proper decay length, $c\tau$, of the B_d^0 candidates. The curves show: the signal contribution (dotted); the background (dashed); and total (solid).

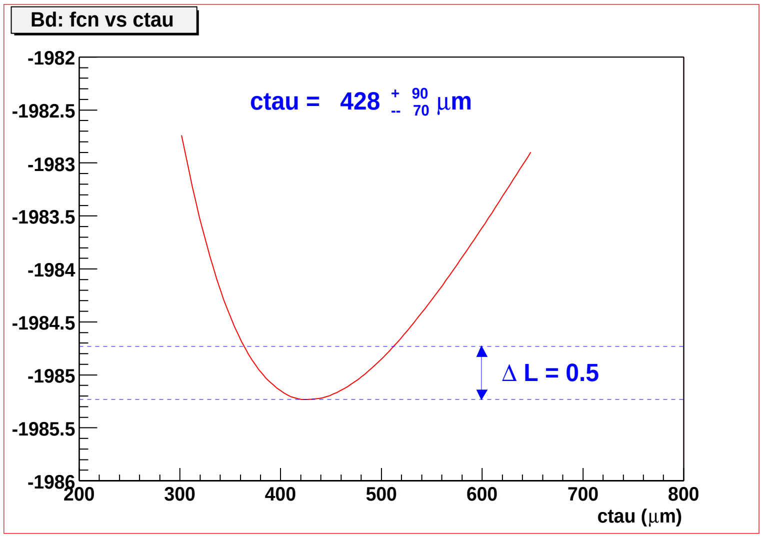

Figure 9.6: The behavior of the likelihood function vs $c\tau$ around its minimum.

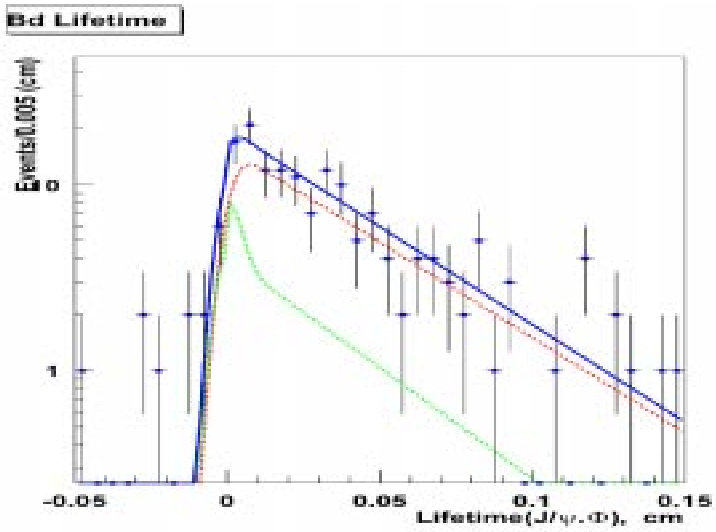

Figure 9.7: The proper decay length, $c\tau$, of the B_d^0 candidates. The curves show: the signal contribution (dotted); the background (dashed); and total (solid).

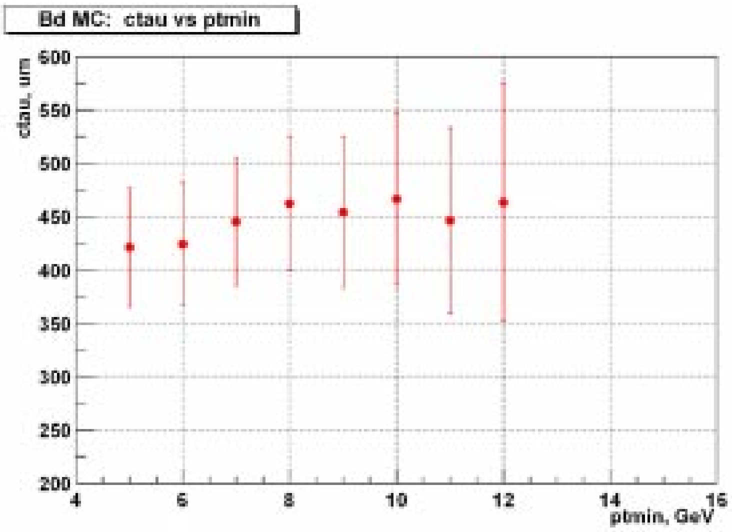

Figure 9.8: The fitted decay length, $c\tau$, for the B_d^0 MC sample as a function of the $p_T(B)$ threshold.

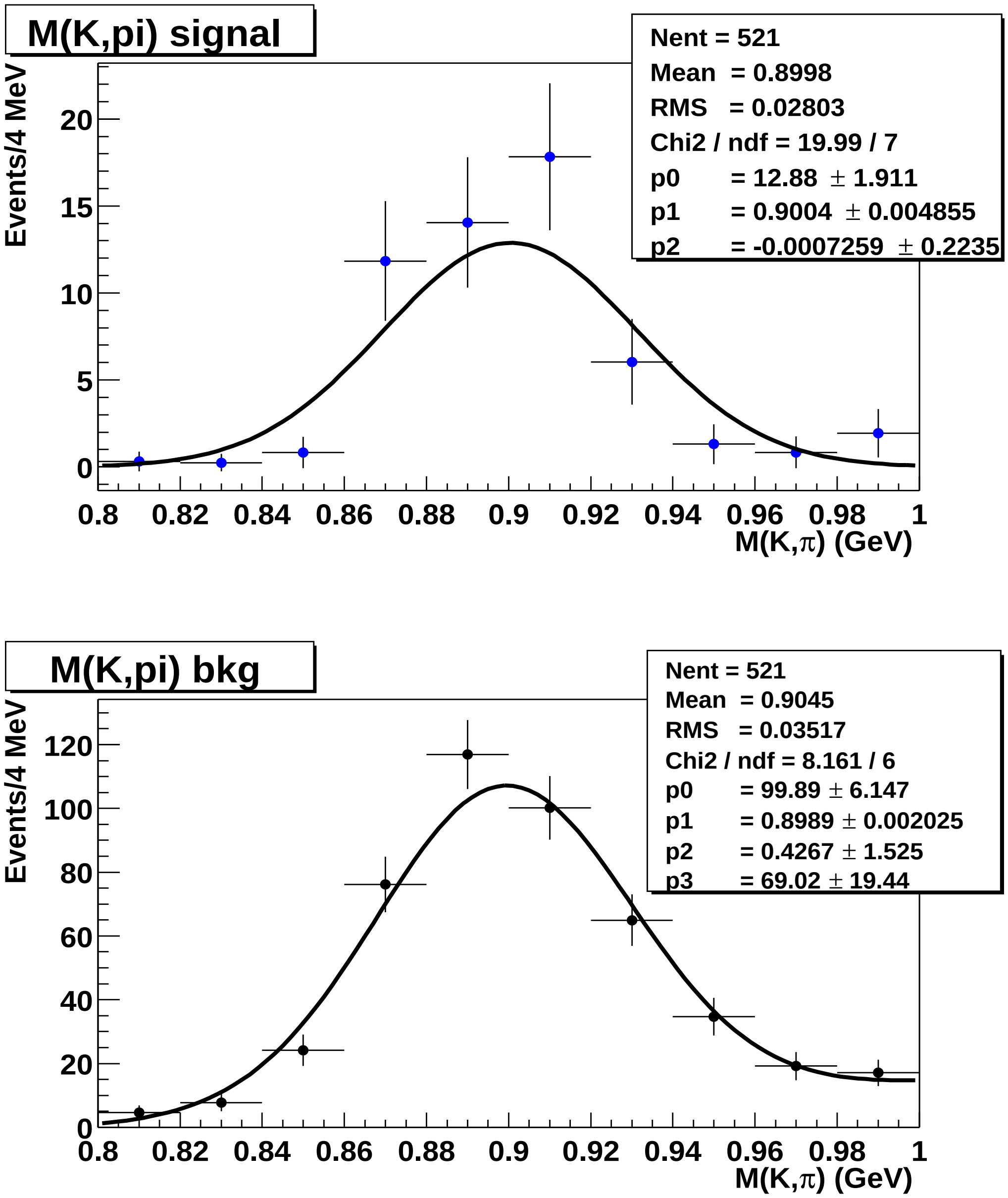

Figure 9.9: Projected invariant mass distribution of $(K^{\pm},\pi^{\mp})$ pairs for the signal B_d signal (top) and for background (bottom) based on the maximum likelihood fit to the data.

Chapter 10

Conclusions

This thesis is based on the data from the DØ experiment at the Tevatron collider. The Run II of the Tevatron started in March of 2001 and by December of 2002 DØ accumulated 47 pb^{-1} of data.

The author's primary "service" contribution to DØ experiment has been to the DØ software. The author's major projects, all documented in this thesis, include:

- Muon particle identification package. Muon particle identification is the final step in muon reconstruction. It is based on a variety of information including a match between a charged particle detected in the central tracker and a signal in the muon system.
- Muon thumbnail package. This package serves for storing the relevant information on muon candidates in the most compact way. Muon thumbnail size is limited to 1.5 Kb per event.
- Muon analysis package. This package makes use of all the available methods for retrieving muon reconstruction results.

- PDT time-to-distance studies. The author derived the relationship of drift distance with respect to drift time and a muon track incident angle. The achieved hit position resolution varies from 700 μm for small incident angles ($\theta = 0°$), to 1400 μm at $\theta = 60°$. My parametrization is the basic ingredient for the local muon segment and track reconstruction.

- Global Monitoring. The author developed software to monitor muon detector performance online. It has been used for the quality control of the collected data.

The author's physics project included:

- J/ψ cross section measurement.

  The author used the first 4.8 pb^{-1} of data to determine J/ψ production cross section over a rapidity region(0 to 1.8) and two transverse momentum regions. This measurement serves both as a test of QCD, and as an evaluation of the detector performance.

  Run I results for charmonium production cannot be adequately described by the existing models. The author has initiated J/ψ polarization studies that, once we have enough data, will provide decisive tests of the models.

- Lifetime measurement for B_s and B_d. The author performed a preliminary measurement of the B_s meson lifetime using the decay mode $B_s^0 \to J/\psi\phi$. The data sample corresponds to the integrated luminosity of 47 pb^{-1}. The author found 33±7 B_s^0 candidates and determine the lifetime of the B_s^0 meson to be $\tau(B_s)$=$1.25^{+0.30}_{-0.22}$ (stat) ± 0.14 ps. Simultaneously, the author has also measured B_d meson lifetime using the decay mode $B_d^0 \to J/\psi K^*$. The lifetime of B_d is determined to be $\tau(B_d)$=$1.43^{+0.30}_{-0.23}$ (stat) ± 0.20 ps. Combining the results, the author measured the ratio of the lifetimes to be $\tau(B_s)/\tau(B_d) = 0.87 \pm 0.24$. These results are consistent with previous B meson lifetime measurements.

In the future, with increased statistics, DØ should be able to carry out a competitive measurement of the B_s^0 lifetime and its decay amplitudes, and, in the further future, of the possible lifetime difference of the two B_s^0 states.

Appendix A

Contents of the Muonid Root Branch

This chapter describes DØ software production version p11, it is based on Ref. [78].

General info

Nmuonid

Number of *MuonParticle* objects in the event.

Idndeck

nwdeckA+10*nwdeckBC+1000*nsdeckA+10000*nsdeckBC.

Idnseg

Matching segments (0: no segments;)

(1:A layer; 2:BC; 3:A+BC; -3:A+BC w/o GTrack).

Idmtc

MTC track: -1 not done, 0 not found, 1 found.

Idcharge

Charge of reconstructed muon track.

Nmumu

Number of $\mu^+\mu^-$ combinations in the event.

Idmass, err_mass

Mass and error of the leading $\mu^+\mu^-$ pair.

deltaR

Distance to the nearest MC muon.

Indices to parent objects

idxseg

Index of parent segment for Idnseg=1 or 2 (=−1 for Idnseg!=1,2).

idxtrack

Index of $Muon :: Track$ for abs(Idnseg)=3 (=−1 for abs(nseg)!=3).

idxchp

Index of the matching ChargedParticle.

Best parameters at Pca:

from global match for Idnseg=3;

from $Muon :: Track$ for Idnseg=-3;

from the parent ChargedParticle for Idnseg=0,1,2.

Idpx, Idpy, Idpz, IdE, Idphi, Ideta

track 4-momentum, phi, etc information.

IdzAtPca

z coordinate at the point of closest approach — Pca (cm).

IdimpPar

Impact parameter in xy plane (cm).

IdimpPS

impact parameter significance.

eimpPar, ezAtPca, ephi, etanLam, ept

parameter errors.

Track matching quality

Iddeleta

delta_eta between the A layer segment (or track at A layer) and the matching ChargedParticle.

Iddelphi

azimuthal difference between A layer segment and the matching ChargedParticle.

Iddeldft

distance in the drift direction between A layer segment and the matching ChargedParticle at the A layer.

Idchisq

χ^2 from global matching

Idncentralmatch

Number of ChargedParticle objects matching.

Idcentralrank

Rank of track matching.

(1 to Idncentralmatch, ordered in ascending Idchisq, i.e. 1 - best match)

Local Track info

Idcategoryloc

-2 : BC segement only

-1 : A-stub

0 : A+BC but no fit

Idqualityloc

Local muon quality definition.

category=-2 : $\geq$ 3 wire hits and $\geq$ 1 scint hits quality = 3

: $\geq$3 wire hits, no scint hit quality = 2

: all other: quality = 1

category=-1 : $\geq$2 wire hits and $\geq$1 scint hit: quality = 3

: $\geq$2 wire hits, no scint hit: quality = 2

: all other: quality = 1

category= 0 : $\geq$2 A wire $\geq$3 BC wire: quality = 3

: $\geq$1 A wire $\geq$1 BC wire: quality = 2

category= 1 : quality = 1, 2, 3 like category = 0

: quality=4: quality=3 && chi2 > 0 && A scint $\geq$1 && BC scint $\geq$ 1

Idstatusloc

Status of local muon fitting.

tightmuon

Flag for "tight" muons, v1 definition.

Idchisqloc

χ^2 for fitting track through the toroid in the local muon system.

IdsctimeA, IdsctimeB

Scintillator time for A-segment, BC segment.

Idqptloc

charge times p_T of the local muon track.

Track angle and momentum at A layer (uncorrected for eloss)

IdxA, IdyA, IdzA IdpxA, IdpyA, IdpzA IdphiA, IdetaA, IdthetaA

Ideloss

expected energy loss in the calorimeter.

Calorimeter confirmation

hfr_hit

Fraction of hadronic cal cells hit by the muon.

etra_hit

Energy in cal cells hit by the muon.

hfr_best

Fraction of hadron calorimeter layers with energy, from the matching MTC track.

etra_best

Energy in calorimeter cells associated with the matching MTC track.

elast

Energy in last hadronic layer.

e33, e55

Energy in a 3 by 3 (5 by 5) tower around the muon.

Appendix B

Contents of the Muon Thumbnail

The various types of muons stored in the thumbnails are listed in table B.1.

nseg	**Muon Type**	**Central Matching Algorithm**	**MTC Matching**
3	centralTrack+local muon track	Muon → central if $\chi^2_{loc} > 0$ central → muon if $\chi^2_{loc} = -1$	$\Delta\eta$, $\Delta\phi$ between MTC and GTrack extrapolated to CAL
2	centralTrack+BC-seg	GTrack extrapolated straight through the calorimeter	as above
1	centralTrack+A-seg	central to muon	as above
0	centralTrack+muon hit or + MTC	GTrack straight through or extrapolated to CAL	as above
-1	A-segment only	no match	$\Delta\eta$, $\Delta\phi$ between MTC and A-layer segment
-2	BC-segment only	no match	$\Delta\eta$, $\Delta\phi$ between MTC and BC-layer segment
-3	Local muon track	no match	$\Delta\eta$, $\Delta\phi$ between MTC and local muon track at A-layer if fit or A-segment if no fit

Table B.1: Muon types in p13 thumbnail. χ^2_{loc} is the χ^2 of the local muon fit. MTC: Muon Tracking in the DØ Calorimeter

The muons are classified [80] according to the information available in the muon system (A-segment only, BC-segment only or A+BC segments also called local muon tracks). The variable used to make the classification is **nseg**. A positive value of **nseg** means that the muon could be matched to a central track. Here a “central track” indicates a track reconstructed in the central tracker, and “zAtPca” is the z coordinate at the point of the closest approach with respect to the center of the detector. A negative value of **nseg** means no central track could be matched to the muon. Depending on **nseg**, different algorithms might be used to attempt the matching with a central track. In the case when a central track could be matched, the muon 4-vector, as well as its η, ϕ, $\tan(\lambda)$ are given at the DCA. If no central track could be matched then the 4-vector and η, ϕ and $\tan(\lambda)$ are given at the A-layer position. The normalization of the 4-vector is corrected for the most probable energy loss in the calorimeter using the Run I parametrization.

B.1 Local Muon Track with Central Track Match (nseg=3)

nseg=3: A MuonParticle consists of an A- and a BC-segment (a local muon track) matched to a central track. The local muon track and the central track are combined to give the 4-vector of the muon, its charge, $\tan(\lambda)$, η, ϕ, and zAtPca.

B.2 BC-segments with Central Track Match (nseg=2)

nseg=2: A MuonParticle consists of a BC-segment matched to a central track. In this case the 4-vector of the muon, its charge, η, ϕ, $\tan(\lambda)$ and zAtPca are directly coming from the central track.

B.3 A-segments with Central Track Match (nseg=1)

nseg=1: A MuonParticle consists of an A-segment matched to a central track. In this case the central track and the A-segment are combined to give the muon 4-vector, its charge, η, ϕ, $\tan(\lambda)$ and zAtPca.

B.4 Muon Hits or MTC Matched to Central Track (nseg=0)

nseg=0: A MuonParticle does not have any muon segment. It is either a central track matched to a muon hit or to a calorimeter muon (MTC). The 4-vector of the muon, its charge, η, ϕ, $\tan(\lambda)$ and zAtPca are directly coming from the central track.

B.5 A-segments Only (nseg=-1)

nseg=-1: A MuonParticle consists of an A-segment only, not matched to a central track. The momentum measured by the muon system is set to 0 and the p_T is set to 100000. The η, ϕ and $\tan(\lambda)$ give the position of the A-segment.

B.6 BC-segments Only (nseg=-2)

nseg=-2: A MuonParticle consists of a BC-segment only, not matched to a central track. The transverse momentum and the 4-vector of the muon are estimated from the direction of the BC-segment with respect to the center of the detector.

B.7 A+BC-segments Only (nseg=-3)

nseg=-3: A first estimate of the transverse momentum is made from the curvature between A- and BC-segments. A fit of the A- and BC-segments into a local muon track is made. If the fit is successful the momentum of the fitted local muon track becomes the momentum of the muon. Otherwise the initial momentum estimate is kept.

Appendix C

Fitting Methods

The unbinned maximum likelihood fitting method is used in many current high energy physics analysis. It maximizes the use of available information to obtain the shape of a distribution in the face of limited statistics.

Suppose we have N measurements $x_i, \ldots, x_N$ in the range $x_{low} \leq x_i < x_{high}$. The set x_i is fitted to a normalized probability distribution function, $f(x|\mathbf{p})$, where the $\mathbf{p}$ is the fit parameter. $f(x|\mathbf{p})$ is normalized such that $\int_{x_{low}}^{x_{high}} f(x|\mathbf{p})dx \equiv A(\mathbf{p})$ [114] [116].

C.1 Probability Density Functions

In an experiment whose outcome is characterized by a single continuous variable x the probability to observe this variable in the interval $[x, x + dx]$ is $f(x)dx$. The function $f(x)$ is called the probability density function (PDF). It gives the fraction of times that x is observed in the interval $[x, x + dx]$ in the limit of an infinitely large number of observations. It is normalized to one:

$$\int_{x_{min}}^{x_{max}} f(x)dx = 1. \tag{C.1}$$

Some terms used in this paper are listed in table C.1.

The normalized term is given by $G(x), S(x), E(x), P(x)$, or

$C(x) = T(x)/(I(x_{high}) - I(x_{low}))$, where $I(x)$ is the indefinite integral of term $T(x)$ and

Function	Symbol	Term, $T(x)$	Indefinite integral, $I(x)$
Gaussian	$G(x)$	$e^{-(x-\mu)^2/2\sigma^2}$	$\sqrt{2\pi}\,\sigma P(\frac{x-\mu}{\sigma})$
Smeared exponential	$S(x)$	$e^{-\kappa x+\frac{1}{2}\kappa^2\sigma^2}\; P(x/\sigma-\kappa\sigma)$	$P(x/\sigma)-T(x))/\kappa$
Exponential	$E(x)$	$e^{-x/\lambda}$	λ
Polynomial(1st order)	$C(x)$	$1+mx$	$x+\frac{1}{2}x^2$

Table C.1: Probability density function (PDF) terms.

$x_{low} : x_{high}$ is the plot range. x and σ are the data points and their measurement errors respectively. μ, κ (or $1/\tau$), and x_0 are fit parameters. $P(x)$ is the Normal Frequency function: $P(x) \equiv \frac{1}{\sqrt{2\pi}}\int_{-\infty}^{x} e^{-\frac{1}{2}u^2}\mathrm{d}u = \frac{1}{2}+\frac{1}{2}erf(x/\sqrt{2})$.

C.2 Maximum Likelihood

For a PDF $f(x|\mathbf{p})$, where the functional form is known, but which contains at least one unknown parameter ($\mathbf{p}$) the method of maximum likelihood can be used to estimate $\mathbf{p}$ from a finite sample of data. For n measurements the probability that x_i is in $[x_i, x_i+dx_i]$ is

$$\prod_{i=1}^{n} f(x_i|\mathbf{p})dx_i. \tag{C.2}$$

If the PDF and the assumed value for $\mathbf{p}$ are correct, the probability for the measured data should be high. As the dx_i do not depend on $\mathbf{p}$ the same is true for

$$\mathcal{L}(\mathbf{p}) = \prod_{i=1}^{n} f(x_i|\mathbf{p}). \tag{C.3}$$

$\mathcal{L}$ is called the likelihood function. Provided that $\mathcal{L}$ is differentiable for $\mathbf{p}$, maximizing $\mathcal{L}$ by imposing

$$\frac{\partial\mathcal{L}}{\partial\mathbf{p}} = 0 \tag{C.4}$$

will provide an estimator $\hat{\mathbf{p}}$ for the parameter $\mathbf{p}$.

Instead of maximizing $\mathcal{L}$ it is more common to maximize $\log \mathcal{L}$. As the logarithm is a monotonically increasing function it will be at its maximum for the same $\mathbf{p}$ as $\mathcal{L}$ would be, but now the product of $\mathcal{L}$ becomes a sum:

$$\log(\mathcal{L}) = \sum_{i=1}^{n} \log f(x_i|\mathbf{p}). \tag{C.5}$$

C.3 Unbinned Maximum Likelihood Fit

If we now define $f'(x|\mathbf{p}) \equiv f(x|\mathbf{p})/A(\mathbf{p})$, so that $f'(x|\mathbf{p})$ is normalized to 1, we obtain the standard Maximum Likelihood function

$$F_u(\mathbf{p}) = -\sum_{i=1}^{N} \ln f'(x_i|\mathbf{p}). \tag{C.6}$$

The normalization of $f'(x|\mathbf{p})$ can be any constant (with respect to $\mathbf{p}$), not just 1, since this A does not have to be 1, and anything else would merely introduce an additive constant which will not change the fit results, just the value of $F'_u(\mathbf{p})$ at the minimum.

Appendix D

Implementation of Maximum Likelihood Fitting

We use The MINUIT minimization program in root (TMinuit class) to implement unbinned maximum likelihood for B_s mass and lifetime fitting. In the implementation, mass and lifetime are fitted simultaneously using an unbinned maximum log-likelihood method. The likelihood function $\mathcal{L}$ is given by:

$$\mathcal{L} = \prod_{i=1}^{N}[f_{sig}\mathcal{F}^i_{sig} + (1 - f_{sig})\mathcal{F}^i_{bck}]. \tag{D.1}$$

The source code and user tips are available at this web site [117]. The source code includes 4 programs:

- ltfitting.C

  This is the main function which calls other auxiliary functions to read data, perform minimization, draw BsMass, Lifetime plots. To run the program, do "root ltfitting.C".

- ltfitting.h

  This is the file of component "ltfitting". It defines variable arrays, such as mass, lifetime, lifetimeError, and it initializes parameters for maximum likelihood fitting.

- likelihood.cpp (define function "MinuitFit()")

  The function "MinuitFit()" is called by "ltfitting.C".

It performs the maximum likelihood fitting by using MINUIT.

The minimization object is: LogLikelihood.

LogLikelihood is the sum of –log(normLikelihood) for each event.

normLikelihood = fraction*Func_mass_sigB*Func_life_sig

+ (1-fraction)*Func_mass_bkgB*Func_life_bkg;

1. fraction – fraction of signal over all candidates.
2. Func_mass_sigB = Gaus(Mass, M0, sigmaM, minM0, maxM0);

   Bs mass signal is described as a normalized Gaussian function in the mass region minM0 and maxM0.
3. Func_mass_bkgB = Polynomial1(Mass, slope, minM0, maxM0);

   Bs mass background is described as a 1st-order polynomial with a straight line and slope in the mass range minM0–maxM0.
4. Func_life_sig = GausExp(Lifetime, L0, ctauresol);

   Bs lifetime signal is described as an exponential convoluted with a Gaussian of width equal to the calculated event-by-event uncertainty.

   ctauresol=LifetimeError*scalefactor.
5. Func_life_bkg = lifetime_background(Lifetime,ctauresol, slopeleft,

   sloperight,fracleft,fracright,tmin,tmax);

   The background lifetime is parametrized as the sum of a zero-lifetime Gaussian, a positive long-lived exponential decay and a negative exponential decay function.

- fitfun.cpp

  Define useful normalized Probability Density Function (PDF).

References

[1] "B Physics at the Tevatron: Run II and Beyond", Fermilab-Pub-01/197 (2001).

[2] "The CKM Matrix and the Unitarity Triangle", Proceedings of the First Workshop on the CKM Unitarity Triangle, CERN, February 2002.

[3] C. Murphy, Indiana University, PhD dissertation, "Inclusive J/ψ Production at DØ" (1995).

[4] Particle Data Group (see webpage http://pdg.lbl.gov).

[5] E. Abers and B. W. Lee, Phys. Rep. C **9** (1973) 1.

[6] C. N. Yang and R.L. Mills, Phys. Rev. **96** (1954) 191.

[7] W. Marciano and H. Pagels, Phys. Rep. C **36** (1954) 137.

[8] S. Glashow, Nucl. Phys. **22** (1961) 22; S. Weinberg, Phys. Lett. **12** (1967) 132; A. Salam, "Elementary Particle Physics".

[9] J. Goldstone and S. Weinberg, Phys. Rev. **127** (1962) 965.

[10] P. W. Higgs, Phys. Lett. **12** (1964) 132; Phys. Rev. Lett. **13** (1964) 508.

[11] D. E. Groom *et al.* [Particle Data Group], Eur. Phys. J. C **15** (2002) 1.

[12] L. Wolfenstein, preprint No. NSF-ITP-90-29; Phys. Rev. D **43** (1991) 151.

[13] P. Schewe, J. Riordon, and B. Stein, "High-Precision Tests of the Standard Model"; Physics News Update, Number 600 #1, (August 1, 2002).

[14] Y. Nir, "CP Violation: The CKM Matrix and New Physics", hep-ph/0208080.

[15] F. Wilczek, "Inventory and Outlook of High Energy Physics", hep-ph/0212128.

[16] J. H. Christenson, J. W. Cronin, V. L. Fitch and R. Turlay, "Evidence For The 2 Pi Decay Of The K(2)0 Meson," Phys. Rev. Lett. **13** (1964) 138.

[17] NA48 Collaboration, G. Unal, invited talk at ICHEP 2002 (Amsterdam).

[18] BELLE Collaboration, M. Yamauchi, invited talk at ICHEP 2002 (Amsterdam).

[19] BABAR Collaboration, Y. Karyotakis, invited talk at ICHEP 2002 (Amsterdam).

[20] A. Stocchi, "Experimental Results on Heavy Quarks", talk at ICHEP 2002 (Amsterdam).

[21] CERN, R. Fleischer, invited talk at the 14th topical conference on Hadron Collider Physics, Karlsruhe, Germany, September 29–October 2002.

[22] CERN working group on B oscillations (http://lepbosc.web.cern.ch/LEPBOSC/).

[23] M. Beneke and A. Lenz, J. Phys. G **27** 1219 (2001).

[24] I. Dunietz, Phys. Rev. D **52** 3048 (1995);
R. Fleischer and I. Dunietz, Phys. Rev. D **55** 259 (1997).

[25] E. Braaten and S. Fleming, Phys. Rev. Lett. **74**, 3327 (1995).

[26] M. Kramer, Prog. Part. Nucl. Phys. **47**, 141 (2001).

[27] CDF Collaboration, T. Affolder *et al.*, Phys. Rev. Lett. **85**, 2886 (2000).

[28] T. LeCompte, H. T. Diehl, "The CDF and DØ Upgrades for Run II"; Fermilab Annual Review (2000).

[29] R. Baier, R. Ruckl, ZP **C19**, 251 (1983). M. Vanttinen *et al.*, PR bf D51, 3332(1995); G. Schuler CERN-TH.7170/94

[30] H. Fritzsch PL 67B, 217(1977); R. Gavai *et al.* IJ of MP A10, 3043(1995);
J. Amundson *et al.* PL **B390**, 323 (1997);
O. J. P. Eboli *et al.* PRD **60**, 117501 (1999);
C. B. Mariott, M. B. Ducati, G. Ingelman, hep-ph/0111379 (2001).

[31] A. Edin, G. Ingelman, J. Rathsman, PRD **56**, 7317 (1197).

[32] G. Bodwin, E. Braaten and G. Lepage, PRD **51**, 1125 (1995), PRD **55**, 5853 (1997); E. Braaten and S. Fleming PRL **74**, 3327 (1995); M. Cacciari *et al.* PL B **356**, 553 (1995); P. Cho, A. Leibovitch PR **D53** 150(1996); 6203(1996).

[33] A. Zieminski, invited talk at the Charm Workshop, Trento, June 17-22, 2002; Also

invited talk at "Proceedings of the 1999 Conference on Physics in Collision", Ann Arbor, Michigan.

[34] A. Zieminski, "Color Octet Model predictions for direct J/ψ production", `http://hep.physics.indiana.edu/~zieminsk/dimuon/c8_plots_jpsi.txt`.

[35] BABAR Collaboration, B. Aubert *et al.*, Phys. Rev. Lett. **87**, 091801 (2001); Belle Collaboration, K. Abe *et al.*, Phys. Rev. Lett. **87**, 091802 (2001).

[36] J. L. Rosner, Phys. Rev. D**42**, 3732 (1990).

[37] A. S. Dighe *et al.*, Phys. Lett. B**369**, 144 (1996).

[38] A. S. Dighe, I. Dunietz and R. Fleischer, Eur. Phys. J. C **6**, 647 (1999).

[39] M. Paulini and K. Burkett, CDF/ANAL/BOTTOM/CDFR/4665 (1998).

[40] I. Dunietz *et al.*, hep-ph/0012219 (2000).

[41] I. Dunietz *et al.*, Phys. Rev. D**43**, 2193 (1991).

[42] A. S. Dighe and S. Sen, Phys. Rev. D**59**, 074002 (1999).

[43] S. D. Holmes, "Design Criteria and Performance Goals for the Fermilab Main Injector", Part. Accel. **58**, 39 (1997); Fermilab-Conf-97/038.

[44] G. P. Jackson, "The Fermilab Recycler Ring Technical Design Report", Fermilab-TM-1991 (1996).

[45] DØ Collaboration, S. Abachi *et al.*, "The DØ Upgrade: Detector and it's Physics", Fermilab-Pub-96/357-E (1996); "The DØ Upgrade Forward Preshower, Muon System, and Level 2 Trigger", Fermilab-FN-639 (1996).

[46] DØ Collaboration, S. Abachi *et al.*, "The DØ Detector", Nucl. Instr. Methods Phys. Res. A **338**, 185 (1994).

[47] R. Lipton for the DØ Collaboration, "The DØ Silicon Tracker", Nucl. Instr. Meth. **A418**, 85 (1998).

[48] R. Yarema *et al.*, "A beginners Guide to the SVX II Chip", Fermilab-TM-1892 (1994).

[49] M. Wayne for the DØ Collaboration, "The DØ Upgrade", Nucl. Instr. Meth. **A408**, 103 (1998).

[50] T. Zimmermann *et al.*, "SVX3: A Deadtimeless Readout Chip for Silicon Strip Detectors", Nucl. Instr. Methods Phys. Res., **A409**, 1 (1998); FERMILAB-Conf-97/427.

[51] B. S. Acharya *et al*, "Scintillation Counters for the DØ Upgrade", Nucl. Instr. Meth. **A401**, 45, (1997).

[52] V. Abramov *et al.*, "Forward muon system for the DØ Upgrade", Nucl. Instr. Meth. **A419**, 660 (1998).

[53] O. Eroshin, D. Denisov, "Status of forward muon reconstruction program", DØ Note 3714 (1999).

[54] DØ Collaboration, "The DØ Upgrade", DØ internal technical documentation (1995).

[55] H. U. Bengtsson and T. Sjostrand, Comp. Phys. Comm. **46**, 43 (1987).

[56] CERN Application Software and Database Division, "Dector Description and Simulation Tool", see `http://wwwasd.web.cern.ch/wwwasd/geant/`.

[57] DØ Collaboration, S. Abachi *et al.*, Nucl. Instr. & Meth. paper, in preparation, see `http://www-d0.fnal.gov/computing/MonteCarlo/simulation/d0gstar.html`.

[58] DØ Collaboration, S. Abachi *et al.*, Nucl. Instr. & Meth. paper, in preparation, see `http://www-d0.fnal.gov/computing/MonteCarlo/simulation/d0sim.html`.

[59] DØ Collaboration, S. Abachi *et al.*, Nucl. Instr. & Meth. paper, in preparation, see `http://www-d0.fnal.gov/computing/trigsim/general/docs.html`.

[60] F. Paige and S. Protopopescu, Brookhaven National Laboratory Report BNL-37066 (1985) (unpublished).

[61] QQ – the CLEO event generator, see the webpage: `http://www.lns.cornell.edu/public/CLEO/soft/QQ` .

[62] A. Ryd and D. Lange (BarBar and CLEO Collaboration), see the webpage: `http://www.slac.stanford.edu/~lange/EvtGen/` .

[63] "Pythia 6.2: Physics and Manual", hep-ph/0108264.

[64] F. Stichelbaut and M. Narain, Proceedings of the CHEP'98 Conference.

[65] DØ Collaboration, S. Abachi *et al.*, Nucl. Instr. & Meth. paper, in preparation, see `http://www-d0.fnal.gov/computing/MonteCarlo/MonteCarlo.html`.

[66] DØ Collaboration, S. Abachi *et al.*, Nucl. Instr. & Meth. paper, in preparation, see `http://www-d0.fnal.gov/computing/algorithms/#intro`.

[67] DØ Collaboration, emid webpage, see `http://www-d0.fnal.gov/phys_id/emid/d0_private/emid.html`.

[68] DØ Collaboration, muonid webpage, see `http://www-d0.fnal.gov/phys_id/muon_id/d0_private/muon_id.html`.

[69] DØ Collaboration, jetid webpage, see `http://www-d0.fnal.gov/~d0upgrad/d0_private/software/jetid`.

[70] DØ Collaboration, S. Abachi *et al.*, Nucl. Instr. & Meth. paper, in preparation, see "DØ Computing and Software Operations and Upgrade Plan", May 22, 2002.

[71] DØ Collaboration, S. Abachi *et al.*, Nucl. Instr. & Meth. paper, in preparation, see `http://wwwasdoc.web.cern.ch/wwwasdoc/hbook_html3/hboomain.html`.

[72] CERN, "Root: An Object Oriented Data Analysis Framework", see webpage: `http://root.cern.ch`.

[73] FNAL database group, "SAM: Sequential data Access via Meta-data", see webpage: `http://d0db.fnal.gov/sam/`.

[74] DØ Collaboration, S. Abachi *et al.*, Nucl. Instr. & Meth. paper, in preparation, see O. Peters, documentation at "d0release/muo_hit/doc".

[75] O. Peters, "Muon Segment Reconstruction – Linked List Algorithm", DØ Note 3901 (2002).

[76] F. Deliot, "The Fit Algorithm in muo_trackreco", DØ private documentation (Nov. 2002).

[77] L. Chevalier *et al.*, "Track Parameter Error Matrix Propagation in Matter and Magnetic Field, Error Matrices Combination", DØ Preliminary (2001).

[78] D. Zieminska, C. Luo, Muon ID note (version 1,2), DØ private material.
S.Soldner-Rembold *et al.*, "DØ Muon Identification Primer", DØ webpage.

[79] S. Protoposescu, "ThumbNail: a compact data format", DØ Note 3979, April 28, 2002.

[80] "Contents of the Muon Thumbnail in p13", DØ Note 4091 (2003).

[81] DØ Collaboration, S. Abachi *et al.*, Nucl. Instr. & Meth. paper, in preparation, see `http://www-d0.fnal.gov/d0dist/dist/packages/muo_analyze/devel/doc/`.

[82] J. Butler, "Local Muon Momentum Resolution", DØ Note 4002 (2002).

[83] H. Haggerty, R. Markeloff, D Mueller, and Y. Shao , "Time-to-Distance Relationship for DØ Muon Drift Tubes", DØ Note 2104.

[84] CERN software documentation, "Garfield: Simulation of gaseous detectors", see `http://consult.cern.ch/writeups/garfield`.

[85] B. Gomez, "Time-to-Distance Relationship for the DØ Proportional Drift Tubes PDTs using Garfield", DØ Note 3892.

[86] Maxwell 3D Field Simulator, Ansoft Corporation, USA, supported at CERN.

[87] Y. A. Yatsunenko, "Reconstruction of the drift characteristic by the integral equation", DØ Note 3181.

[88] DØ Collaboration, S. Abachi *et al.*, Nucl. Instr. & Meth. paper, in preparation, see `http://hep.physics.indiana.edu/~chuluo/time-to-distance`.

[89] M. Naarin, plenary talk at ICHEP 2002 (Amsterdam).

[90] D. Bauer, invited talk at "Hadron Collider Physics 2002", Karlshure, Germany, Sept 29-Oct 4, 2002.

[91] S. Willenbrock, "Hadron Collider, the Standard Model and Beyond", 2002, hep-ph/0201071.

[92] H. Castilla, invited talk at the Workshop on the Quarkonium, November 8-10, CERN, 2002.

[93] C. Luo, talk at the "American Physics Society April Meeting 2003", Philadelphia, April 5-7, 2003.

[94] DØ Collaboration, S.Abachi *et al.*, Phys.Lett. B 370, 239 (1996); Phys. Rev Lett. 82 35 (1999).

[95] CDF Collaboration, F. Abe *et al.*, Phys. Rev. Lett. **69**, 3704 (1992); **79**, 572 (1997); **79**, 578 (1997).

[96] CDF Collaboration, D. Acosta *et al.*, Phys. Rev. D **66**, 092001 (2002).

[97] M. Mangano, P. Nason, G.Ridolfi, NP B373, 295 (1992).

[98] DØ Collaboration, S. Abachi *et al.*, Nucl. Instr. & Meth. paper, in preparation, see `http://www-d0.fnal.gov/~ghesketh/tracking/index.html`.

[99] DØ Collaboration, S. Abachi *et al.*, Nucl. Instr. & Meth. paper, in preparation, see `http://www-d0.fnal.gov/~diehl/diehl.html`.

[100] `http://hep.physics.indiana.edu/~chuluo/Jpsi-production/pre-geant`.

[101] `http://hep.physics.indiana.edu/~chuluo/Jpsi-production`.

[102] J. Huang, C. Luo, A. Zieminski, "Run II J/ψ cross sections in bins of rapidity", see `http://hep.physics.indiana.edu/~zieminsk/jpsi_cross_sect/JPsiCS.html`.

[103] CDF Collaboration, F. Abe *et al.*, Phys. Rev.D **65**,052005 (2002).

[104] DØ webpage, muonid group, see `http://www-d0.fnal.gov/phys_id/muon_id/d0_private/muon_id.html`.

[105] DØ webpage, *b*-Physics Working Group, see `http://www-d0.fnal.gov/Run2Physics/ckm/d0_private/computing`.

[106] R. McCroskey, "Measurements of Level-1 Trigger Efficiencies from DØ Data", DØ Note 3949.

[107] DØ webpage, *b*-Physics Working Group, see

`http://www-d0.fnal.gov/Run2Physics/ckm/` .

[108] DØ webpage, Tracking Algorithm group, see `http://www-d0.fnal.gov/global_tracking/` .

[109] A. Spiridonov, “An Approach to Global Vertex Fitting”, DESY-IfH Zeuthen/IHEP Protvino, October 15, 1996.

[110] R. Luchsinger and C. Grab, ”Vertex Reconstruction by means of the method of Kalman Filtering”, Computer Physics Communications 76 (1993) 263-280.

[111] DØ webpage, A. Schwartzman, ”Vertex fitting and finding in ROOT”, see `http://www-d0.fnal.gov/~sch/d0_private/d0root/rootVertex.html`.

[112] F. Abe *et al.*, CDF Collaboration, Phys. Rev. D.**65**, 052005 (2000).

[113] F. Abe *et al.*, CDF Collaboration, Phys. Rev. Lett., **77**, 1945 (1996).

[114] T. J. Adye, PhD dissertation, Lincoln College, Oxford (April 1998).

[115] O. Peters, PhD dissertation, University of Nijmegen, NIKHEF at Amsterdam (2001).

[116] D. Bauer, PhD dissertation, Imperial College of Science, Technology and Medicine (August 2002).

[117] `http://hep.physics.indiana.edu/~chuluo/BsJpsiPhi/lifetime`.

Curriculum Vitae

Personal

Name:	Chunhui Luo
Date of birth	April 9, 1969
Citizenship	P.R.China

Education

1998-2003	**Ph.D.**, Indiana University, Bloomington, IN
1994-1997	**M.Sc.** Institute of High Energy Physics, Beijing, China
1987-1992	**B.Sc.** University of Science and Technology of China

Research Experience

FNAL D0	Muon Identification and B physics studies
BEPC BES	Inclusive D0 meson's branching fraction measurement

Work Experience

1997-2003	Research Assistant – Department of Physics, Indiana University
1992-1997	Engineer – Institute of High Energy Physics, Beijing, China

Honors

2003	Outstanding Graduate Student in Experimental Research Award